

AD-A177 358

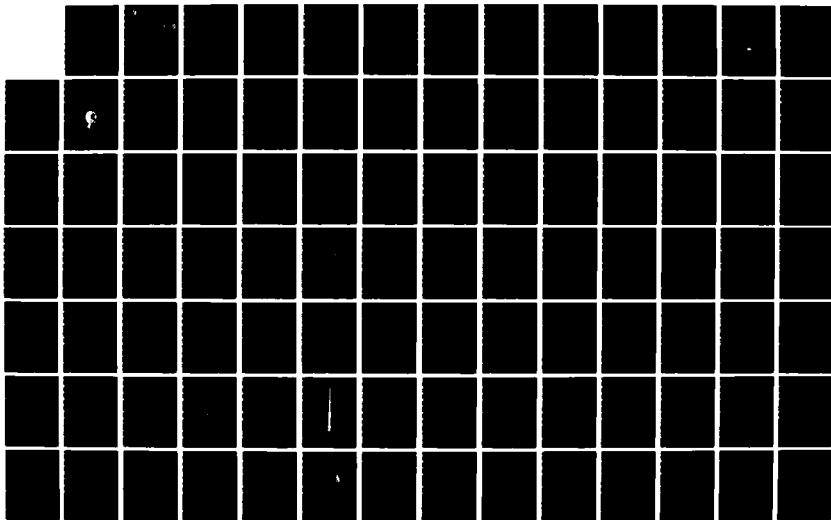
FLUID MECHANICS OF SPINNING ROCKETS(U) UTAH UNIV SALT
LAKE CITY FLUID DYNAMICS LAB G A FLANDRO ET AL JAN 87
AFRPL-TR-86-072 F04611-83-K-0047

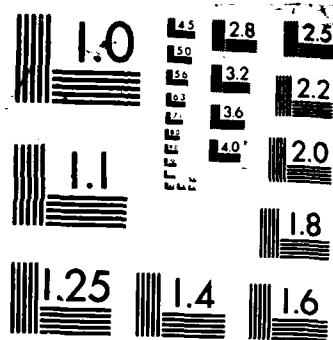
1/2

UNCLASSIFIED

F/G 28/4

NL





MICROCOPY RESOLUTION TEST CHART
NATIONAL BUREAU OF STANDARDS-1963-A



AFRPL TR-86-072

AD:

Final Report
for the period
1 January 1984 to
1 December 1985

Fluid Mechanics of Spinning Rockets

DTIC
ELECTE
FEB 25 1987
S D

January 1987

Authors:

G. A. Flandro
W. K. VanMoorhem
R. Shorthill
K. Chen
M. Woolsey
C. D. Clayton
P. A. Findlayson

University of Utah
Fluid Dynamics Laboratory
Salt Lake City, Utah 84112

F04611-83-K-0047

Approved for Public Release

Distribution is Unlimited. The AFRPL Technical Services Office has reviewed this report, and it is releasable to the National Technical Information Service, where it will be available to the general public, including foreign nationals.

AD-A177 350

DTIC FILE COPY

prepared for the:

**Air Force
Rocket Propulsion
Laboratory**

Air Force Space Technology Center
Space Division, Air Force Systems Command
Edwards Air Force Base,
California 93523-5000

87 2 25 018

NOTICE

When U.S. Government drawings, specifications, or other data are used for any purpose other than a definitely related government procurement operation, the government thereby incurs no responsibility nor any obligation whatsoever, and the fact that the government may have formulated, furnished, or in any way supplied the said drawings, specifications, or other data, is not to be regarded by implication or otherwise, or conveying any rights or permission to manufacture, use, or sell any patented invention that may in any way be related thereto.

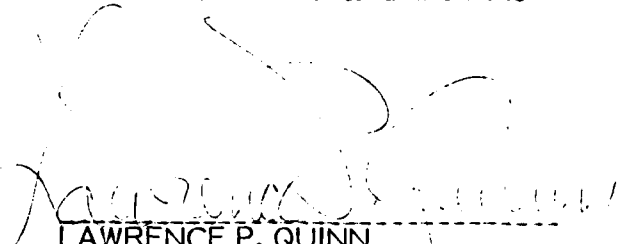
FOREWORD

This report on the Fluid Mechanics of Spinning Rockets was prepared by the University of Utah under contract F04611-83-K-0047 with the Air Force Rocket Propulsion Laboratory (AFRPL), Edwards Air Force Base, CA. AFRPL Project Manager was Mr Gary L. Vogt.

This technical report has been reviewed and is approved for publication and distribution in accordance with the distribution statement on the cover and on the DD Form 1473.

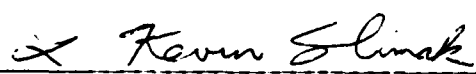


GARY L. VOGT
Project Manager



LAWRENCE P. QUINN
Chief, Aerothermochemistry
Branch

FOR THE COMMANDER



L. KEVIN SLIMAK
Acting Chief, Propulsion Analysis
Division

AD-A177350

REPORT DOCUMENTATION PAGE

1a. REPORT SECURITY CLASSIFICATION UNCLASSIFIED			1b. RESTRICTIVE MARKINGS		
2a. SECURITY CLASSIFICATION AUTHORITY			3. DISTRIBUTION/AVAILABILITY OF REPORT Approved for Public Release. Distribution is Unlimited.		
2b. DECLASSIFICATION/DOWNGRADING SCHEDULE					
4. PERFORMING ORGANIZATION REPORT NUMBER(S)			5. MONITORING ORGANIZATION REPORT NUMBER(S) AFRPL-TR-86-072		
6a. NAME OF PERFORMING ORGANIZATION University of Utah		6b. OFFICE SYMBOL (If applicable)		7a. NAME OF MONITORING ORGANIZATION Air Force Rocket Propulsion Laboratory	
6c. ADDRESS (City, State and ZIP Code) Fluid Dynamics Laboratory Salt Lake City, UT 84112		7b. ADDRESS (City, State and ZIP Code) AFRPL/DYCR Edwards Air Force Base, CA 93523-5000			
8a. NAME OF FUNDING/SPONSORING ORGANIZATION		8b. OFFICE SYMBOL (If applicable)		9. PROCUREMENT INSTRUMENT IDENTIFICATION NUMBER F04611-83-K-0047	
8c. ADDRESS (City, State and ZIP Code)		10. SOURCE OF FUNDING NOS.			
		PROGRAM ELEMENT NO.		PROJECT NO.	TASK NO.
		62302F		5730	00
11. TITLE (Include Security Classification) FLUID MECHANICS OF SPINNING ROCKETS (U)		WORK UNIT NO. HP			
12. PERSONAL AUTHOR(S) Flandro, G.A., VanMoorhem, W.K., Shorthill, R., Chen, K., Woolsey, M., Clayton, C.D., and Finlayson, P.A.					
13a. TYPE OF REPORT Final		13b. TIME COVERED FROM 84/1/1 TO 85/12/1		14. DATE OF REPORT (Yr., Mo., Day) 87/1	
				15. PAGE COUNT 185	
16. SUPPLEMENTARY NOTATION The author is now associated with the Guggenheim School of Aerospace Engineering, Georgia Institute of Technology, Atlanta, GA 30332					
17. COSATI CODES			18. SUBJECT TERMS (Continue on reverse if necessary and identify by block number.)		
FIELD	GROUP	SUB GR.	Spinning Rockets, Spin Stabilized, Internal Ballistics, Nutation Instability, Axial Vortex Flow, Gasdynamic Driving, Jet Damping, Gas Sloshing.		
21	08	2			
19. ABSTRACT (Continue on reverse if necessary and identify by block number.) This report presents the results of a detailed investigation of the influence of time-dependent combustion gas flows on the attitude dynamics of spinning rocket propelled space vehicles. The work was motivated by a need to understand the origins of a potentially serious system performance problem first detected in the PAM-D series of spin stabilized upper stages. Small wobbling (often referred to as "nutation" or "coning") induced during separation of the spacecraft from its spin platform in the space shuttle bay, was enormously amplified during the rocket motor burn. The growth ceased abruptly at motor burnout, and final cone angles as large as 17° were reached in some flights. The same phenomenon was encountered in two flights of the PAM-DII, a similar vehicle utilizing a larger motor. Conventional theories of spinning rocket dynamics failed to explain this behavior. Since the telemetry data shows that the severity of the problem depends on spacecraft mass properties and other system parameters, it is crucial that the origins of the instability be understood completely in order that serious mission degradation can be avoided in future orbit raising operations. A costly interim fix, which sidesteps the need to understand the physical origins of the problem, is the use of a strap-on nutation control system as used in the Air Force SGS II missions. This approach is in direct conflict with the philosophy of solid rocket space propulsion, which is based on its inherent simplicity and low cost.					
20. DISTRIBUTION/AVAILABILITY OF ABSTRACT UNCLASSIFIED/UNLIMITED <input checked="" type="checkbox"/> SAME AS RPT. <input type="checkbox"/> DTIC USERS <input type="checkbox"/>			21. ABSTRACT SECURITY CLASSIFICATION UNCLASSIFIED		
22a. NAME OF RESPONSIBLE INDIVIDUAL Gary L. Vogt			22b. TELEPHONE NUMBER (Include Area Code) (805) 275-5258		22c. OFFICE SYMBOL DYCR

Block 19.

This program of research resulted in a greatly improved understanding of the role played by the internal ballistics of the rocket motor in the PAM-D coning phenomenon. A comprehensive computational fluid dynamic simulation of the complete solid rocket motor/spacecraft system shows that observed PAM-D nutation instability is caused by the interaction of the complex unsteady internal flow field within the rocket motor with vehicle wobbling motions.

A major element of the phenomenon is the strong axial vortex core produced within the combustion chamber by the vehicle spin. The circumferential flow velocity induced by the vortex velocity field is greatly intensified as the vortex core is "stretched" through the nozzle throat. Small wobbling (nutation) of the spacecraft induces an unsymmetrical pressure pattern within the combustion chamber that is similar to the classical inertial wave phenomenon. The fluctuating velocity field associated with this wave interacts strongly with the vortex core, and the resulting unsteady gas motion is an undulating vortex filament, orbiting the chamber axis as it leaves through the nozzle. From a control volume point of view, there results a net outflow of lateral angular momentum from the system. This angular momentum flux is balanced by a net torque acting on the spacecraft that can exceed the well-known jet damping moment. Under certain conditions related to the size of the chamber, moments of inertia of the spacecraft, size and location of the nozzle throat, and position of the motor with respect to the center of mass, the system is unstable and the amplitude of the nutation increases with time.

The phenomenon just described is referred to throughout the report as "gasdynamic driving" and is the direct, unsteady analog of the jet damping effect. Jet damping accounts only for the steady part of the internal flow. Previous jet damping calculations have accounted for neither the vortex mean flow component nor the gas flow fluctuations induced by wobbling.

A detailed numerical study was conducted in which the theoretical results were employed in the simulation of the flights of several actual spinning rocket systems. The simulations employed only actual spacecraft mass distributions, geometry, and propulsion system properties. Account was taken of changes in properties with time as propellant is consumed. The STAR 48 propelled PAM-D, DII, and SGS II flights were simulated, along with two examples of an earlier system using the STAR 37 motor that did not experience coning. The results showed that the gasdynamic effects account for all major features of the instability.

Since the coning instability phenomenon had not been encountered prior to the PAM-D experience, it is necessary to identify those features of this spacecraft design that lead to the difficulty. On the basis of the results of this study, it has become clear that the nutation instability is not the result of a design fault in either the rocket motor or any other element of the system. The following features of the system have a direct bearing on the growth of the instability and the final amplitude of the nutation angle: (1) the prolate spacecraft mass distribution dictated by packaging constraints, (2) the large, nearly spherical rocket motor dictated by the impulse requirements of the missions, (3) thick propellant web and resulting long motor burning time, and (4) the highly submerged nozzle with a small throat and nozzle entrance within the combustion chamber. Growth of the instability is largest near motor burnout because the longer stay-time of gas particles within the chamber allows a longer interaction with the inertial forces related to the spin. The long burning time of STAR 48 and PAM DII motors is a direct contributory factor since the small perturbing torques caused by the unsteady flow are given a sufficiently long period to influence the vehicle dynamics.

Preliminary system design guidelines based on the results of the study are presented. It is recommended that additional experimentation be performed to enhance the understanding of the phenomenon. It is especially important that experiments be conducted using properly instrumented rocket motors. Data from spinning rocket tests conducted in test facilities employing a fixed axis of rotation does not contribute useful information relating to the nutation instability phenomenon. It will be necessary either to make the measurements under freefall conditions or to construct tests stands with lateral degrees of freedom in order that the unsymmetrical, time-dependent internal ballistics effects can be activated.

TABLE OF CONTENTS

SECTION	PAGE
1.0 INTRODUCTION	1
1.1 DESCRIPTION OF PROBLEM	2
1.2 DESCRIPTION OF RESEARCH PROGRAM	3
1.3 SYNOPSIS OF RESULTS	6
2.0 SPACECRAFT NUTATION INSTABILITY OBSERVATIONS	9
2.1 DESCRIPTION OF DATA SET	9
2.2 CHARACTERISTICS OF CONING BEHAVIOR	11
2.3 PAM-D OBSERVATIONS	19
2.4 SGS II (SECOND STAGE) FLIGHT OBSERVATIONS	28
2.5 PAM-DII FLIGHT DATA	28
2.6 CORRELATION OF CONING DATA WITH SYSTEM PARAMETERS	31
2.7 SUMMARY OF KEY FEATURES FROM THE CONING DATA	35
3.0 SPACECRAFT MOTION	37
3.1 ROTATIONAL DYNAMICS OF ROCKET PROPELLED VEHICLES	37
3.2 SPACECRAFT FREE FALL ATTITUDE DYNAMICS	41
3.3 SPACECRAFT DYNAMICS WITH STEADY MOTOR GAS FLOW	42
3.4 EFFECTS OF UNSTEADY GAS FLOW ON VEHICLE DYNAMICS	43
3.5 SOLUTIONS FOR SIMPLE DISTURBING MOMENTS	44
4.0 PROPOSED NUTATION INSTABILITY MECHANISMS	49
4.1 DISTURBING TORQUES FIXED WITHIN THE SPACECRAFT	49
4.2 EFFECT OF FLEXIBLE SPACECRAFT COMPONENTS	49
4.3 LIQUID SLOSHING MECHANISMS	51
4.4 INTERACTIONS INVOLVING MOTOR COMBUSTION GASES	52
4.5 PRELIMINARY EVALUATION OF PROPOSED MECHANISMS	53
5.0 INTERACTION OF VEHICLE MOTION WITH GAS FLOW	55
5.1 FORMULATION	55
5.2 JET DAMPING	58
5.3 UNSTEADY FLOW EFFECTS	65
6.0 FLUID DYNAMICS OF SPINNING ROCKET MOTORS	71
6.1 FORMULATION	72
6.2 MEAN FLOW IN A SPINNING ROCKET MOTOR	73
6.3 UNSTEADY FLOW IN A SPINNING ROCKET CHAMBER	76
6.3.1 Inertial Waves	76
6.3.2 Modeling of the Unsteady Flow Field	81
6.3.3 Classical Inertial Wave Solutions	82
6.3.4 Forced Motion of the Combustion Gases	93
6.3.5 Effect of Convection of Wave Energy by the Mean Flow	95
6.3.6 Pumping of Inertial Waves by Vehicle Wobbling	96
6.3.7 Combustion Effects	97
6.4 CHARACTERISTICS OF UNSTEADY FLOW FIELD	100



Codes	
Dist	avail d/or Special
A-1	

7.0	EFFECTS OF GAS DYNAMIC TORQUES	107
7.1	EVALUATION OF GROUP 3 MOMENTS	107
7.2	TORQUES DUE TO CONVECTION OF ANGULAR MOMENTUM	109
7.3	CHARACTERISTICS OF GAS DYNAMIC DISTURBING MOMENT	112
7.4	CALCULATION OF NUTATION GROWTH RATE	114
8.0	COMPARISON OF ANALYTICAL RESULTS TO FLIGHT DATA	123
8.1	SIMULATION OF WESTAR V NUTATION OSCILLATIONS	125
8.2	SIMULATION OF SGSII (STAGE 2) CONING	136
8.3	SIMULATION OF STAR 37E VEHICLES	136
8.4	SIMULATION OF PAM-DII NUTATION BEHAVIOR	141
8.5	OTHER FEATURES OF THE ANALYTICAL RESULTS	146
9.0	CORRECTIVE PROCEDURES	147
9.1	SENSITIVITY OF CONING TO SPACECRAFT/MOTOR PARAMETERS	147
9.2	MINIMIZATION OF CONING IN EXISTING VEHICLES	155
9.3	AVOIDANCE OF NUTATION INSTABILITY IN SYSTEM DESIGN	157
10.0	EXPERIMENTAL STUDIES	159
10.1	DESCRIPTION OF EXPERIMENTAL TASKS	159
10.2	FLOW VISUALIZATION EXPERIMENTS	160
10.3	MEASUREMENT OF UNSYMMETRICAL INERTIAL PRESSURE FIELD	160
10.4	DEVELOPMENT OF FIBER OPTIC LASER-DOPPLER FACILITY	161
11.0	CONCLUSIONS	163
11.1	ASSESSMENT OF GASDYNAMIC NUTATION INSTABILITY MODEL	163
11.2	RECOMMENDATION FOR CONTINUED RESEARCH	165
11.3	CONCLUDING REMARKS	166
	REFERENCES	169
	NOMENCLATURE	175
	APPENDIX	177

ILLUSTRATIONS

<u>Figure</u>	<u>Title</u>	<u>Page</u>
1	Development of Coning Instability	1
2	Angular Velocity Components in Body-Fixed Coordinate Frame	3
3	Cross Section of STAR 48 Motor Showing Vortex Core	6
4	Typical Pitch Angular Velocity (From Rate Gyro Data)	12
5	Comparison of Measured and Predicted Nutation Frequency	14
6	Precession and Nutation vs Time	15
7	Projection of Angular Velocity Vector on Lateral Plane	16
8	Placement of Instrumentation (WESTAR-V)	17
9	Pitch Rate vs Yaw Rate Amplitude (WESTAR-V)	18
10	Comparison of Actual and Predicted Angular Rate	20
11	Behavior of Pitch Rate at Start of Instability	21
12	STAR 48 Burnback Profiles	22
13	Amplitude of Yaw Rate Signal vs Time (WESTAR-V)	24
14	Yaw Rate Gyro Signal vs Time (WESTAR-V)	25
15	Nutation Instability Growth Rate WESTAR-V	26
16	Predicted Motion Using Measured Growth Data (WESTAR-V)	27
17	SGS-II, Flight 2 Second Stage Rate Gyro Signal Data	29
18	PAM-DII Burnback Contours	30
19	Correlation Between Measured Growth Rate and α^*	33
20	Correlation of Moment with Transverse Angular Rate	34
21	Coordinate System	38
22	Plots of Simple Solutions of Spinning Rocket Equations of Motion	47
23	Motor Chamber and Nozzle Geometry	60
24	Effect of Axisymmetric Flow Field on Jet Damping	62
25	Jet Damping Exponential Decay Rate vs Time (WESTAR-V)	63
26	Assumed Axisymmetric Flow Pattern in Simplified Motor	64
27	Simulated Jet Damping Perturbation, SGS II	66
28	Stretching of Lateral Angular Momentum of Particle	68
29	Finite Element Grid for Mean Flow Calculation	77
30	Streamline Pattern in STAR 48 at 50 Seconds	78
31	Streamlines in STAR 48 motor with Spin	79
32	Azimuthal Velocity Component in Rotating STAR 48	80
33	Velocity Components vs Radius (Mode 1,1,1)	86
34	Velocity Components vs Radius (Mode 1,2,1)	87
35	Velocity Components vs Radius (Mode 1,3,1)	88
36	Velocity Components vs Radius (Mode 1,4,1)	89
37	Velocity Components vs Radius (Mode 1,5,1)	90
38	Plots of Inertial Mode Velocity Components vs Axial Position	91
39	Inertial Mode Frequencies vs Fineness Ratio, b	92
40	Radial Velocity Distribution of Forced Motion	101

<u>Figure</u>	<u>Title</u>	<u>Page</u>
41	Flow in Nozzle Entrance	103
42	Axial Distribution of Perturbation Velocity Amplitudes	104
43	Effect of Rossby Number on Radial Perturbation Velocity	105
44	Orientation of Disturbing Moments to Nutation Velocity	113
45	Dimensionless Disturbing Moments (WESTAR-V)	117
46	Disturbing Moment Factors (WESTAR-V)	118
47	Instantaneous Growth Rate vs Time (WESTAR-V)	120
48	Phase Lag of Disturbing Moment (WESTAR-V)	121
49	Effect of Gasdynamic Disturbance on Coning Frequency	122
50	Block Diagram of Nutation Instability Algorithm	124
51	Fineness Ratio b vs Time (STAR 48)	126
52	Mass Flow Rate vs Time (STAR 48)	127
53	Nozzle Throat Area vs Time (STAR 48)	128
54	Moment Scaling Parameter δ vs Time	129
55	Rossby Number vs Time	130
56	Effect of Number of Modes on Growth Rate (WESTAR-V, $t=80$ s)	132
57	Simulated Coning Perturbation (WESTAR-V)	133
58	Simulated Yaw Rate Perturbation (WESTAR-V)	134
59	Nutation Growth Rate vs Time, SGSII (Stage 2)	137
60	Simulated Yaw Rate History, SGSII (Stage 2)	138
61	Calculated Growth Rate Plots for IMP-H (STAR-37E Motor)	139
62	Simulated Spacecraft Motion (IMP-H)	140
63	Calculated Growth Rate, TELESAT-C (STAR-37E Motor)	142
64	Simulated Spacecraft Motion (TELESAT-C)	143
65	Instantaneous Growth Rate vs Time, (RCA-KuBAND, PAM-DII)	141
66	Simulated Nutation Instability, (RCA-KuBAND, PAM-DII)	144
67	Effect of Spin Rate on Nutation Instability Growth	148
68	Sensitivity of Growth Rate to Throat Radius	149
69	Sensitivity of Growth Rate to Nozzle Submergence	151
70	Effect of Residual Nutation at Ignition on Final Amplitude	152
71	Sensitivity of Coning Growth Rate to Moment of Inertia Ratio	153
72	Effect of Lateral Moment of Inertia on Nutation Growth Rate	154
73	Sensitivity of Growth Rate to Fineness Ratio	156
74	Experimental Demonstration of Inertial Mode Resonance	162

1.0 INTRODUCTION

The PAM-D series of spin stabilized upper stage vehicles have exhibited an unexpected wobbling instability appearing during the final half of the motor burn with an apparent growth rate that increases rapidly during the final few seconds of operation. This has been commonly referred to as "coning" or "nutation" of the spacecraft. Figure 1 illustrates the motion and defines the nutation or cone angle between the direction of the flight path and the spin axis of the spacecraft. The final value of angle θ averages about 10° and has reached magnitudes as large as 17° at the end of motor burn in some flights. The rocket motor is believed to be the source of the instability, since growth of the cone angle θ ceases at burnout.

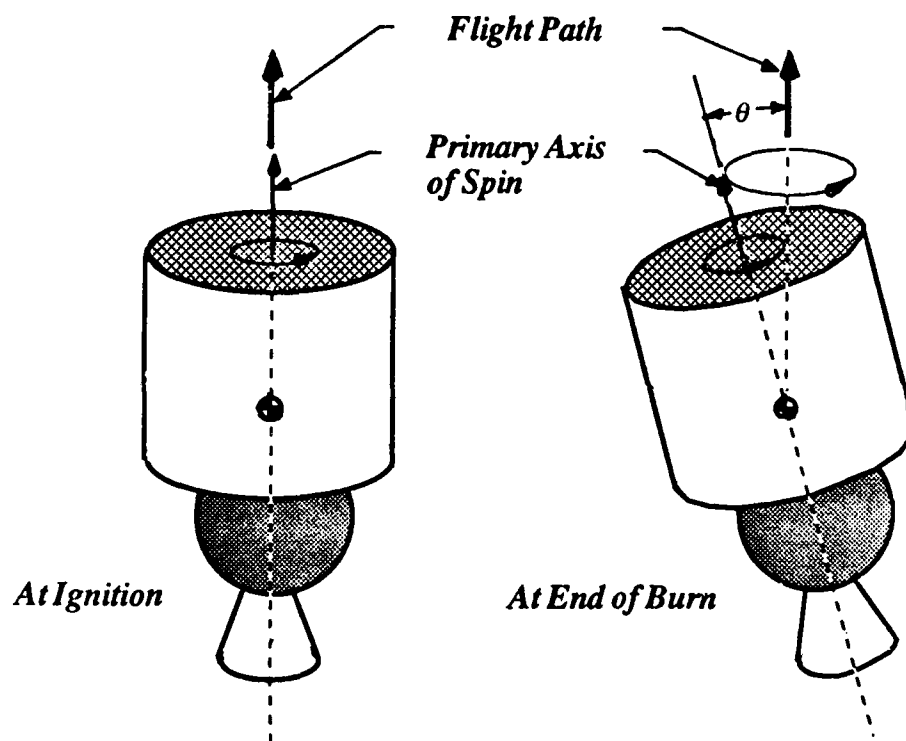


Figure 1. Development of Coning Instability

The PAM-D stage has carried a variety of communication satellites to geosynchronous orbit. It utilizes a solid propellant rocket motor of the STAR 48 family for the perigee propulsion maneuver. It is during operation of the perigee burn that the coning anomaly occurs. Recent flights (PAM-D II) have used a new motor based on the IPSM-II technology with larger diameter and increased total impulse. The two PAM-DII vehicles launched before the cessation of Space Shuttle operations in January 1986 also exhibited significant coning that was similar in most respects to the earlier STAR 48 observations.

1.1 DESCRIPTION OF PROBLEM

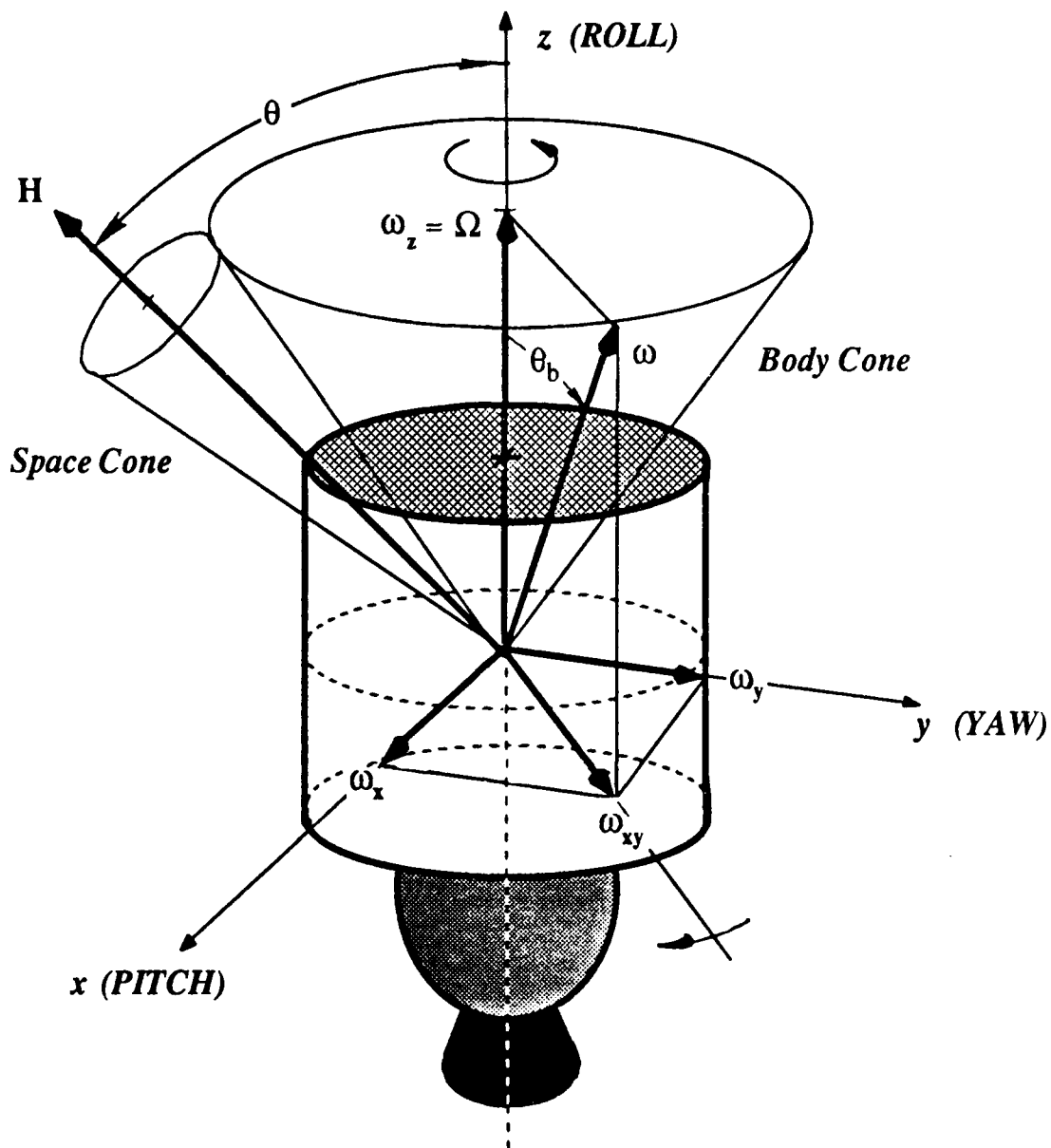
The oscillatory spacecraft motion observed in telemetry data is consistent with conventional spinning, variable mass, rigid body dynamics. In body-fixed coordinates, the motion can be described as a rotation of the vehicle angular velocity vector about the axis of symmetry at nearly the free-precession or "coning" frequency. The projection of the angular velocity vector on a plane normal to the spin axis grows nearly exponentially during the period of instability and always rotates in a direction opposite to the vehicle spin as illustrated in Figure 2. Since instability of this type has not been noticed in other very similar spinning upper stage vehicles, it is essential that the combination of system features or environmental factors that lead to the instability be understood in complete detail. This report describes the results of a comprehensive two-year investigation designed to emphasize the motor gasdynamics as the origin of the observed coning instability.

The correct identification of the disturbing entity responsible for the coning instability is rendered difficult by the apparent smallness of the forces that generate the motion; an estimate of the maximum energy flux driving the wobble is approximately a tenth of a kilowatt. Another difficulty is the plethora of small effects that can cause instability in rotating systems. Wobbling or tumbling due to sloshing of liquids or the vibration or flexing of the spacecraft structure are familiar examples. Spinning, prolate bodies become unstable if any form of internal energy dissipation is present. A classic case was the instability exhibited by the first American earth satellite, the Explorer I, which transitioned from axial spin into an end-over-end tumble not long after its injection into orbit due to the mechanical energy dissipation in its four flexible antennae. Unfortunately, such simple mechanisms fail to explain key features of the PAM-D motion.

Since there is an obvious connection between the growth of the coning and the operation of the propulsion system (*growth of the coning motion either ceases abruptly at motor burnout or shows a dramatic change in its characteristics*), it is appropriate to examine possible interactions between the motor gasdynamics and the vehicle motion. This is the central focus of the research described herein.

1.2 DESCRIPTION OF RESEARCH PROGRAM

The program described was designed to determine the role played by the rocket motor gasdynamics in the generation of nutation instability. Since very little is known of the internal ballistics of spinning solid propellant rocket motors, major effort was focused on study of effects in the rotating combustion gas flow brought about by vehicle motion. Previously, the only known effects were: (1) the pronounced increase of the propellant burning rate caused by spin, and (2) the axial vortex flow produced within the chamber. Erosion of the motor forward closure and the nozzle entrance due to the vortex flow have been observed frequently.



Notes: Angular momentum vector \mathbf{H} is fixed in inertial space and points along the original direction of flight. Body cone rolls on the space cone. For prolate spacecraft, ω_{xy} (projection of the angular velocity vector on x-y plane viewed in body-fixed coordinates), rotates in lateral plane in retrograde direction (opposite to direction of axial spin ω_z). Body cone angle is $\theta_b = \tan^{-1}(\omega_{xy}/\omega_z)$. θ is the nutation "coning" angle.

Figure 2. Angular Velocity Components in Body-Fixed Coordinate Frame

One well-known effect of the motor gas flow on the dynamics of spinning rocket propelled vehicles represents an important clue to the source of the coning disturbance. This is the familiar jet damping phenomenon representing the interaction between vehicle angular motions and the steady part of the flow of combustion products through the motor. The magnitude of this damping torque is found to be of the same order as the apparent driving moment that causes the coning growth. The jet damping effect has been studied since the earliest days of modern rocketry. However, in all previous modeling efforts, only *steady* gas motions were investigated. The work described herein has as a major objective the inclusion of the time-dependent counterpart of the steady jet damping mechanism. This interaction can either add additional damping or, more importantly, can produce a destabilizing influence under some conditions.

There is a vast literature on rotating fluids that has been motivated mainly by meteorological and astrophysical research. This material gives much guidance in the study of the dramatic effects of spin on rocket motor gas flows. It is known from experiments and the theory of rotating fluids that time-dependent flow effects are likely to be excited in the interior of a spinning, wobbling chamber. Detailed treatment of these motions form the backbone of the present investigation. Studies of other possible propulsion-related phenomena, such as deflections of a flexible nozzle exit cone and interactions with aluminum oxide slag material within the motor chamber, have been carried out by other investigators and are reviewed for completeness. It is possible that these effects can influence coning growth, but it is demonstrated in this report that the gas flow interactions are capable of generating all features of the coning phenomenon observed in telemetry data.

An observation indicating the potential importance of the interaction between the combustion chamber motion and the time-dependent flow of combustion gases is provided in the many studies of inertial wave phenomena in spinning confined fluids. Recent work has shown that interactions of this type are responsible for nutation instability of spinning projectiles containing liquid propellants or payloads in the form of viscous fluids. Organized pressure disturbances known as "inertial" or "elastoid-inertial" waves are supported in spinning fluid systems. The inertial forces (especially the Coriolis force) give rise to effects playing a role analogous to compressibility in nonrotating systems. The characteristic frequencies of these waves are very low compared to the fundamental acoustic frequencies of the chamber. They form an infinite set of natural frequencies, proportional to the rate of spin, all of which have magnitudes in the range

$$0 < |\lambda| < 2\Omega \quad (1)$$

where Ω is the spin rate and λ is the inertial mode frequency. Since the vehicle coning (free-precession) frequency is also in this range, it is clear that motion of the chamber will be felt by the contained gas flow as a driving force in a frequency

range that readily excites the inertial waves. The phenomenon is similar to the sloshing of a liquid in a wobbling container. However, inertial pressure waves rather than free surface gravity waves represent the response in the contained gas.

In order to understand the unsteady gas flow in a spinning rocket chamber, several elements must be introduced that have not been studied previously. It is necessary to address the following features:

- Inertial oscillations in the presence of a mean gas flow field with an axial vortex component and recirculation zones,
- Rossby number (a measure of the relative importance of gas particle speed to rotation speed) typically unity or greater implying the importance of convective effects
- Complex chamber boundary geometry changing in size and shape at a rate comparable to the time scale of the angular disturbances.

This combination of features posed a difficult unsolved problem in rocket motor internal ballistics involving coupling of the combustion flow field to the vehicle angular motion.

The research was carried out during a two year period in the form of several analytical and experimental phases. This report gives a detailed account of the key findings. Since so many new elements of rocket motor gas flow required study, most emphasis was placed on clarification of theoretical issues. To maximize physical understanding, a thorough analytical formulation was developed involving approximate solutions of the gasdynamics and its coupling with the spacecraft rotational dynamics. This was backed by a program to develop detailed computational fluid dynamic solutions and by a series of experiments designed to clarify vital features of the fluid flow in spinning systems with strong internal convection. The four main research tasks were:

1. Development of the theory of unsteady internal ballistics of spinning solid propellant rocket motors.
2. Application of the theoretical results in the form of detailed simulations of the rotational dynamics of actual spacecraft configurations.
3. Development of detailed numerical solutions of both steady and unsteady combustion gas flow in spinning rocket motors.
4. Experimental verification of key theoretical findings by means of laboratory cold flow simulations of spinning rocket fluid dynamics.

1.3 SYNOPSIS OF RESULTS

The combined analytical/numerical/experimental study resulted in a much improved understanding of the behavior of the combustion gas flow in a spinning, nutating rocket motor. Major effort was expended to apply this knowledge to several realistic vehicle configurations. A few of the key results are described here.

A finding of major practical importance was that motor internal ballistics effects do produce interactions with vehicle motion that are consistent in a detailed manner with the PAM-D nutation instability observations. *Thus, it is the main conclusion of this investigation that these gasdynamic effects are the principal source of this form of spinning spacecraft dynamic instability.*

Figure 3 illustrates important features of the time-dependent flow in a spinning rocket that affect the coning problem. Shown is a cross-section of the motor during coning growth. The strong vortex core produced by angular momentum conservation as gas particles approach the nozzle entrance is highlighted.

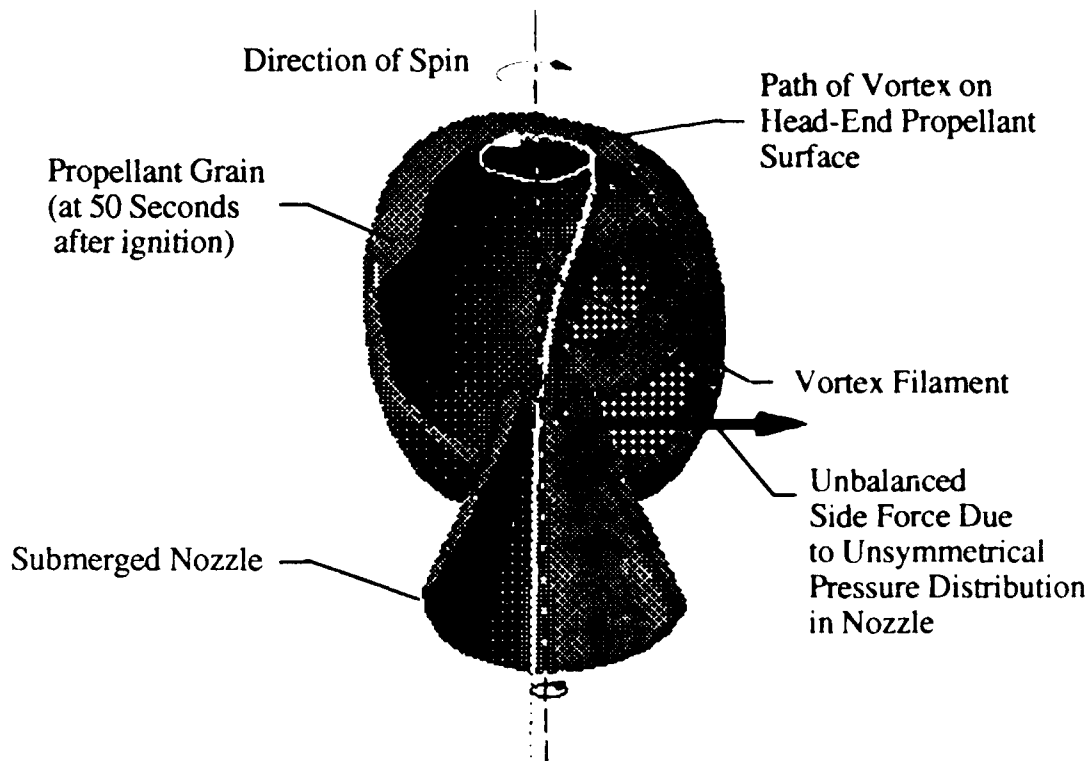


Figure 3. Cross Section of STAR 48 Motor at 50 Seconds after Ignition
Showing Vortex Core

Of major significance is the indication that the vortex does not lie along the longitudinal axis of the motor during vehicle nutation instability. Rather, it orbits about the axis in a helical pattern. This is the result of unsteady flow effects related to the inertial wave phenomenon described earlier. The helical motion is a symptom of an unsymmetrical pressure pattern within the motor chamber. The integrated pressure forces, especially in the nozzle where the most intense unsymmetrical velocity fluctuations and associated pressures act, represent a disturbing torque about the vehicle center of mass that leads to coning instability if its direction relative to the vehicle angular velocity perturbation is in a critical range and if its magnitude is sufficiently large to overcome the jet damping. That is, the component of disturbing torque parallel to the lateral rocking angular velocity vector representing the coning of the spacecraft must be greater than and opposite in sense to the jet damping moment.

A control volume analysis gives useful insight. To an observer in inertial space, the asymmetrical flow emerging from the wobbling rocket nozzle represents a discharge of lateral angular momentum rotating with respect to the vehicle. This momentum flux must be accompanied by a lateral moment vector acting on the motor. This mechanism is analogous to the familiar momentum thrust phenomenon in which the rearward flow of axial linear momentum generates the thrust force on the motor. Only special combinations of chamber size and shape, flow speed, and spin rate result in nutation instability. The gasdynamic interaction can be either an additional stabilizing entity or a source of coning energy.

The program results demonstrate that significant driving energy for coning motions arises in the gasdynamic interactions. This is demonstrated by applying the analysis to four representative spacecraft/propulsion system combinations. Included are simulations of the earlier STAR 37E series that did not exhibit appreciable coning perturbations, the PAM-D (STAR 48) flights, the SGSII (second stage, also employing the STAR 48 motor), and the recent PAM-DII (IPSM II) missions. The results are consistent with the flight telemetry data in a rather complete way both in the timing of key events and in the magnitude of the disturbing torques. It is expected that refinement of the computational algorithm developed in this program will yield a predictive design tool. Improvements would involve inclusion of a more realistic combustion coupling, a detailed mean flow model, and a more realistic combustion chamber geometry. Increased emphasis on numerical solutions will be appropriate in subsequent studies.

Proper understanding of the system interactions yields design guidelines that can be used to avoid the coning instability in a rather straightforward way. The sensitivity of the final nutation amplitude (final cone angle) to a variety of design parameters is established in a preliminary way. The effects of variation of the initial nutation disturbance, nozzle geometry, combustion chamber geometry, location of the rocket relative to the vehicle center of mass, moment of inertia ratio for the

spacecraft, and the vehicle spin rate were studied using a typical PAM-D spacecraft as a baseline. The results showed that the phenomenon is insensitive to the shape of the combustion chamber, but the relative size of the chamber is important. Another important factor in the instability is the long burning time of the STAR 48 and IPSM motors. This gives the small perturbing effects a sufficiently long period in which to affect the system dynamics in a significant manner. Reducing the spin rate deprives the instability of its principal source of energy. However, a major reduction in spin rate is required to reduce the coning growth to an acceptable degree. An area requiring additional study is the sensitivity of the nutation phenomenon to the placement of the nozzle entrance within the motor chamber. On the basis of the preliminary numerical calculations it is shown that careful attention to the amount of nozzle submergence and the contouring of the combustion chamber geometry especially in the aft portion of the motor may allow reduction or elimination of the disturbing torque. Application of annular or plug nozzle technology may allow the complete elimination of the nutation instability problem in future spinning upper stage motor development.

It should be emphasized that the PAM-D coning problem is not the result of an error in the rocket motor design. It is a *system problem* arising from a combination of factors related to the spacecraft geometry and mass distribution, spin rate, the size and configuration of the combustion chamber, the geometry and placement of the nozzle, and the manner in which the spacecraft is deployed from the launch vehicle. In other words, it is a natural phenomenon that has been overlooked because simpler points of view applied satisfactorily to earlier systems.

Finally, it is necessary to observe that much work remains to be accomplished to achieve a complete understanding of the set of phenomena described in this report. Of particular importance will be the eventual verification of the proposed mechanisms in laboratory cold flow experiments, small scale hot rocket motor firings, full scale static motor tests in rotating/nutating test stands, and full scale flight tests of properly instrumented PAM flight hardware. Of great interest would be measurements of the pressure distribution within the nozzle entrance. Experiments conducted in static test stands employing a fixed axis of rotation will not yield relevant data in the search for understanding of the coning phenomenon. A suggested plan for further experimental and analytical research is described.

2.0 SPACECRAFT NUTATION INSTABILITY OBSERVATIONS

The coning phenomenon was first encountered in PAM-D flight operations involving spacecraft delivered into orbit by Delta launch vehicles. The problem has continued into the Space Shuttle-carried series of PAM-D spacecraft. All of these spinning space motor systems utilized the Thiokol STAR-48 (TE-M-711) motor with two different nozzle configurations. One motor, that used in the WESTAR V mission, employed a nozzle stiffened by steel inserts. The appearance of the instability was a distinct surprise, since similar problems had not arisen in earlier orbit raising operations using very similar, but smaller, spun upper stage solid rocket propulsion systems (Thiokol TE-364-4, STAR-37E, for example). Another surprising feature was the appearance of such a disturbance during the motor burn since jet damping was expected to dominate the system dynamics during motor operation.

The importance of determining the cause of the instability has been reinforced by the appearance of coning in the PAM-DII flights (of which two have taken place at the time of writing, the RCA Ku-Band and RCA Ku-Band-2 missions). The DII variant uses the Thiokol IPSM-II motor that is similar in design to the STAR-48 but has an increased diameter of about 63 inches. It is imperative that the motor design features that affect the coning amplitude be determined in order that similar problems can be avoided in the design of new spin stabilized upper stage propulsion systems. Careful review of the data yields important guidance in this regard.

2.1 DESCRIPTION OF DATA SET

In this section we review what is known of the nutation instability problem from telemetered flight measurements. All information presented here was provided by the McDonnell Douglas Astronautics Company¹. Table 1 is a summary of nutation instability observations for three groups of data corresponding to each of the three motor types. Within each group there is significant variation in the severity of the coning as represented by the final cone angle, the average time-constant of the growth of the instability (inverse of the exponential growth rate), and by the final amplitude of the lateral angular velocity perturbation. The latter indicator is the most convenient one to use since it can be estimated directly from rate gyroscope data for flights where such data were available. Since coning was not a problem in the STAR-37E vehicles, comprehensive flight measurements were not made; the corresponding coning information shown in Table 1 was reconstructed from accelerometer data.

The variability of the nutation angular motion is evidently related to a large set of parameters that includes: (1) length of motor run (as affected by grain temperature and propellant off-loading), (2) spacecraft mass, (3) location of the

Table 1. Summary of Spinning Upper Stage Coning Data

Group	Mission	Spin Rate (rpm)	I_0	I_1	Transverse Rate ω_{xy} (Deg/sec)	Growth Rate (Sec ⁻¹)	Cone Angle (Deg)
1 PAM-D (STAR 48)	SBS-A	50.8	365	630	30.0	-	10.5
	SBS-B	50.3	365	630	25.3	0.227	8.6
	SBS-C	51.0	365	658	17.5	0.278	5.9
	SBS-D	51.8	365	658	33.8	-	11.1
	RCA-C'	61.1	273	557	53.4	0.260	16.5
	RCA-D	60.7	273	557	36.3	0.235	11.7
	WESTAR-IV	50.8	339	630	19.7	0.231	6.8
	WESTAR-V	52.4	339	630	24.3	0.190	8.2
	INSAT-1A	41.4	277	828	25.3	0.175	17.1
	GALAXY-A	48.3	386	654	15.0	0.160	5.0
	GALAXY-C	43.2	386	654	20.7	-	7.7
	SGS-II (Stg.2)	70.0	477	2363	~2	~0.05	~1
2 (STAR 37-E)	IMP-H	48.5	150	542	1.19	-	0.85
	TELESAT-C	94.9	123	322	0.72	-	0.19
	HELIOS-B	86.5	169	406	0.83	-	0.22
	PALAPA-A	96.0	123	322	0.81	-	0.21
	MARISAT-C	96.2	188	416	0.36	-	0.08
	PALAPA-B	96.2	123	322	0.73	-	0.19
	GOES-B	90.9	111	541	0.55	-	0.28
	GMS	50.4	141	625	0.15	-	0.13
3 PAM-DII	RCA KuBand-1	50.0	836	1260	53.3	~0.1	13.5
	RCA KuBand-2	50.0	836	1260	~50	~0.1	12.7

Notes: Moments of inertia I_0 (roll) and I_1 (average of pitch and yaw) are values at motor burnout. Growth Rates are average values for the last 7 seconds of the motor run. Cone angle is the final value at the end of the motor run. Cone angle and transverse rate (at burnout) are assumed to be related by the expression:

$$\theta = \tan^{-1}[(\omega_{xy}/\omega_z)(I_1/I_0)]$$

where θ is the cone angle and $\omega_{xy} = \sqrt{\omega_x^2 + \omega_y^2}$ is the transverse rate amplitude. All STAR 37E data is reconstructed from accelerometer data. The PAM-DII data is from first-look telemetry, and is therefore preliminary. The writer is indebted to M. N. Cantwell of McDonnell Douglas Astronautics for making this information available.

motor relative to the spacecraft mass center, (4) travel of the mass center during motor burn, (5) moments of inertia of the spacecraft and their variation during motor operation, (6) spin rate, (7) nozzle configuration (length, throat size, submergence ratio, and expansion ratio), (8) geometry change (size and shape) of burning port during motor operation, (9) motor chamber pressure, and (10) initial lateral angular velocity residual due to tipoff effects from the spin platform. The large number of variable parameters makes it difficult to detect trends in the rather sparse data set. This difficulty is compounded by the small number of samples representing each unique configuration.

Detection of trends is further compounded by the sensitivity of the final cone angle to the length of the motor burn. Since growth is rapid in the last few seconds, small differences in burning time resulting from many factors, such as the initial temperature of the propellant grain, can result in large differences in the final amplitude of the instability. Nevertheless, scrutiny of the data provides information of considerable value in illuminating the origins of the instability. The data set is sufficiently complete to allow a realistic assessment of the comprehensive theoretical model presented later. The laboratory experiments were also strongly influenced by the flight test information.

2.2 CHARACTERISTICS OF CONING BEHAVIOR

Figure 2 describes the observed spacecraft motion in body fixed coordinates. At ignition, the system is spinning about the axis of symmetry at a rate in the range 40-70 rpm with small amounts of wobble about the two lateral (pitch and yaw) axes that represents the residual of the tipoff disturbance initiated at separation from the spin platform in the spacecraft lower stage or Space Shuttle cargo bay. The initial nutation at motor ignition is typically of the order of 1 degree/second. In the STAR 37-E vehicles, this wobble apparently decayed during motor operation in the manner anticipated on the basis of conventional jet damping theory. However, in most STAR 48 and PAM-DII vehicles, the jet damping decay rate is smaller than expected from the beginning of the motor burn. At approximately 50 seconds after ignition, further decay appears to cease, and an unexpected rise in pitch (ω_x) and yaw (ω_y) angular velocities shown in the typical rate gyroscope data in Figure 4. In all data, the most dramatic growth occurs during the last 5 to 10 seconds of motor operation.

The angular velocity measurements represent the best source of experimental information regarding the coning phenomenon, since high-resolution rate gyroscopes were carried on most of the flights after the coning phenomenon was first observed. From the point of view of an observer in inertial space, the spacecraft coning would appear to be a wobbling motion about the primary spin direction as depicted in Figure 2. The body cone angle θ_b (θ_b is the cone half-

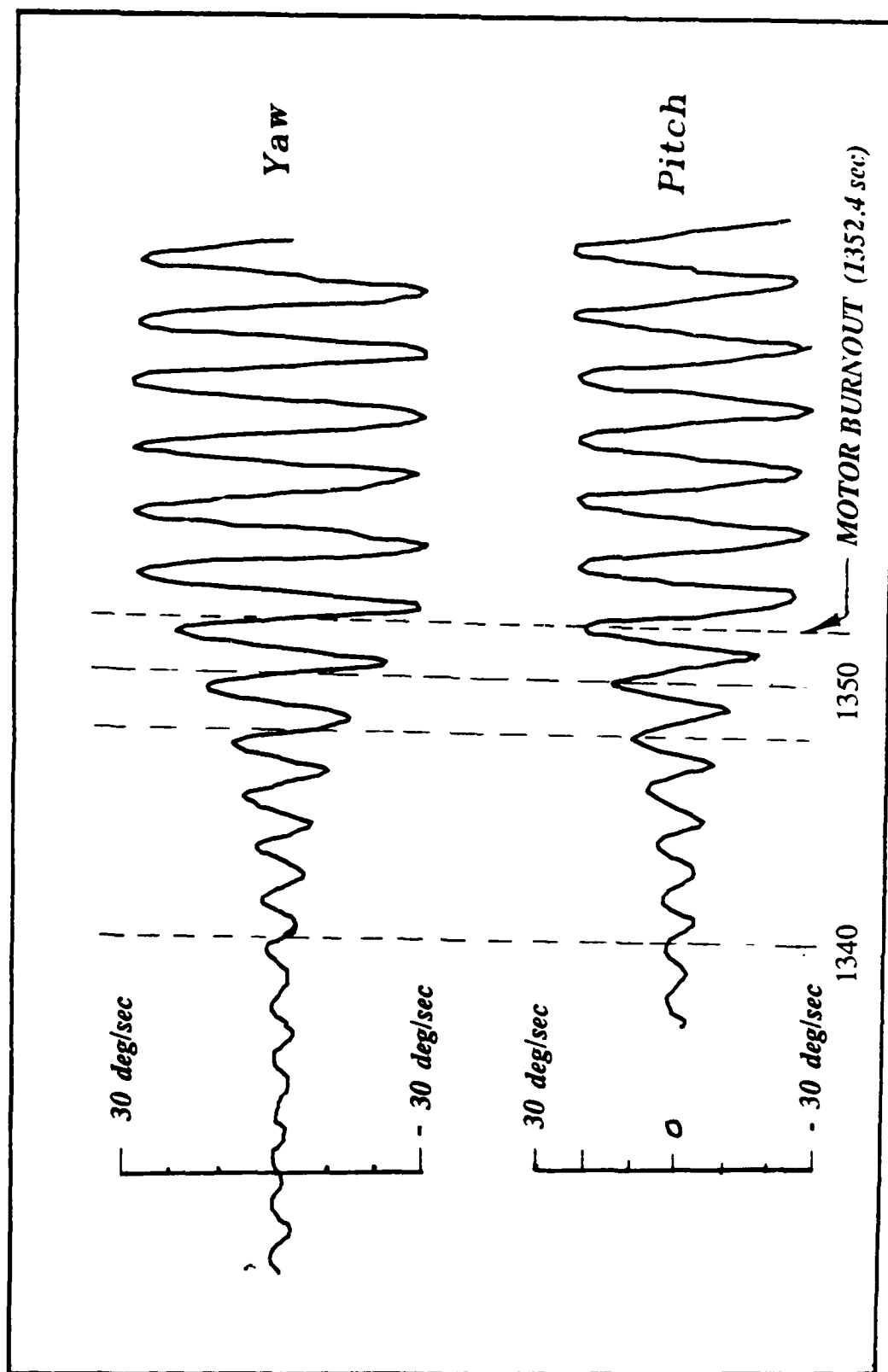


Figure 4. Typical Angular Velocity Histories from Rate Gyroscope Data

angle, but since most other investigators have used the "cone angle" terminology, this will be adhered to herein to avoid confusion) between the axis of symmetry (roll axis, z) and the spin angular velocity vector increases gradually during the last half of the motor run. In terms of the more convenient coordinate system fixed in the vehicle, the disturbance can be described as a rotation of the vehicle angular velocity vector about the symmetry axis at very nearly the free-precession frequency as given by

$$\lambda_s = \Omega(1 - I_0/I_1) \quad (2)$$

I_0 and I_1 are the roll and pitch (or yaw) moments of inertia if axial symmetry is assumed. Since the latter assumption is justified for all vehicles in question (see Table 1), it will be used in all of the analytical portions of the report to simplify the dynamics of the problem. Figure 5 is a plot of λ_s vs time for a typical PAM-D flight (WESTAR V). Superimposed on the solid curve representing the theoretical frequency given by Equation (2), is actual flight data. For the first half of the motor run, there is close correspondence between the actual and calculated frequency. There are marked deviations from theory during the latter half. The undulations in frequency are highly correlated with periods of growth and decay of the coning instability.

The projection of the angular velocity vector on a plane normal to the spin axis (labeled in Figure 2 as ω_{xy}) apparently rotates at the coning rate in a direction opposite to the primary spin and grows in amplitude nearly exponentially during the period of instability. Figure 6 shows the development of the cone angle θ as a function of time and also shows the precession angle for comparison. The spacecraft angular velocity vector typically revolves about 15 times during the last 30 seconds of motor burn during which the cone angle may grow to as much as 17 degrees. Figure 7 shows the growth of the lateral angular velocity perturbation ω_{xy} for a typical flight (WESTAR V). The retrograde travel of ω_{xy} relative to the spin direction is emphasized.

Figure 4 shows typical pitch and yaw rate gyroscope data (WESTAR V). A feature of some of the angular velocity data is an apparent amplitude discrepancy between the pitch and yaw channels as is quite noticeable in Figure 4. For the WESTAR V vehicle, the ratio of pitch to yaw angular velocity at burnout was $\omega_x/\omega_y = 0.87$, which is typical of the entire data set. Such a discrepancy can be readily explained in those vehicles that are not axially symmetric, as represented by the lateral moment of inertia ratio, I_x/I_y . This ratio for WESTAR V was nearly unity, so the angular velocity discrepancy is either a feature of the instrumentation or an attribute of the driving mechanism. Figure 8 illustrates the placement of the rate gyroscopes and accelerometers on a typical PAM-D spacecraft.

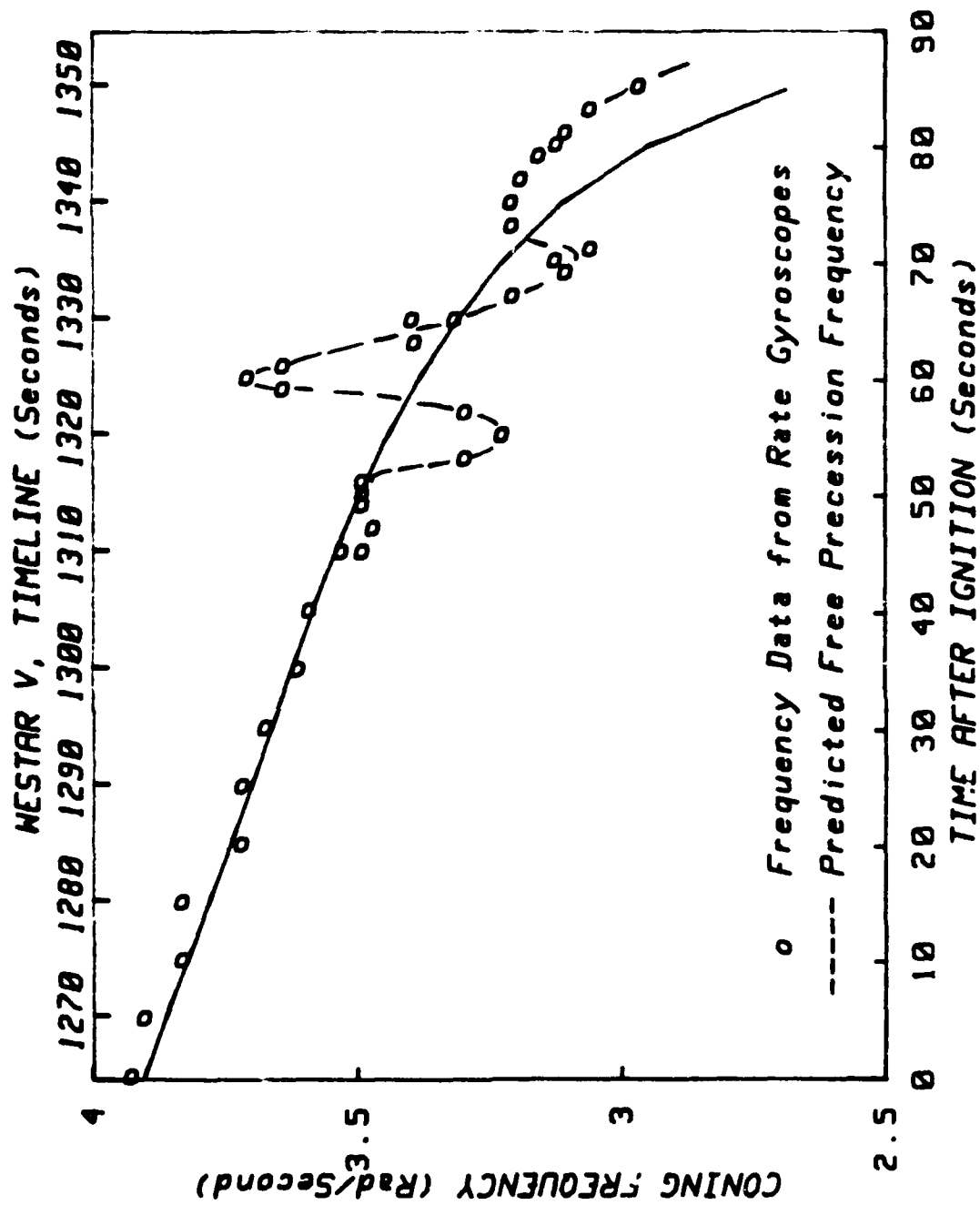


Figure 5. Comparison of Measured and Predicted Nutation Frequency

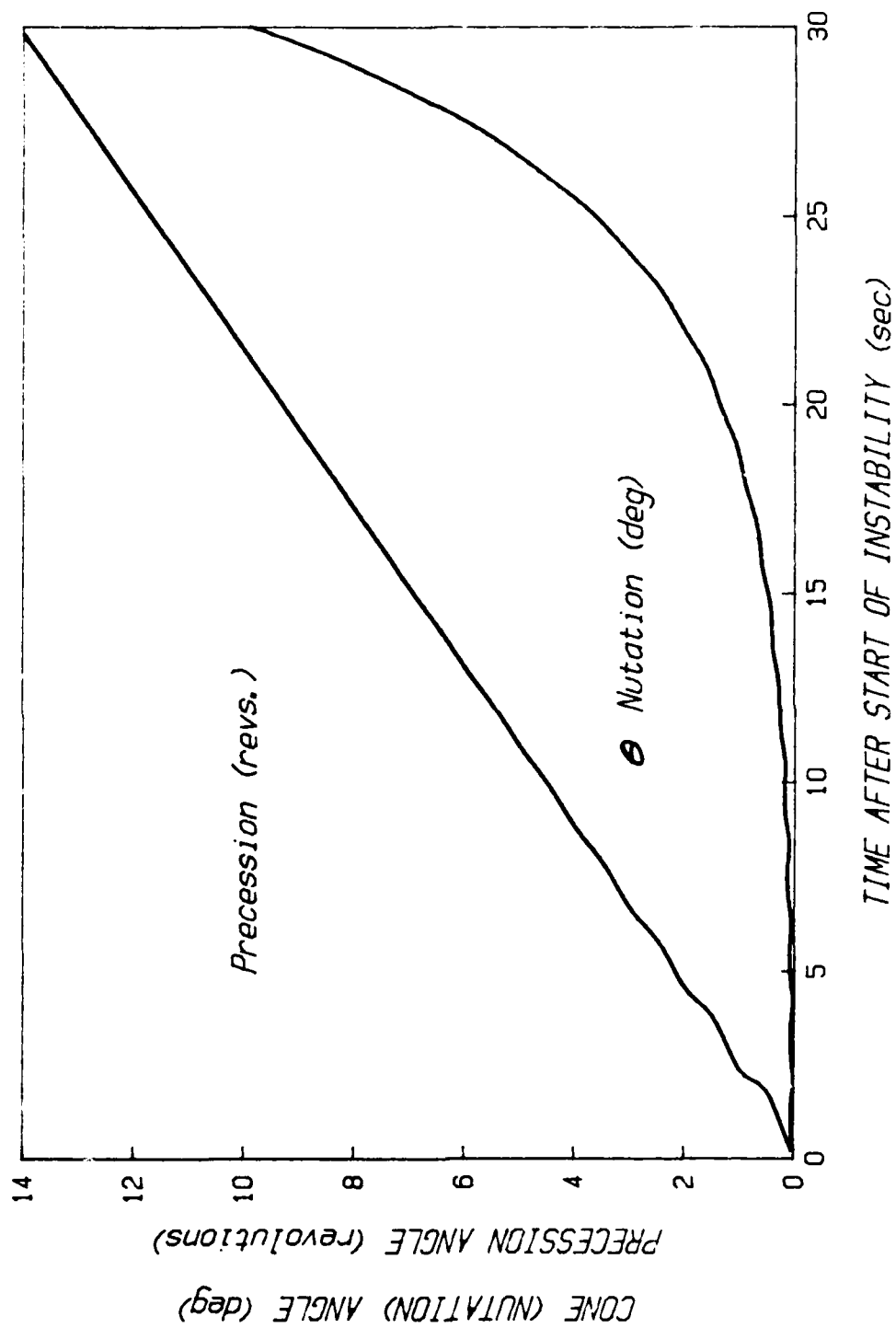


Figure 6. Precession and Nutation vs Time

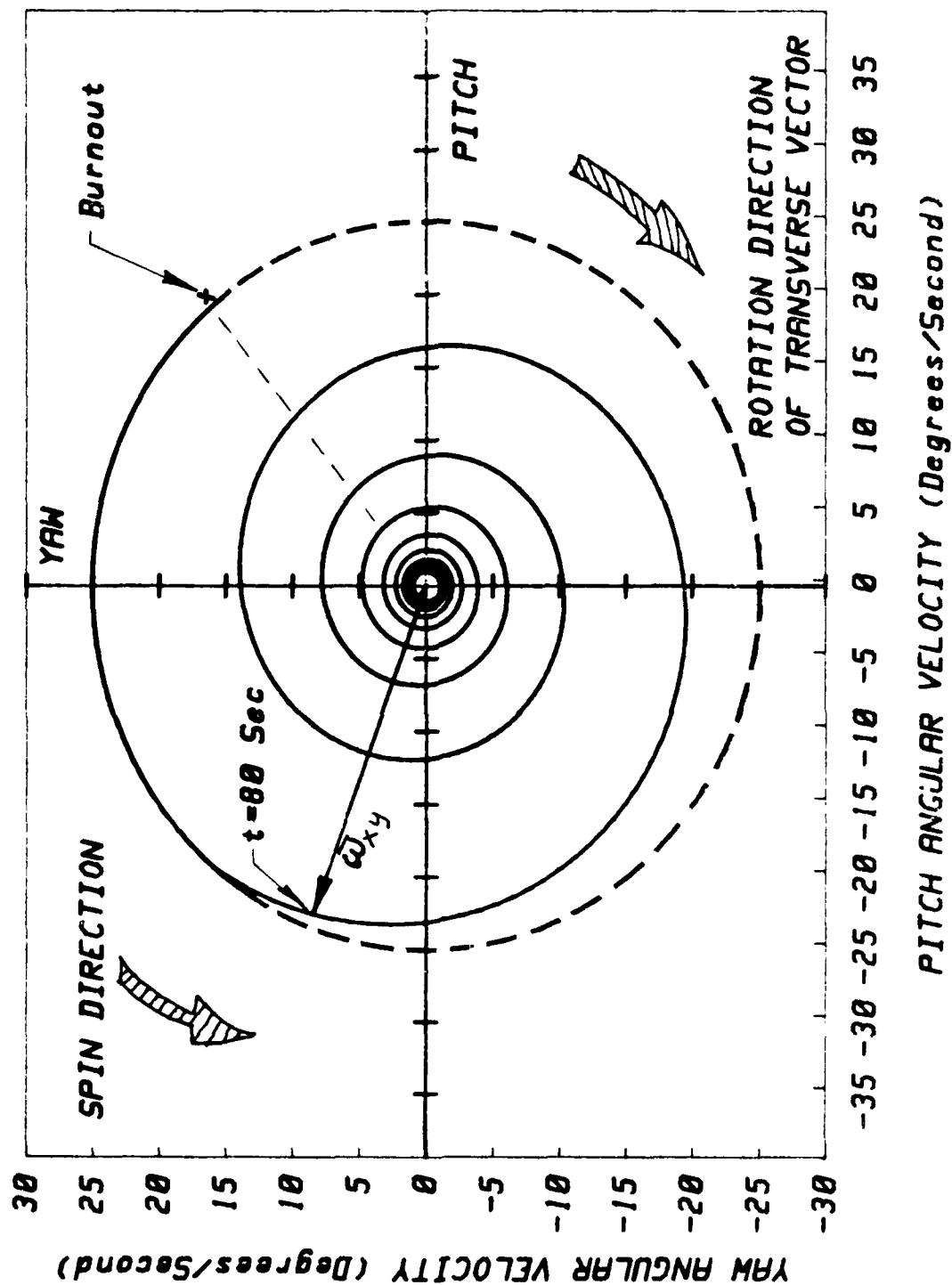


Figure 7. Projection of Perturbation Angular Velocity Vector on Lateral Plane

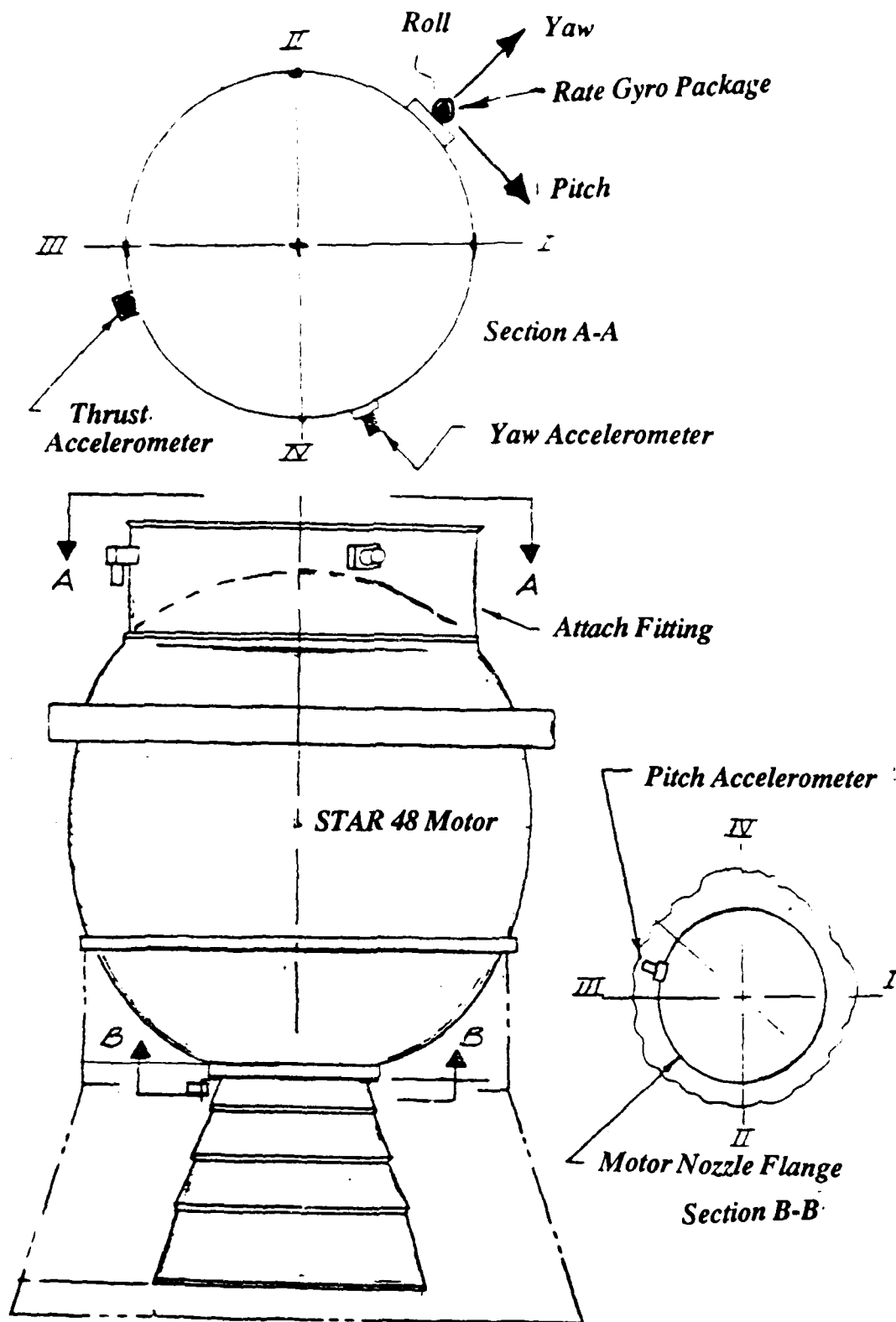


Figure 8. Placement of Instrumentation (WESTAR V)

Figure 9 is a cross-plot of the instantaneous amplitudes of the pitch and yaw rate gyroscope signals. The amplitude discrepancy is not important until the last few seconds of the motor burn. Since at this point the amplitude is relatively large, it seems likely that it is related to instrumentation effects. It is plausible that the ω_x/ω_y discrepancy is related to either the details of the orientation of the sensitive axes or some other feature of the rate gyroscope. It is perhaps significant that the ratio is always less than unity; that is, the yaw channel always records a larger amplitude than the pitch channel. At least part of the discrepancy appears to be caused by cross-coupling with the PAM roll rate. Preliminary analysis by McDonnell Douglas¹ indicates that about ten percent of the apparent yaw rate gyro amplitude at end of burn is due to this cross-coupling. This is verified by the presence of an oscillatory signal superimposed on the roll rate gyro output that is exactly in phase with the yaw signal. On this basis, it appears that the amplitude discrepancy is an instrumentation effect rather than an important attribute of the disturbing entity. However, great care was exercised in carrying out the analysis to ensure that any possible implications in terms of the modeling would not be overlooked.

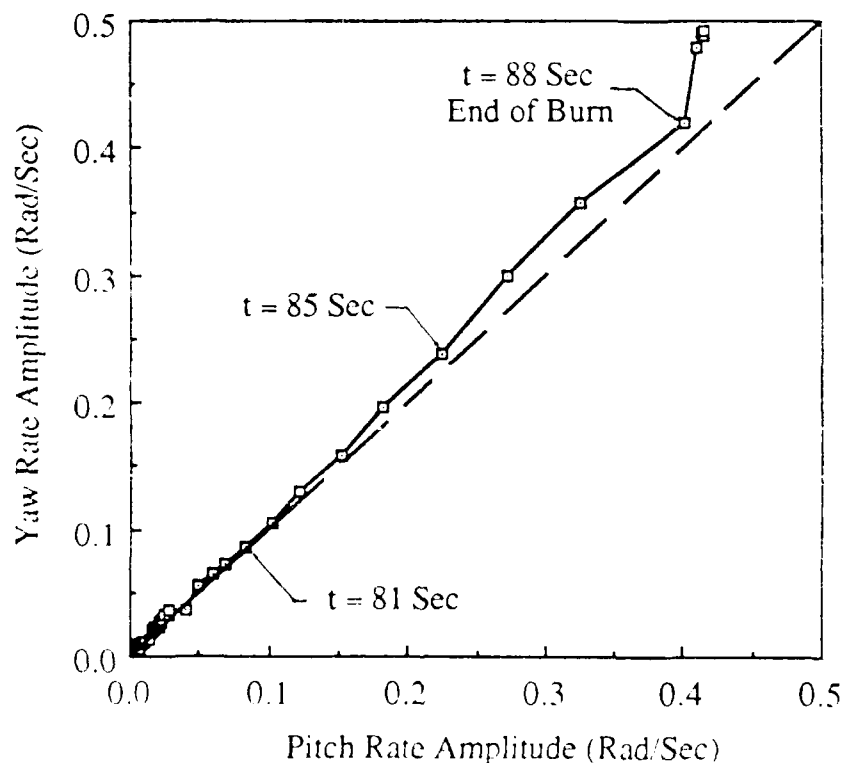


Figure 9. Pitch Rate vs Yaw Rate Amplitude (WESTAR V)

2.3 PAM-D OBSERVATIONS

The PAM-D data set along with data from the SGSII missions constitute the bulk of experimental evidence. Considerable attention is devoted in this section to the PAM-D WESTAR V flight because of the rather complete nature and the relatively high resolution of the available flight information. WESTAR V was carried into orbit by a Delta booster in 1982, and is also noteworthy in that it was equipped with a stiffened nozzle exit cone to test one of the early coning instability theories.

Figure 10 shows the rate gyro signal present at the beginning of the STAR 48 motor run on WESTAR V. At ignition, the pitch and yaw angular velocities are nearly constant amplitude sinusoids. There is little evidence in Figure 10 for appreciable perturbations from the ignition transient. Whatever entity is eventually responsible for the later rapid growth of the coning may be present from the very beginning of motor operation. Conventional jet damping analysis would indicate that the initial sinusoidal motions should immediately begin to decay after the ignition transient as shown in the lower plot in Figure 10. The motion shown is based on the jet damping model currently in use by McDonnell Douglas (Refs. 2-6).

The upper plot in Figure 10 is the actual yaw rate gyro data from the WESTAR V flight during the first half of the motor burn. The rate of decay is seen to be significantly lower than predicted, and there are short periods very early in the burn during which the amplitude even appears to rise slightly. These disturbances do not appear to be related to the ignition transient.

An expanded plot of the pitch rate gyro output for WESTAR V during the mid part of the burn is shown in Figure 11. Again, there is evidence that the motion is anything but a smoothly decaying oscillation as predicted by jet damping theory. Just before the actual growth is triggered, there is a significant increase in rate of decay followed by rapid growth in which the pitch amplitude grows by a factor of two in three or four cycles. This is associated with the period during motor operation at which the most rapid increase in mass flow rate is present as can be shown from the motor chamber data shown in Table 2. About ten seconds later, there is a marked dropoff in mass flow rate. This event correlates closely with the drop in coning growth mentioned previously and is seen in all PAM-D data. Table 2 also shows typical values of important flow variables, mass flow rate, propellant average burning rate, normal gas velocity at the burning surface, and other properties that will be needed in evaluations of the analytical models presented later. Figure 12 shows the burn-back profiles for the STAR 48 motor. It will be noticed that during the period of maximum coning growth, the propellant in the aft half of the chamber has been entirely consumed. The propellant grain assumes a nearly end-burning configuration during the last few seconds of motor operation.

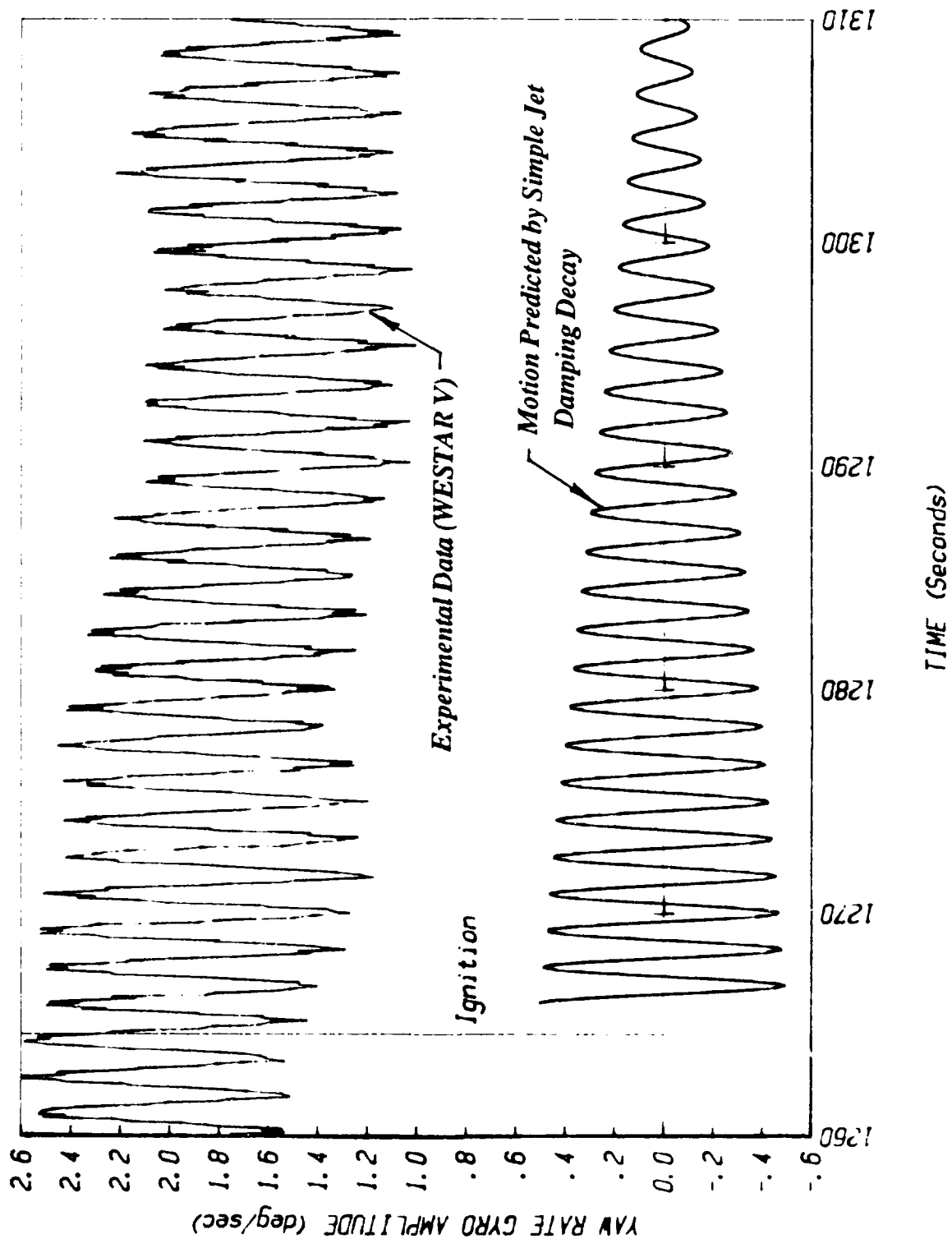


Figure 10. Comparison of Actual and Predicted Yaw Rate at Beginning of Motor Run

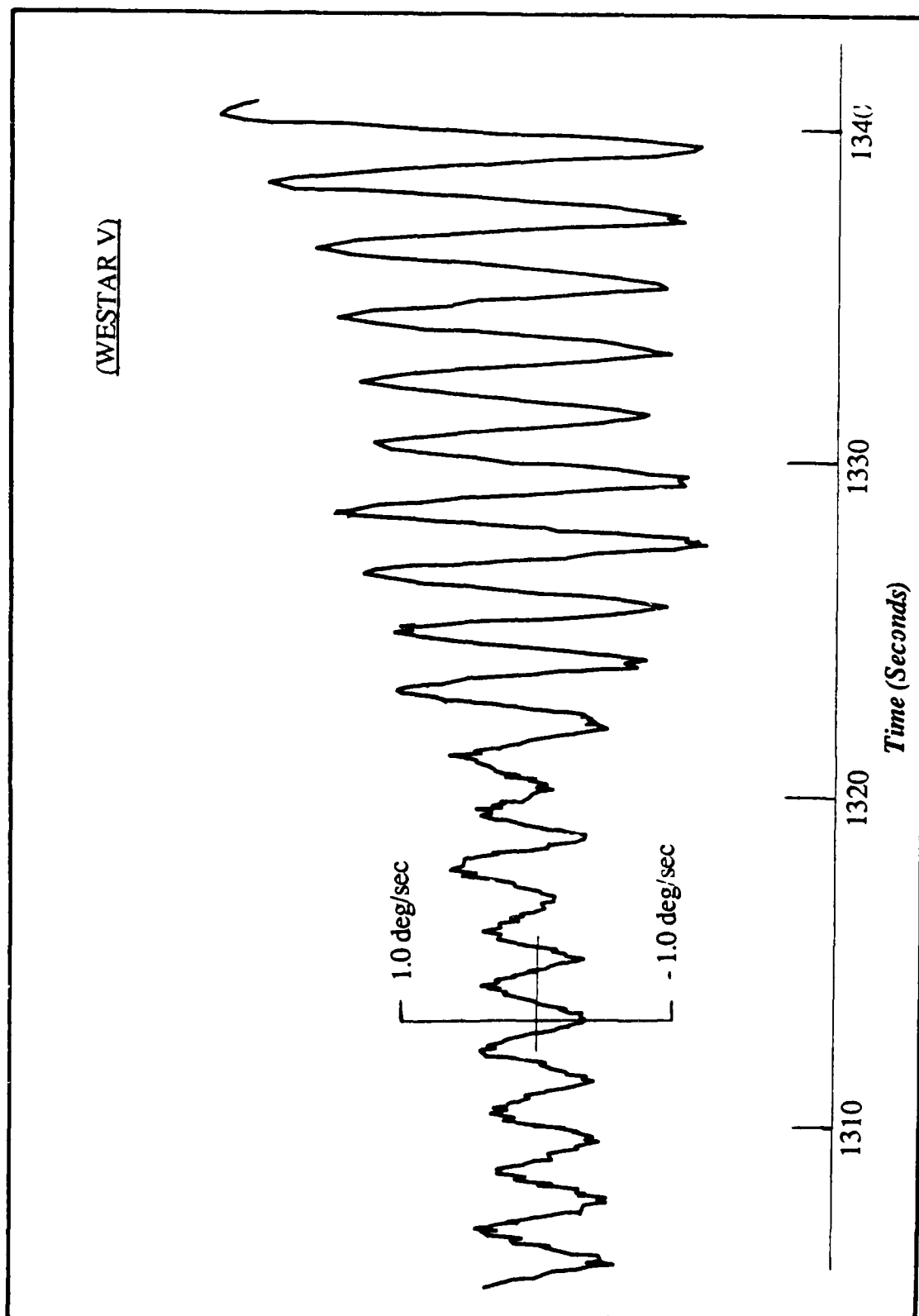


Figure 11. Behavior of Pitch Angular Rate at Start of Instability

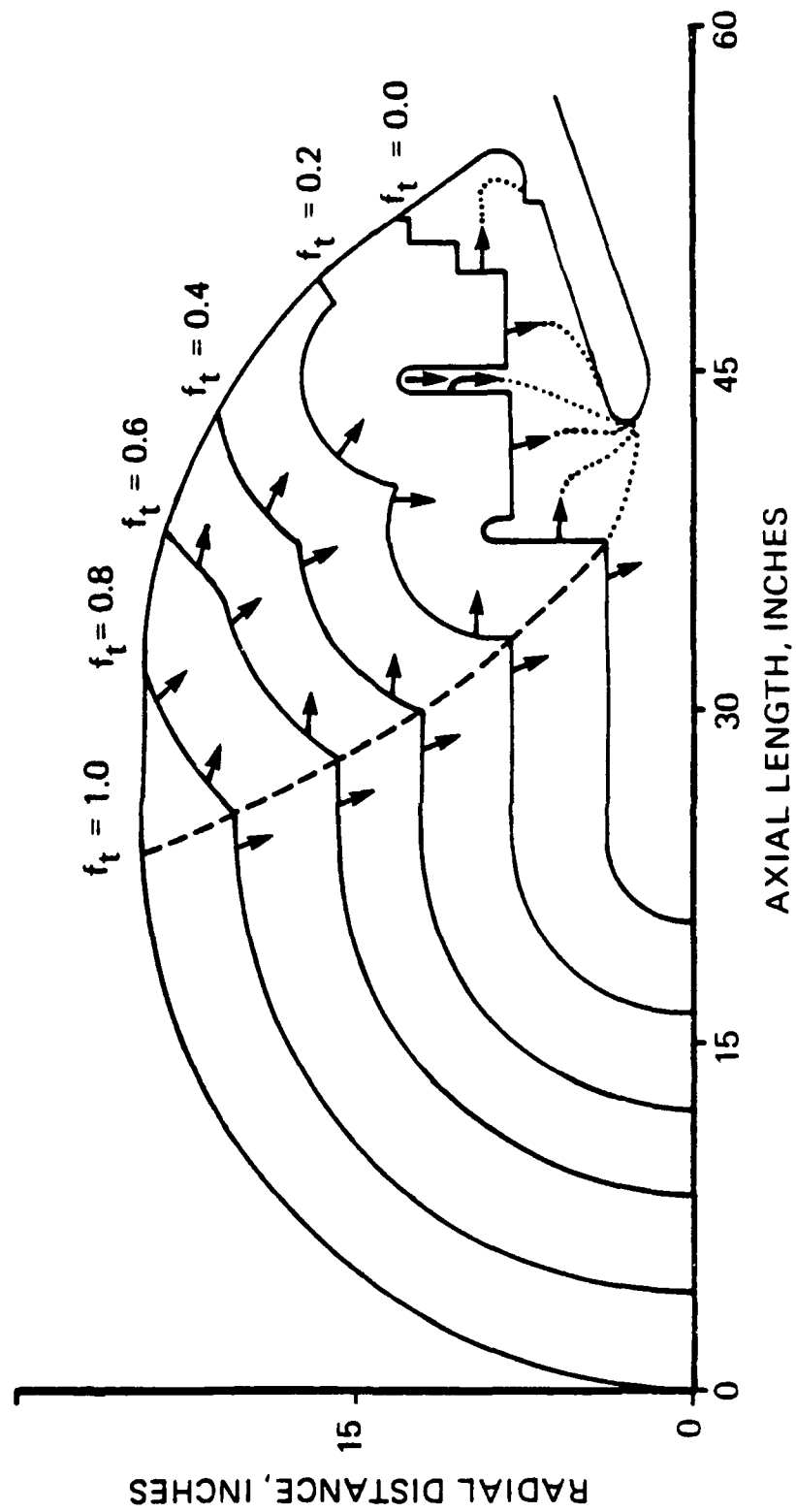


Figure 12. STAR 48 Burnback Profiles

Table 2. Typical STAR 48 Internal Ballistics Data

Time t	Chamber Pressure	Burn Rate r	Dist Burned	Density ρ	Throat Area A^*	Mass Flow Rate \dot{m}	Slenderness Ratio, b	Velocity at Burn Surface, V_b	Rosby Number
(Sec)	(psi)	(In/Sec)	(In)	(Slug/ft ³)	(In ²)	(Slug/Sec)	-	(Ft/Sec)	-
0	530	0.23	0.00	0.00750	12.44	1.316	2.06	8.71	3.787
5	580	0.24	1.16	0.00821	12.66	1.466	1.86	8.18	2.781
10	600	0.24	2.35	0.00849	12.88	1.542	1.16	7.99	0.935
15	550	0.23	3.56	0.00779	13.10	1.438	1.11	8.49	0.784
20	570	0.24	4.73	0.00807	13.31	1.515	1.07	8.28	0.666
25	600	0.24	5.91	0.00849	13.53	1.621	1.03	7.99	0.571
30	570	0.24	7.12	0.00807	13.75	1.564	1.00	8.28	0.494
35	600	0.24	8.30	0.00849	13.97	1.673	0.97	7.99	0.432
40	610	0.24	9.51	0.00864	14.19	1.727	0.95	7.89	0.379
45	620	0.24	10.72	0.00878	14.40	1.783	0.93	7.80	0.336
50	630	0.24	11.93	0.00892	14.62	1.839	0.94	7.72	0.321
55	630	0.24	13.16	0.00892	14.84	1.866	0.96	7.72	0.319
60	610	0.24	14.38	0.00864	15.06	1.834	0.99	7.89	0.317
65	600	0.24	15.59	0.00849	15.28	1.830	1.01	7.99	0.316
70	560	0.24	16.79	0.00793	15.50	1.732	1.04	8.38	0.314
75	540	0.23	17.97	0.00764	15.71	1.694	1.06	8.60	0.312
80	520	0.23	19.14	0.00736	15.93	1.654	1.09	8.83	0.311
85	520	0.23	20.29	0.00736	16.15	1.676	1.11	8.83	0.310

Figure 13 is a plot of the yaw rate gyroscope amplitude as a function of time on a logarithmic scale. It is evident that the motion is much more complex than a simple exponential growth. Instantaneous growth rates can be estimated from the digitized data.

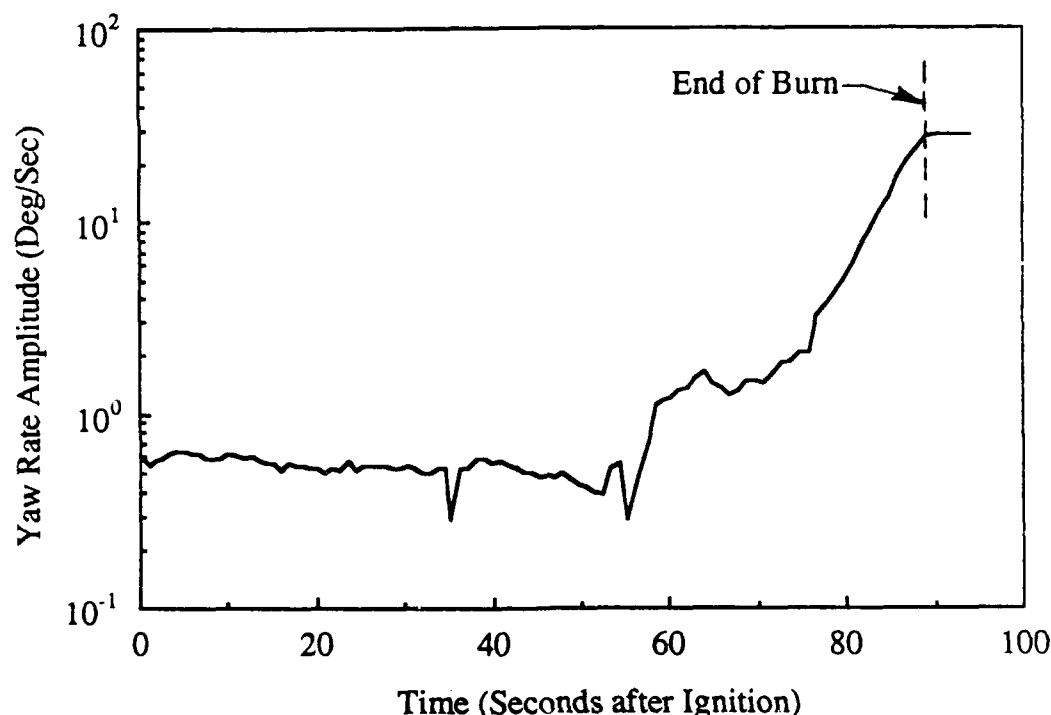


Figure 13. Amplitude of Yaw Rate Signal vs Time (WESTAR-V)

Figure 14 shows the entire yaw rate gyro output on a larger scale. The growth at about 1320 seconds (WESTAR V timeline) is evident. This is followed by several seconds of decay and then about fifteen seconds of rapid growth that abruptly ceases at taildown. The latter observation characterizes all vehicles not carrying liquid stores. Additional coning growth at a distinctly different growth rate may persist after burnout if sloshing liquids are aboard the spacecraft. Figure 15 is a plot of the instantaneous growth rate for WESTAR V. These values were tested by applying them in a simulation program developed to allow evaluation of the instability theory to be described later. Figure 16 shows plots of the motion predicted by this program using the growth rate data plotted in Figure 15. This validates the dynamic model to be employed extensively in later sections since it will be seen that the results correspond closely to the actual motion depicted in Figure 14.

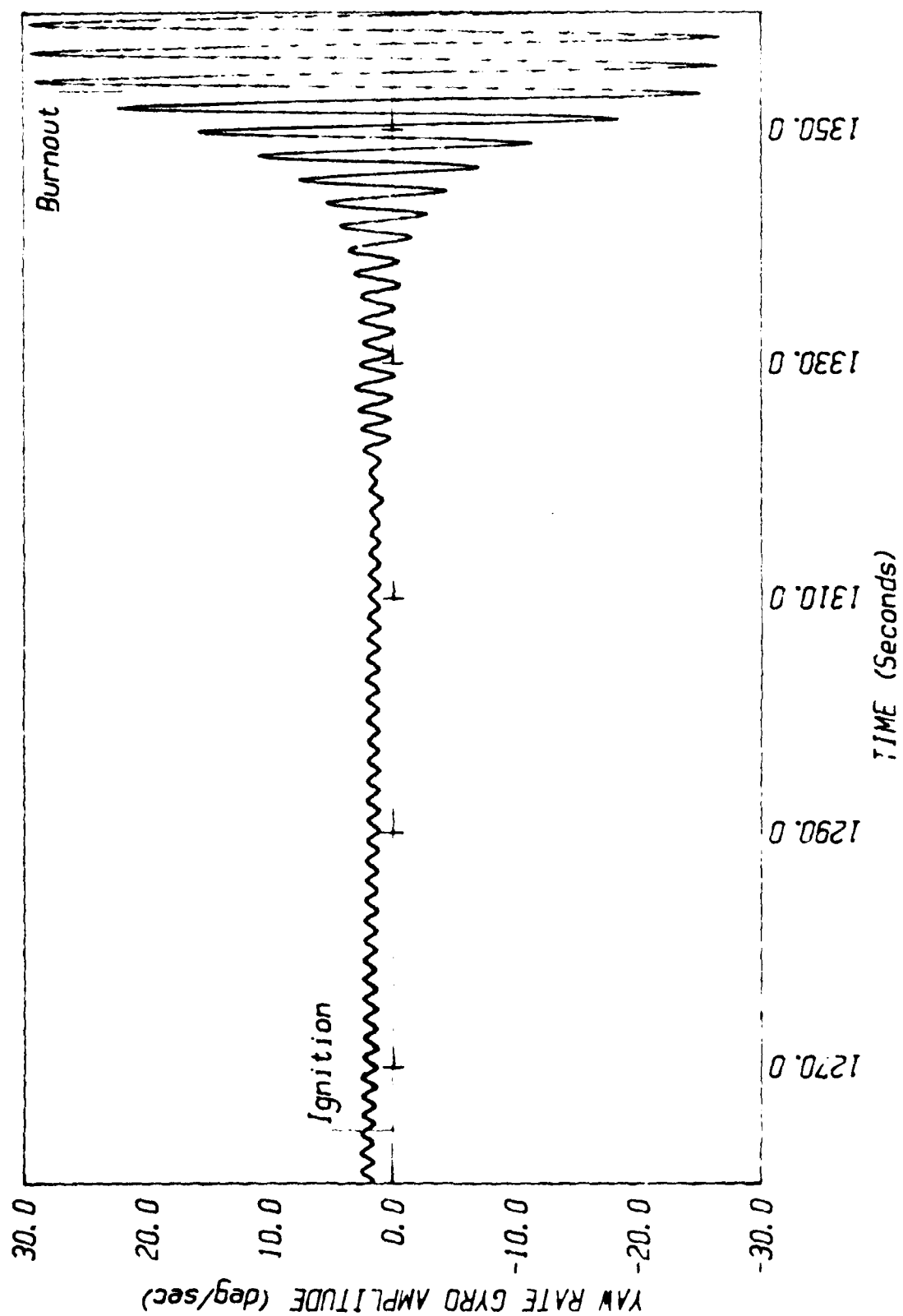


Figure 14. Yaw Rate Gyro Amplitude vs Time (WESTAR V)

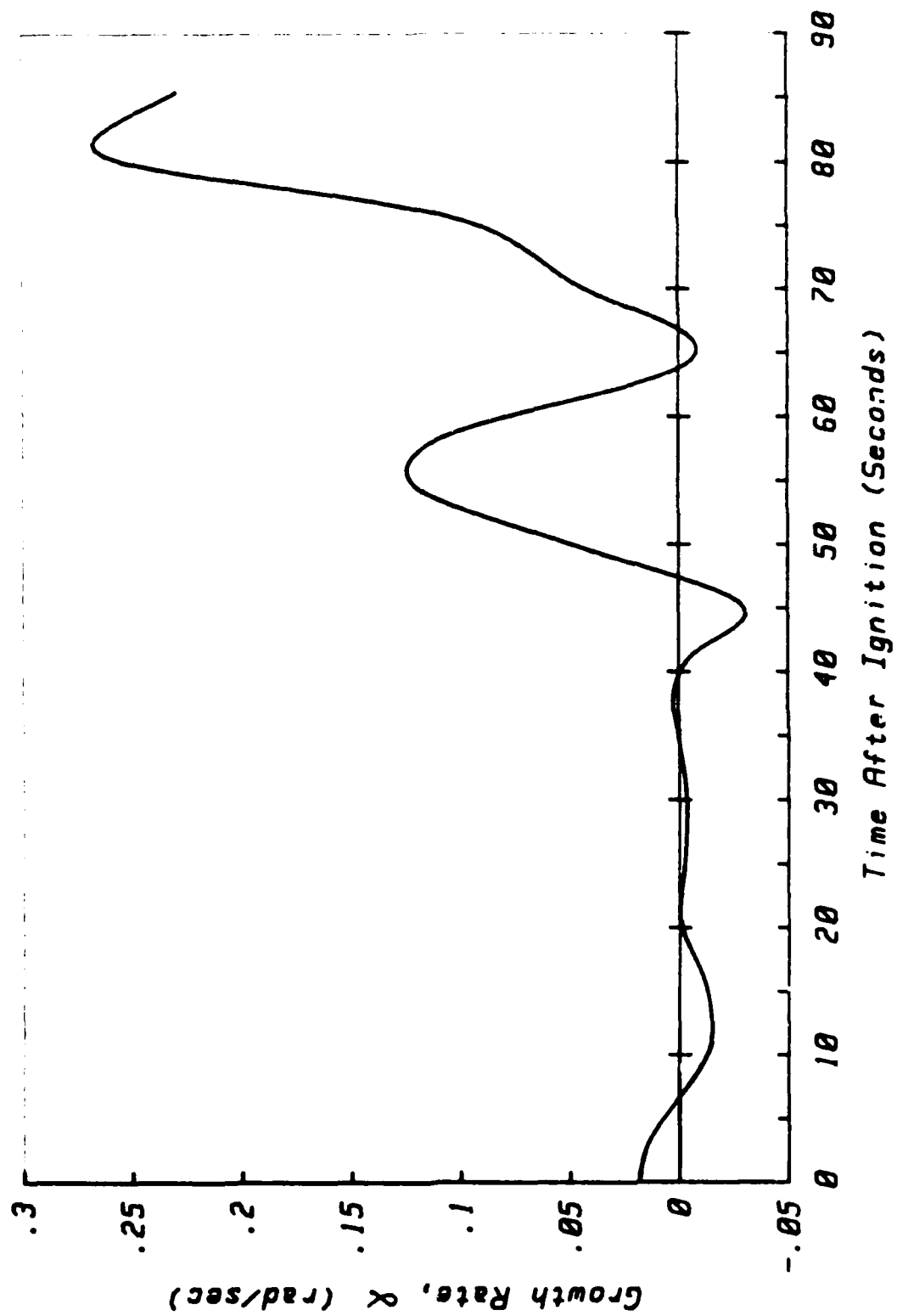


Figure 15. Nutation Instability Growth Rate (WESTAR V)

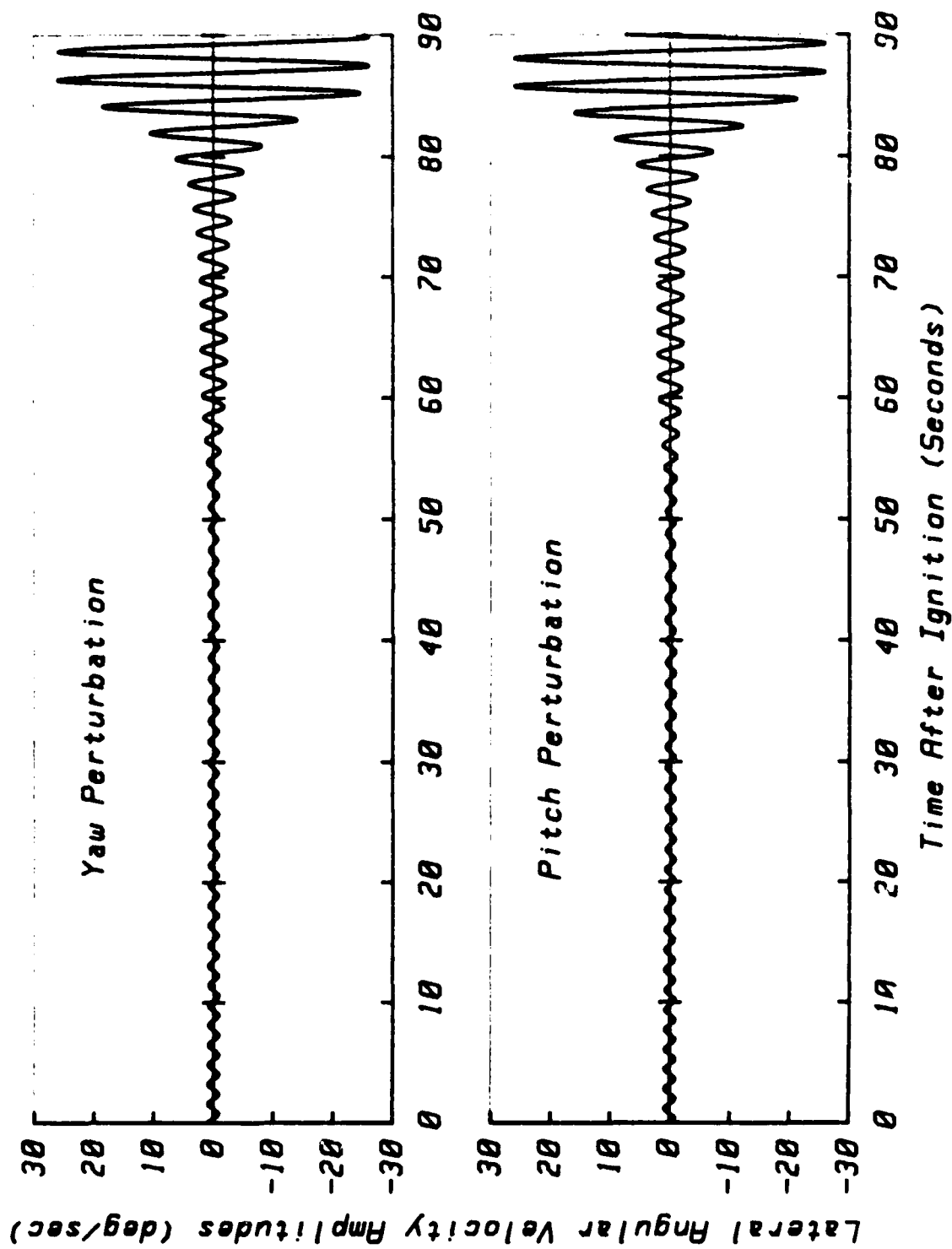


Figure 16. Predicted Angular Velocity Perturbations from Growth Data (WESTAR V)

2.4 SGS II (SECOND STAGE) FLIGHT OBSERVATIONS

If the PAM-D data are examined carefully, it is possible to distinguish at least two periods of rapid growth of the wobble followed by equally rapid periods of decay. These periods are quite evident in Figure 14 and in the corresponding growth rate plot in Figure 15. The SGS II second stage, which did not attain a large cone angle (mainly as a result of its large lateral moment of inertia), exhibits this feature very clearly. Figure 17 shows the rate gyroscope data for the SGS II stage 2 (NAVSTAR 9). The typical jet damping decay is evident during the first 40-50 seconds and is followed by coning growth at about 55 seconds. This growth pulse then rapidly decays in the 65-70 second period, and the growth reappears at 80 seconds. An unusual feature of this particular sample is the rapid decay just before burnout that may be associated with complex phenomena associated with the taildown process. A later SGS II flight did not exhibit this feature but was identical to the earlier flight in all other respects. The taildown decay is not apparent in any of the PAM-D data. Most of the features just described are also present in the more typical PAM-D missions, but are somewhat obscured by the large coning growth during the last third of the motor burn. The major difference between the SGS (Stage 2) and PAM-D spacecraft configurations is the large moment of inertia difference; the SGS lateral moment of inertia is approximately 4 times larger than the PAM-D at burnout.

The SGS vehicles also carried a nutation control package⁷ in each of the two STAR 48 stages that was designed to damp out coning disturbances. The upper stage (referred to here as the third stage) was quite similar to the PAM-D vehicles in terms of its mass properties. The nutation control system successfully prevented growth of coning in the third stage vehicles. The nutation control system was not activated during the SGS(Stage 2) motions described, since the coning amplitude did not exceed the 2 degree/second angular rate threshold^{1,7}. It is worth mentioning that use of the nutation control system is an example of treating the symptom of the problem without understanding the cause. This is a costly approach both in terms of extra hardware development and loss of system payload capability.

2.5 PAM-DII FLIGHT DATA

Two flight operations involving the larger PAM-DII rocket motor (RCA KuBand and SATCOM-2) were carried out before space shuttle flights stopped in January 1986. Figure 18 shows the propellant burn-back profiles for comparison with the STAR 48 profiles in Figure 12. Transition to head-end web configuration in the latter seconds of operation is indicated. Due to the thicker propellant web, the DII motor operates approximately 30 seconds longer than the STAR 48.

High resolution rate gyroscope data for the two PAM-DII flights was not available at the time of writing. However, telemetry data shows evidence of a

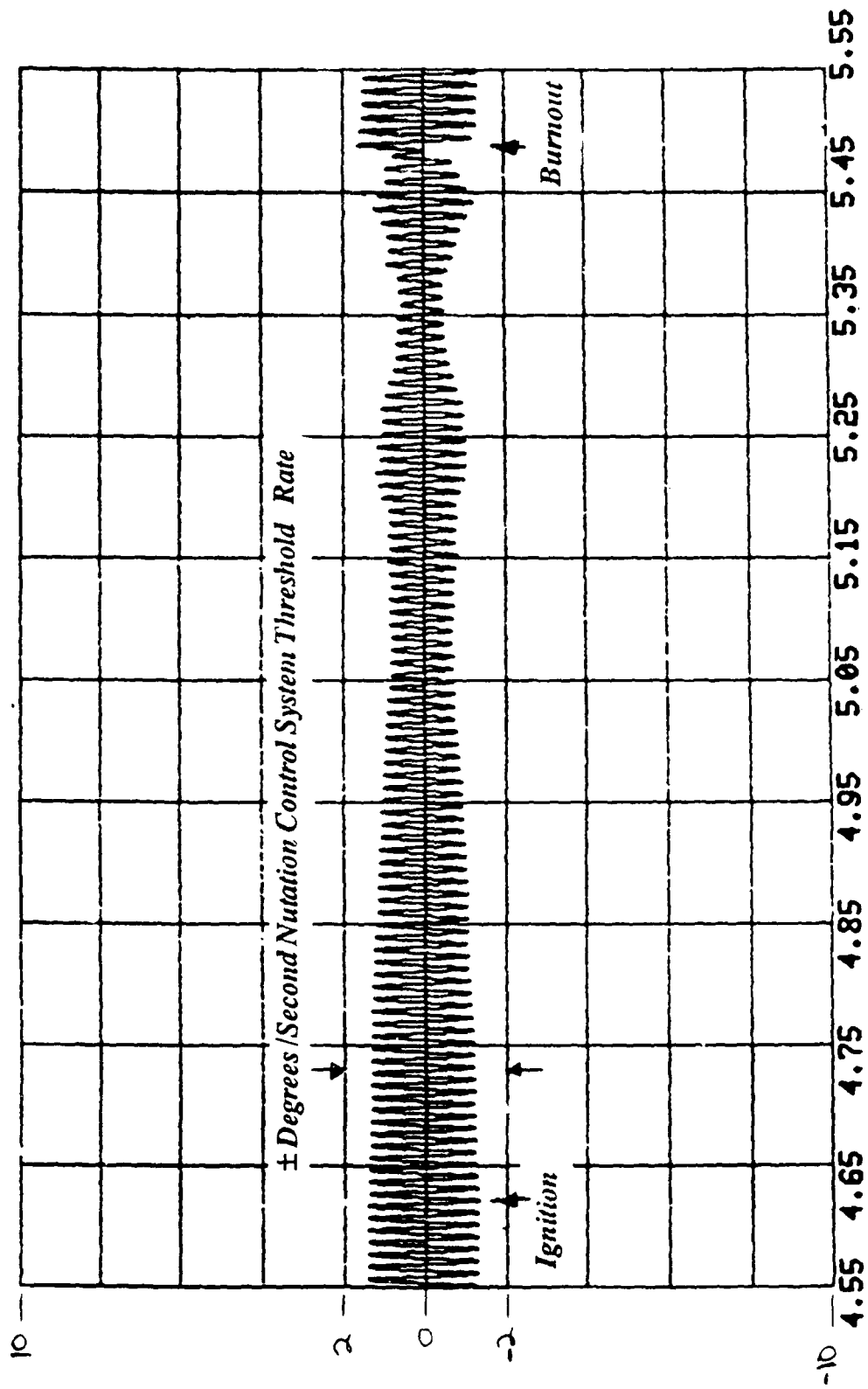


Figure 17. SGS-II, Flight 2 Second Stage Rate Gyroscope Data

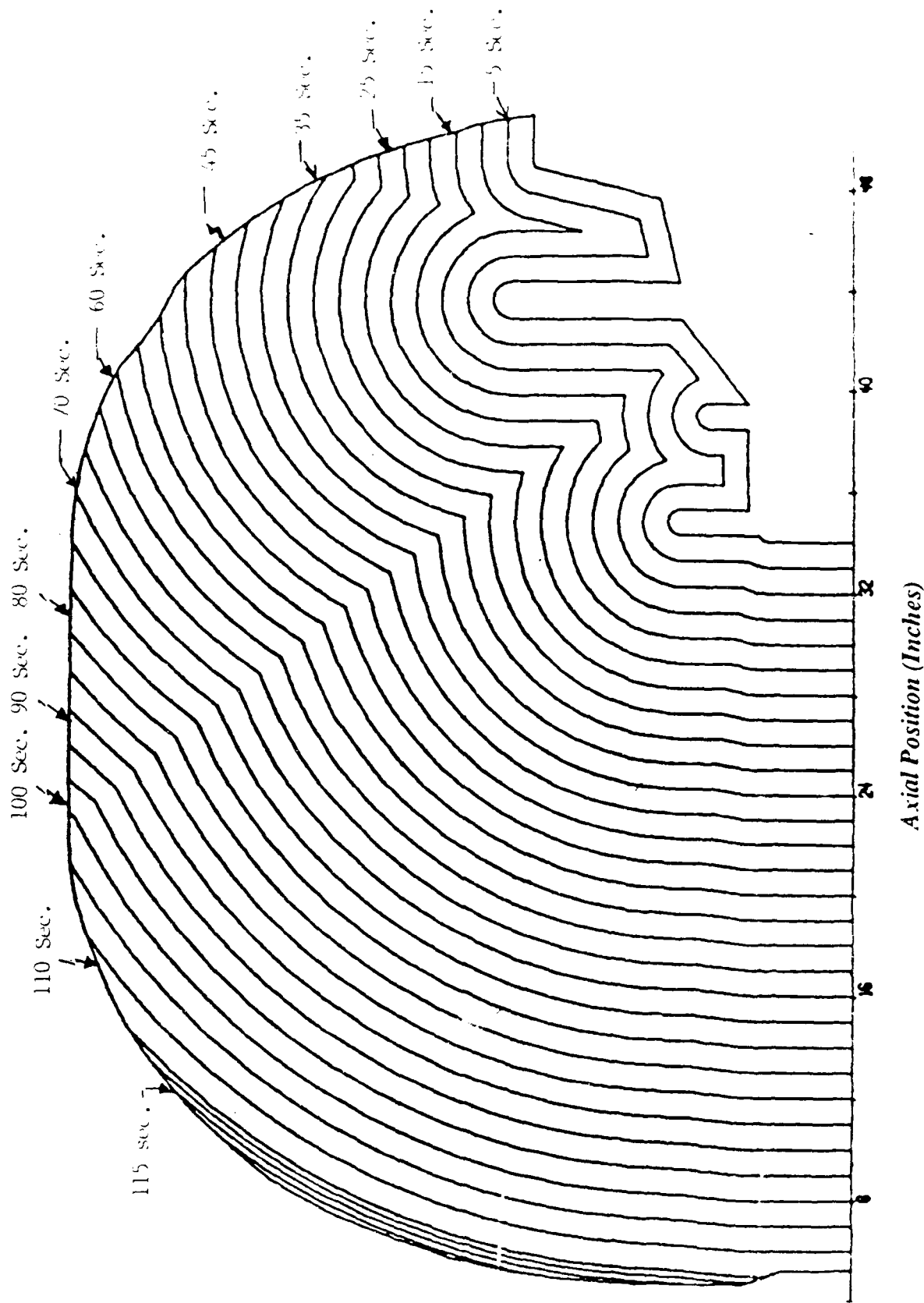


Figure 18. PAM-D2 Burnback Contours

coning instability similar to that experienced in the PAM-D systems. Growth occurred only during the final 20 seconds of the motor burn. Growth stopped at motor burnout in SATCOM-2, but continued (at a much lower rate) in the RCA KuBand mission. It is noteworthy that the latter vehicle carried liquids. It is also important to notice that while the final coning amplitude (about 50 degrees/second final angular rate perturbation and 15° cone final angle) this growth would not have been observed had the motor burned for the same period (about 85 seconds) as in the STAR 48 flights. This suggests that the same mechanism is responsible for coning in both configurations, but that it is less severe in the PAM-DII. The significant coning growth in the DII is clearly related to the long burn time, giving the small disturbing effects an extended period of influence on the system angular motion.

2.6 CORRELATION OF CONING DATA WITH SYSTEM PARAMETERS

All PAM-D vehicles have experienced coning as is clear from the summary in Table 1. Since there is considerable variability in the final cone angle and in the final amplitude of the angular velocity perturbation, it is appropriate to attempt to relate the source of these differences to variations in physical parameters. A simple correlation based on dimensional analysis provides useful guidance.

It is assumed that the gas flow in the motor chamber and nozzle is the source of the coning growth. If this is the case, then the disturbing moment, and therefore the growth rate, should depend on several key parameters. A set including (1) the mass flow rate \dot{m} , (2) the lateral moment of inertia of the vehicle I_1 ($I_x = I_y = I_1$ for a symmetric vehicle), and (3) the distance between the spacecraft mass center and the motor, L_{cg} is appropriate. The latter length would be selected almost automatically as a key parameter, since the magnitude of the torque produced by a disturbance located in the rocket motor is proportional to the moment arm. However, the internal radius of the combustion chamber R_0 is another likely candidate for a scaling length, and since it is common to all vehicles in the PAM-D data set, it is selected as the characteristic length.

Other lengths may also be involved. There is evidence, to be discussed later, that the nozzle geometry could be important. The radius of the nozzle throat, R_t , is used here to represent the nozzle. Nozzle length, expansion ratio, and submergence distance are other parameters that could be involved, but are not displayed.

The mass flow rate governs the changes in angular momentum related to the motor operation. The lateral moment of inertia represents the dynamic resistance of the vehicle to the applied moment. Other parameters that might play a role are the characteristic velocity v_b of the motor gas flow (defined at a convenient point such as the burning surface) and the spin rate Ω . Clearly, the initial amplitude of the angular velocity perturbation as represented by ω_i might also be involved.

A simple dimensional analysis utilizing m , R_0 , and I_1 as the running variables yields the following result. The (dimensional) growth rate α^* , can be written as

$$\alpha^* = (m R_0^2 / I_1) f[\epsilon, \omega_i / \Omega, R_t / R_0, L_{cg} / R_0, \dots] \quad (3)$$

where f is an undetermined function of the dimensionless groups ω_i / Ω , R_t / R_0 , L_{cg} / R_0 and ϵ . The latter parameter is the Rossby number, $\epsilon = v_b / R_0 \Omega$, based on the velocity of combustion gases, chamber size, and spin rate. Since, all flights in the PAM-D series and also the SGS-II vehicles should have similar values for f , it is expected that α^* should be directly proportional to the group of running parameters in (2.2). That is

$$\alpha^* \sim m R_0^2 / I_1 \quad (4)$$

Figure 19 is a plot of this group against the average coning growth rate over the last seven seconds of motor operation as tabulated in Table 1. A data point for the SGS-II second stage (which carried a second STAR-48 motor as a third stage) is included in the plot although that vehicle had a significantly different mass distribution. Data for the SGS-II third stage are not included, since this vehicle was equipped with an active nutation control system that prevented nutation perturbations from growing beyond about 2 degrees per second.

The parameters used in evaluating equation (4) are the values corresponding to the system configuration at motor burnout as tabulated in Table 1. The correlation between (4) and the observed growth rate is striking; the correlation coefficient is 0.95. This is a convincing indication that a mechanism for the instability based on a direct involvement of the motor gas dynamics is appropriate. Attempts to correlate other proposed instability models in a similar straightforward manner have not been completely successful.

Another analysis of the flight data by Meyer⁸ shows also that the amplitude of the apparent destabilizing lateral moment responsible for driving the nutation is proportional to the transverse perturbation rate component (the projection of the vehicle angular velocity vector on a plane perpendicular to the axis of symmetry). Figure 20 shows this relationship as deduced by Meyer for the PAM-D vehicles described in Table 1. Results are shown at different times during motor burn. The data are strongly correlated. This is a clear indication that the driving mechanism must be such that

$$M = K \omega_{xy} \quad (5)$$

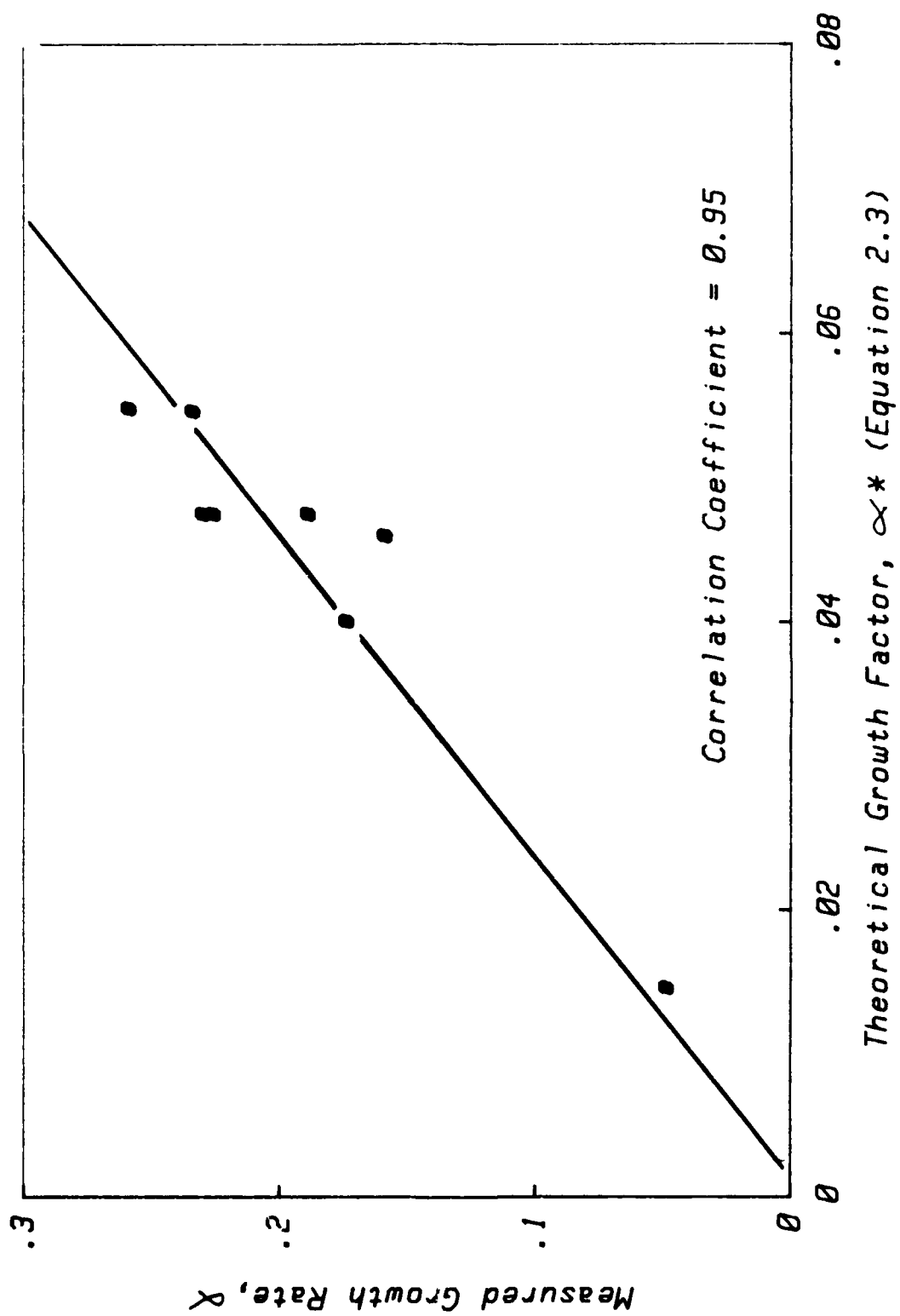


Figure 19. Correlation Between Actual Growth Rate and Parameter α^*

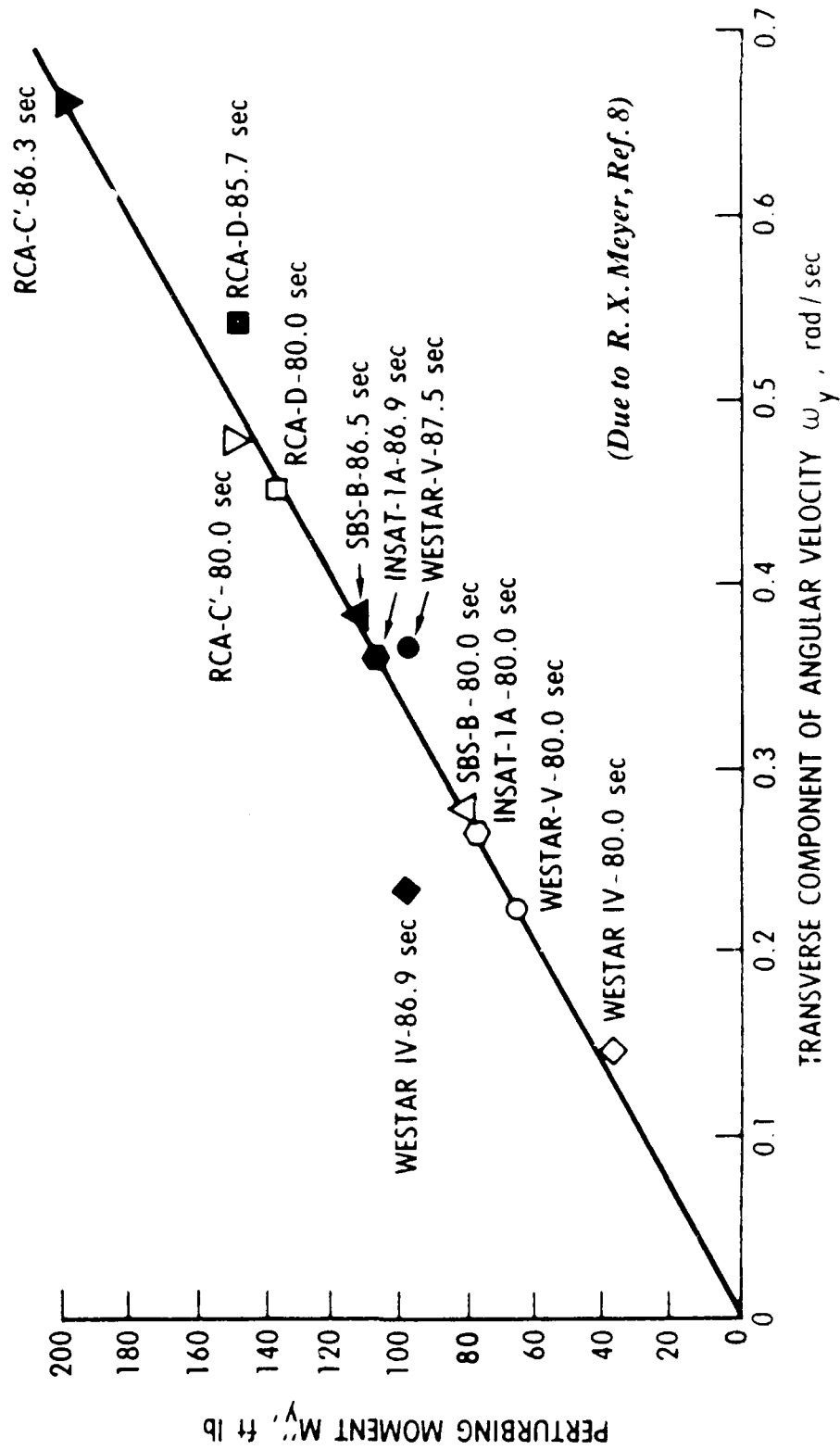


Figure 20. Correlation of Apparent Perturbing Moment with Transverse Angular Rate

where K is a factor of proportionality dependent upon the vehicle and motor parameters. That is, the disturbing moment is a linear function of the angular disturbance it produces. This proportionality indicates that a closed-loop driving mechanism is involved. This feature of the data eliminates a large number of potential driving mechanisms as discussed in the next section.

2.7 SUMMARY OF KEY FEATURES FROM THE CONING DATA

It is useful to summarize several important general features of the data that represent clues to the source of the instability. Perhaps of most significance is the cessation of growth at motor taildown. This indicates that the *source of coning growth lies within the propulsion system itself* as repeatedly emphasized in this report. Since the angular velocity disturbance moves relative to the vehicle (see Figure 7), it can be shown (from the dynamical model presented in a later section) that the disturbing torque cannot be related to anything fixed in the vehicle such as nozzle or grain misalignments or nonuniform burning of the propellant. The disturbing entity must orient itself freely within the system in response to feedback from the spacecraft motions. This key observation severely limits the list of candidate mechanisms.

One must obviously examine possible interactions with flexible elements of the structure, sloshing of particulate materials accumulating within the rocket motor during its operation, or with the combustion gas itself. The latter possibility had received the least attention until the present program was initiated.

Features that appear in all PAM-D data are:

- Growth of the coning perturbation either ceases or abruptly decreases at motor tailoff.
- The apparent torque causing the disturbance is proportional to the magnitude of the lateral perturbation angular velocity indicating a closed loop, self-excited oscillation.
- The pitch/yaw rate amplitude growth is accompanied by shifts of frequency, which are strongly correlated with the instantaneous growth rate.
- Yaw (y-axis) angular velocity perturbation always leads the Pitch (x-axis) by very nearly 90° throughout motor burn.
- Yaw angular rate is approximately 10% larger than pitch at the end the period of growth, but this appears to be related to instrumentation (probably roll/yaw coupling).

- Coning growth always occurs during the last part of the rocket motor burn with average growth rate rapidly becoming larger with time as tailoff is approached.
- There is sometimes evidence of short periods of coning growth (followed by rapid decay) before the main instability begins.

The potential importance of gas/vehicle interactions is strongly indicated by the jet damping phenomenon itself. It is of the greatest significance that the expected jet damping torques are of the same order of magnitude as the torques that *drive* the coning. This is ample proof that gasdynamics interactions can produce torques of the correct size. Another similarity is that the jet damping moment is also proportional to the vehicle angular rate perturbation. These observations strengthen the conclusion from the data correlation of subsection 2.6 that indicates the central importance of the rocket motor gas flow in the coning phenomenon. Section 4 of the report briefly outlines several mechanisms that have been proposed as potential causes of the PAM-D problem, and examines them critically in light of the observations. It first necessary to establish the set of conditions that lead to the type of rotational dynamics described in the data set. This is done in next section. Jet damping is then subjected to careful scrutiny in Section 5.

3.0 SPACECRAFT MOTION

A detailed dynamical model for the spacecraft/rocket motor system is required in order to deduce the characteristics of the disturbing torque responsible for driving the nutation instability discussed in Section 2. Such a model is also useful for eliminating inappropriate mechanisms from the list of potential disturbing entities. Section 4 presents a review of the list of mechanisms that have been proposed to date, and will explain, on the basis of the dynamics described in this section, why only a single class of disturbing moment can account for the PAM instability.

If a sufficiently general dynamic model is to be constructed, it is necessary to account for both the steady and unsteady motions of gas particles within the rocket motor and nozzle and their interaction with the rotational dynamics of the vehicle. Since much controversy surrounds the modeling of spacecraft/combustion gas interactions, it is appropriate to provide detailed documentation of the dynamical analysis that couples the rotational mechanics of the spacecraft itself to the time-dependent gas flow inside the motor chamber. The protocol needed for casting the problem in control volume form is emphasized. This is a crucial step, since it provides the linkage between the vehicle motion and the internal gas flow in a readily evaluated form. Simple solutions of the spacecraft equations of angular motion give insight into the nature of the disturbing torques responsible for the nutation instability.

3.1 ROTATIONAL DYNAMICS OF ROCKET PROPELLED VEHICLES

The necessary dynamics will be derived from fundamental principles. All steps are shown in order to emphasize the origins of important interaction effects. Figure 21 defines the coordinate system. The system to be analyzed consists of all solid elements of the spacecraft, the gas contained within the motor combustion chamber, and all gas particles that have been expelled from the system from the moment of motor ignition. If the motion of this system of particles is described in terms of an inertial reference coordinate system, the dynamical equations describing translation and rotation are

$$\begin{aligned} \mathbf{F} &= \frac{d\mathbf{P}}{dt} \\ \mathbf{M} &= \frac{d\mathbf{H}}{dt} \end{aligned} \tag{6}$$

where \mathbf{F} and \mathbf{M} are the sum of all *external* forces and moments, respectively, acting on the system, and \mathbf{P} and \mathbf{H} are the total linear and angular momenta of all mass elements comprising the system. Since only the three rotational degrees of freedom

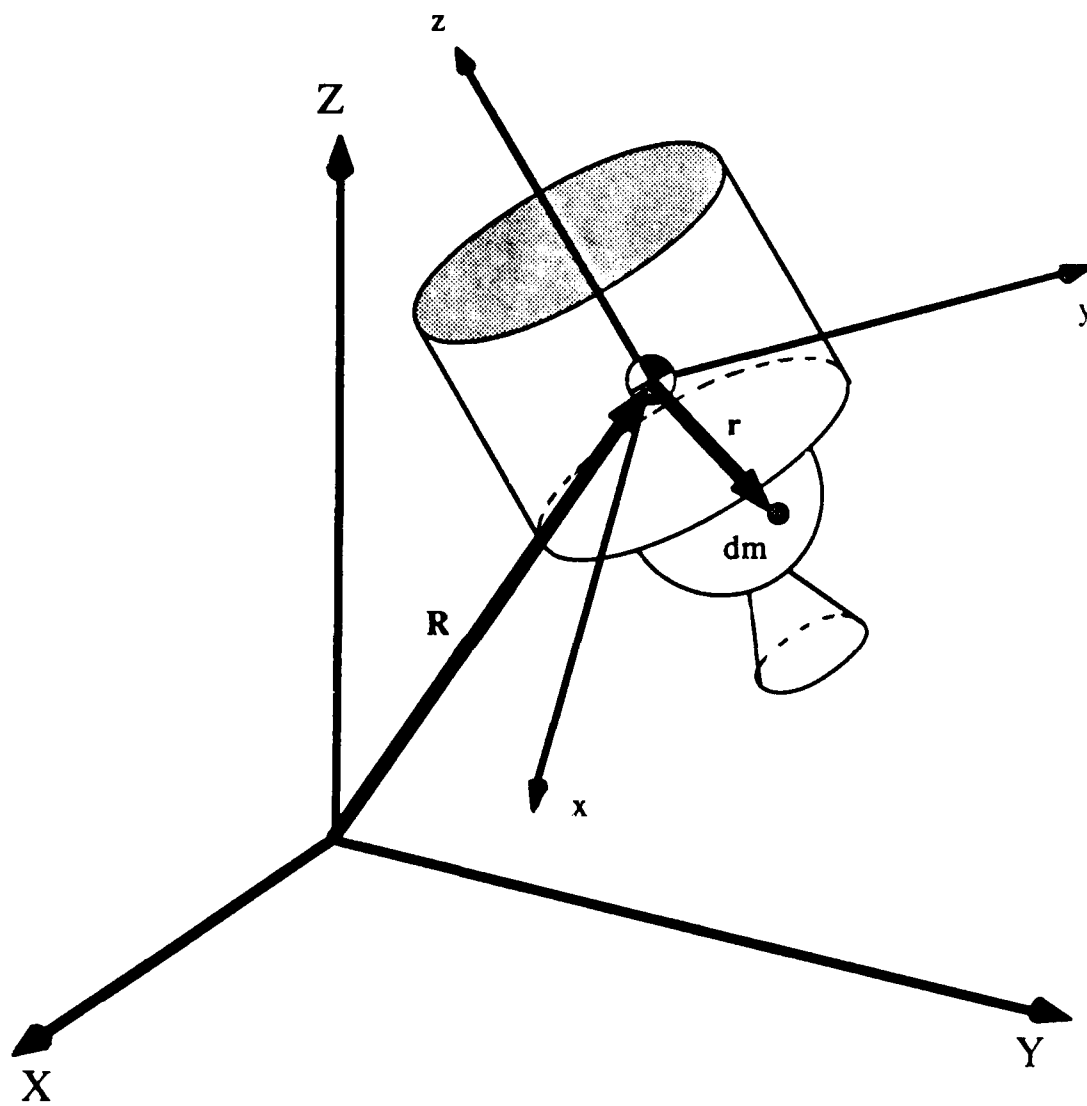


Figure 21 - Coordinate System

are of concern in the nutation instability problem, only the second of equations (6) requires attention. If vector \mathbf{R} locates the reference point in the body (usually the center of mass of the solid portion of the system) with respect to the inertial reference frame, and \mathbf{r} locates points within the system with respect to the body-fixed axes (x (pitch), y (yaw), z (roll) coordinates), then the angular momentum is

$$\mathbf{H} = \int_m (\mathbf{R} + \mathbf{r}) \times \mathbf{v}_{\text{abs}} dm \quad (7)$$

where \mathbf{v}_{abs} is the absolute velocity (velocity with respect to the inertial reference frame) of particle dm . Subscript "abs" refers to quantities described relative to the inertial (XYZ) coordinate system; subscript "rel" indicates quantities described relative to the body-fixed (xyz) coordinates.

Since, by definition, the *system* mass is constant, the time derivative of \mathbf{H} acts only on the integrand. Also, since the system is composed of elements (gas, solid, and possibly liquid) with different densities it is convenient to replace the mass element dm with its equivalent ρdV in terms of the associated volume element. Thus the equation of motion becomes

$$\mathbf{M} = \int_V \frac{d}{dt} [(\mathbf{R} + \mathbf{r}) \times \mathbf{v}_{\text{abs}}] \rho dV. \quad (8)$$

Since the absolute velocity is, by definition,

$$\mathbf{v}_{\text{abs}} = d/dt(\mathbf{R} + \mathbf{r}), \quad (9)$$

then the first term in the expansion of the integrand is zero ($\mathbf{v}_{\text{abs}} \times \mathbf{v}_{\text{abs}} = 0$). Thus

$$\mathbf{M} = \int_V (\mathbf{R} + \mathbf{r}) \times \mathbf{a}_{\text{abs}} \rho dV \quad (10)$$

\mathbf{a}_{abs} is the absolute acceleration of the particle located at position $\mathbf{R} + \mathbf{r}$. It is far more convenient to employ noninertial body-fixed coordinates in describing the motion. Therefore, the familiar transformation

$$\mathbf{a}_{\text{abs}} = \mathbf{a}_0 + \mathbf{a}_{\text{rel}} + \boldsymbol{\omega} \times \boldsymbol{\omega} \times \mathbf{r} + 2\boldsymbol{\omega} \times \mathbf{v}_{\text{rel}} + \boldsymbol{\alpha} \times \mathbf{r} \quad (11)$$

must be invoked. As a convenience, one can locate the origin of the inertial reference system at the instantaneous position of the center of mass of the solid part of the system ($\mathbf{R} = 0$). Then the system dynamical equation can be written as

$$\mathbf{M} = \int_V (\mathbf{R} + \mathbf{r}) \times \mathbf{a}_{\text{rel}} \rho dV + \int_V \mathbf{r} \times (\mathbf{a}_0 + \boldsymbol{\omega} \times \boldsymbol{\omega} \times \mathbf{r} + 2\boldsymbol{\omega} \times \mathbf{v}_{\text{rel}} + \boldsymbol{\alpha} \times \mathbf{r}) \rho dV. \quad (12)$$

The term involving $\mathbf{r} \times \mathbf{a}_0$ (where \mathbf{a}_0 is the acceleration of the mass center) is displayed, although for cases of interest the nearly axial symmetry of the body with the mass center located on this axis precludes any significant influence from this source. As the system consists of both fluid and solid components, it is a great advantage to shift now to the control volume point of view. A control volume encompassing the solid part of the system as well as the gas particles contained within the motor is most useful. The mass flux through the nozzle exit plane must be allowed for. Using the Reynolds transport theorem, the time rate of change of the angular momentum relative to the moving coordinates can be written as

$$(d\mathbf{H}/dt)_{\text{rel}} = \int_V \mathbf{r} \times \mathbf{a}_{\text{rel}} \rho dV = \frac{\partial}{\partial t} \int_V \mathbf{r} \times \mathbf{v}_{\text{rel}} \rho dV + \int_S \mathbf{r} \times \mathbf{v}_{\text{rel}} (\mathbf{v}_{\text{rel}} \cdot \mathbf{n}) \rho dS \quad (13)$$

where the partial time derivative notation is used in the standard fluid mechanics fashion to distinguish between spatial and local time rates of change. For a steady flow, the first term on the right would vanish although angular momentum flux through the control surface as represented by the second term is not, in general, equal to zero. Thus, the general equation of angular motion in control volume form is

$$\begin{aligned} \mathbf{M} = & \int_V \mathbf{r} \times (\mathbf{a}_0 + \boldsymbol{\omega} \times \boldsymbol{\omega} \times \mathbf{r} + \boldsymbol{\alpha} \times \mathbf{r}) \rho dV + \int_V \mathbf{r} \times (2\boldsymbol{\omega} \times \mathbf{v}_{\text{rel}}) \rho dV + \\ & + \frac{\partial}{\partial t} \int_V (\mathbf{r} \times \mathbf{v}_{\text{rel}}) \rho dV + \int_S \mathbf{r} \times \mathbf{v}_{\text{rel}} (\mathbf{v}_{\text{rel}} \cdot \mathbf{n}) \rho dS. \end{aligned} \quad (14)$$

It is useful to treat the three terms involving relative motion within the control volume as internally generated reaction torques. Thus we write

$$\int_V \mathbf{r} \times (\mathbf{a}_0 + \boldsymbol{\omega} \times \boldsymbol{\omega} \times \mathbf{r} + \boldsymbol{\alpha} \times \mathbf{r}) \rho dV = \mathbf{M}_{\text{ext}} + \mathbf{M}_{\text{int}} \quad (15)$$

where \mathbf{M}_{ext} is the moment from external interactions (due to drag, gravitational or electromagnetic body forces, etc.). \mathbf{M}_{int} is the internally generated torque represented by the inertial correction terms arising from relative motion of elements such as sloshing liquids or the gas flow in a rocket motor. Jet damping is an example of such an interaction. \mathbf{M}_{int} is expressed in terms of the fluid motions inside the control volume as

$$\mathbf{M}_{\text{int}} = - \int_V \mathbf{r} \times (2\boldsymbol{\omega} \times \mathbf{v}_{\text{rel}}) \rho \, dV - \frac{\partial}{\partial t} \int_V (\mathbf{r} \times \mathbf{v}_{\text{rel}}) \rho \, dV - \int_S (\mathbf{r} \times \mathbf{v}_{\text{rel}}) \mathbf{v}_{\text{rel}} \cdot \mathbf{n} \, \rho \, dS. \quad (16)$$

It is within the disturbing moment \mathbf{M}_{int} that one must seek the source of the PAM-D nutation instability phenomenon, since \mathbf{M}_{ext} is usually very small (if gravity gradients, micrometeorite drag, and electric and magnetic field effects are negligible).

The next three subsections are devoted to further manipulation of this result for specific applications in the analysis of spinning rocket nutation instability. Simple examples are first carried out to demonstrate the connection of the general formulation to familiar special cases and to highlight the nature of some simplifying assumptions used in previous analyses of the attitude dynamics of rotating vehicles with jet propulsion.

3.2 SPACECRAFT FREE FALL ATTITUDE DYNAMICS

Equation (15) is first shown to properly reproduce the simplest type of spacecraft angular motion in which only externally generated torques are present. In general, \mathbf{M}_{ext} consists of moments due to body forces (the gravity-gradient torque for example), and attitude control torques. It is often appropriate to assume that the vehicle behaves as a rigid body, and in this case there are no relative velocities within the control volume ($\mathbf{v}_{\text{rel}} = 0$). The angular motion is governed by (15) with the appropriate terms deleted. Assuming that the center of mass lies at the origin of the body-fixed coordinate system, we find

$$\mathbf{M}_{\text{ext}} = \int_V \mathbf{r} \times (\boldsymbol{\omega} \times \boldsymbol{\omega} \times \mathbf{r} + \boldsymbol{\alpha} \times \mathbf{r}) \rho \, dV, \quad (17)$$

and the volume integrals yield the classical result:

$$\mathbf{M}_{\text{ext}} = \mathbf{I} \cdot \boldsymbol{\alpha} + \boldsymbol{\omega} \times \mathbf{I} \cdot \boldsymbol{\omega} \quad (18)$$

where \mathbf{I} is the inertia tensor

$$\mathbf{I} = \begin{bmatrix} I_{xx} & I_{xy} & I_{xz} \\ I_{yx} & I_{yy} & I_{yz} \\ I_{zx} & I_{zy} & I_{zz} \end{bmatrix} \quad (19)$$

If the axes are also principal axes, then (18) in component form yields the familiar Euler differential equations of motion as expected.

3.3 SPACECRAFT DYNAMICS WITH STEADY MOTOR GAS FLOW

Most previous analyses of the PAM-D nutation problem that have attempted to account for the influence of combustion gas flow (cf Refs. 2-6) have invoked the simplifying assumption that the internal gas flow is steady. The steady part of the Coriolis term representing the interaction between the axial spin and the chamber flow is also neglected in all analyses known to the writer. The gas motion is most often represented by a very simple axial flow field of the form

$$\mathbf{v}_{rel} = \mathbf{U} = -U\mathbf{k}. \quad (20)$$

Both tangential and radial components are disregarded. It is also usually the case in spaceflight applications with spin stabilized vehicles that the externally applied moments are negligible ($\mathbf{M}_{ext} = 0$) so the governing equation becomes:

$$\int_V \mathbf{r} \times (\boldsymbol{\omega} \times \boldsymbol{\omega} \times \mathbf{r} + \boldsymbol{\alpha} \times \mathbf{r}) \rho \, dV = - \int_V \mathbf{r} \times (2\boldsymbol{\omega} \times \mathbf{v}_{rel}) \rho \, dV \quad (21)$$

or

$$\mathbf{I} \cdot \boldsymbol{\alpha} + \boldsymbol{\omega} \times \mathbf{I} \cdot \boldsymbol{\omega} = - \int_V \mathbf{r} \times (2\boldsymbol{\omega} \times \mathbf{v}_{rel}) \rho \, dV \quad (22)$$

The inertia tensor now includes a contribution to the total mass distribution from the instantaneous mass of combustion gas contained within the motor chamber and nozzle.

The convective term $\int_V \mathbf{r} \times \mathbf{v}_{rel} \mathbf{v}_{rel} \cdot \mathbf{n} \rho \, dS$ in \mathbf{M}_{int} is ignored since the simplified flow model fails to account for the axial vortex flow generated by the Coriolis torque. This axial moment component is responsible, in part, for the increase in axial angular velocity of the spacecraft during motor operation. The term on the right of (22) is the jet damping torque to be evaluated in Section 5. Pottsepp^{4,5} shows that this form for the steady flow interaction is equivalent to the more complex form often exhibited in the literature (cf Refs. 2-6):

$$\mathbf{I} \cdot \boldsymbol{\alpha} + \frac{d\mathbf{I}}{dt} \cdot \boldsymbol{\omega} + \boldsymbol{\omega} \times \mathbf{I} \cdot \boldsymbol{\omega} = \mathbf{D} + \boldsymbol{\omega} \times \mathbf{Q} + \frac{d\mathbf{Q}}{dt} \quad (23)$$

where \mathbf{Q} represents the angular momentum of gas particles moving within the control volume

$$\mathbf{Q} = \int_V \boldsymbol{\omega} \times \mathbf{r} \rho \, dV \quad (24)$$

and \mathbf{D} is the jet damping moment given by

$$\mathbf{D} = \int_S \mathbf{r} \times (\mathbf{r} \times \boldsymbol{\omega}) (\mathbf{u} \cdot \mathbf{n}) \rho dS \quad (25)$$

The simpler form (Equation (22)) derived here is obviously more easily evaluated and, as will be shown, more plainly indicates the physical origins of the jet damping interactions. These will be described in complete detail in Section 5.

3.4 EFFECTS OF UNSTEADY GAS FLOW ON VEHICLE DYNAMICS

It is now obvious that many potentially important interactions have been neglected in the standard analyses of spinning powered flight angular motion. For example, it is clearly not justified to ignore the time dependent gas motions when the motor chamber is undergoing lateral wobbling or nutation.

In order to properly assess the effects of the combustion gas flow, we must represent the spacecraft motion with the full equation

$$\begin{aligned} \mathbf{I} \cdot \boldsymbol{\alpha} + \boldsymbol{\omega} \times \mathbf{I} \cdot \boldsymbol{\omega} = \mathbf{M}_{int} = & - \int_V \mathbf{r} \times (2\boldsymbol{\omega} \times \mathbf{v}_{rel}) \rho dV - \\ & - \frac{\partial}{\partial t} \int_V \mathbf{r} \times \mathbf{v}_{rel} \rho dV - \int_S \mathbf{r} \times \mathbf{v}_{rel} (\mathbf{v}_{rel} \cdot \mathbf{n}) \rho dS. \end{aligned} \quad (26)$$

It is important to recognize that the disturbing torques arise from relative motions within the system arising in response to the angular motions of the vehicle. A detailed analysis of the internal flow field will be required in order to explicitly determine these influences. *Attention must be paid to both steady and unsteady parts of \mathbf{v}_{rel} .* For a complete representation, it is also necessary to account for the axial vortex component of the mean flow. Before this is undertaken, it is beneficial to examine general solutions of (26) to determine what forms of disturbing moments \mathbf{M}_{int} will best account for the motion observed in the experimental data

If the part of the system that can be described as a rigid body is also axially symmetric, then Equation 26 is equivalent to the set of scalar equations given by

$$\begin{aligned} d\omega_x/dt &= \lambda_s \omega_y + M_x/I_1 \\ d\omega_y/dt &= -\lambda_s \omega_x + M_y/I_1 \\ d\omega_z/dt &= M_z/I_0 \end{aligned} \quad (27)$$

where the coordinates are as defined in Figure 21. I_0 is the centroidal moment of inertia about the spin axis; I_1 is the moment of inertia about the lateral axis through the center of mass. $I_1 = I_x = I_y$ for symmetrical vehicles.

The assumption of symmetry as used in the derivation of Equations 27 is justified for the majority of the vehicles described in Section 2 (see Table 1). λ_s is the "free-precession" frequency,

$$\lambda_s = (1 - I_0/I_1) \omega_z. \quad (28)$$

λ_s closely matches the oscillatory frequency observed in the flight rate gyroscope data. Figure 5 shows a plot of this equation for the WESTAR V vehicle. The variation of λ_s with time reflects both the changes in the moments of inertia as propellant mass flows from the system, and a slow increase in spin rate which is related to the formation of an axial vortex in the combustion chamber. The net result is a slow decrease in λ_s during motor operation.

3.5 SOLUTIONS FOR SIMPLE DISTURBING MOMENTS

Although the exact nature of the disturbing moment function remains to be determined, it is instructive to deduce appropriate simple models inspired by the experimental data. Numerical integration of the Euler equations (with due attention to the variation with time of parameters such as the moments of inertia and the important gas dynamic perturbation moments) is employed in later sections to produce detailed simulations of the system behavior.

Much guidance in the interpretation of the more precise simulations comes from study of simple closed form solutions. Straightforward calculations are facilitated by assuming constant spacecraft parameters. That is, the slow changes in mass, moments of inertia, and moment arms can be neglected, since they occur on a time scale that is long compared to the period of the angular velocity oscillations. The magnitude of the axial angular velocity is also assumed constant for similar reasons.

Introducing dimensionless variables based on scaling parameters that will be used throughout the report, Euler's equations become

$$\begin{aligned} d\omega_x/dt &= -\lambda_s \omega_y + \delta M_x \\ d\omega_y/dt &= \lambda_s \omega_x + \delta M_y \\ d\omega_z/dt &= \delta M_z (I_1/I_0) \end{aligned} \quad (29)$$

where the perturbation angular velocity vector $\omega = (\omega_x \mathbf{i} + \omega_y \mathbf{j} + \omega_z \mathbf{k})$, is made dimensionless by dividing by the spacecraft spin rate Ω . Time is nondimensionalized by multiplying by the same parameter. δ is the moment scaling parameter given by

$$\delta = M_0/I_1\Omega^2 = \rho_0 R_0^4 v_b/I_1\Omega \quad (30)$$

where $M_0 = (\rho_0 R_0^4 v_b \Omega)$ is proportional to the (dimensional) magnitude of the applied moment. ρ_0 is the gas density, R_0 is the chamber radius, and v_b is the gas velocity at the burning surface. The last three quantities are the primary scaling parameters for the rocket chamber flow field. Their presence here results from the need to use a common set of variables in dealing with the combined motions of the spacecraft and the gas flow.

Since δ is a very small number (of the order of $2 \cdot 10^{-4}$), it is clear that the effects of interaction moments related to the flow field can be treated as small perturbations. To the first approximation, the vehicle motion should be that of a freely spinning rigid body. The governing equations are found by applying the limit process $\delta \rightarrow 0$. This suggests the application of simple perturbation methods in solving the problem to take advantage of the smallness of the disturbing torques. This is not a necessary step, but it clarifies and simplifies much of the analysis to be undertaken later. Define the perturbation series

$$\omega = \omega^{(0)} + \delta \omega^{(1)} + O(\delta^2), \quad (31)$$

and use it to expand Equations 29. To zeroth order in δ , the system is governed by

$$\begin{aligned} d\omega_x^{(0)}/dt &= \lambda_s \omega_y^{(0)} \\ d\omega_y^{(0)}/dt &= -\lambda_s \omega_x^{(0)} \\ d\omega_z^{(0)}/dt &= 0. \end{aligned} \quad (32)$$

Since $\omega_z^{(0)} = \Omega$ is constant as indicated by the third equation, then $\lambda_s = (1 - I_0/I_1)$ is the dimensionless free-precession frequency characterizing the motion. The two lateral equations are easily solved with the result

$$\omega^{(0)} = (\omega_x^{(0)} \mathbf{i} + \omega_y^{(0)} \mathbf{j}) = \omega_0 (\mathbf{i} + i \mathbf{j}) \exp i(\lambda_s t + \phi) \quad (33)$$

where ω_0 is an arbitrary reference amplitude and ϕ is the phase angle. λ_s , ω_0 , and ϕ are slowly varying functions of time reflecting the fact that the perturbing forces are very small and the variation in parameters such as moments of inertia take place quite slowly compared to the period of oscillation λ_s . Equation 33 describes the lateral component of the angular velocity perturbation. It can be seen that the solution represents either a retrograde or posigrade precession depending on the sign of λ_s . For prolate vehicles such as a PAM-D spacecraft, I_0 is smaller than I_1

and the angular velocity perturbation rotates relative to the vehicle in the retrograde direction. That is, to an observer rotating with the spacecraft, the projection of ω on the x-y plane rotates in the opposite direction to the spin at the angular rate λ_s . This is precisely the motion described in Section 2 over a sufficiently short period of time. Figure 22(a) shows the trajectory of $\omega_{xy} = \omega^{(0)}$ on the x-y plane for the prolate case. The arbitrary phase angle ϕ is set to zero for convenience.

It is also necessary to determine what effects can cause the amplitude ω_0 to grow in the manner observed. Thus one must investigate the influence of perturbing moments. It is convenient to introduce complex notation such that:

$$\begin{aligned}\omega &= \omega_x - i \omega_y \\ M &= M_x - i M_y\end{aligned}\tag{34}$$

This results in the compact form of Euler's equation

$$d\omega/dt - i\lambda_s\omega = \delta M.\tag{35}$$

As shown in Section 2, there is experimental evidence indicating that the disturbing moment is proportional to the magnitude of the angular velocity perturbation. Thus on this basis it is useful to consider perturbing moments of the form

$$\delta M = A\omega\tag{36}$$

where A is a complex factor of proportionality to indicate that M and ω might be out of phase with ω . That is, vectors M and ω may not be parallel. For this simple case, motivated by the experimental data, the forced solution is

$$\omega = \omega_0 e^{(A + i\lambda_s)t}\tag{37}$$

Note that if A is zero, the simple free precession solution shown in vector form in Equation (33) is recovered. If A is complex as suggested above, then the solution can be written as

$$\omega = \omega_0 e^{(A_r)t} e^{i(A_i + \lambda_s)t}\tag{38}$$

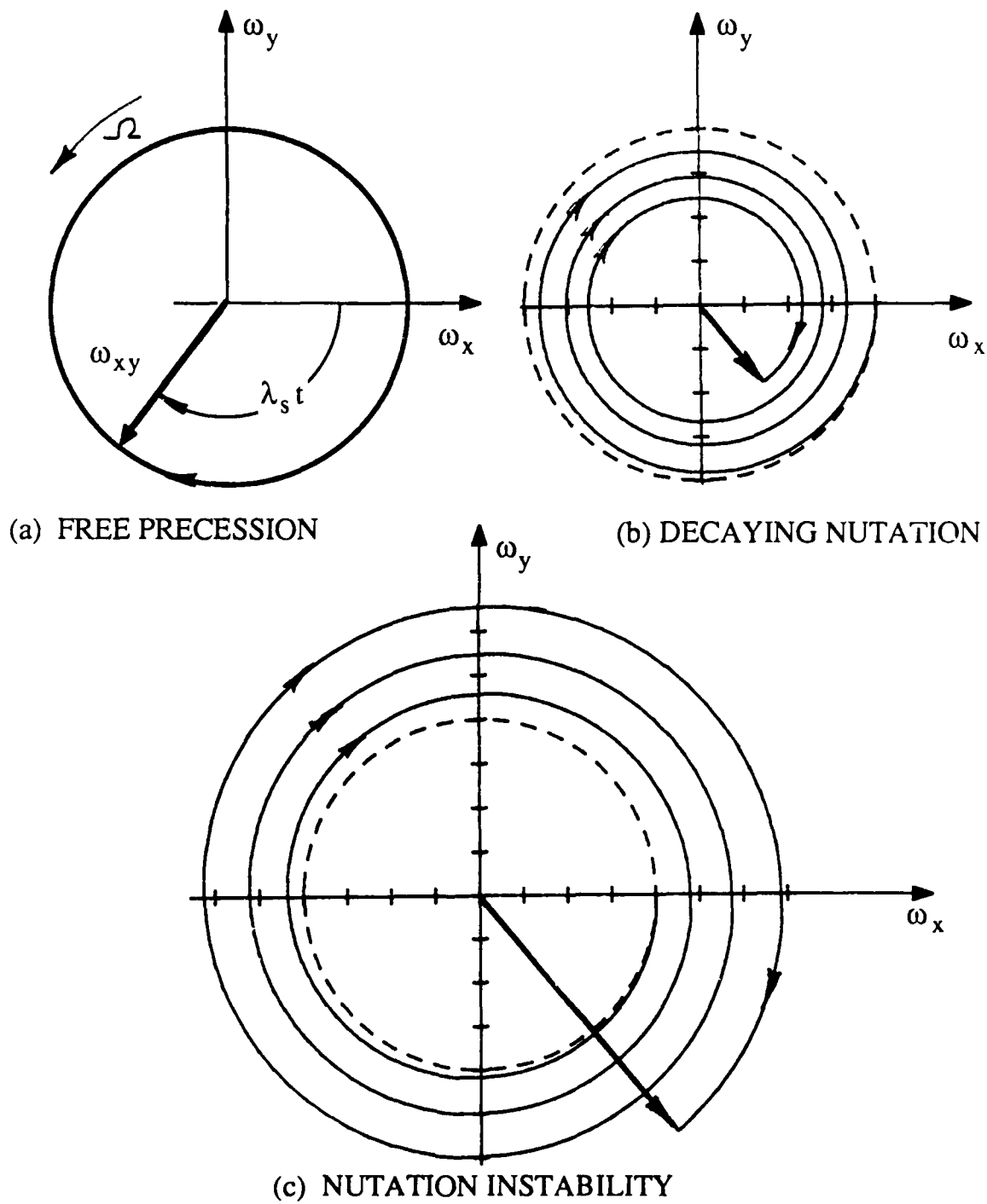


Figure 22. Plots of Simple Solutions Spinning Rocket Equations of Motion

Now the amplitude grows or decays if the real part A_r is positive or negative, respectively. There is also a related frequency correction caused by the imaginary part, A_i . It will be demonstrated that the jet damping moment behaves in precisely this fashion. The corresponding A_r is always negative for the jet damping interaction. Evaluation of the unsteady flow counterparts of the jet damping, to be carried out in later sections of the report, will show that they are also proportional to the angular velocity perturbation. An important task will be to determine the conditions that lead to a net positive value for the growth rate A_r . Figures 22(b) and 22(c) show the effects of negative or positive values of A_r on the motion. If Figure 22(c) is compared to the experimental data (WESTAR V) as plotted in Figure 7, it is evident that the simple model closely simulates the observed disturbance.

Two very important features of the interaction of motor gas flow with spinning spacecraft dynamics have been uncovered in the above analysis. They are:

- There exist potentially important disturbing moments caused by the unsteady motions of the combustion gases. These are related to, but not contained within, the classical jet damping analysis.
- A simple disturbing moment vector that is proportional to the angular velocity perturbation vector generates motion identical to the nutation behavior observed in flight.

More general representations for the disturbing moment can be readily formulated, but the simple relationship shown in Equation 36 reproduces all attributes of the nutation instability. Thus one is led to examine potential disturbing mechanisms that interact with the vehicle motion as a linear proportionality between the torque amplitude and the angular velocity perturbation. This drastically narrows the array of possible disturbing influences.

4.0 PROPOSED NUTATION INSTABILITY MECHANISMS

This section reviews some of the mechanisms that have been proposed as the origin of the coning disturbance observed in the PAM-D space missions. Many proposals are not described in detail because they obviously do not fit the requirements posed by the data set. Emphasis is placed on mechanisms that satisfy criteria summarized at the end of the previous section. The effect of sloshing liquids carried in the spacecraft is not discussed herein for the reason that only a few of the vehicles in question carried such materials. The liquid sloshing effects clearly affect the motions both during and after motor operation as detailed in numerous papers⁹⁻¹⁷. A recent note by S. Ono of the National Space Development Agency of Japan is an excellent example of this type of analysis¹⁸.

4.1 DISTURBING TORQUES FIXED WITHIN THE SPACECRAFT

The most commonly suggested coning mechanism is that represented by misalignment of the motor thrust vector. Such misalignment would result from a variety of sources such as a warped nozzle exit, nonuniform erosion of the nozzle throat, mechanical misalignment of the motor thrust vector relative to the vehicle principle axes of symmetry, or distortion of the propellant grain or the motor case. It has also been frequently suggested that nonuniform combustion of the propellant charge would result in a thrust misalignment and consequent generation of a lateral moment which would grow with time during motor operation.

None of these mechanisms can generate the type of disturbance represented by the rate gyroscope measurements described in Section 2. The review of the spinning spacecraft flight dynamics (see Section 3) makes it evident that only a disturbance torque that can move within a body-fixed coordinate frame attached to the vehicle is capable of generating the observed motion. An important feature of the torque is that it must move relative to this frame in the retrograde sense with respect to vehicle spin (for a prolate spacecraft mass distribution). Thus, although it is possible to hypothesize body-fixed moments (such as torques caused by thrust misalignment, nozzle distortion, nonuniform regression of the propellant surface and so on) that grow in time during motor operation, it is not possible to fit the crucial requirement just reviewed with such models. Consequently, no further consideration of body-fixed disturbances is necessary in this report. All further discussion centers on disturbances free to move relative to the spacecraft.

4.2 EFFECT OF FLEXIBLE SPACECRAFT COMPONENTS

One of the best known destabilizing mechanisms in spinning space vehicles is the dissipation of mechanical energy or influence of periodic flexing of structural elements¹⁹. There have been many cases of unexpected instabilities of this type.

For example, the tumbling of the Explorer I mentioned earlier that was caused by the energy dissipation in its whip antennas. Explorer XX underwent rapid spin decay as a result of Solar torque on a thermally deformed structure. The ATS 5, which was equipped with an active nutation damper during orbital injection, became unstable as a result of energy dissipation in a heat pipe. Early study was made of similar possibilities in the PAM-D series. It is important to understand that there was great variability in the spacecraft configuration in these vehicles. While it is possible that flexing structural members, loose deployables, or thermally induced distortion could play some role, it is clear that the basic source of nutation driving could not be associated with this class of disturbance since there was such a large variation in geometry.

One of the earliest valid coning mechanisms to be proposed was based on the possibility that the flexing of the nozzle exit cone could be the source of unstable behavior. Clearly, any element of the vehicle that is capable of relative motion must be considered. Other similar effects were investigated including elastic deformation of the motor case and nozzle support. The proposal was made that the nozzle flexibility increases with time during motor operation due to heat transfer and changes of material properties in critical nozzle components.

A comprehensive program was undertaken to test the compliant nozzle hypothesis in laboratory analysis of the nozzle materials, in static motor firings on a rotating test stand at AEDC (Tullahoma, Tennessee), and in actual flight with a modified nozzle. Since the findings of this study are available only in McDonnell Douglas and Aerospace Corporation internal reports, no attempt is made here to give details. The single flight test of the stiffened exit cone (WESTAR V) showed that this mechanism is not alone capable of generating the coning instability. The WESTAR V data is described in detail in previous sections. It is interesting to note that it was possible to generate convincing computer simulations of coning growth based on the flexible nozzle hypothesis by proper choice of input parameters and assumed changes in mechanical properties of the nozzle structure. Thus the flexible nozzle represented a very plausible theoretical mechanism that could be made to match the observations.

It is possible that nozzle flexibility is one variable that might affect the coning growth. However, in comparing WESTAR V to WESTAR IV, a very similar vehicle without the stiffened nozzle, it is seen that the latter flight had a *lower* final cone angle (but an apparently slightly higher average growth rate). Thus it is concluded that nozzle flexibility cannot, of itself, represent the source of the nutation instability.

4.3 LIQUID SLOSHING MECHANISMS

Sloshing of liquid stores is another well-known destabilizing mechanism. It is undoubtedly a factor in some of the PAM-D observations. In some flights, coning growth continued after motor burnout at a lower rate of increase. The cone angle at the end of burn was always larger in these missions than that experienced in vehicles not exhibiting the post-burn growth. The latter spacecraft did not carry liquids. Thus it appears to be unnecessary to consider liquid sloshing as a primary mechanism in the nutation instability problem.

Recent studies of wobbling instabilities observed in spinning liquid-filled projectiles should also be mentioned²⁰⁻²⁸. An excellent example of the type of analysis required to deal with interactions between the projectile motion and the time-dependent motion of the contained viscous fluid is that given by Vaughn, Oberkampf, , and Wolfe²⁸. They demonstrate the central importance of classical spinning fluid effects such as the inertial wave phenomenon. The problem dealt with in References 20-28 is similar in some respects to the PAM-D instability. A major difference is that viscous forces plays a key role in the former, while in the PAM-D case, the response of the gas motions to the vehicle wobbling must be dominated by convective effects because of the massive throughflow of combustion gases. Nevertheless, the projectile instability observations provide valuable guidance in seeking the source of the PAM nutation phenomenon.

Another proposed sloshing mechanism that has received very detailed consideration is one based on the notion that aluminum oxide slag produced in the combustion of the solid propellant is entrapped within the motor chamber due to a combination of the spin, axial acceleration, highly submerged nozzle, and the tendency of the heavy oxide particles in the two-phase chamber flow to lag the motion of the gaseous component. Again, a comprehensive experimental and analytical study was undertaken to assess this proposal. An elaborate test fixture was used at McDonnell Douglas to simulate the motion of slag trapped within a cavity shape like that formed aft of the nozzle entrance in the actual motor chamber. It was assumed that slag accumulates during motor operation in liquid form. The details have not been published, but it is the understanding of the writer that it was not possible to establish the validity of the slag mechanism on the basis of the experiments.

The theoretical studies²⁹ apparently indicated that slag sloshing could cause coning, but that the amount of slag required was significantly greater than could be expected to accumulate in flight. The amount of aluminum oxide material required depends critically on assumptions related to the configuration and location of the supposed liquid pool of slag. A more acceptable model might result if slag effects were to be incorporated in the form of two-phase flow in combination with the

primary gas flow. That is, it seems more likely that particle motion of slag trapped in recirculation zones would be dominated by the local gas convection as a two-phase gas/particle mixture. The current status of the slag model is not known to the writer.

4.4 INTERACTIONS INVOLVING MOTOR COMBUSTION GASES

On the basis of careful consideration of the spacecraft observations, it has been apparent to some investigators that the flow of gases through the combustion chamber and the nozzle might represent a significant influence on nutation of the vehicle. The earliest suggestions of this type known to the author were described in an internal NASA document by Bolster³⁰ with an attachment written by J. F. McGarvey. McGarvey anticipated, conceptually, some of what has come forth in detailed form in the present study. His suggestions were based on the possibility of unsymmetrical internal flows related to the recirculation regions at the aft end of the rocket motor.

The work described in the body of this document has focused on the influence of the time-dependent part of the chamber gas motion on the vehicle/gas interactions. This effort has evolved into a comprehensive model that forms the basis of the entire report and will be elaborated in detail in the following sections. An off-shoot of the general philosophy adopted early in the program can be seen in recent work by Meyer^{7,31}. His approach is similar in certain respects to that described herein. Meyer's analysis is carried out in a ballistic coordinate system that moves relative to the body in the retrograde direction with the free-precession angular velocity. This is done in order to simplify the modeling of the gas flow. Unfortunately, the flow field is assumed to be steady from the outset. Crucially important effects are thus automatically dropped from consideration. In particular, the well-established inertial wave phenomenon is thereby eliminated; it will be shown later that such waves must be included in arriving at a complete description of the time-dependent gas motion in the combustion chamber. Also it appears that potentially important effects related to convection of angular momentum by the mean flow are not accounted for. In order to achieve agreement with observed data, Meyer found it necessary to invoke phase shifts caused by unsymmetrical flow through the nozzle³¹. These calculations are based on the paper by Walter³²; unfortunately, at least on the basis of simple extrapolation of Walter's results, the results are not consistent with observations. For example, the effects of variation in nozzle length are not in agreement either in magnitude or direction with PAM-D spacecraft nutation data. It is important to emphasize that Walter's analysis is only valid for steady gas flows. Consideration of the entire time-dependent flow field, including that in the nozzle, is required if the combustion gas flow interactions are to be properly evaluated. Thus nozzle effects are of potential importance, but the necessary detailed theory has not yet been worked out.

4.5 PRELIMINARY EVALUATION OF PROPOSED MECHANISMS

The removal of all potential nutation instability mechanisms related to forces or moments fixed within the vehicle greatly reduces the list of possibilities. Again, such mechanisms are inconsistent with the experimental data. As shown above, there remain just three possible mechanisms. These are: (1) Internal flexing of spacecraft structural elements such as the nozzle exit cone, (2) Sloshing of liquid stores or slag particles trapped in the combustion chamber, and (3) Interaction between the combustion flow field and the vehicle motion. The first item has been effectively eliminated from the list by experiment; a stiffened nozzle had no important influence on the nutation instability. Furthermore, the large variability in PAM-D spacecraft structure seems to eliminate the effects of loose deployables or other structural energy dissipation from the list. Thus at the present time only two mechanisms remain in the list of possibilities. Further work is apparently in progress on slag effects, but its status is unknown at the time of writing.

There are excellent physical arguments (see Section 3 for examples) indicating that the vehicle interacts with the combustion gas flow to generate the coning instability. Of the many mechanisms proposed, this one has met with the most resistance from the community of investigators. A major reason for the hesitance to accept the gas dynamics mechanism is that such effects have not been observed in a myriad of previous spaceflight operations. It will be important to examine the results presented later to discover what features of the PAM-D vehicles depart so radically from previous experience that a new phenomenon has appeared. It will be demonstrated that the main differences are related to the relative size of the propulsion system combustion chamber and its placement relative to the vehicle mass distribution. Another factor will be shown to be the nearly spherical or even oblate combustion chamber shape.

The remainder of this report is devoted to a careful investigation of the interactions between the motor gas flow and nutational instability. In order to establish the details of this interaction, it is necessary to construct a comprehensive mathematical model that can be backed by appropriate experiments. The bulk of the report deals with the extensive analytical treatment required. The laboratory cold flow experiments that guided the analysis are also described.

It has not been possible up to the present time to verify any of the proposed models by means of static test firings of full-scale spin motors. The principal difficulty in such testing is the necessity to mount the rocket motor on a fixed spin axis. Fixed axis rotation does not bring about combustion gas flow interactions related to vehicle wobbling. The prohibitive cost of conducting research on full-size system in actual space flight forces heavy reliance on theory and appropriate laboratory simulations as described in what follows.

The present program was carried out with the above considerations as the guiding philosophy. In order that such an effort be successful, it is necessary that great care be taken not to exclude at the outset any phenomenon that could conceivably be involved. In particular, in treating the unsteady gas flow within a wobbling combustion chamber it is necessary to account in a realistic way for the following: (1) time-dependent motions in a spinning contained gas with strong convection and a choked nozzle, (2) combustion at the walls of the container, (3) a strong axial vortex flow induced by the motor spin, and (4) a highly submerged nozzle entrance. These requirements lead to a quite difficult problem in gas dynamics containing elements that have not been studied previously.

The simplest possible representations of the fluid dynamics effects that are consistent with the nutation problem are used herein to provide a clear physical understanding of a myriad of interactions. Each simplifying assumption is justified in detail as it is introduced. Reliance on numerical solutions is minimized in order to retain the greatest possible degree of physical touch with the problem. Nevertheless, extensive development of computational techniques was undertaken in order to build the necessary foundations for later work. Also, efficient computational algorithms were essential in evaluating the analytical models and were employed in application of the theoretical results to actual spacecraft configurations. Later models that address the complex motor flow field geometry in a more complete way will undoubtedly require greater reliance on computational fluid dynamics in producing fully quantitative calculations appropriate for use in a predictive mode.

5.0 INTERACTION OF VEHICLE MOTION WITH GAS FLOW

In seeking an understanding of the influence of the motor gasdynamics on the PAM-D nutation instability problem, it is useful to undertake a review of classical jet damping theory. This is an appropriate exercise, because the jet damping moments are of the same order of magnitude as the disturbing moments that generate the observed coning instability. This is significant for two reasons: (1) It establishes the fact that internal ballistics effects are capable of generating torques of the correct amplitude and (2) It indicates the magnitude of the primary damping effect that must be overcome by the destabilizing entity. It is also clear from the discussions in previous sections that there is considerable evidence linking the motor gas flow to the coning effects. For example, coning growth abruptly ceases at the end of the rocket motor burn.

A general analysis of the interaction between vehicle motion and the combustion gas flow is discussed first. It will become evident as the origins of jet damping are reviewed that several potentially important vehicle/gas flow interactions have not been properly accounted for in previous analyses. It will be demonstrated that application of simplified jet damping models generally indicates a somewhat larger damping than is actually present.

5.1 FORMULATION

In determining the coupling between the flow of combustion gases in the rocket motor and the motions of the vehicle, it is convenient to employ the control volume illustrated in Figure 21. The coordinate system is fixed at the center of mass of the composite system and rotates with the spacecraft. The solid parts are assumed to constitute a rigid body. The analysis of Section (3) yields the necessary mathematical model as represented by Equation (16). Since only internally generated torques will be of interest in the remainder of the report, it is not necessary to carry the subscript "int" used previously. Thus $\mathbf{M} \equiv \mathbf{M}_{int}$. Also, since only relative gas motions are of interest, it is unnecessary to distinguish them by use of the subscript "rel". Therefore, we define $\mathbf{u} \equiv \mathbf{v}_{rel}$ as the relative gas velocity vector and (16) becomes

$$\mathbf{M} = - \int_V \mathbf{r} \times (2\boldsymbol{\omega} \times \mathbf{r}) \rho \, dV - \frac{\partial}{\partial t} \int_V (\mathbf{r} \times \mathbf{u}) \rho \, dV - \epsilon \int_S (\mathbf{r} \times \mathbf{u}) \mathbf{u} \cdot \mathbf{n} \, \rho \, dS, \quad (39)$$

where \mathbf{r} locates any point in the chamber relative to the system center of mass. Lengths are made dimensionless with respect to a representative chamber radius, R_0 , velocities by dividing by the gas speed at the burning surface, v_b , and angular velocity and time by multiplying and dividing, respectively, by the spin angular

velocity Ω . ϵ is the Rossby number, a similarity parameter that arises in a natural way, defined by

$$\epsilon = \text{Rossby Number} = \frac{v_b}{R_o \Omega} , \quad (40)$$

which expresses the relative importance of flow convection and angular motion related to the spin of the chamber. \mathbf{u} is the velocity of the gas particles relative to the mass center, ρ is the gas density, α is the angular acceleration, and ω is the angular velocity vector. dS and dV are surface and volume elements respectively, and \mathbf{n} is an outward pointing unit normal. It is useful to separate the mean and fluctuating parts of the gas velocity and system angular velocity such that

$$\begin{aligned} \mathbf{u} &= \mathbf{U} + \mathbf{u}' \\ \omega &= \Omega + \omega' \end{aligned} \quad (41)$$

\mathbf{U} represents the mean flow velocity vector and Ω is the steady part of the vehicle angular velocity vector. \mathbf{u}' and ω' are the unsteady velocity and angular velocity perturbations. Both of these quantities can be assumed small compared to the corresponding steady velocities. Products of time-dependent quantities are thus of second order and will be neglected. Examination of the experimental data described in Section 2 provides justification for this assumption; it is apparent that the angular velocity perturbations represented by the nutation instability at its largest amplitude are typically less than ten percent of the vehicle spin rate.

Inserting Equations (41) into the angular momentum balance (39) yields the expansions summarized in Table 3. It is convenient to group the terms as shown. Group 1 represents a steady torque responsible for generation of secondary flows within the chamber. For example, the important axial vortex flow that is superposed on the combustion gas flow is created by the combination of the Coriolis volume integral and the radial and axial convection of angular momentum in the surface integral.

The Group 2 terms represent interaction of the *time-dependent motions of the vehicle* with the steady part of the chamber flow. The volume integral containing the Coriolis acceleration $2 \omega' \times \mathbf{U}$ is the source of the classical jet damping effect that will be described in detail presently. It will be demonstrated that the jet damping moment vector exhibits the same order of magnitude (but opposite sense) as the apparent disturbing moment that drives the nutation instability. This is treated in what follows as a major clue in the search for the root of the PAM-D instability.

Table 3. Moment on Spacecraft due to Interaction with Internal Flow Field

$\mathbf{M} = - \int_V \mathbf{r} \times (2 \boldsymbol{\omega} \times \mathbf{r}) \rho \, dV - \frac{\partial}{\partial t} \int_V (\mathbf{r} \times \mathbf{u}) \rho \, dV - \epsilon \int_S (\mathbf{r} \times \mathbf{u}) \mathbf{u} \cdot \mathbf{n} \, \rho \, dS$	
<p>Expanded Form:</p> $\mathbf{M} = - \left\{ \begin{aligned} & \epsilon \int_S (\mathbf{r} \times \mathbf{U}) \mathbf{U} \cdot \mathbf{n} \, \rho \, dS + \int_V \mathbf{r} \times (2 \boldsymbol{\Omega} \times \mathbf{U}) \rho \, dV \\ & + \int_V 2 \mathbf{r} \times (\boldsymbol{\omega}' \times \mathbf{U}) \rho \, dV \\ & + \int_V 2 \mathbf{r} \times (\boldsymbol{\Omega} \times \mathbf{u}') \rho \, dV + \frac{\partial}{\partial t} \int_V (\mathbf{r} \times \mathbf{u}') \rho \, dV \\ & + \epsilon \int_S (\mathbf{r} \times \mathbf{U}) \mathbf{u}' \cdot \mathbf{n} \, \rho \, dS + \epsilon \int_S (\mathbf{r} \times \mathbf{u}') \mathbf{U} \cdot \mathbf{n} \, \rho \, dS \\ & + \text{Terms of Higher Order (} O(u'^2, \omega'^2, u' \omega') \text{)} \end{aligned} \right.$	<p>Group 1 Steady Flow Effects</p> <p>Group 2 Jet Damping Moment</p> <p>Group 3 Unsteady Flow Effects</p> <p>Group 4 Unsteady Convection of Angular Momentum</p> <p>Group 5 Nonlinear Interactions</p>
<p>Notes: \mathbf{U} is the mean flow (steady) velocity vector including an axial vortex component. $\boldsymbol{\Omega}$ is the primary spin angular velocity vector along the motor axis. \mathbf{u}' is the time-dependent velocity fluctuation in the gas flow due to nutational motion of the combustion chamber. $\boldsymbol{\omega}'$ is the nutation angular velocity perturbation.</p> <p>\mathbf{r} locates the position of any particle in the combustion chamber or nozzle relative to the vehicle center of mass. \mathbf{n} is an outward pointing unit vector that is perpendicular to the surface of the control volume. The control volume is bounded by a surface surrounding the entire spacecraft and rocket motor. Gases leave the system through the part of the boundary across the nozzle exit. ϵ is the Rossby number indicating the relative importance of internal convection as compared to motion due to the primary spin.</p>	

Groups 3 and 4 describe interactions of the *unsteady part of the chamber gas flow* with the steady mean flow and the principal vehicle spin. Unsteady flow of the combustion gases is forced by the motion of the chamber walls, represented in the body-fixed coordinates by the inertial corrections. First order reaction moments are represented by the Coriolis and acceleration terms in the volume integral and by the convective effects in the surface integrals. Terms of great potential importance are the surface integrals describing convection of angular momentum disturbances from the system through the nozzle exit with the mean gas stream. Before detailing the reasons for this importance, it is useful to carry out a detailed review of the classical jet damping effect of Group 2. A reliable jet damping evaluation will be required in later simulations of the vehicle response to the internal torques.

Group 5 terms are not shown in expanded form. These represent nonlinear interactions of the order of the square of the amplitude of the small parameters u' and ω' . It is therefore appropriate to neglect them in comparison to the linear terms.

5.2 JET DAMPING

A detailed presentation of jet damping concepts is given in the classical text on rocket flight mechanics by Rosser, Newton, and Gross³². Careful reading of this material makes it clear that there were questions at that time (the late 1940's), regarding discrepancies between observed and calculated jet damping as experienced in testing of small tactical solid rockets. Some very clever experimental procedures were suggested (Ref. 32, p. 23) as a means for clarifying the difficulties, but apparently were never carried out. The questions were not resolved, and the traditional results are still in widespread use. The classical approach is also reviewed in the well-known text by Thomson² and by Davis, et al³³, and by Kolk³⁴. Thomson and Reiter³ applied the results to spinning rocket flight data from the Explorer series of space flights. A method presented by Rott and Pottsepp⁴ has been used extensively in jet damping calculations and has been used by McDonnell Douglas in analysis of PAM-D coning⁵⁻⁷.

All of the referenced analyses are based on the notion of a "quasi-steady" flow field. It is also traditional to make the "... apparently radical simplifying assumption ..." (Ref. 4) that the gas flow is everywhere parallel to the axis of symmetry. It will be demonstrated that the latter approximation may lead to significant error when applied in low fineness ratio (low L/D) motors, such as the STAR series rockets. That is, neglect of the effects of radial velocity components may not be justified in the more nearly spherical or oblate combustion chamber shapes used in modern solid propellant space motors. However, the most important errors affecting the PAM-D investigation result from application of the quasi-steady approximation. It was a major goal of this study to determine if the unsteady terms can, under certain conditions, dominate the flow/vehicle interactions in such

a way that the jet damping is overwhelmed and nutation instability results.

The jet damping moment is represented by the Coriolis volume integral from the Group 2 interactions:

$$\mathbf{M}_J = - \int_V 2\mathbf{r} \times (\boldsymbol{\omega}' \times \mathbf{U}) \rho \, dV \quad (42)$$

It is useful to examine evaluations of (42) for simple models of a solid rocket combustion chamber. Figure 23 shows the simplified motor geometry assumed for all of the estimates made in this report. A cylindrical chamber shape is used to simplify the time-dependent calculations to be carried out in Section 6. The size and shape of the cylinder will be varied throughout the motor run in the simulation calculations to match the actual motor combustion chamber geometry volume and fineness ratio, b (length to diameter ratio). A more realistic boundary shape would greatly complicate the task of carrying out analytical solutions. There is a strong motivation to produce analytical models, since they display important relationships between variables in a way that cannot be accomplished by strictly numerical solutions. The overwhelming need to generate a clear physical understanding of all the gas flow interactions need not be argued.

Assuming combustion occurs at both the sidewalls and the forward wall of the cylindrical chamber, it is reasonable to assume that the mass flow rate increases linearly along the combustion chamber. With this type of axisymmetric velocity variation, the jet damping moment becomes

$$\mathbf{M}_J = - \dot{m}(L_{cg} - 2b/3)(L_n + 2b)\boldsymbol{\omega}' = K_J \boldsymbol{\omega}' \quad (43)$$

where L_{cg} is the position of the nozzle exit with respect to the spacecraft center of mass, L_n is the length of the nozzle, and $2b$ is the length of the combustion chamber as defined in Figure 23. All lengths are referenced to the chamber radius R_0 as indicated earlier. \dot{m} is the magnitude of the motor mass flow rate, a positive quantity. K_J will be referred to as the jet damping factor indicating the proportionality of \mathbf{M}_J to the angular velocity perturbation $\boldsymbol{\omega}'$. For the simple one-dimensional flow model assumed, one finds

$$K_J = - \dot{m}(L_{cg} - 2b/3)(L_n + 2b), \quad (44)$$

a negative real number. Compare this to the classical value $K_J = - \dot{m}(L_{cg}^2)$ used by many investigators². Notice that the jet damping moment applied to the vehicle is opposite in sense to the perturbation angular velocity vector, thus it acts always to damp the nutation oscillations as shown by Equation 38 in Section 3. This equation also indicates that $\alpha_J = \delta K_J$ is the inverse of the (dimensionless) "time constant" or

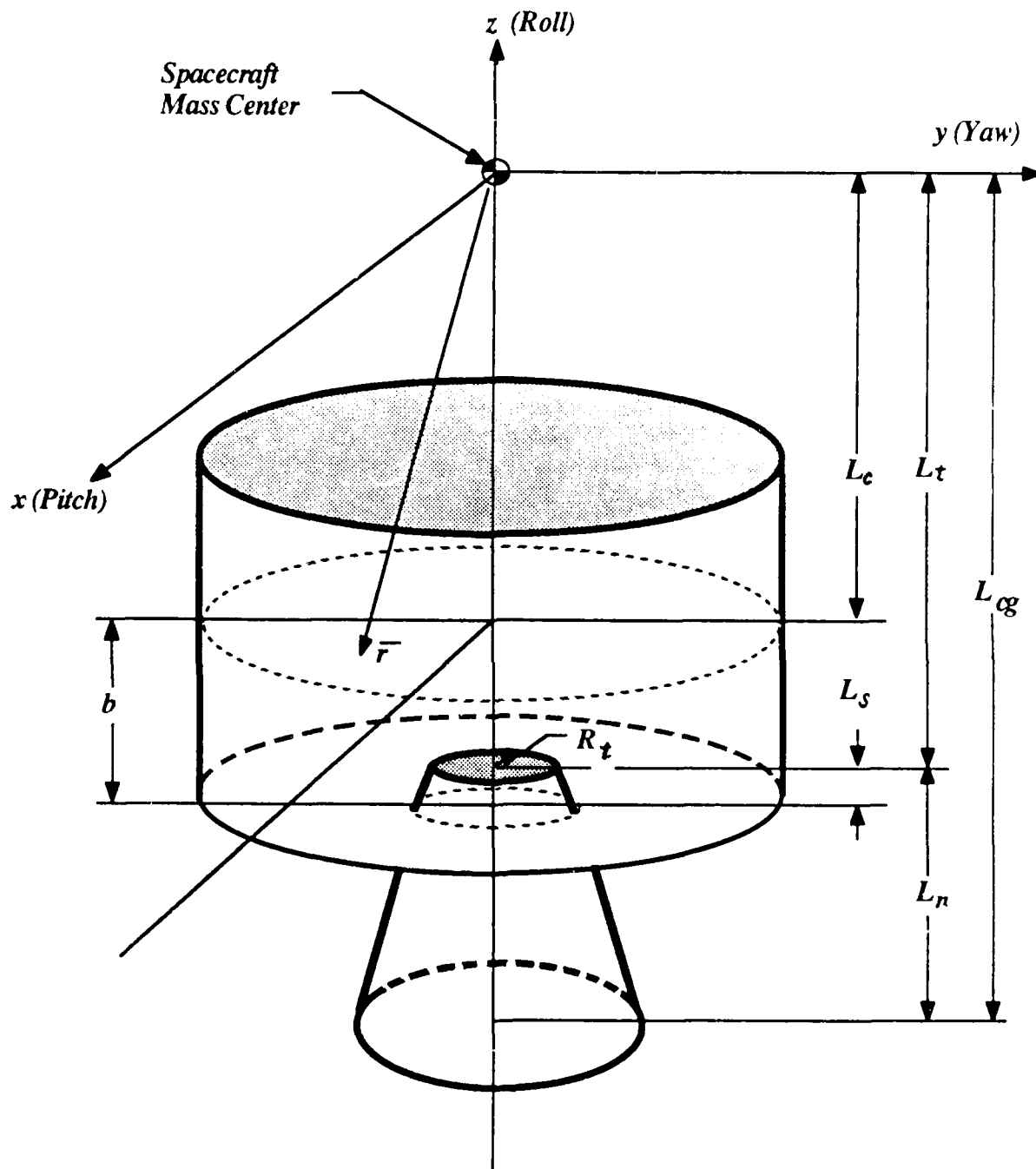


Figure 23. Motor Chamber and Nozzle Geometry

what we will refer to as the "growth rate" of the nutational motion. δ is the dimensionless moment scaling factor defined in Equation 30. The importance of the spacecraft and motor geometry are clearly displayed in Equation 44. Since the center of mass moves forward during motor operation, and the chamber length increases due to regression of the burning propellant surface, then the jet damping moment factor, K_J tends to increase with time during motor operation. Figure 24 shows the K_J factor based on Equation 44 plotted as a function of time (for WESTAR V spacecraft configuration). The classical result and a computation for a best-fit spheroidal chamber instead of the cylindrical geometry used in the derivation of Equation 44 are shown for comparison.

Figure 10 (lower graph) shows a plot of the vehicle motion assuming this is the only interaction moment present. A numerical integration (fourth-order Runge-Kutta) of the equations of motion (Equations 22) was utilized to properly account for variations in vehicle mass properties, spin rate, and motor geometry. This approach will also be employed in subsequent calculations as other interactions are evaluated in order to display their influence over the entire period of motor operation. Figure 25 shows the decay rate, α_J , of the lateral angular velocity as a function of time assuming WESTAR V configuration and the axisymmetric jet damping effect. The residual perturbation angular velocity at motor ignition was taken to be approximately 1 degree/second as determined from flight rate gyro-scope data. Comparison of this plot to the actual flight data (rate gyro telemetry) shown in Figure 15 indicates that the jet damping effect alone does not match the actual motor behavior at any time during the burn. This is of special significance at the start of the motor run because it indicates that the disturbing entity was present right from the beginning. Thus it is necessary to examine other gas/spacecraft reaction moments that have not been accounted for in jet damping theory. Also, this comparison leads to some concerns as to the amount of damping predicted by the simple theory. It will be shown in the next paragraphs that a small reduction in the damping results if the one-dimensional flow assumption is relaxed.

It is important to determine the validity of the flowfield assumptions used in evaluation of the jet damping function. If an axisymmetric flow field model is employed that more adequately represents the mean flow in a motor like the STAR 48, one finds that modifications result. Motors with a low fineness ratio b are characterized by large radial mean flow velocity components. A submerged nozzle with an entrance placed close to the center of the chamber also contributes to the generation of strong radial components. A more representative mean flow field will be developed in Section 6. Figure 26 shows the streamline pattern to be used.

An important feature of a realistic assessment of the mean flow in a spinning rocket is the presence of a strong axial vortex core stretching from the forward end of the chamber and through the nozzle. This circumferential flow component has been neglected in other studies of spinning rockets. The only attempts to examine

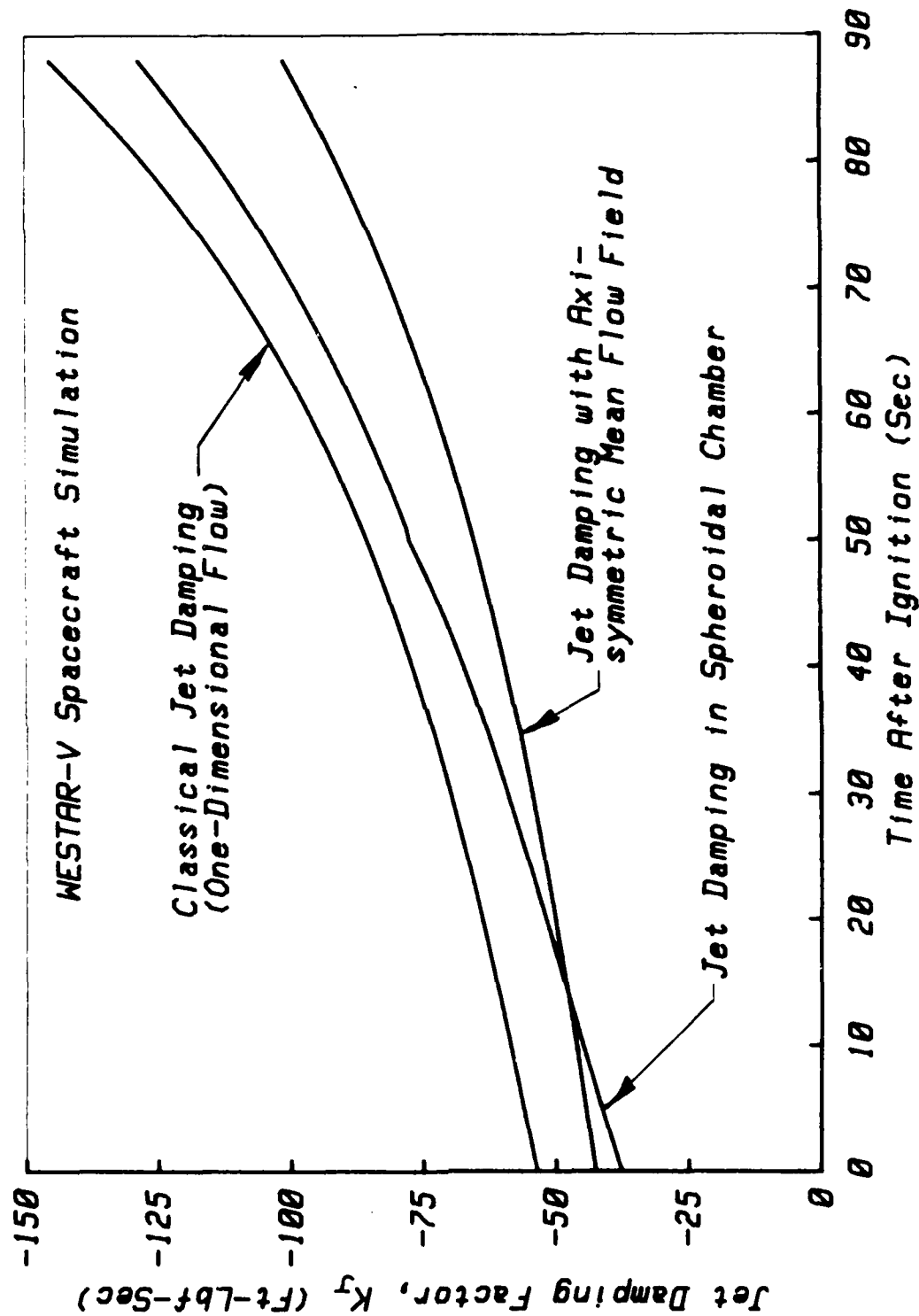


Figure 24. Effect of Axisymmetric Flow Field on Jet Damping

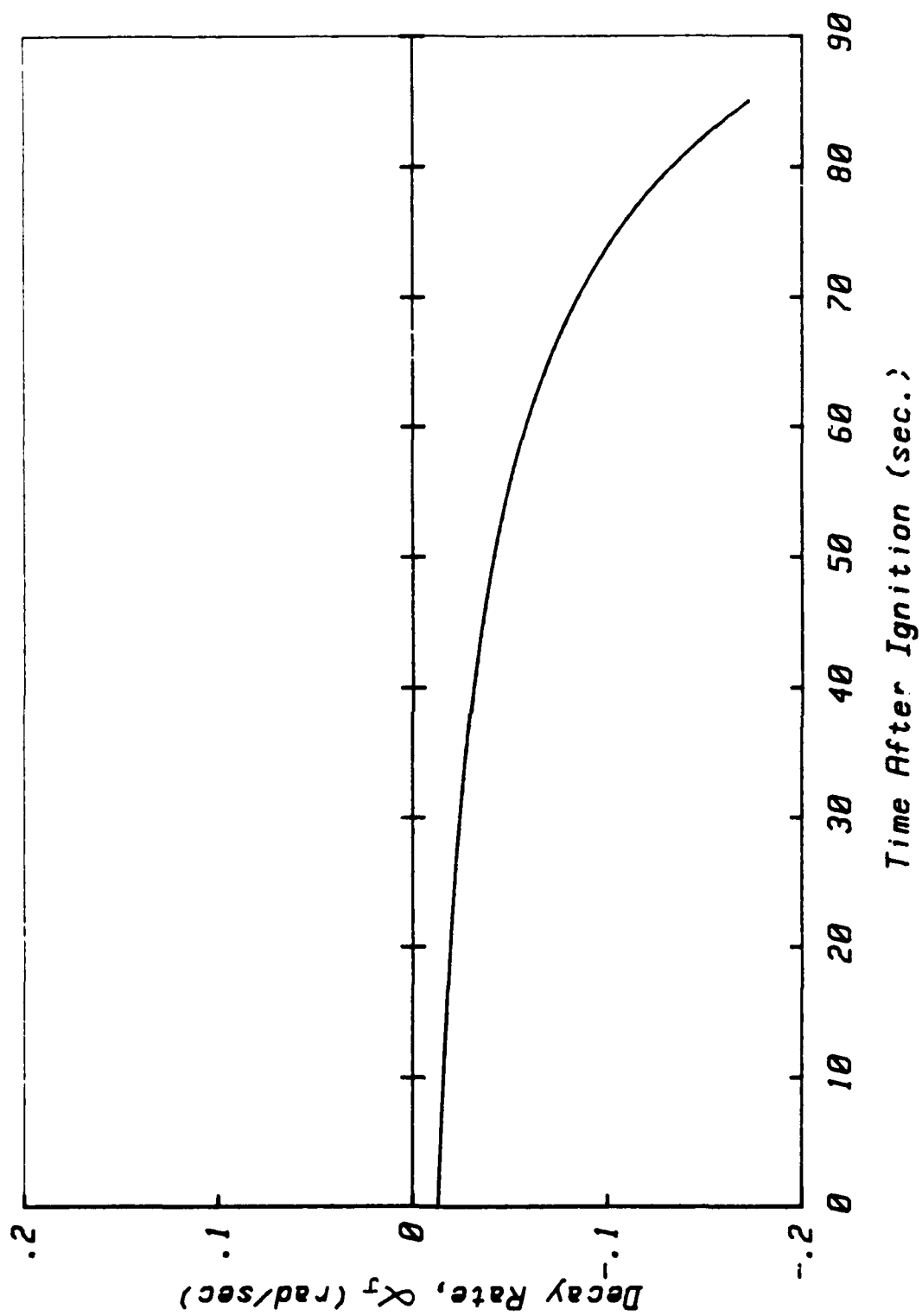


Figure 25. Jet Damping Exponential Decay Rate vs Time (WESTAR V)

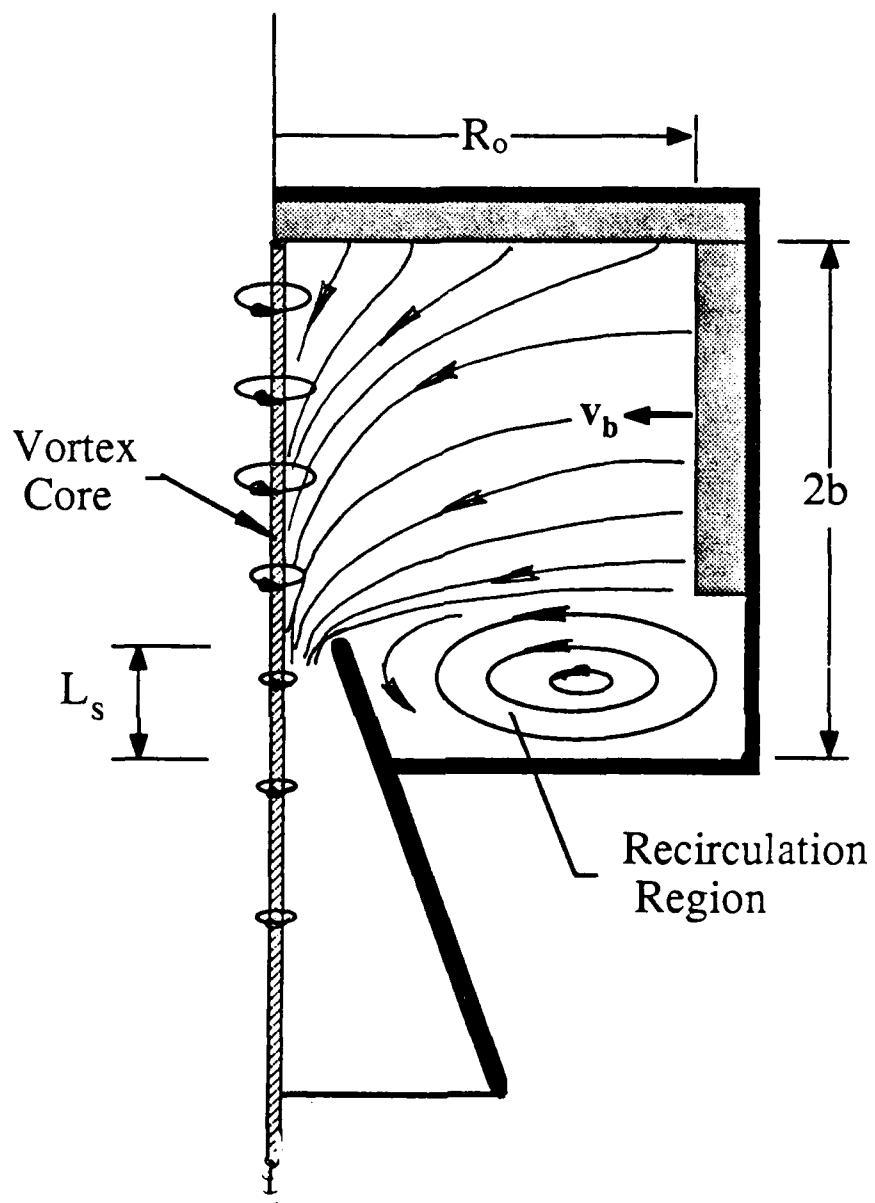


Figure 26. Assumed Axisymmetric Flow Pattern in Simplified Motor

the flow effects in spinning solid propellant motors have, apparently, been made by ONERA in France. Motion pictures taken through transparent head ends in spinning rocket firings clearly show the presence of the strong vortex core. A nearly potential vortex flow results from the vortex stretching produced by the gases as they accelerate through the nozzle and by the mass transpiration from the burning propellant surfaces. There are many implications of this phenomenon in terms of effects on nozzle flow and resulting chamber pressure and burning rate response, but these will not be pursued here. Of considerable interest, however, is the possibility that the axial vortex flow generated in the gases due to the chamber spin might affect the jet damping. This will be explored in Section 6. Figure 26 illustrates the streamline pattern assumed for the evaluations to be carried out later. The details of the analysis will be presented in Section 6. The effect of a more realistic flow pattern is to slightly reduce the jet damping. The lower curve in Figure 24 is representative of the jet damping moment for this type of flow model. It is significant that the damping becomes progressively larger during motor operation, and that at the end of the motor burn, the damping is approximately 30% less than predicted by the classical jet damping equation.

The modified jet damping model based on the axisymmetric flow of Figure 26 was tested by applying it in the SGS II second stage motion simulation. Figure 27 shows the predicted spacecraft yaw angular velocity as a function of time over the entire motor burn. The damping corresponds to the lower curve of Figure 24. Comparison of the predicted motion to the actual spacecraft rate gyroscope data illustrated in Figure 17 indicates very close agreement over the first half of the burn during which coning perturbations have not yet become significant. This appears to validate the jet damping model. Thus, it will be used as the basis for all system simulations to be described in later sections. For emphasis, it appears that application of the classical assumptions yields a jet damping amplitude that is about 30% larger than the actual damping. Use of a more realistic mean flow pattern brings the damping into better agreement with the experimental data.

5.3 UNSTEADY FLOW EFFECTS

Groups 3 and 4 in Table 3 describe internal moments on the spacecraft involving interaction between possible time-dependent gas oscillations in the combustion products (u') with the chamber spin and with the mean flow field. These are likely to be complex interactions for several reasons. In particular, the mean flow field itself is complicated. The axial vortex component has been described earlier. Study of the vector products shown in the Table indicates the potential significance of interactions between the circumferential vortex flow and the fluctuating velocity perturbations. Group 3 contains a term that is analogous to the jet damping term arising from the Coriolis acceleration effects and a term representing the time rate of change of the angular momentum contained within the combustion chamber.

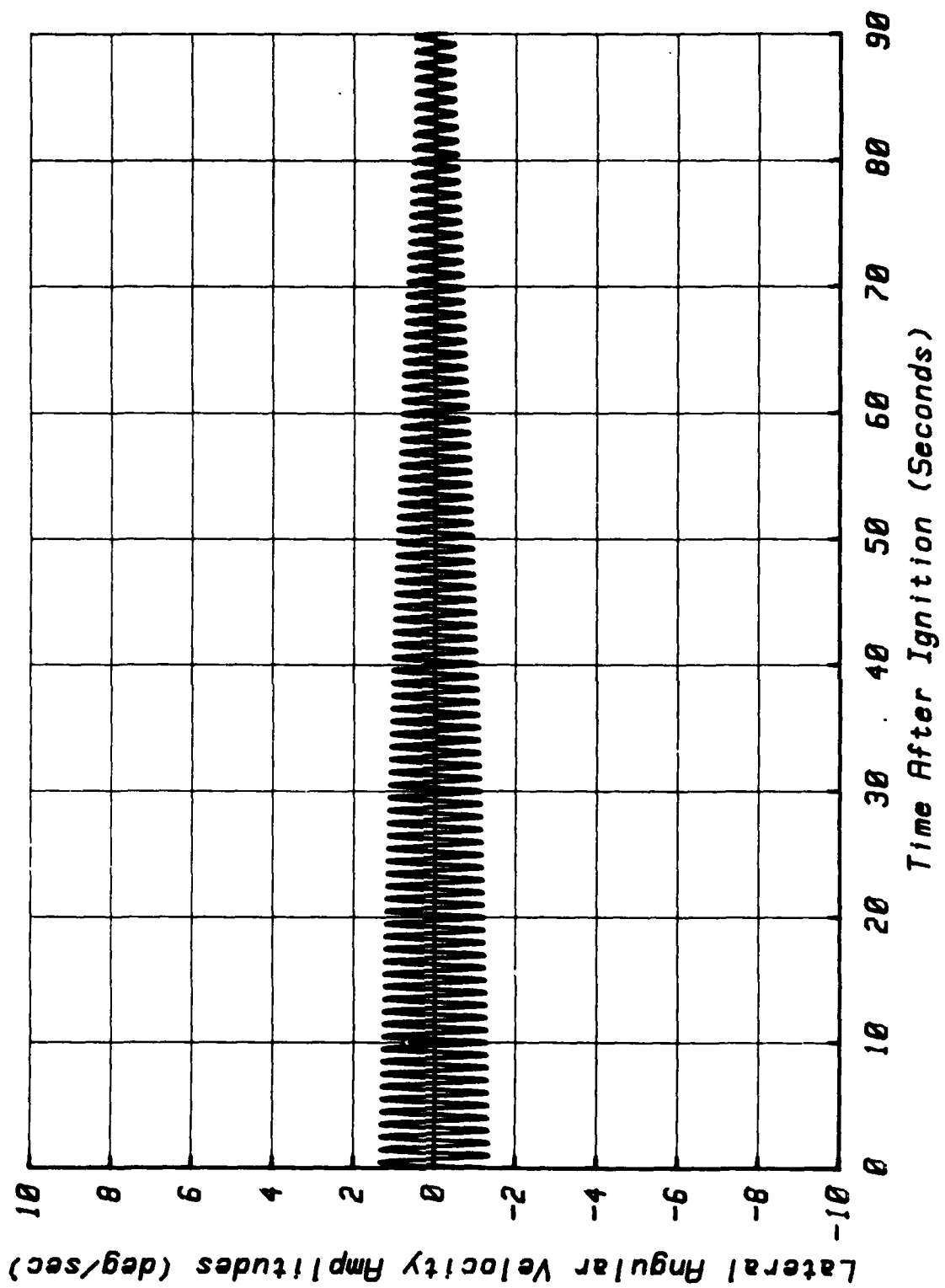


Figure 27. Simulated Jet Damping Perturbation, SGS II

The Group 4 terms describe convection of the mean flow vorticity and time dependent vorticity out of the chamber. It will be demonstrated that the combination of these two surface integrals over the nozzle exit represent convection of a lateral unsteady angular momentum component, which is accompanied by a significant disturbing torque acting on the spacecraft.

Since the details of the flow field have yet to be determined, it is appropriate to attempt only a qualitative evaluation of the time-dependent terms at this juncture. Emphasis will be placed on the interpretation of the second Group 4 term, which produces a reaction torque

$$M_H = -\epsilon \int_S (\mathbf{r} \times \mathbf{u}') \cdot \mathbf{U} \cdot \mathbf{n} \, \rho \, dS. \quad (45)$$

As the area integral is to be taken over the nozzle exit, this term represents the flux of time-dependent angular momentum from the system with the mean gas flow. To appreciate the significance of this disturbing moment, it is first necessary to understand the source of the oscillations in the flow represented by the perturbation velocity \mathbf{u}' . These may be visualized as the response of the gases contained within the combustion chamber to the wobbling oscillations of the spacecraft. It should not be forgotten that the chamber is also spinning. A crude physical analogue is the liquid motion that one can produce in a coffee cup by a properly programmed rotational sloshing. In a spinning gas, such excitation produces a complex traveling wave that will be described in Section 6 as an inertial wave effect. One feature of the waves is that they represent a retrograde traveling disturbance with a lateral component of angular momentum. That is, the combination $dH = (\mathbf{r} \times \mathbf{u}') \rho dV$ represents angular momentum of a gas particle of volume dV due to the inertial traveling wave. Figure 28 is a sketch of the lateral component of this angular momentum for a gas particle at several times as it moves along a mean flow streamline through the chamber and out the nozzle. The magnitude of the angular momentum increases as the particles approaches the axis due to vortex stretching effects (conservation of angular momentum) already mentioned in connection with the mean flow axial vortex. The precise origins of the angular momentum and its exact dependence on geometrical parameters and details of the motion of the chamber require solution of the time-dependent flow field. This is the main goal of Section 6. Let it suffice for now to notice that the flux of lateral angular momentum must be balanced by a lateral torque component on the spacecraft as Equation (39) indicates. This moment therefore moves relative to the vehicle in the retrograde direction and, depending on its phase relative to the spacecraft wobbling angular velocity, may represent a destabilizing effect. Figure 28 illustrates the conditions that would correspond to nutation instability. If the moment M_H has a component parallel to the angular velocity vector ω' that is larger in magnitude than the jet damping moment M_J , then the coning oscillations grow.

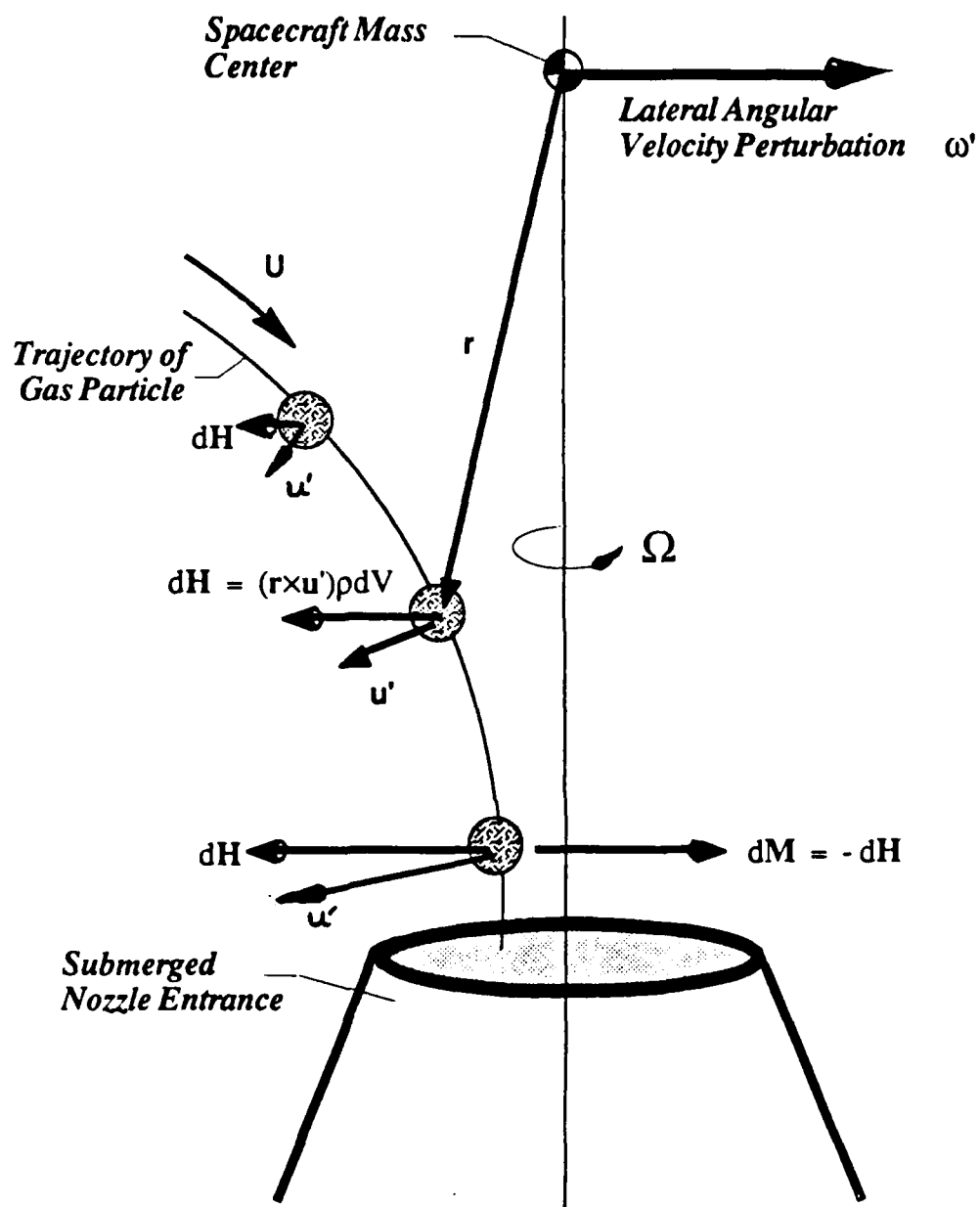


Figure 28. Stretching of Lateral Angular Momentum of Particle

Since it is difficult to visualize the complicated moving vectors in three dimensions described in Equation 45, a simple analogy to a better known rocket motor phenomenon may be a help in arriving at the correct interpretation. Consider the *linear* momentum balance involving the spacecraft/gas interaction. The term describing the flux of linear momentum of the combustion products is

$$\mathbf{F} = - \int_S (\mathbf{U}) \mathbf{U} \cdot \mathbf{n} \rho \, dS \quad (46)$$

where \mathbf{U} is the mean flow velocity in the motor. This integral is completely analogous to the *angular* momentum integral of (45) with attention directed here to the mean part of the motion and force rather than torque. Evaluation of this expression by integrating over the boundary of the control volume (only the nozzle exit plane contributes to the result) yields the familiar expression for the axial momentum thrust:

$$\mathbf{F} = \dot{m} U_e \mathbf{k} \quad (47)$$

where \dot{m} is the mass flow rate and U_e is the average exhaust velocity over the nozzle exit. This demonstrates precisely the same mechanism being described by Equation 45 except that it is lateral angular momentum flux and associated torque rather than axial linear momentum flux and the force that is the focus of attention.

To summarize, if care is taken to account for all interactions between the motor gas flow and the spacecraft motion, then potentially destabilizing mechanisms become apparent. One of these, the convection through the nozzle of lateral angular momentum in the combustion gases generated by the vehicle wobbling, has been identified as a potential source of a coning disturbance. The goal of the next section is to construct a detailed model of the time-dependent flow in a spinning, nutating chamber with mean flow. This model will then enable a quantitative assessment of all of the potential disturbing mechanisms identified in Table 3.

6.0 FLUID DYNAMICS OF SPINNING ROCKET MOTORS

The previous sections have established the role of the combustion chamber flow field and its response to the angular motions of the spacecraft as a contribution to nutation instability. A detailed description of this flow is required to enable a complete evaluation of the interaction moment M between the vehicle and the contained combustion gases as described in Table 3. This torque is been represented traditionally as the jet damping effect alone; that is, only part of the interaction has been accounted for. It is difficult to justify the use of the jet damping model, as it is currently applied in interpretation of flight data, if other gas dynamic interactions of equal or potentially greater impact on the flight mechanics are ignored.

The purpose of this section is to extend the theory of vehicle/gas interactions to account for all of the additional terms identified in Section 5. This can only be accomplished if the motor flow field is treated as a time-dependent system. It is necessary to determine the detailed velocity distributions, both steady and unsteady, in a spinning chamber with internal mass addition and combustion. The extensive literature base in rotating fluid dynamics provides valuable guidance. Nevertheless, there are many features in the present situation that have not been studied previously. These problems and the techniques for handling them are discussed in this section.

The motor flow field modeling effort had three main goals:

- A complete analytical description of the flow interactions in a spinning, nutating rocket motor including effects of combustion.
- Computational fluid dynamics solutions for the mean flow field in a spinning rocket motor with a realistic grain geometry.
- Numerical solutions for the time-dependent flow field in a spinning rocket motor including interactions with the mean flow and nutational motions of the vehicle.

Much attention was devoted to the first goal, since the need to gain a physical understanding of the complex flow field was of the highest priority. Considerable progress was made on the numerical tasks. This work provides a foundation for future studies with the ultimate goal of producing a general purpose numerical algorithm for time-dependent spinning rocket problems. The remainder of this section is devoted to a detailed development of the fluid mechanics needed for accomplishing the stated goals.

The analysis makes full use of the relative smallness of the flow perturbations superimposed on the mean flow by the wobbling of the combustion chamber. This allows the steady and unsteady parts of the solution to be treated separately. The main purpose here is to establish a physical description of the nutation instability phenomenon that clarifies the origins of the disturbing entities involved. Although approximate solutions will be emphasized, these are of considerably better quality than those routinely employed in spinning rocket jet damping estimates. This is largely the result of relaxation of the standard assumptions such as the one-dimensional mean flow and the quasi-steady assumptions.

6.1 FORMULATION

This subsection introduces the notation, assumptions, and fundamental equations for analysis of the time-dependent flow in rotating rocket motors. It will be necessary to account for the steady as well as the unsteady parts of the field in order to evaluate the interaction equations of Section 5.

Several simplifying assumptions will be made in order to trim the problem complexity as much as possible without losing the essential physics. Although an oscillatory flow field is anticipated, neglect of compressibility effects is justified. Flow oscillations in the combustion chamber caused by the coning motion are in the frequency range set by the nutation rate of the vehicle,

$$\lambda_s = (1 - I_0/I_1) \omega_z, \quad (48)$$

which is generally several orders of magnitude smaller than the lowest acoustic wave frequencies of the combustion chamber. Thus, waves of compressibility are not activated, and the flow through the rocket motor can be assumed to be incompressible everywhere except in the nozzle and the nozzle entrance regions. Additional assumptions will be introduced as the analysis proceeds. All notation is defined in the list of symbols at the end of the report. Figure 23 shows the coordinate system to be employed. Evaluations of the flow field solutions will be based on a simplified chamber geometry in the form of a circular cylinder having the same fineness ratio (L/D), mass flow rate, and radius as the actual motor combustion chamber at a given instant in the burn.

Assuming that only inertial body forces are present, the flow system, described in terms of rotating coordinates fixed in the spacecraft, is governed by the continuity and momentum equations:

$$\nabla \cdot \mathbf{u} = 0 \quad (49)$$

$$\partial \mathbf{u} / \partial t + \epsilon \mathbf{u} \cdot \nabla \mathbf{u} + 2 \boldsymbol{\omega} \times \mathbf{u} + \epsilon^{-1} (d\boldsymbol{\omega} / dt) \times \mathbf{r} = -\epsilon \nabla p + E \nabla^2 \mathbf{u} \quad (50)$$

ϵ is the Rossby number ($\epsilon = v_b / R_0 \Omega$), and E is the Ekman number ($E = \nu / \Omega R_0^2$), expressing the relative importance of Coriolis effects and viscous forces, respectively. These similarity parameters appear as a result of the definition of dimensionless variables based on chamber radius R_0 and mean flow speed at the burning surface v_b as characteristic length and velocity, respectively. Time and angular velocities are rendered dimensionless by multiplying and dividing, respectively, by the axial spin angular velocity ω_z . The latter is assumed to be a slowly varying function of time, $\omega_z = \Omega$. p is the dimensionless reduced pressure,

$$p = P - (1/2\epsilon^2)(\omega \times r)^2, \quad (51)$$

which is a combination of the thermodynamic pressure, P , and the centripetal acceleration in gradient form. Thus the centripetal effects can be represented in the analysis as part of the pressure fluctuations. Centripetal mean pressure corrections at the maximum chamber radius are typically of the order of 1 psi for a STAR 48 motor rotating at 60 rpm.

Much simplification in the formulation results from exploitation of the smallness of the time-dependent corrections compared to their mean flow counterparts. The mean and the unsteady quantities are separated by defining

$$\begin{aligned} \mathbf{u} &= \mathbf{U} + \mathbf{u}' \\ p &= P_0 + p' \\ \omega &= \Omega + \omega' \end{aligned} \quad (52)$$

where primes will always denote fluctuating variables. Expressions (52) are inserted in (49) and (50) and the time-dependent and steady parts of the resulting equations can then be conveniently separated. It is appropriate to neglect products of the perturbation quantities. That is, combinations such as $\omega' \cdot \omega'$, $\omega' \cdot \mathbf{u}'$, and $\mathbf{u}' \cdot \mathbf{u}'$ are of higher order than terms eventually retained.

6.2 MEAN FLOW IN A SPINNING ROCKET MOTOR

A reasonably complete and realistic model for the mean flow is required as a basis for the unsteady calculations to follow. As demonstrated in Section 5, the vehicle/flow interactions are sensitive to the velocity field assumed for the mean flow. The main purpose here is to provide a sufficiently accurate representation that accounts for the three-dimensional nature of the flow field in a combustion chamber with low slenderness ratio. Also, attention will be paid to a proper assessment of the circumferential mean flow generated by the chamber spin.

The nonoscillatory part of the gas flow is governed by the continuity and momentum equations including inertial corrections.

$$\nabla \cdot \mathbf{U} = 0 \quad (53)$$

$$\epsilon \mathbf{U} \cdot \nabla \mathbf{U} + 2 \boldsymbol{\Omega} \times \mathbf{U} = -\epsilon \nabla P_0 + E \nabla^2 \mathbf{U} \quad (54)$$

Since the Ekman number E is very small, and the field is dominated by the injection of combustion products at the propellant surfaces, it is appropriate to ignore the viscous forces by assuming $E = 0$ as a simplification in determining analytical solutions. However, viscous effects do play a role in setting up recirculation patterns at separated flows. Such recirculation is anticipated in the region of the chamber aft of the submerged nozzle entrance. A numerical approach was undertaken for treating the full Navier-Stokes form of equation (54).

The Coriolis force due to chamber rotation has a major influence. Since $\boldsymbol{\Omega}$ is parallel to the axis of symmetry, $\boldsymbol{\Omega} = \Omega \mathbf{k}$, and the flow without rotation may be assumed to be axisymmetric, then the Coriolis effect induces an axial vortex flow in the combustion gases. An important step is to estimate the strength of this vortex, since it plays a potentially important role in the coning phenomenon.

Direct analytical solution of equations (53) and (54) is most difficult. For the present, we will utilize simple representations that retain the essential features of the mean flow field. Jet damping calculations are usually made using crude models of the flow that are not sufficiently detailed for the instability calculations. A more realistic model consists of a combined stagnation-point/free-vortex/rotational vortex flow as given by

$$\mathbf{U} = -r \mathbf{e}_r + \frac{\Gamma}{2\pi} \left(r - \frac{1}{r}\right) \mathbf{e}_\theta + [2(z - b) - 1] \mathbf{k} \quad (55)$$

This representation accounts for the radial part of the flow velocity induced by combustion at the sidewalls of the chamber. b is the combustion chamber length-to-diameter ratio, and Γ is the strength of the induced vortex. The wheel vortex or rotational vortex component makes the circumferential velocity zero at the chamber surface. Vorticity is introduced because gas particles emerging from the burning surface into the chamber possess azimuthal velocity (in an inertial coordinate frame) due to chamber rotation. The magnitude of Γ is established by employing an angular momentum balance. Taking the curl of equation (55), one finds

$$\nabla \times \mathbf{U} = (\Gamma / \pi) \mathbf{k} \quad (56)$$

for the mean flow vorticity. This must satisfy the angular momentum balance represented by the curl of the Eulerian form of momentum equation (54). That is,

$$2 \nabla \times \Omega \times U = -\epsilon \nabla \times (U \cdot \nabla U) = -\epsilon \nabla \times [\nabla (U^2/2) - U \times \nabla \times U]. \quad (57)$$

Noting that $\Omega = k$, (angular velocities are normalized to the chamber spin rate Ω), one finds

$$2 \nabla \times k \times U = -\epsilon \nabla \times [(\Gamma/\pi) k \times U]. \quad (58)$$

Thus, the Coriolis force determines the magnitude and direction of the vortex flow, and the required vortex strength is, by inspection,

$$\Gamma = -2\pi/\epsilon \quad (59)$$

where the influence of the Rossby number is clearly indicated. The vortex strength is of relatively lesser importance for high Rossby numbers. The physical meaning of this result is clarified if the magnitude of the Rossby number is rewritten in the form

$$\epsilon = (1/\Omega)/(R_0/v_b) \sim T_{\text{rotation}}/T_{\text{convection}} \quad (60)$$

That is, ϵ is approximately the ratio of the time required for one revolution of the chamber to the time for a gas particle to traverse the distance from the burning surface to the nozzle. Thus a small Rossby number indicates that the chamber residence time for gas particles is large compared to the period of rotation. As the chamber size increases due to regression of the propellant burning surface, the vortex strength increases because gas particles remain longer in the presence of the Coriolis acceleration field. For the present case (PAM-D), ϵ decreases from about 3 to 0.6 during the 87 second motor burn. The swirling mean flow component plays a significant role, especially toward the end of the motor run when the Rossby number is always less than unity.

The presence of a nearly potential vortex flow in a spinning rocket has been verified in window motor tests at ONERA in France. Tests by Dunlap and Hermesen at United Technologies (UTC 2197-FR, April 1967) demonstrated that the vortex could be sufficiently strong to cause severe erosion at the forward motor closure in spinning rocket experiments. A hole piercing the steel forward closure corresponding to the vortex core, was caused by the spinning gas flow in a motor test. Curvature of the streamlines was clearly evident in erosion patterns in the aft closure and nozzle insert. Thus there is considerable experimental evidence for the essential feature of the nutation mechanism proposed in the present study.

In order to provide a more realistic solution for the mean flow than simple models such as that given in equation (55), one must resort to a numerical approach. This is especially true if the effects of the complex chamber boundary shape are to be assessed. One task of the present program was to develop a numerical solution to be used, ultimately, in the nutation instability calculations. This proved to be a formidable task, but important progress was made. Two techniques were developed in parallel. An explicit/implicit finite difference Navier Stokes code had not been completed at the end of the program. A finite element algorithm was developed to solve equations (49) and (50). Although the completed program was not available in time to affect the stability calculations, the results are of considerable interest and are briefly summarized here. Details of the numerical analysis are given in a PhD thesis by Clayton³⁵.

Figure 29 shows the finite element grid used to represent the STAR 48 motor chamber at the 50 second burnback configuration. It was necessary to assume conditions corresponding to very small Reynolds numbers to achieve converged solutions. Figure 30 shows a typical flow pattern for the non-spinning case. The recirculation region aft of the nozzle entrance is a dominant feature. Surprisingly, as rotation was added to the system, and the Reynolds number increased (to match the flight Rossby number range), the recirculation zone disappeared as indicated in Figure 31. This may be an artifact of the low Reynolds number range, and further study is required. Figure 32 shows the circumferential velocity distribution at several axial locations. The presence of the vortex core in the vicinity of the nozzle entrance is indicated; its extreme width is an artifact of the low Reynolds number.

6.3 UNSTEADY FLOW IN A SPINNING ROCKET CHAMBER

Before undertaking the formal treatment of the unsteady flow in the rotating rocket, it is appropriate to present a brief review of pertinent literature of rotating fluid dynamics. A well-known property of contained rotating fluids is their ability to support traveling wave motions even in the absence of compressibility. This feature is of obvious importance in the present problem, since the spacecraft perturbation frequencies of interest are in the same range as the natural frequencies of these "inertial" waves.

6.3.1 Inertial Waves

Waves of the inertial or "elastoid-inertial" type have been studied for many years with emphasis on applications in atmospheric physics and description of the fluid cores of rotating planetary bodies and stars. Early experiments showed that rotating containers filled with a fluid are capable of unexpected behavior. Lord Kelvin³⁶ described experiments with liquid filled gyroscopes that became violently unstable when released from the normally stable "sleeping-top" orientation. Greenhill³⁷ provided a detailed analysis of this problem in 1880 and showed that

STAR 48 Rocket Motor at 50 Sec
Burnback Configuration

330 Elements

1399 Nodes

4567 Variables

Bandwidth: 239

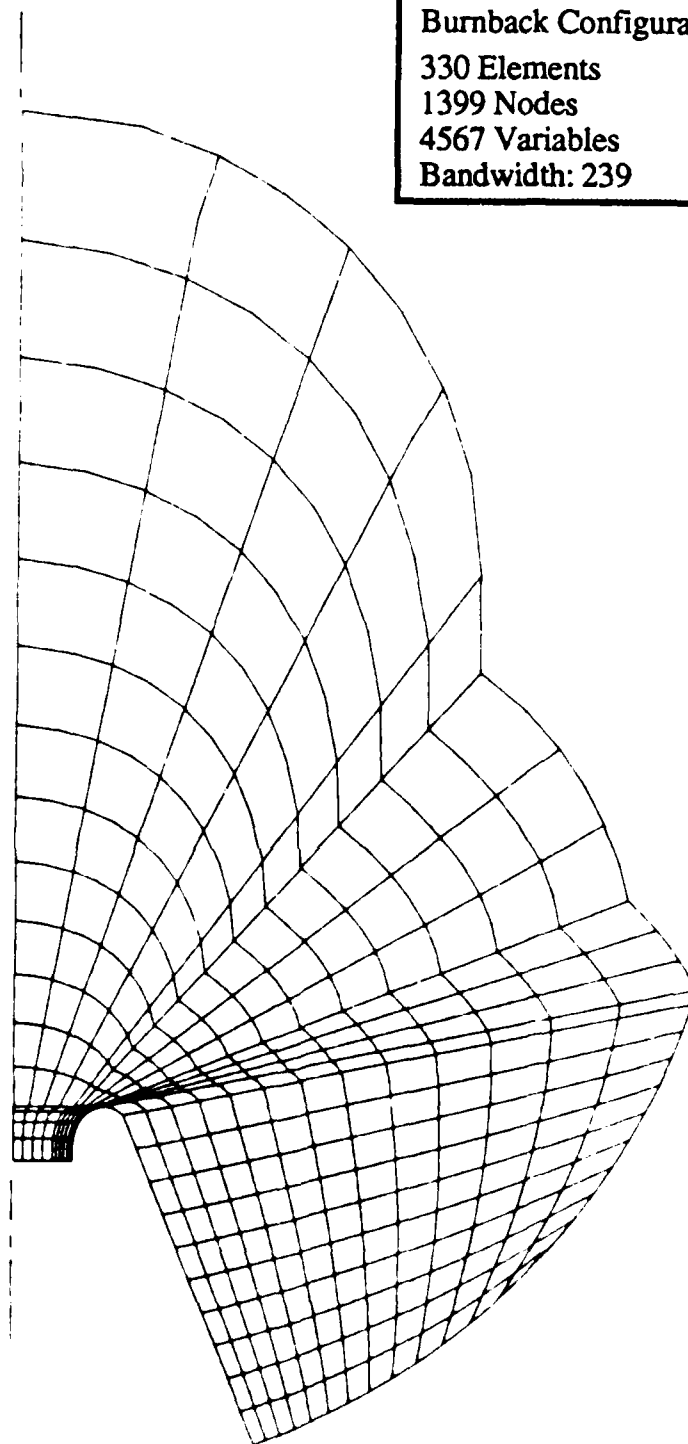


Figure 29. Finite Element Grid for Mean Flow Calculation

STAR 48 at 50 Second Burnback

Reynolds No. = 0.8

$\Omega = 0$

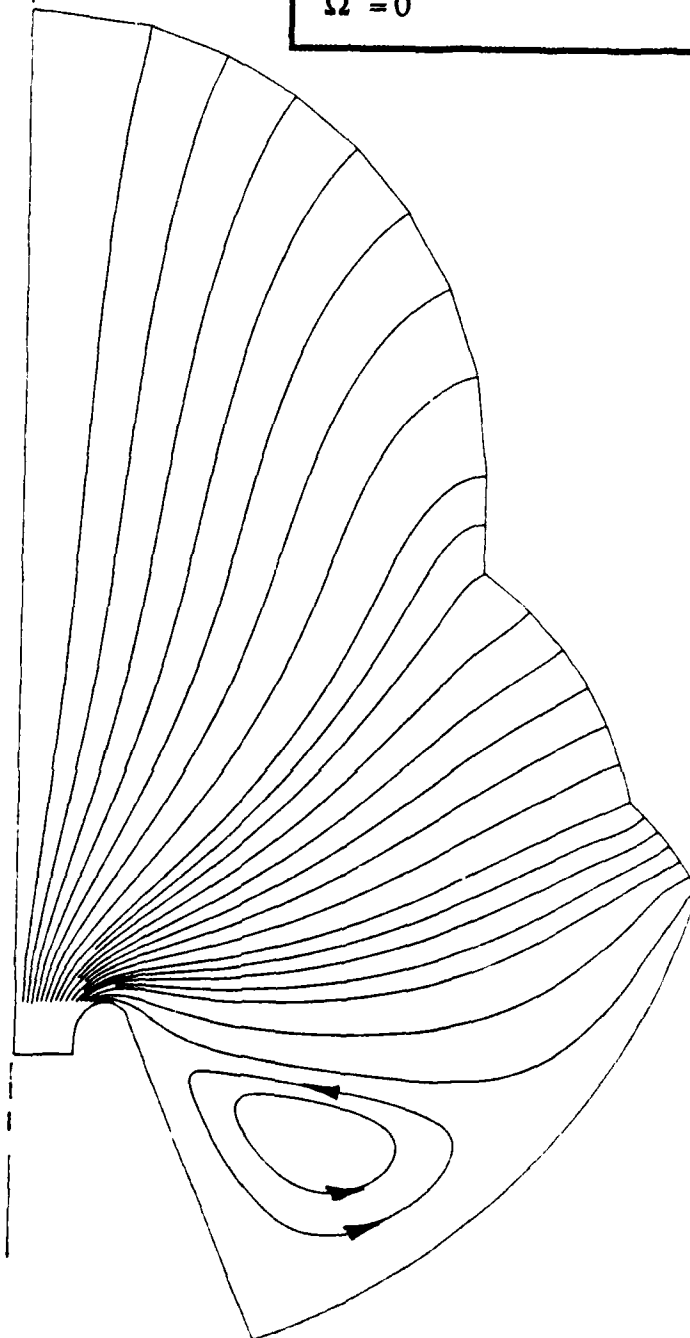


Figure 30. Streamline Pattern in STAR 48 at 50 Seconds

STAR 48 Rocket Motor at 50
Second Burnback Configuration

Reynolds Number = 15
 $\Omega = 0.004$ RPM

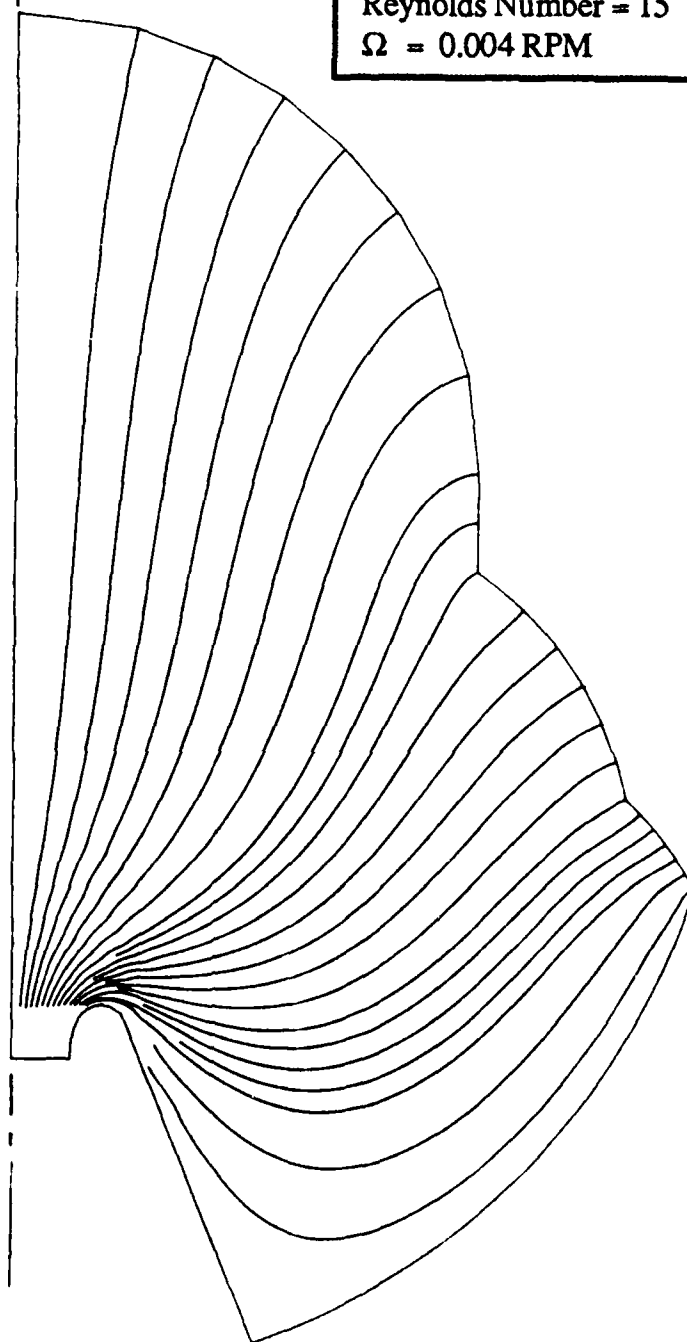


Figure 31. Streamlines in STAR 48 motor with Spin

STAR 48 Rocket Motor at 50 Second
Burnback Configuration

Reynolds Number = 15
 $\Omega = 0.004$ RPM

Note: Effect of vortex stretching in
nozzle entrance and viscous core are
shown. Core is very wide relative to
the throat radius because of the low
Reynolds number.

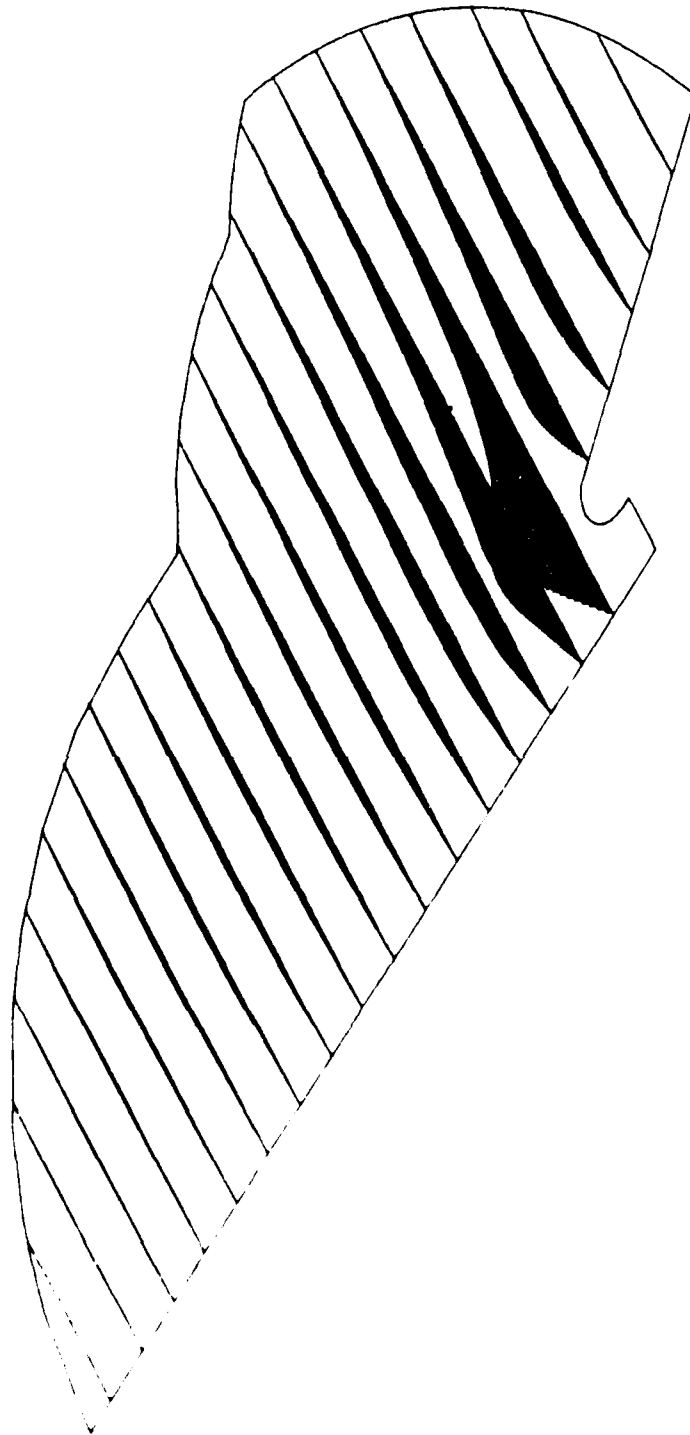


Figure 32. Azimuthal Velocity Component in Rotating STAR 48

the perturbed fluid motions within the spinning chamber produce a destabilizing moment on the system. He demonstrated that the fluid filled gyro would be unstable only for certain geometrical combinations. More recently, Stewartson³⁸ carried out a detailed computation that indicated the connection of the instability to the presence of inertial waves in the spinning fluid. The analysis was verified in a clever experiment by G. N. Ward reported in an appendix³⁸. This work formed the basis of the study by D'Amico and Miller²⁰ of the flight instability of liquid filled projectiles. Problems of this nature have been subjected to intense study recently²¹⁻²⁸.

The instabilities experienced in fluid filled spinning projectiles are similar to those of interest in the present study. One is tempted to attribute the PAM-D problem to the same mechanism. It will be shown that although inertial waves are of central importance in both situations, there are major differences in the destabilization mechanism. In particular, the presence of the mean convection in the spinning rocket gives rise to a vastly different physical situation. In the projectile problem, viscous forces represent the dominant interaction between the fluid and the container. Viscous forces may not play an important role in the spinning rocket problem, which is dominated by convection of angular momentum carried by the flow of exhaust gases. This mechanism was highlighted in Section 5 as one of several that will require very careful evaluation.

Inertial waves represent a major feature of time-dependent motions in a contained spinning flow. They result mainly from the Coriolis acceleration. As elegantly expressed by Kudlick³⁹, "... *rotation endows an incompressible fluid with the ability to support traveling waves, a remarkable property.*" The treatise by Greenspan⁴⁰ contains an extensive discussion of this phenomenon.

Flow visualization of inertial waves was first accomplished by Fultz⁴¹ for axisymmetric inertial modes; his work provided inspiration for the unsymmetrical mode flow visualization experiments described later. These appear to be the first experiments in which the existence unsymmetrical modes has actually been visually verified. The origins and implications of the inertial wave phenomenon will become evident in the detailed presentation of the unsteady flow field calculations.

6.3.2 Modeling of the Unsteady Flow Field

As in the case of the mean flow, it is appropriate to neglect the viscous forces, since the flow is dominated by convective effects. It should be pointed out that inclusion of viscous terms would be expected to increase the likelihood of instability (in keeping with the well-known principle that frictional energy dissipation effects render unstable the rotational motion of prolate bodies). Therefore, neglect of friction effects results in a conservative estimate of the system stability characteristics.

The equations that describe the unsteady flow are

$$\nabla \cdot \mathbf{u}' = 0 \quad (61)$$

$$\begin{aligned} \frac{\partial \mathbf{u}'}{\partial t} + 2 \mathbf{k} \times \mathbf{u}' + \nabla p' = & - \epsilon [\mathbf{u}' \cdot \nabla \mathbf{U} + \mathbf{U} \cdot \nabla \mathbf{u}'] - \\ & - [2 \boldsymbol{\omega}' \times \mathbf{U} + \epsilon^{-1} (d\boldsymbol{\omega}'/dt) \times \mathbf{r}] \end{aligned} \quad (62)$$

The convective terms and effects related to the perturbations in the rocket motion have been moved to the right. The former terms are proportional to the Rossby number. Classical treatment of rotating fluids is based on the assumption of a very small Rossby number. This is not an appropriate simplification in the present problem since the Rossby number is of the order of unity. This greatly complicates the analysis because use cannot be made of the Rossby number as a perturbation parameter.

The terms involving $\boldsymbol{\omega}'$ represent the forcing of the gas motion by the angular motions of the spacecraft. This is analogous to the sloshing of a liquid in a container. The Coriolis force is again in evidence; the interaction of the vehicle oscillations with the chamber mean flow provides a driving force that produces an unsteady response in the motor flow field. It will be noticed that this is the same force that was identified in Section 5 as the principle source of jet damping. This is an important point that must be understood completely. The jet damping from the traditional point of view is the reaction force on the chamber created by interaction of the wobbling motion of the boundaries with the steady part of the mean flow of combustion products. Equation (62) makes it clear that the reaction of this force on the gas flow itself takes the form of an oscillating driving force. If one neglects the time-dependent gas motions (as is done in the classical jet damping analysis), then this is of no consequence. If unsteady flow effects are considered, then it is clear that the effects of the jet damping reaction forces on the gas must be evaluated. This introduces a dramatic change in the interpretation of jet damping as will be evident in the solutions of equations (61) and (62).

6.3.3 Classical Inertial Wave Solutions

The classical inertial wave results are recovered if the terms on the right of equation (62) are treated as small perturbations. The boundary condition is then equivalent to that appropriate for an enclosed inviscid fluid. That is, the normal velocity component must be zero everywhere on the inner chamber surface. Manipulation of the momentum equation yields the wave equation

$$\frac{\partial^2}{\partial t^2} [\nabla^2 p'] + 4(\Omega \cdot \nabla)^2 p' = 0 \quad (63)$$

with the boundary condition

$$\mathbf{n} \cdot \nabla p' = -\mathbf{n} \cdot [2\boldsymbol{\Omega} \times \mathbf{u}' + \partial \mathbf{u}' / \partial t] \quad (64)$$

on the surfaces of the container. This problem was first studied by Poincare' ⁴² and the wave equation (63) was named after him by Cartan⁴³. This is a hyperbolic differential equation and thus describes wave-like motions. Solutions have been carried out only for simple geometries. The plane wave case, and solutions for cylindrical and spherical cavities have been studied extensively (cf References 39, 40). Kudlick³⁹ obtained the eigenfunctions for spheroidal domains and carried out detailed numerical evaluations for both spheroids and cylinders including estimates of viscous corrections. Solutions for the cylindrical geometry will be used here to approximate the inertial waves in a spinning rocket motor. It will be demonstrated that the results are not overly sensitive to the exact shape of the chamber, but the fineness ratio, or chamber L/D, is an important geometrical parameter.

Since inertial waves are not likely to be a familiar concept to most readers, it is appropriate to review the fundamental results here. These will be of direct utility in the solution of the problem. The familiar stratagem of representing the actual solution as a superposition of the unperturbed normal modes will be exploited. This is not a mathematically efficient technique in this particular application since it is likely that a great number of modes will be necessary to synthesize the gas response to the chamber motion. This comes about because the mode frequencies (an infinite number of them) all lie in a narrow range of the same order of magnitude as the vehicle coning frequency. Nevertheless, the conceptual simplicity of Fourier synthesis is of considerable benefit in constructing the required solutions; high-speed computational facilities render feasible the large number of calculations needed for assessment of the results.

Assuming that the chamber is axially symmetric and that oscillatory disturbances are expected, put

$$p' = \phi \exp(i \lambda t), \quad (65)$$

where ϕ is the fluctuating pressure amplitude. The Poincare' wave equation can then be written in polar coordinates as

$$\partial^2 \phi / \partial r^2 + r^{-1} \partial \phi / \partial r + r^{-2} \partial^2 \phi / \partial \theta^2 + (1 - 4/\lambda^2) \partial^2 \phi / \partial z^2 = 0. \quad (66)$$

The boundary conditions are

$$\begin{aligned} r \frac{\partial \phi}{\partial r} - (2i/\lambda) \frac{\partial \phi}{\partial \theta} &= 0 & \text{on } r=1 \\ \frac{\partial \phi}{\partial z} &= 0 & \text{on } z=0, 2b \end{aligned} \quad (67)$$

for the assumed cylindrical chamber geometry. This problem is easily solved by standard techniques. The result for the pressure amplitude is

$$\phi = J_k(\xi r) \exp(ik\theta) \cos(n\pi z/2b). \quad (68)$$

The eigenvalue ξ is one of the infinite set of roots of the transcendental equation

$$\xi \frac{dJ_k(\xi)}{d\xi} + k \left[1 + (2\xi b/n\pi)^2 \right]^{1/2} J_k(\xi) = 0 \quad (69)$$

The roots ξ set the frequencies

$$\lambda_{kmn} = 2 \left[1 + (2\xi b/n\pi)^2 \right]^{-1/2} \quad (70)$$

where k , m , and n are the mode integers. Increasing values of these integers correspond, respectively, to an increasing number of azimuthal, radial, and axial nodal surfaces. Only positive values for m and n are relevant, but negative values of k , corresponding to waves traveling in the posigrade direction (relative to the chamber direction of revolution) are possible. These yield frequencies differing from those associated with positive values of k that correspond to retrograde traveling waves. In this regard, the order subscript k in the Bessel functions must be taken as the absolute value of k . Thus the inertial pressure and velocity waves are

$$p' = J_k(\xi r) \cos(n\pi z/2b) \exp[i(\lambda t + k\theta)] \quad (71)$$

$$\mathbf{u}' = Q \exp(i\lambda t) = [i f_1 \mathbf{e}_r + f_2 \mathbf{e}_\theta + i f_3 \mathbf{k}] \exp[i(\lambda t + k\theta)]. \quad (72)$$

The velocity component functions are given by

$$\begin{aligned} f_1 &= -(4 - \lambda^2)^{-1} \left[2kr^{-1} J_k(\xi r) + \lambda \xi J'_k(\xi r) \right] \cos(n\pi z/2b) \\ f_2 &= (4 - \lambda^2)^{-1} \left[\lambda kr^{-1} J_k(\xi r) + 2\xi J'_k(\xi r) \right] \cos(n\pi z/2b) \\ f_3 &= -(n\pi/2\lambda b) J_k(\xi r) \sin(n\pi z/2b) \end{aligned} \quad (73)$$

The motion can be described as a complex three-dimensional sloshing of the gas. Flow visualization experiments are a valuable aid to the understanding the velocity distributions. These are described in a later section of the report. Three-dimensional computer animation of the results was also of great utility in gaining a proper appreciation of the velocity field. Either posigrade or retrograde traveling waves are possible depending on the sign of k . It will be shown later that only modes with azimuthal wave number $k = 1$ are of potential interest in the coning problem. Figures 33-37 show radial velocity distributions for several such modes. Figure 38 shows axial distribution of the velocity amplitudes for a typical radial position. It should be noted that only the radial velocity component is required to vanish at the sidewall of the cylinder, since inviscid flow is assumed.

Figure 39 is a plot of frequency vs the chamber shape parameter, b for several inertial modes. In general, the frequency increases with increasing number of axial nodal points as indicated by mode integer n . However, as shown in the figure, mode frequency decreases with increase in the number of radial nodal points (increasing values of the integer m). This is one of several ways in which inertial waves differ from other more familiar oscillation problems. The higher harmonics can have both higher and lower frequencies than the "fundamental" ($k=1, m=1, n=1$).

Several other features of the inertial frequencies must be understood. The eigenvalues represent an infinite set tightly packed into the finite range $-2 < \lambda_m < 2$. The single subscript m or n will often be employed in what follows to represent the combination (kmn) to keep the notation as simple as possible. Thus, when speaking of a mode m , reference to a particular (kmn) combination is implied. It is significant that these inertial frequencies are in the same range (assuming a prolate spacecraft) as vehicle frequencies represented by the (dimensionless) spacecraft coning frequency:

$$\lambda_s = (1 - I_0/I_1) \quad (74)$$

Thus some type of resonant interaction is clearly possible. A feature that was overlooked early in the study is that frequencies of higher-order modes are not necessarily higher than the lowest order frequencies. For the cylindrical modes, increasing m gives lower frequencies, but increasing n corresponds to increasing frequency. This is clearly depicted in the frequency plots (Figure 39). Thus at a given instant of time, there may be many modes with frequencies close to the natural coning frequency. This greatly complicates questions relating to resonance between the vehicle motion and any particular mode of inertial oscillation since it is difficult to be sure which of many modes near a given vehicle nutation frequency is being excited. In experiments such as those carried out by Fultz (see Refs. 41 and 42) determination of which inertial mode is present becomes increasingly difficult with increasing order of the mode. This is in accordance with the well-known property that lower-order modes require less energy input for their activation.

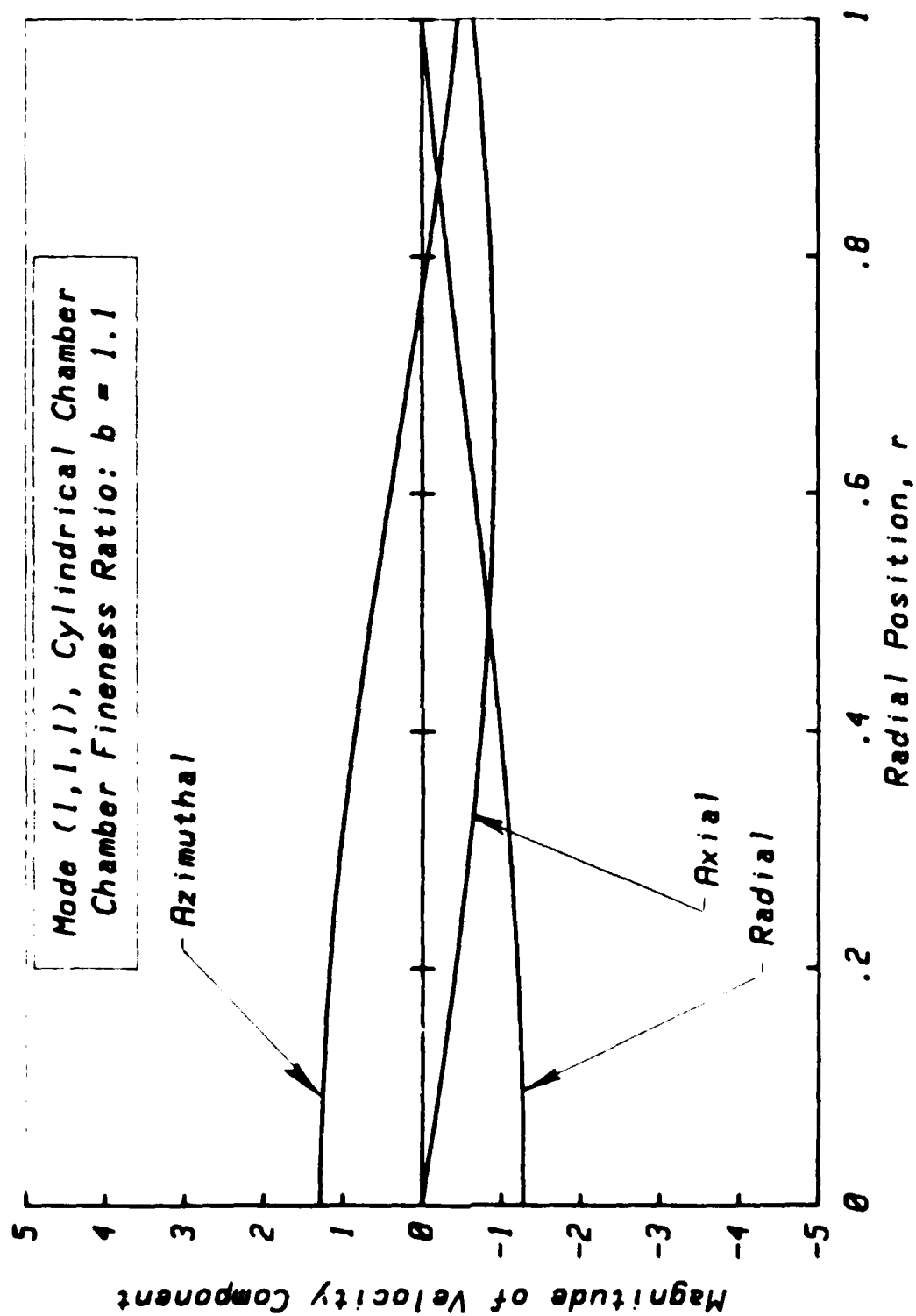


Figure 33. Plots of Inertial Mode Velocity Components vs Radius

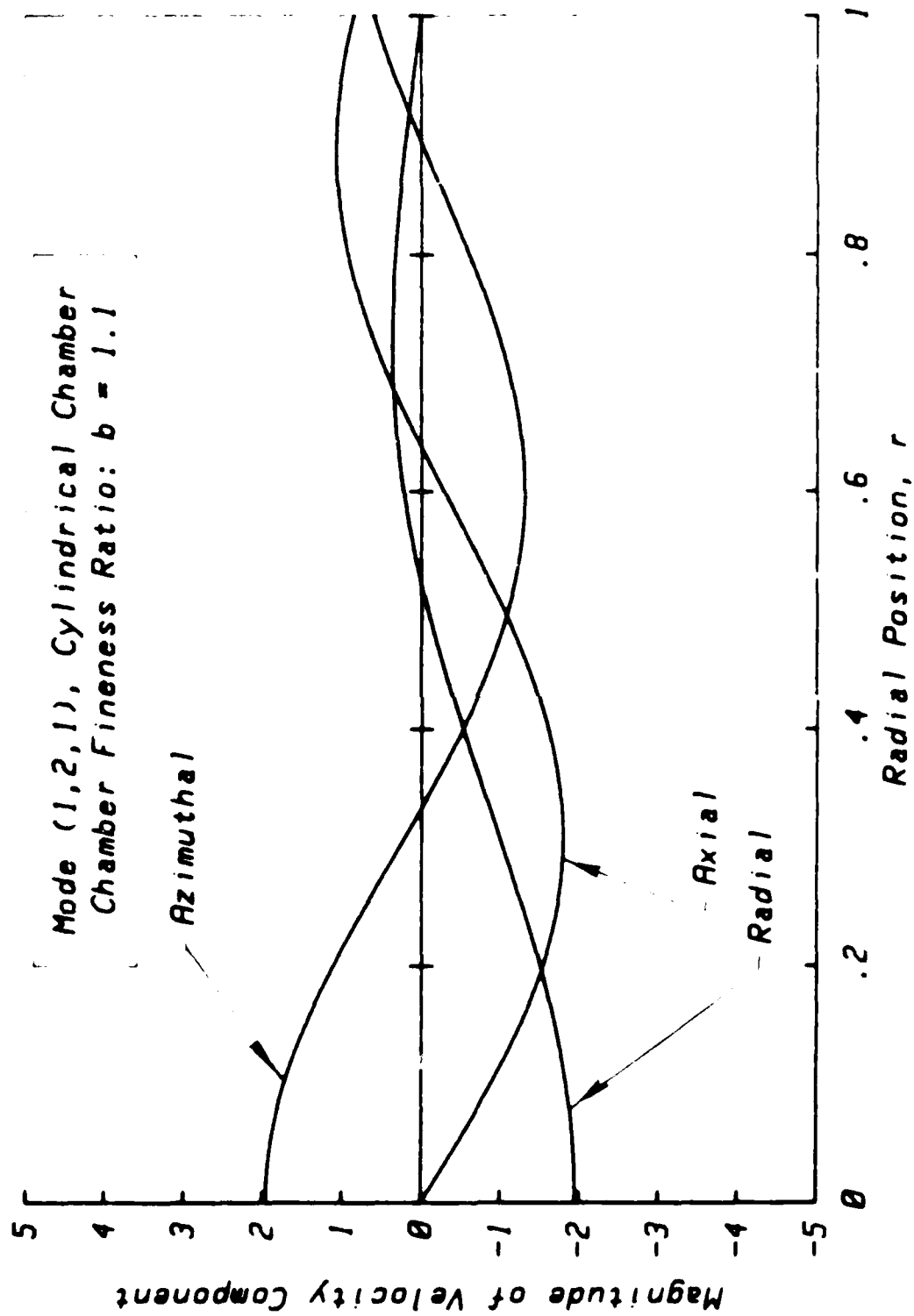


Figure 34. Plots of Inertial Mode Velocity Components vs Radius

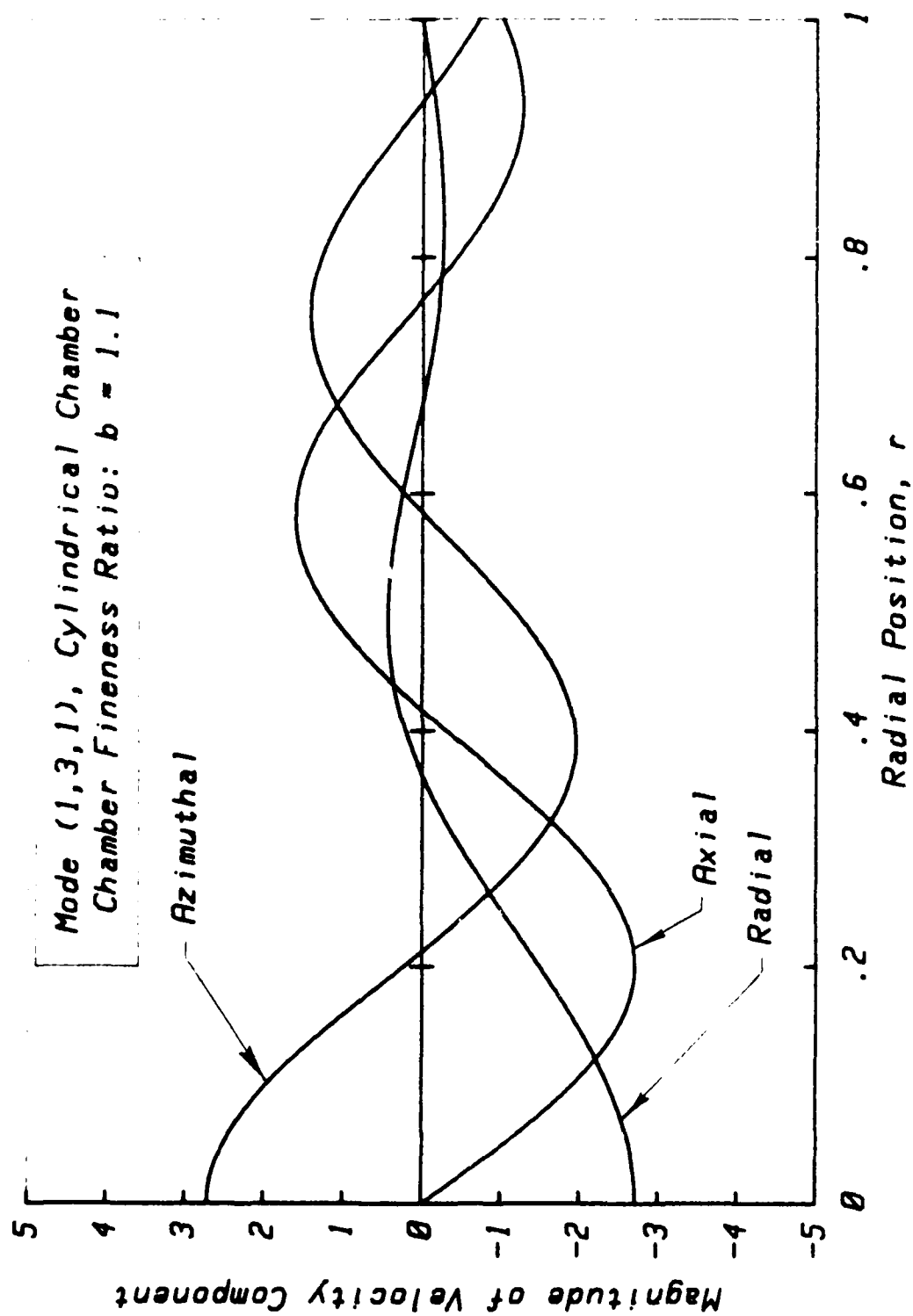


Figure 35. Plots of Inertial Mode Velocity Components vs Radius

AD-A177 350

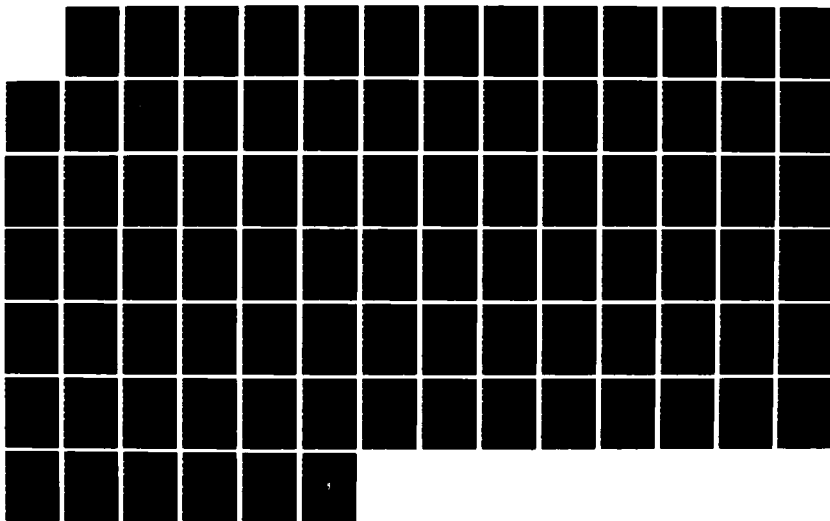
FLUID MECHANICS OF SPINNING ROCKETS(U) UTAH UNIV SALT
LAKE CITY FLUID DYNAMICS LAB G A FLANDRO ET AL. JAN 87
AFRPL-TR-86-072 F04611-83-K-0047

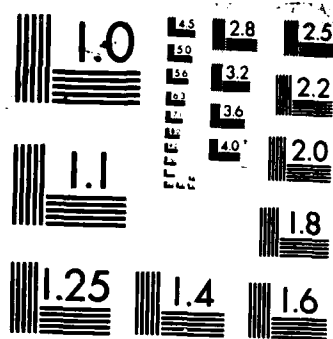
2/2

UNCLASSIFIED

F/G 28/4

NL





MICROCOPY RESOLUTION TEST CHART
NATIONAL BUREAU OF STANDARDS 1963-A

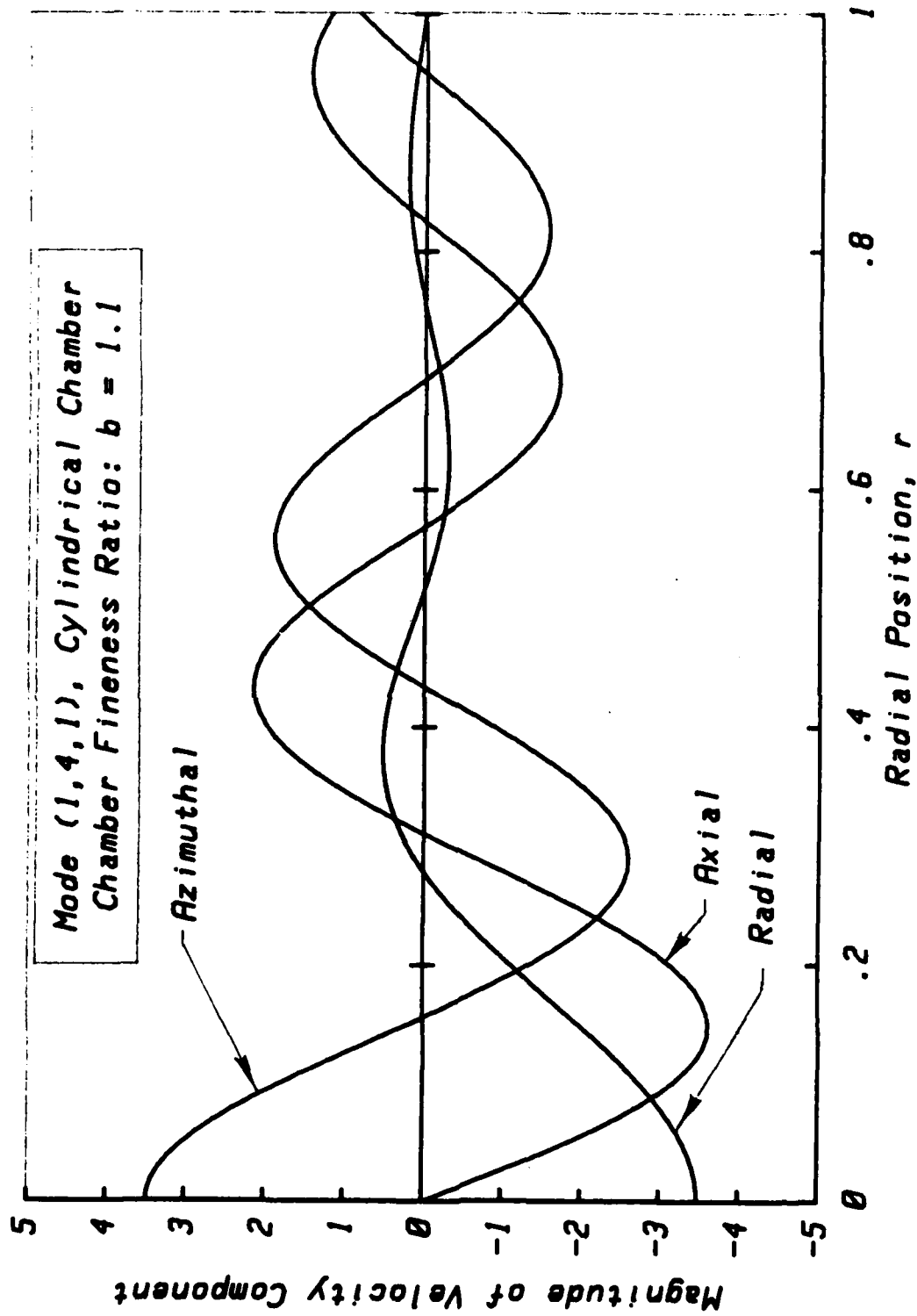


Figure 36. Plots of Inertial Mode Velocity Components vs Radius

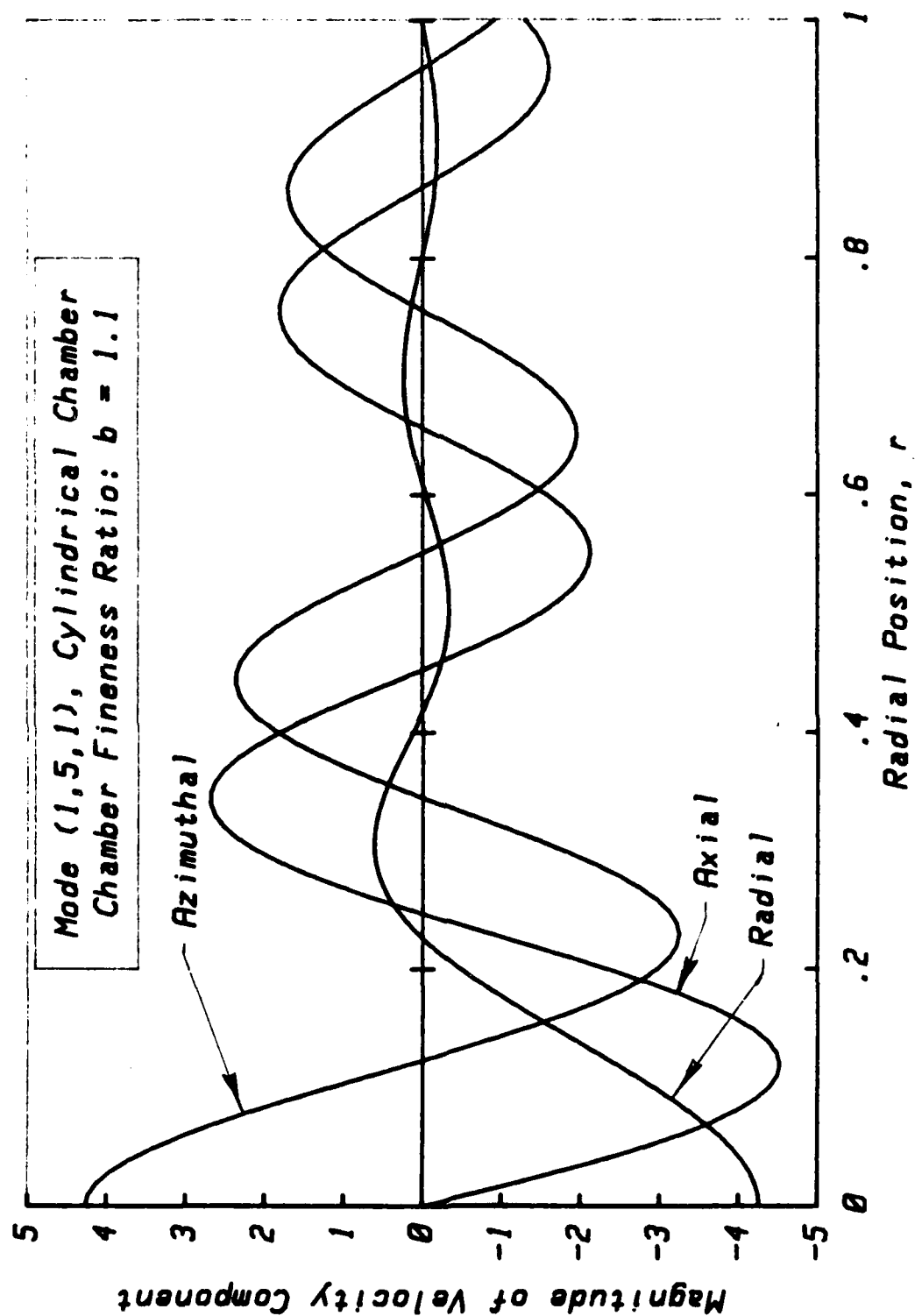


Figure 37. Plots of Inertial Mode Velocity Components vs Radius

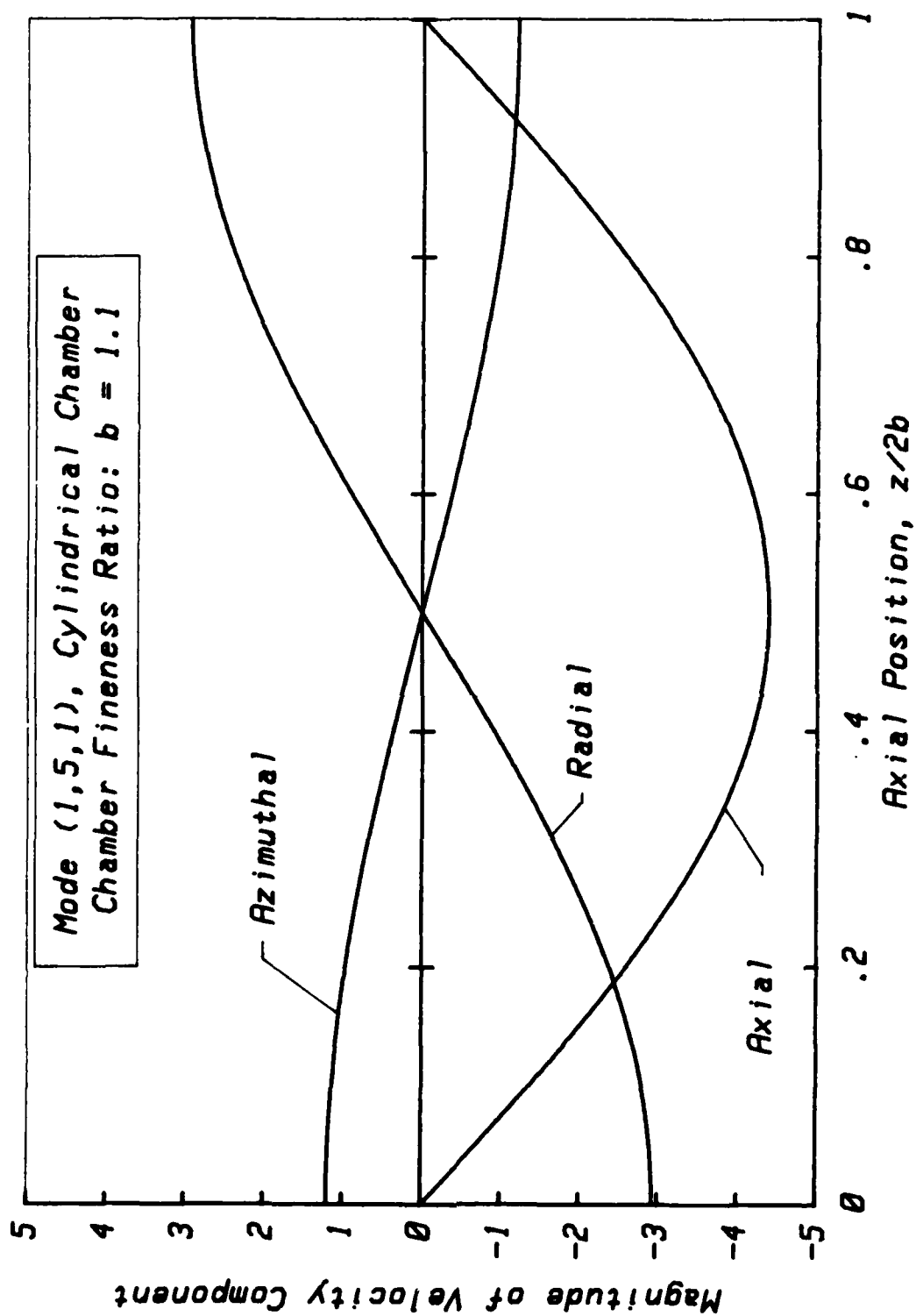


Figure 38. Plots of Inertial Mode Velocity Components vs Axial Position

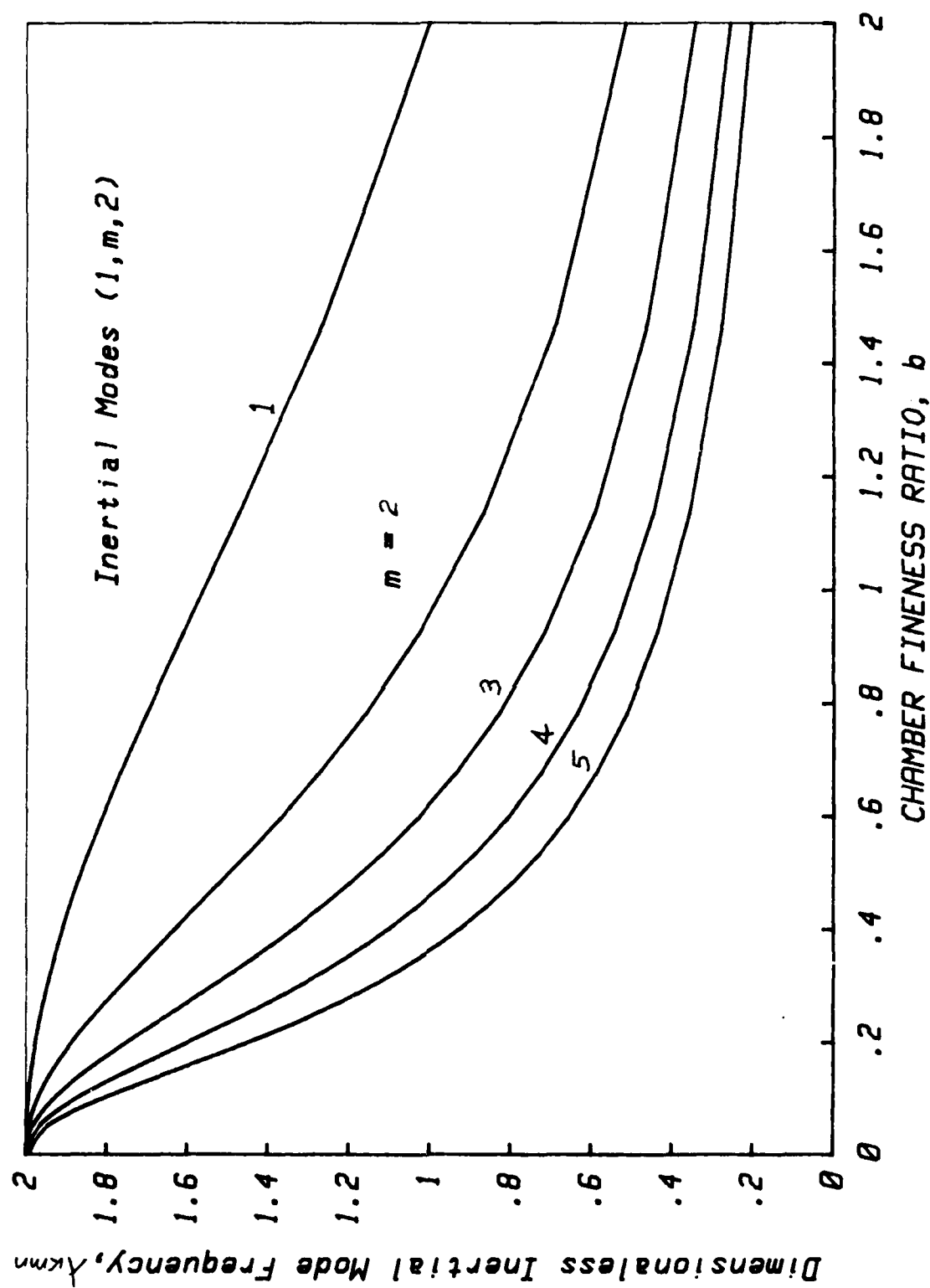


Figure 39. Inertial Mode Frequencies vs Fineness Ratio

Certain other properties of the inertial eigenvectors will prove useful later. Of considerable importance are the orthogonality relationships. It is readily shown (see Greenspan⁴⁰ for a detailed discussion) that

$$\int_V \mathbf{Q}_m \cdot \mathbf{Q}_n^* dV = \begin{cases} E_m^2 & (m = n) \\ 0 & (m \neq n) \end{cases} \quad (75)$$

and

$$\int_V \mathbf{k} \cdot \mathbf{Q}_m \times \mathbf{Q}_n^* dV = \begin{cases} -(i/2) \lambda_m E_m^2 & (m = n) \\ 0 & (m \neq n) \end{cases} \quad (76)$$

The * denotes the complex conjugate of the complex velocity amplitude, \mathbf{Q} .

6.3.4 Forced Motion of The Combustion Gases

The problem of central interest is one in which the gas flow through the motor is excited by the motions of the spacecraft. This class of fluid excitation has been studied extensively for *closed chambers* (cf Refs. 44-56). These solutions are not of direct applicability in the present case, since account must be taken of the convection of combustion gases through the chamber. This requires major changes in strategy from previous analyses.

In order to adequately represent the unsteady flow, it is necessary to construct solutions that account for the perturbation terms on the right hand side of equation (62) consisting of the inertial driving (Coriolis and angular rate terms) and the important convective terms proportional to the Rossby number. Since the gas response is likely to be dominated by the Coriolis signal at the nutation frequency, then the proper approach is to represent the solution as a superposition of unperturbed inertial modes. On the basis of the description of the spacecraft motion presented in Section 3 (see equation (33)), the proper form for ω' is

$$\omega' = \omega \exp(\beta t) \quad (77)$$

where β is the complex frequency

$$\beta = (\alpha + i\lambda_s) \quad (78)$$

and the amplitude is ω , both of which remain to be determined. It will be possible

to simplify solutions at a later stage by noting that the real part of β (the growth rate or inverse of the time constant), α is much smaller than λ_s , the spacecraft coning frequency. Vector ω is a slowly varying function of time. Inserting (77) into equation (62), and representing the solution the perturbation velocity and corresponding pressure by

$$\begin{aligned} \mathbf{u}' &= \sum_m B_m \mathbf{Q}_m \exp (\beta t) \\ p' &= \sum_m A_m \phi_m \exp (\beta t). \end{aligned} \quad (79)$$

One can construct an equation for the modal coefficients, B_n . This is accomplished by multiplying through by the complex conjugate of the velocity amplitude, \mathbf{Q}_n^* , and integrating over the combustion chamber domain. Use of the orthogonality relationships leads to the result

$$\begin{aligned} B_m E_m^2 (\beta - i \lambda_m) = & - \epsilon \int_V \mathbf{Q}_m^* \cdot [\mathbf{u}' \cdot \nabla \mathbf{U} + \mathbf{U} \cdot \nabla \mathbf{u}'] dV \\ & - \int_V \mathbf{Q}_m^* \cdot [2 \boldsymbol{\omega} \times \mathbf{U} + \epsilon^{-1} \beta \boldsymbol{\omega} \times \mathbf{r}] dV \\ & - \sum_n A_n \int_S \mathbf{n} \cdot \mathbf{Q}_m^* \phi_n dS \end{aligned} \quad (80)$$

where the substitution for \mathbf{u}' has not yet been made in the convective term.

The three integral terms on the right of equation (80) represent three distinct driving forces that control the energy flux to the wave motions. If the steps leading to this equation are carefully studied, one sees that in effect the basic steps were as follows:

- Multiplication of the momentum equation by the velocity vector.
- Integration over the volume of the chamber.
- Representation of the velocity and pressure fluctuations by Fourier expansions using inertial wave eigenfunctions.

The first two steps are equivalent to conversion of the problem to mechanical energy form if it is recalled that the terms in the momentum equation are proportional to force per unit volume. Multiplying by the velocity converts each term into a contribution to the rate of change of energy per unit volume. Integration over the volume then produces the energy balance for the system.

The first volume integral represents the effect of convection. Energy flow resulting from the work done by the chamber motion is propagated through the system by the mean flow field. An analogous term represents convection of the mean flow vorticity by the inertial wave fluctuations. The second volume integral on the right of equation (80) is the main source of wave motion. It represents the pumping of the internal flow by the wobbling motion of the spacecraft. The surface integral requires special attention. It is not zero at the burning propellant where the normal gas velocity is controlled by the pressure dependent burning rate.

In order to assess the net growth of wave energy in the system, it is necessary to determine the sum of the three perturbation integrals. The balance between these three effects, (1) transport of gas fluctuations by mean flow convection, (2) driving of the waves by motion of the chamber walls due to spacecraft nutation, and (3) driving of waves by pressure coupling with the propellant will determine whether the nutation disturbance will grow or decay. If the net kinetic energy of the wave system grows, then the coupled spacecraft nutation may also grow. The three perturbation terms are evaluated separately in the next three subsections.

6.3.5 Effect of Convection of Wave Energy by the Mean Flow

A major difference between the PAM-D nutation instability and other similar problems such as the unstable behavior of liquid filled projectiles²⁰⁻²⁸ is that the fluctuations generated in the flow must be carried out of the rocket motor by the mean gas flow. In the projectile problem, the wave motions are contained within the system, and their amplitude is controlled by frictional losses in the viscous boundary layers (Ekman layers). In the present situation, one must account for the energy loss to the wave system represented by the convective volume integral.

The first volume integral on the right of equation (80) contains expressions proportional to the mode amplitude that must be determined before B_m can be isolated. The symbolic form for the convective accelerations must be replaced by the proper vector form to enable correct evaluation. Thus,

$$\mathbf{u}' \cdot \nabla \mathbf{U} + \mathbf{U} \cdot \nabla \mathbf{u}' = \nabla (\mathbf{u}' \cdot \mathbf{U}) - \mathbf{u}' \times \nabla \times \mathbf{U} - \mathbf{U} \times \nabla \times \mathbf{u}' \quad (81)$$

Equation (79) is used to write the velocity fluctuation in terms of the series of eigenfunctions, and the mean flow is represented by the model described in Equation (55). The integrals over the volume can then be carried out with due attention to the orthogonality relationships. The result is

$$\epsilon \int_V Q_m^* [\mathbf{u}' \cdot \nabla \mathbf{U} + \mathbf{U} \cdot \nabla \mathbf{u}'] dV = B_m E_m^2 [i \lambda_m + G_m(\lambda_m)] \quad (82)$$

The first term on the right represents the effect of convection of the mean flow vorticity by the wave motions, and is the result of integration of the second term on

the right of (81) dotted with the complex conjugate velocity amplitude. G_m , an exceedingly complicated function of the mode frequency, comes from the third term in equation (81). It represents the convection of inertial wave vorticity by the mean flow, and its evaluation requires numerical treatment of certain Bessel function integrals that cannot be carried out in closed form. The expanded form of G_m and other expressions that emerge in the analysis are displayed in the Appendix. G_m contains terms describing the effect of convection of wave vorticity through the chamber both in the axial and the azimuthal directions. These are due to azimuthal convection by the vortex mean flow component.

It will be noticed that one major effect of the convection is to eliminate the term $i\lambda_m$ from the left hand side of equation (80) represented by the combination

$$B_m E_m^2 (\beta - i\lambda_m) \quad (83)$$

Thus when all integrals on the right hand side of (80) have been evaluated and B_m is found by dividing through by the coefficient $E_m^2 (\beta - i\lambda_m)$, the usual simple resonance phenomenon is lost. Resonance is indicated when the imaginary part $i\lambda_m$ cancels with the imaginary part of $\beta = (\alpha + i\lambda_s)$ when the mode frequency λ_m is the same as the driving frequency λ_s . This emphasizes the strong damping influence of the mean flow field. This does not mean, necessarily, that a resonance effect is not present. Function G_m is a function of frequency. What is indicated is that simple resonance between the nutation and a given inertial mode is not a primary feature of the driving mechanism.

6.3.6 Pumping of Inertial Waves by Vehicle Wobbling

The second volume integral in equation (80) is the main source of inertial wave energy. It represents the mechanical pumping by the oscillatory motion of the spacecraft. If the system is viewed from inertial (nonspinning) coordinates located (instantaneously) at the spacecraft center of mass, it can be seen that the nutation wobbling represents a cyclical pumping action in which the walls of the combustion chamber force a periodic response from the gas particles. The spin greatly modifies the response. The resulting waves, the inertial waves, have already been described.

In order to evaluate the forcing integral, the spacecraft dynamics must be represented. On the basis of the experimental data and the analysis of Section 3, the proper form for the angular velocity of the spacecraft is a retrograde traveling disturbance. Thus it is appropriate to define

$$\boldsymbol{\omega} = \omega_0 [i + ij] \quad (84)$$

where the amplitude ω_0 may be a slowly varying function of time. This corresponds

to the solutions described earlier (see equation (33)). The pumping integrals can be carried out without great difficulty. For the assumed geometry, one finds

$$\int_V \mathbf{Q}_m^* \cdot [2 \boldsymbol{\omega} \times \mathbf{U}] dV = -2 \boldsymbol{\omega} \cdot \int_V \mathbf{Q}_m^* \times \mathbf{U} dV = C_m(\lambda_m) \quad (85)$$

and

$$\int_V \mathbf{Q}_m^* \cdot [\epsilon^{-1} \beta \boldsymbol{\omega} \times \mathbf{r}] dV = \epsilon^{-1} \beta \boldsymbol{\omega} \cdot \int_V \mathbf{r} \times \mathbf{Q}_m^* dV = \beta D_m(\lambda_m) \quad (86)$$

where the complex functions C_m and D_m are summarized in the Appendix.

6.3.7 Combustion Effects

The surface integral on the right of equation (80) requires special attention. For inert surfaces, the normal component of the velocity is zero, thus $\mathbf{n} \cdot \mathbf{Q}_m = 0$ on all parts of the control volume boundary except the burning surfaces. However, $\mathbf{n} \cdot \mathbf{Q}_m$ may not be negligible on the burning propellant. This situation is reminiscent of the classical acoustic combustion instability problem, which will be briefly reviewed for the benefit of readers not familiar with this venerable problem.

The burning rate of a solid propellant is strongly controlled by the pressure of the combustion gases. A well-known representation of the burning rate is

$$r = a (p/P_{\text{ref}})^n \quad (87)$$

where r is the regression rate of the burning surface, a is the burning rate coefficient, and n is the burning rate exponent. For the STAR 48 propellant, the values of these quantities have been measured to be:

$$\begin{aligned} a &= 0.228 \text{ in/sec} \\ n &= 0.30 \\ P_{\text{ref}} &= 500 \text{ psi} \end{aligned} \quad (88)$$

for r in inches per second and p in psi. From this expression, it is readily seen that a local increase in pressure will bring about a local increase in mass flux and corresponding normal velocity component. The surface gas influx velocity may be estimated by means of a local mass balance across the surface giving

$$v_b = (\rho_p/\rho) r \quad (89)$$

where the ratio of the solid propellant density and local gas density is the proportionality factor between surface regression and gas speed. Thus a pressure pulse will generate a mass pulse that can, under certain conditions, represent an

increment of energy to a pressure wave. This phenomenon, usually called "pressure coupling", has usually been associated with the acoustic modes of the combustion chamber. The propellant response to pressure fluctuations may be greatly amplified at special frequencies controlled by unsteady combustion and heat transfer processes, and large amplitude acoustic waves may be driven in a process referred to as acoustic combustion instability^{58,59}. Occasionally, the amplitudes are sufficiently large that nonlinear system behavior may be invoked⁶⁰. This has been a troublesome problem that has seriously affected numerous rocket motor development programs.

It is worth mentioning that mild acoustic instability has been detected in the STAR 48 motor. It is usually present early in the motor run and may be affected by vortex shedding⁶¹⁻⁶² from the edges of the radial slots (see the grain configuration drawing in Figure 12). These oscillations apparently have no impact on the coning problem and can only be detected in spectral analyses of chamber pressure measurements.

With this background, it can be seen by analogy with the acoustic instability problem, that inertial pressure waves can tap the combustion energy release in a similar manner. That is, a local pressure increase related to the traveling inertial pressure wave causes an increase in propellant burning rate. This localized increase in mass flux is completely equivalent to the pumping action by the chamber coning motion; energy flows into the fluctuations. It is essentially the familiar $p \, dV$ work being done on the chamber gases by the boundary fluctuations. In the present situation, the frequencies are so low, that the propellant response can be readily estimated directly from the simple burning rate law. That is, the response can be assumed to be a quasi-steady process. This may not be the case in the acoustic instability problem, since the burning process exhibits strong resonance effects in the acoustic frequency range.

It is first necessary to rewrite the burning rate law (87) in dimensionless form compatible with the present analysis. Using equation (89) and noting that the pressure is rendered dimensionless by dividing by the product ρv_b^2 , one can write for the local velocity vector at a point on the burning surface

$$\mathbf{u} \cdot \mathbf{n} = - K p^n \quad (90)$$

where n is the burning rate exponent, \mathbf{n} is an outward pointing unit normal, and \mathbf{u} is the velocity vector. The negative sign indicates that the velocity vector points into the interior of the chamber. The proportionality factor K is given by

$$K = \left(\frac{\rho_p a}{\rho v_b} \right) \left[\frac{\rho v_b^2}{P_{ref}} \right]^n \quad (91)$$

Using the perturbed forms for the velocity vector and pressure as given in equations (52), one can separate the steady and unsteady part of (90) if the fluctuations are assumed to have very small amplitudes as already established. Using the Taylor series expansion of (90) one finds:

$$\begin{aligned} \mathbf{n} \cdot \mathbf{U} &= -K P_0^n \\ \mathbf{n} \cdot \mathbf{u}' &= -n K P_0^{(n-1)} p' = -R_b p' \end{aligned} \quad (92)$$

where

$$R_b = n K P_0^{(n-1)} \quad (93)$$

is the inertial wave equivalent of the "response function" (related to the surface admittance function) of acoustic instability theory. In the inertial wave case, this is a real quantity indicating that the velocity response at the surface is in phase with the pressure wave due to the low frequencies of the waves (typically 0.5 Hz for a spacecraft spinning at 60 rpm). For the STAR-48 propellant, the value of R_b is approximately $8 \cdot 10^{-3}$ which indicates a very mild propulsion response.

The information necessary to evaluate the surface integral in equation (80) is now available. It is clear that the normal component of the velocity is related to the pressure by

$$\mathbf{n} \cdot \mathbf{u}' = \begin{cases} -R_b p' & \text{on burning surfaces} \\ 0 & \text{on inert surfaces} \end{cases} \quad (94)$$

Using equations (65) and (72) and the eigenfunction expansions as expressed in equations (79), in the boundary condition, one finds, at the chamber boundaries

$$\sum_n B_n \mathbf{n} \cdot \mathbf{Q}_n = -R_b \sum_n A_n \phi_n \quad (95)$$

where \mathbf{Q} and ϕ are the velocity and pressure amplitude functions, respectively. The integral becomes

$$- \sum_n A_n \int_S \mathbf{n} \cdot \mathbf{Q}_n^* \phi_n dS = R_b \sum_n B_n \int_S \phi_n^* \phi_n dS \quad (96)$$

By means of the orthogonality of the pressure eigenfunctions,

$$\int_S \phi_m^* \phi_n dS = \begin{cases} F_n^2 & \text{for } m = n \\ 0 & \text{for } m \neq n \end{cases} \quad (97)$$

one finds, finally

$$- \sum_n A_n \int_S \mathbf{n} \cdot \mathbf{Q}_m^* \phi_n dS = B_m R_b F_m^2. \quad (98)$$

Function F_m^2 is readily determined for any mode m . Results for the cylindrical motor geometry are shown in the Appendix.

6.3.8 Calculation of Forced Velocity Amplitude

It is now possible to write the equation for the relative amplitude of any modal component. Inserting the results of equations (82), (85), (86) and (98) into (80) yields

$$E_m^2 [\beta + G_m - R_b (F_m/E_m)^2] B_m = \omega_0 [C_m + \beta D_m] \quad (99)$$

The modal coefficients can then be found from the combination:

$$B_m = \omega_0 [C_m + \beta D_m] / E_m^2 [\beta + G_m - R_b (F_m/E_m)^2] \quad (100)$$

and the time dependent response of chamber flow to the spacecraft motion is then determined by summing over an appropriate number of modes. As will be demonstrated by numerical means in Section 8, a rather large number of modes must be accounted for (of the order of 1000) to achieve an accurate representation of the solution. This is the result of the very close spacing between the mode frequencies in the range of the disturbing frequency represented by the relative motions of the motor chamber boundaries.

6.4 CHARACTERISTICS OF UNSTEADY FLOW FIELD

To illustrate some features of the forced solutions, equation (79) for the forced time-dependent velocity was evaluated using mode amplitudes computed with (100). Conditions corresponding to the WESTAR V vehicle at 80 seconds after ignition were assumed (Chamber fineness ratio, $b = .96$, and Rossby Number, $\epsilon = 0.7$). 625 modes ($k=1$, $m=1$ to 25, $n=1$ to 25) were evaluated in carrying out the summation. Figure 40 presents plots of the radial variations of the amplitudes of

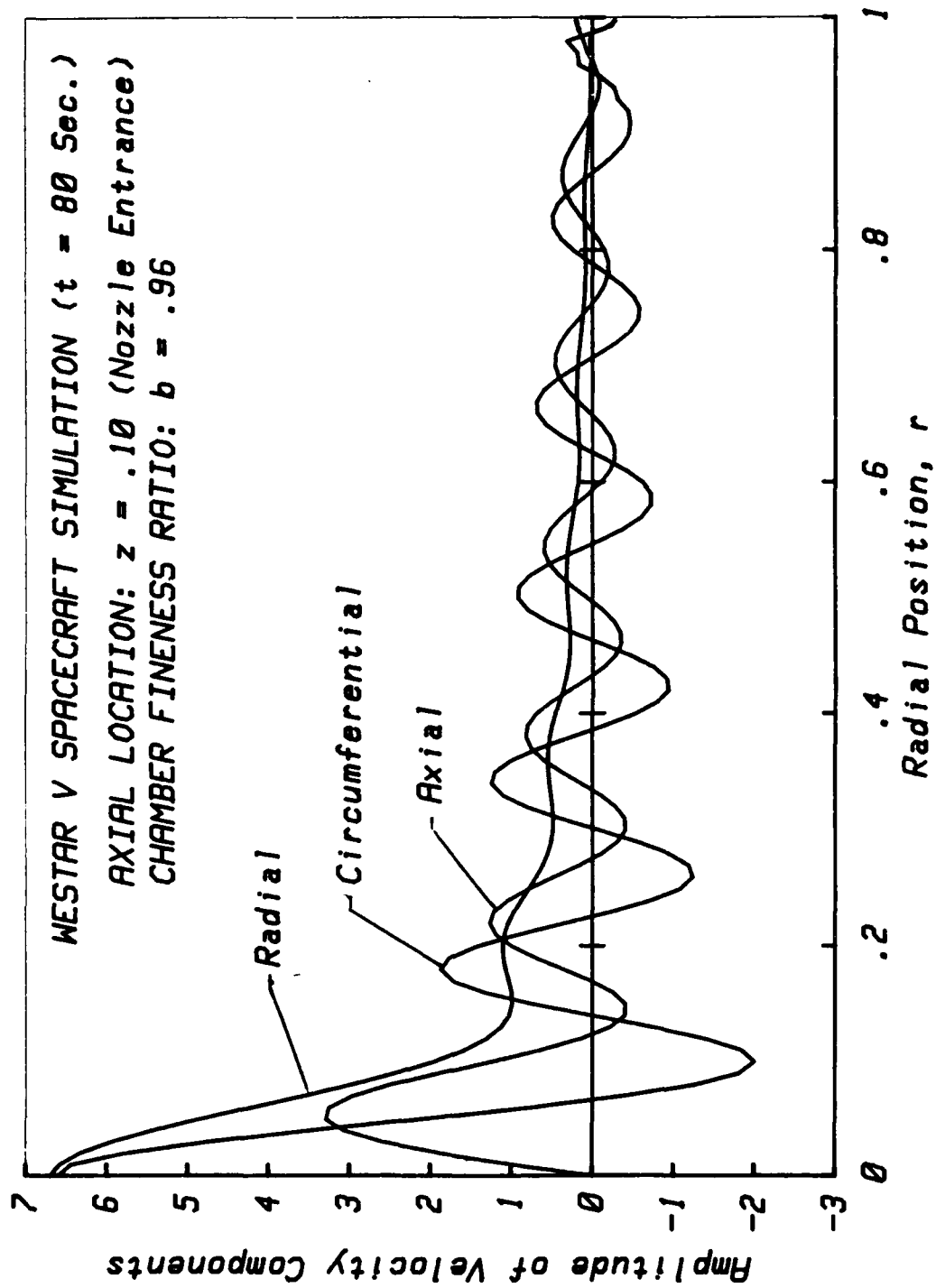


Figure 40 - Radial Velocity Distributions

the three oscillatory perturbation velocity components at an axial position corresponding to the nozzle entrance. It should be emphasized that the amplitude plots do not indicate the relative *phase* relationships between the components. For instance, in the vicinity of the axis ($r = 0$), the radial and transverse velocity components are out of phase by 90° and have similar amplitudes. This indicates that gas particles near the axis orbit in the retrograde direction in response to the forcing by the chamber nutation. When these perturbations are superimposed on the mean flow, it is clear that the flow pattern near the nozzle entrance consists of a vortex core orbiting the nozzle centerline in a helical fashion. Figure 41 illustrates the motion of the vortex core as it passes through the nozzle entrance in response to the coning motions of the spacecraft.

The effect of the mean flow field convection on the forced gas oscillations is clearly apparent in Figure 40. The inward flow toward the nozzle concentrates the angular momentum represented by the oscillatory gas motion along the centerline. This behavior is analogous to the concentration of the mean flow vorticity along the motor axis in the form of the axial vortex. In a sense, then, the wobbling motion of the motor induces a lateral vortex flow that is continuously generated within the chamber and carried out the nozzle with the mean flow.

Figure 42 shows the axial variation of the perturbation velocity components near the motor axis. The nearly equal amplitudes of the radial and transverse velocity components is noteworthy. This indicates, as already suggested, that gas particles near the axis orbit in nearly circular paths in the retrograde direction as they leave through the nozzle. An unexpected feature of the axial velocity variation near the centerline is its nearly constant amplitude in the central part of the motor cavity. At larger radii, the axial velocity fluctuations become larger, and they reach their largest amplitudes near the burning surface at the center of the motor. At $r = 1$, the axial perturbation velocity distribution is nearly sinusoidal.

The perturbation velocities are strongly dependent on the Rossby number and the chamber geometry. Figure 43 shows the variation with ϵ of the radial component near the motor centerline for several values of chamber fineness ratio in the range of interest. As anticipated, the perturbation amplitudes are greater for smaller values of the Rossby number. This reflects the influence of increased residence time of gas particles in the chamber acceleration field as the chamber size increases (ϵ is inversely proportional to the combustion chamber radius, R_0). Thus the time-dependent gas motions are of greatest importance late in the motor burn, and the strongest interactions with the spacecraft motion would be expected to occur just before the end of burn. This result strengthens the suggestion that the gas oscillations are closely related to the mechanism that forces the spacecraft coning.

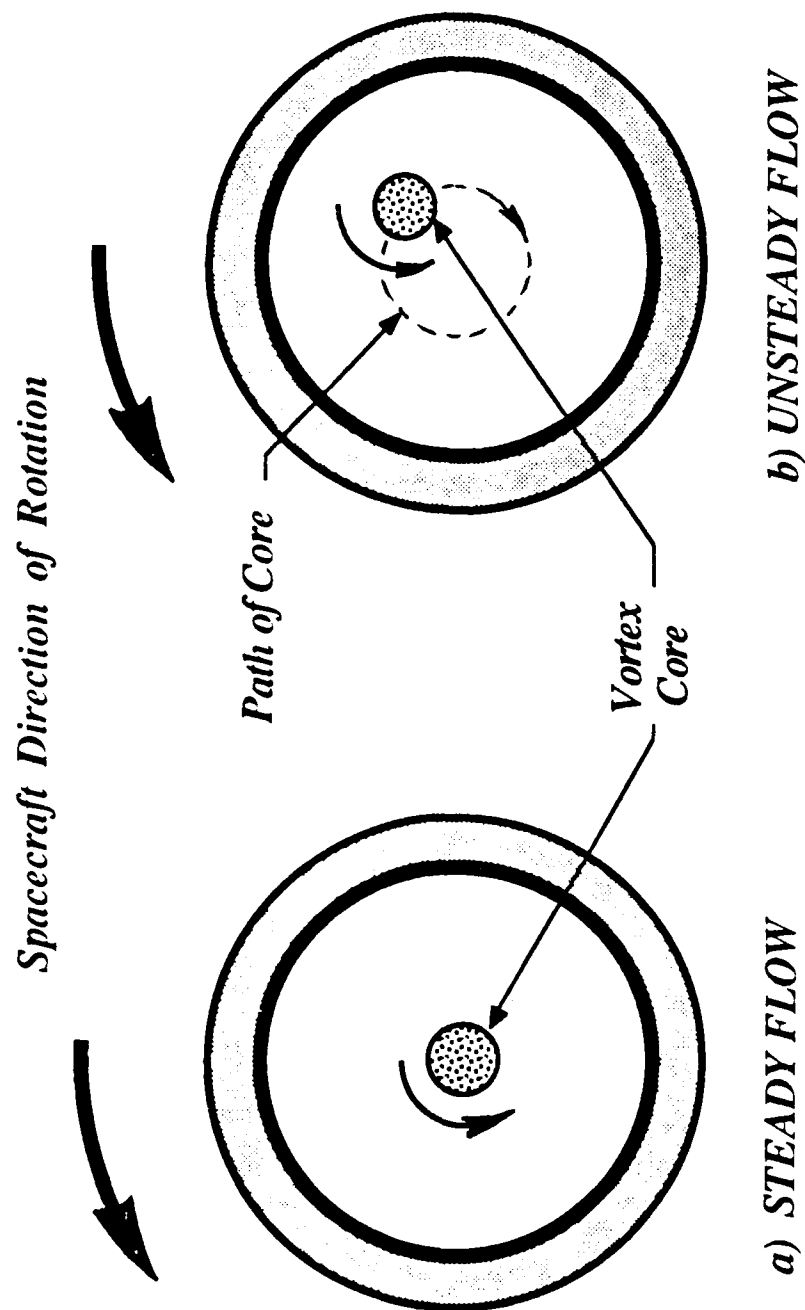


Figure 41. Flow in the Nozzle Entrance

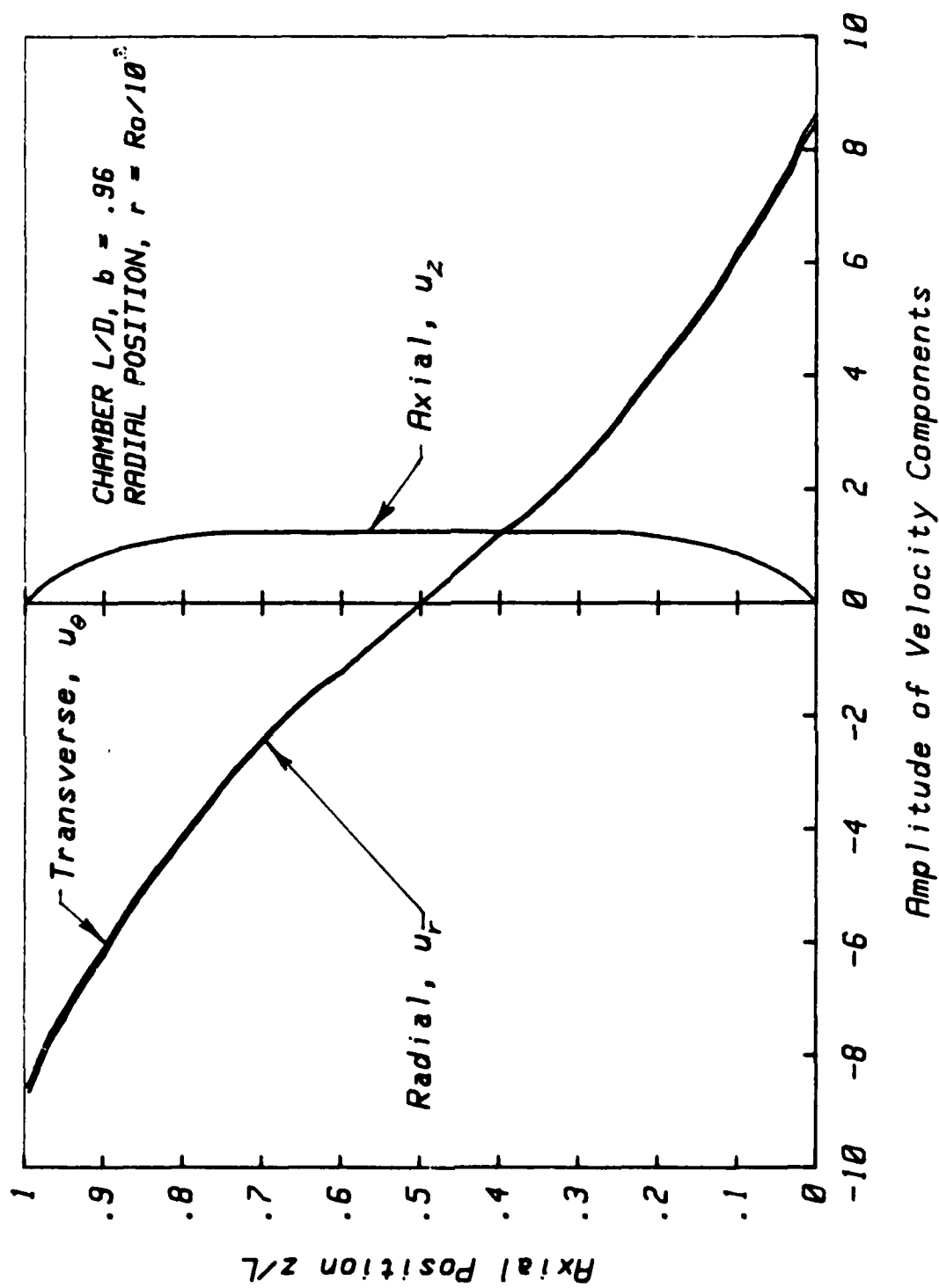


Figure 42. Axial Distribution of Perturbation Velocity Amplitudes

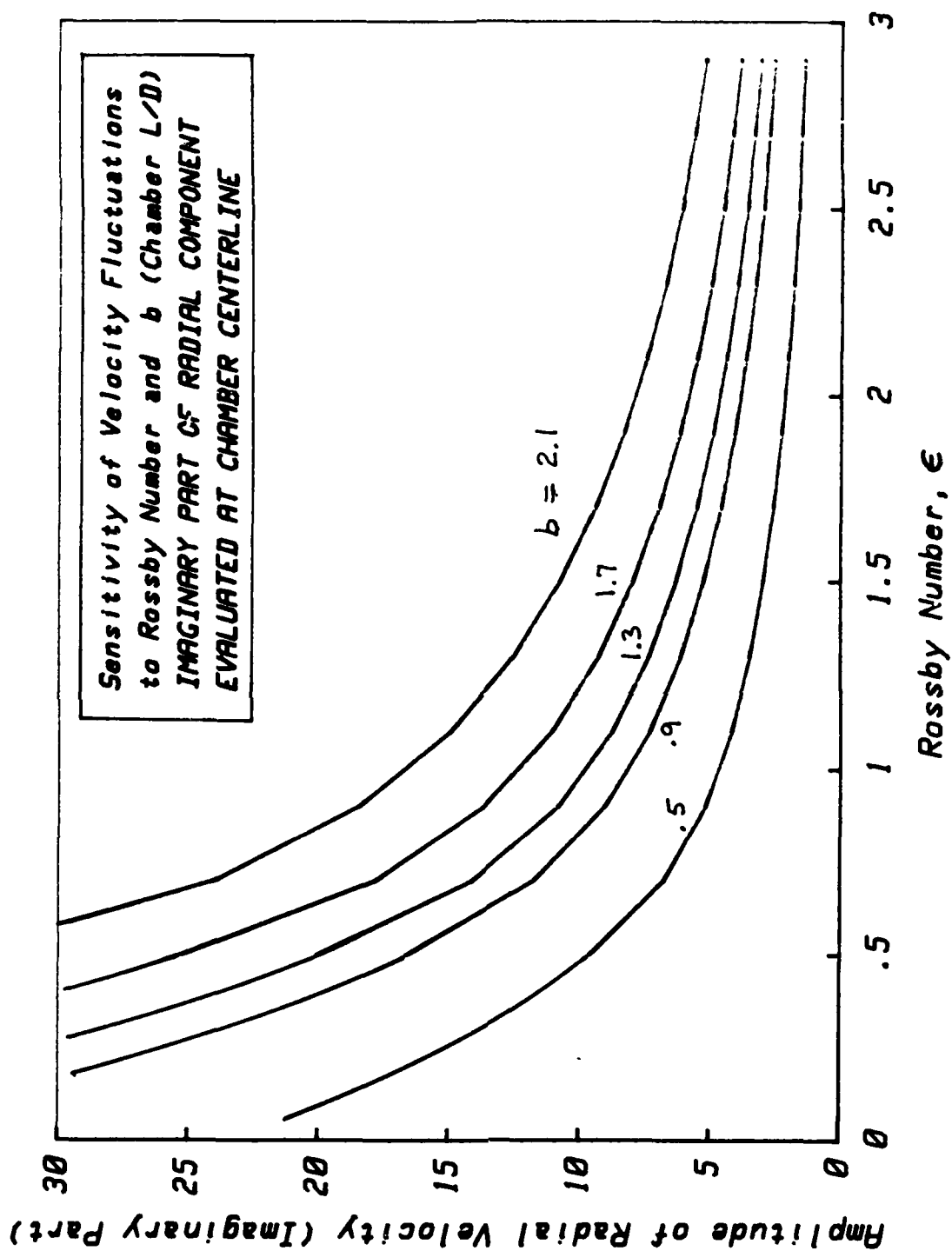


Figure 43. Effect of Rossby Number on Radial Perturbation Velocity

7.0 EFFECTS OF GASDYNAMIC TORQUES

The detailed description of the spinning rocket internal flow field constructed in the last section makes possible an estimate of the reaction torques on the motor chamber and the resulting spacecraft nutation. What is required first is the detailed evaluation of the unsteady moments identified in Groups 3 and 4 of Table 3. Once these results are in hand, it will be possible to determine their effect on the motion of the vehicle, and their influence on the coning instability can be properly assessed. The results are then incorporated into a comprehensive simulation program that estimates the system stability as a function of time throughout the motor run. The Euler differential equations are integrated using the gasdynamic disturbing moments and the jet damping torque. Account is taken of geometry and mass property variations with time. This program will be used in Section 8 to compare the results of the analysis to actual flight telemetry data.

Each moment integral is evaluated in the order shown in Table 3. It will become apparent that each contribution is proportional to the perturbation angular velocity ω' since the gas oscillations are driven by chamber motion. This should not be surprising in view of the similar result for the Group 2 moment, the jet damping torque. For later convenience in assessing the vehicle dynamic response to each component, the moments are expressed in the rotating cartesian spacecraft coordinates. The integrals are, however, carried out in polar form since most expressions inside the integrals are best evaluated in cylindrical polar form to take advantage of the circular symmetry of the assumed chamber geometry. For ease of identification, the four integral terms from Table 3 remaining to be evaluated are labeled with subscripts. For example, M_{31} refers to the first moment component in Group 3.

7.1 EVALUATION OF GROUP 3 MOMENTS

The two terms in Group 3 (See Table 3) represent the interaction of the unsteady gas motions with the mean chamber motion. The Coriolis term, M_{31} is the direct analogue to the similar term involving the mean flow velocity which leads to the jet damping moment. It is required to evaluate

$$M_{31} = - \int_V 2\mathbf{r} \times (\boldsymbol{\Omega} \times \mathbf{u}') \rho \, dV, \quad (101)$$

where \mathbf{r} is the position vector locating any gas particle in the motor relative to the spacecraft instantaneous center of mass. $\boldsymbol{\Omega}$ is the unperturbed vehicle spin angular velocity vector, which will be always assumed to point in the positive z direction (forward) as it does in the actual flight vehicle. Thus the direction of rotation is counterclockwise as viewed aft. The velocity fluctuation \mathbf{u}' is represented by the

Fourier series in the inertial modes developed in the last section. Thus

$$\mathbf{u}' = \sum_m \mathbf{B}_m Q_m \exp(\beta t) \quad (102)$$

with

$$Q_m = [i f_1 \mathbf{e}_r + f_2 \mathbf{e}_\theta + i f_3 \mathbf{k}]_m. \quad (103)$$

The subscript m (or, occasionally, n) stands for the set of three mode integers l, m, n as used previously. Functions f_1 , f_2 , and f_3 that describe the velocity components for a given mode are defined in Section 6 (equations (73)). Inserting these expressions into equation (101) and carrying out the integration over the chamber volume, one finds

$$\mathbf{M}_{31} = \sum_m D_m [(B_m^{(i)} - \omega_y B_m^{(r)}) \mathbf{i} + (\omega_x B_m^{(r)} + \omega_y B_m^{(i)}) \mathbf{j}] \quad (104)$$

where the superscripts (i) and (r) refer to the real and imaginary parts of the mode amplitudes. ω_x and ω_y represent the cartesian components of the angular velocity in the lateral plane, that is the pitch and yaw rate perturbations. It should be noticed that the all-important phase relationship between the lateral angular velocity perturbation and the torque is set by the gas response. No assumption is being made regarding the direction of the reaction moment vector relative to the vehicle wobbling motion as expressed by the vector $\omega_{xy} = \omega_x \mathbf{i} + \omega_y \mathbf{j}$. It is clear that the Coriolis moment velocity vector \mathbf{M}_{31} is not necessarily parallel to ω_{xy} . The contribution of each modal component to the reaction moment is set by function D_m , which, for a cylindrical chamber, is given by

$$D_m = (2b/n\pi)^2 [4\pi J_1(\xi) / (2 - \lambda_m)] \quad (105)$$

where all notation is compatible with that introduced in Section 6. Before evaluating this expression further, all of the Group 3 and 4 contributions will be collected for convenience. It will be shown that the Coriolis term (104) is much less important than the angular momentum flux term \mathbf{M}_{41} that will be discussed presently.

The remaining Group 3 term represents the integrated effect of the time-dependent acceleration of fluid particles in response to the chamber motion. Thus one must evaluate the integral

$$\mathbf{M}_{32} = - \partial/\partial t \int_V (\mathbf{r} \times \mathbf{u}') \rho dV. \quad (106)$$

Following the same procedure used for M_{31} ,

$$M_{32} = \sum_m F_m \left[-(\omega_x B_m^{(r)} + \omega_y B_m^{(i)}) \mathbf{i} + (\omega_x B_m^{(i)} - \omega_y B_m^{(r)}) \mathbf{j} \right] \quad (107)$$

where

$$F_m = 2 \pi \beta \left[((2b/n \pi)^2 / (2 - \lambda_m) - 2/\lambda_m \xi) J_1(\xi) + J_0(\xi)/\lambda_m \xi \right]. \quad (108)$$

Again, it is clear that the reaction moment on the spacecraft is proportional to the lateral angular velocity perturbation, and exhibits components both normal to and parallel to the angular rate vector. It will be shown later that the parallel components either damp or drive the coning instability depending upon sense of the projection on the angular velocity vector. The normal components affect only the nutation frequency.

7.2 TORQUES DUE TO CONVECTION OF ANGULAR MOMENTUM

The Group 4 moments consist of two interactions representing convection of the mean flow angular momentum by the oscillatory flow and convection of inertial wave angular momentum by the mean flow. Evaluation of moment M_{41} is accomplished by integration over the nozzle exit. Since the nozzle entrance is not a solid boundary, the normal component of the local inertial velocity distribution is assumed to represent an appropriate estimate of the velocity fluctuation. Thus,

$$M_{41} = -\epsilon \int_S (\mathbf{r} \times \mathbf{U}) \rho \mathbf{u}' \cdot \mathbf{n} dS, \quad (109)$$

where $(\mathbf{r} \times \mathbf{U})$ is the mean flow angular momentum per unit mass represented mainly by the effect of the axial vortex flow, a feature which dominates the chamber mean flow field. One finds, after accounting for vortex stretching in the nozzle entrance,

$$(\mathbf{r} \times \mathbf{U}) = \frac{L_t}{\epsilon R_t^2} \mathbf{e}_r + r U_{\text{nozzle}} \mathbf{e}_\theta \quad (110)$$

where ϵ is the Rossby number and U_{nozzle} is the average axial mean flow at the nozzle entrance. Evaluation of the surface integral over the nozzle yields

$$M_{41} = \sum_n \left[[\omega_x (H_n^{(r)} B_n^{(r)} - H_n^{(i)} B_n^{(i)}) + \omega_y (H_n^{(r)} B_n^{(i)} + H_n^{(i)} B_n^{(r)})] \mathbf{i} + [\omega_x (-H_n^{(r)} B_n^{(i)} - H_n^{(i)} B_n^{(r)}) + \omega_y (H_n^{(r)} B_n^{(r)} - H_n^{(i)} B_n^{(i)})] \mathbf{j} \right] \quad (111)$$

The amplitude functions H_n are

$$\begin{aligned} H_n^{(r)} &= \epsilon m(n\pi/2\xi\lambda_n b) \sin(n\pi L_s/2b) [J_0(\xi R_t) - 2J_1(\xi R_t)/\xi R_t] \\ H_n^{(i)} &= (n\pi^2/2\xi\lambda_n b) \sin(n\pi L_s/2b) [L_t(J_0(\xi R_t) - 1)/R_t^2] \end{aligned} \quad (112)$$

where R_t is the radius of the nozzle entrance and L_s is the submergence as shown in Figure 23. L_t locates the nozzle relative to the spacecraft center of mass. The presence of the nozzle inlet radius in the denominators of several terms in the amplitude expressions (112) is noteworthy. R_t becomes rapidly smaller during the motor burn since all lengths are made dimensionless with respect to the chamber radius, which grows larger as propellant is consumed. Thus terms with R_t in the denominator increase in importance as burnout is approached.

It is also important to understand the origins of the net unbalanced torque represented by Equation 111. Since $(\mathbf{r} \times \mathbf{U})$ is steady, it is not immediately obvious that a net time-dependent torque can result from the integration. The key to understanding M_{41} is to realize that the direction of the axial component of \mathbf{u}' , which enters the calculation in the dot product with the unit normal to the nozzle entrance plane, changes phase across the axis. That is, two gas particles at equal radii on opposite sides of the nozzle entrance have axial fluctuating velocities out of phase by 180° . The largest torque contribution (the one with the square of the nozzle radius in the denominator) represents the pumping of lateral angular momentum carried by the axial vortex. As Equation 110 shows, the angular momentum per unit mass in the nozzle entrance contains a radial component generated by the circumferential velocity induced by the vortex. Since the radial angular momentum component also changes sign across the axis, its product with the $\mathbf{u}' \cdot \mathbf{n}$ term gives rise to a net moment contribution in the integration. A simple physical explanation for this torque is that it represents the reaction to the "stiffness" of the vortex as it resists the lateral twisting imposed by the axial velocity fluctuations. Thus, this torque contribution is, in effect, a gyroscopic reaction.

For reasons already indicated, it is expected that transport of lateral angular momentum introduced into the flow by the rocking motions of the spacecraft could represent a potentially important destabilizing influence. Moment M_{42} represents this effect. The traveling wave motions generated in the gas flow by the coning are carried out of the system by the mean flow. Conservation of angular momentum dictates that there be a corresponding reaction moment on the spacecraft given by

$$M_{42} = -\epsilon \int_S (\mathbf{r} \times \mathbf{u}') \rho \mathbf{U} \cdot \mathbf{n} \, dS, \quad (113)$$

Again expressing \mathbf{u}' in Fourier series form, the time-dependent angular momentum vector anywhere in the chamber is

$$(\mathbf{r} \times \mathbf{u}') = \sum_n B_n \exp(\beta - ik\theta) [(L_1 f_2) \mathbf{e}_r - i(r f_3 + L_1 f_1) \mathbf{e}_\theta + (r f_2) \mathbf{e}_z] \quad (114)$$

where functions f_1 , f_2 , and f_3 are given in equation (73). Integrating over the nozzle entrance gives the moment due to unsteady angular momentum convection out of the system. The result is

$$M_{42} = -\epsilon \sum_n A_n [[B_n^{(r)} \omega_x + B_n^{(i)} \omega_y] \mathbf{i} + [B_n^{(r)} \omega_y - B_n^{(i)} \omega_x] \mathbf{j}], \quad (115)$$

where amplitude function A_n is

$$A_n = \dot{m} \left[L_1 \cos(n\pi L_s/2b) J_1(\xi R_t)/R_t(2 - \lambda_m) + \right. \\ \left. + (n\pi/2\lambda_m \xi b) \sin(n\pi L_s/2b) [2J_1(\xi R_t)/\xi R_t - J_0(\xi R_t)] \right] \quad (116)$$

R_t is the entrance radius and L_s is the submergence of the nozzle into the chamber as defined in Figure 23. L_1 is the distance from the nozzle entrance to the vehicle center of mass. The velocity distributions shown in Figures 32 and 40 give a clear indication of the vortex stretching effect as the gas particles pass into the nozzle. The reaction torque M_{42} of Equation (116) should increase with time during motor operation because the center of mass moves forward and therefore, L_1 , the main lever arm, increases with time. Note also that the torque depends directly on the motor mass flow rate. The disturbance generated from the flux of lateral angular momentum is more important in larger motors with accompanying increase in the mass flow rate. The vortex pumping term in M_{41} described in the last paragraph also exhibits a similar dependence on L_1 .

Finally, account should be taken of the influence of the nozzle flow field on the angular momentum flux. It is appropriate to assume that the residence time of gas particles in the nozzle is so short compared to the period of coning oscillation that only small modification of the fluctuating angular momentum component occurs in the nozzle. This is one of several elements of the spinning rocket flow problem requiring additional study³¹. The situation is complicated by the dominance of compressibility effects in the nozzle. An approximate correction for nozzle effects is described later.

7.3 CHARACTERISTICS OF GAS DYNAMIC DISTURBING MOMENT

It is useful to collect all the gas dynamic torques in to a single expression showing the dependence on the angular velocity components. If this is done, the net gas dynamic disturbing moment can be expressed in vector form as

$$\mathbf{M}_H = \mathbf{M}_{31} + \mathbf{M}_{32} + \mathbf{M}_{41} + \mathbf{M}_{42} = M_x \mathbf{i} + M_y \mathbf{j} \quad (117)$$

where the pitch and yaw components of the torque can be written as

$$\begin{cases} M_x = K_1 \omega_x + K_2 \omega_y \\ M_y = K_1 \omega_y - K_2 \omega_x \end{cases}$$

and

$$\begin{aligned} K_1 &= \sum_m [B_m^{(r)}(-\varepsilon A_m + H_m^{(r)}) + B_m^{(i)}(D_m + F_m - H_m^{(i)})] \\ K_2 &= \sum_m [B_m^{(i)}(-\varepsilon A_m + H_m^{(r)}) - B_m^{(r)}(D_m + F_m - H_m^{(i)})] \end{aligned} \quad (118)$$

Equation (117) emphasizes the important fact that the net gasdynamic disturbing torque \mathbf{M}_H is proportional to the nutation angular velocity perturbation. \mathbf{M}_H represents a linear response to the vehicle wobbling. The spacecraft and the combustion gases contained within the rocket motor constitute a closed loop, self-excited oscillatory system. Figure 44 shows the orientation of \mathbf{M}_H relative to the nutation angular velocity perturbation vector ω' and the jet damping moment \mathbf{M}_J . In order for the system to exhibit unstable growth, it is necessary that \mathbf{M}_H have a component in the same direction as ω' that is larger than the magnitude of the jet damping. The magnitude of \mathbf{M}_H and its phase angle ϕ relative to ω' can be expressed in terms of the functions K_1 and K_2 as

$$\begin{aligned} M_H &= |\mathbf{M}_H| = \sqrt{K_1^2 + K_2^2} \omega_{xy} = K_H \omega_{xy} \\ \phi &= \tan^{-1} \left[\frac{K_2}{K_1} \right] \end{aligned} \quad (119)$$

where ω_{xy} is the magnitude of the projection of the angular velocity perturbation on the pitch-yaw plane as before. This plainly shows that the gasdynamic moment

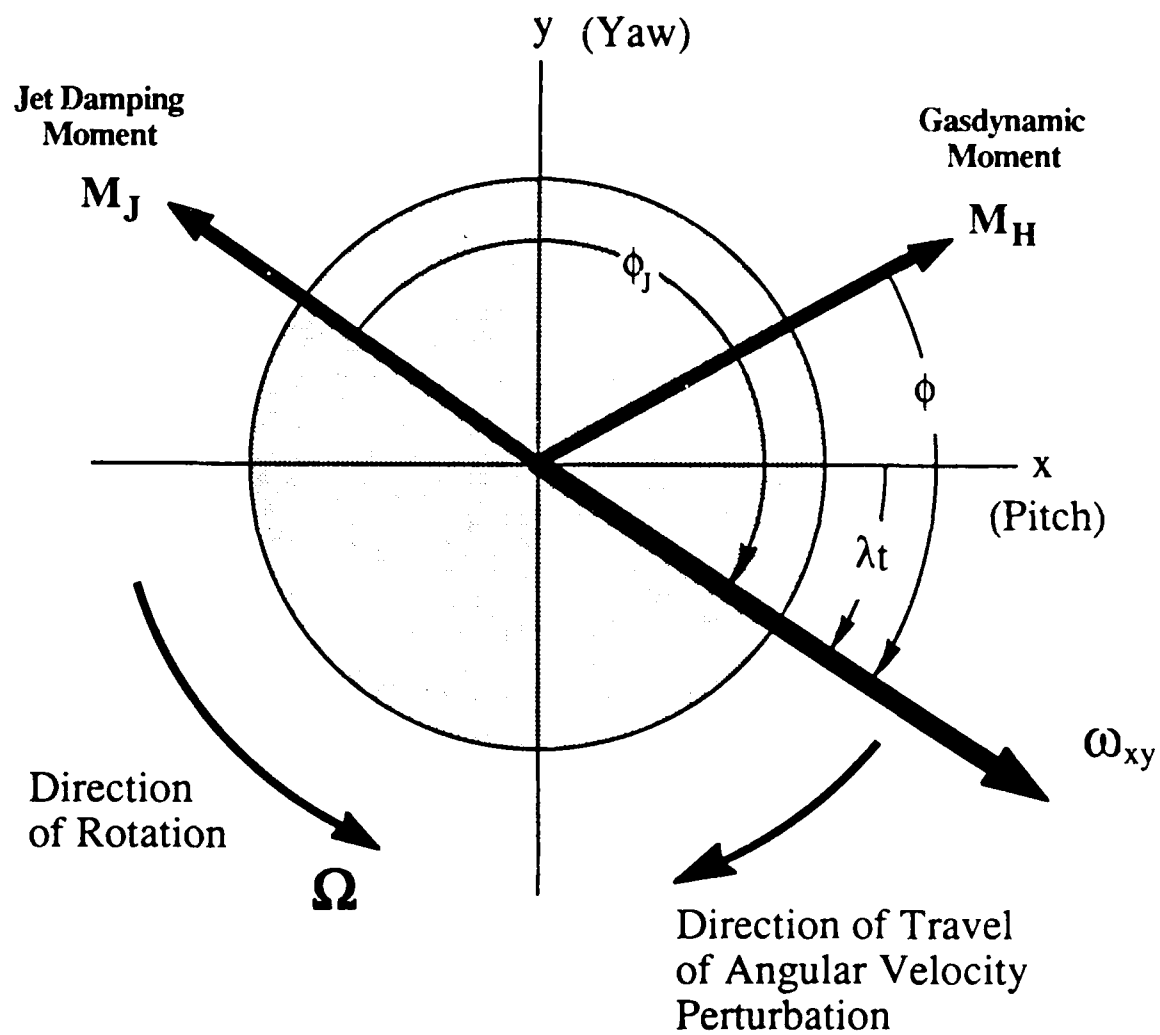


Figure 44. Orientation of Disturbing Moments Relative to Nutation Angular Velocity

is directly proportional to the magnitude of the wobbling amplitude, ω_{xy} . Thus, the necessary conditions for nutation instability are:

$$\begin{aligned} M_H \cos \phi &> 0 \\ M_H \cos \phi &> |M_J| \end{aligned} \quad (120)$$

Or, using the results of the jet damping expression in equation (43), the condition for instability can be expressed by the simple inequality

$$K_1 = K_H \cos \phi > -K_J, \quad (121)$$

where K_J is always a negative quantity as shown in Section 5.

It is not possible to determine by inspection of the numerous expressions superimposed to form K_1 and K_2 whether these conditions for instability can be met. Their complexity also makes it difficult to determine by inspection which geometric and flow field parameters control the system stability; this is best done by numerical means as described in Section 8. However, a few key features can be pointed out at this juncture. Equation (116), which describes one of the main contributions to M_H shows the primary importance of the location of the nozzle relative to the vehicle mass center as shown by the linear dependence on L_t . Also, the direct dependence on the mass flow rate m is indicated. It should be noted that the jet damping factor K_J depends on these parameters in the same manner.

7.4 CALCULATION OF NUTATION GROWTH RATE

All elements of the spacecraft system description required for a detailed nutation stability assessment are now available. This is somewhat superfluous, since the conditions for stability have already been deduced by inspection of the moments. However, it is appropriate to verify the interpretations leading to the stability inequalities of the last subsection. Also, expressions for the coning growth rate can be found, which are useful in comparisons to the experimental data from spacecraft telemetry.

The spacecraft dynamics model as set forth in Section 3 can be employed to find the nutation growth rate. The lateral angular motion is described by means of Euler's equation, which is best expressed in the compact form

$$d\omega / dt - \beta_J \omega = \delta(M). \quad (122)$$

The spacecraft angular velocity vector, ω , and the disturbing moment are

represented in complex form by

$$\omega = \omega_x - i \omega_y \quad (123)$$

$$M = M_x - i M_y$$

as before (see the development leading to equation (35)). M_x and M_y are now interpreted to be the gasdynamic moment components as defined in equation (117). The effect of jet damping is included in the complex frequency β_J for convenience, since the jet damping moment vector is always parallel to the lateral angular velocity vector, and has the opposite sense. That is,

$$\beta_J = (\alpha_J + i \lambda_s) \quad (124)$$

where α_J is the jet damping growth rate

$$\alpha_J = \delta K_J, \quad (125)$$

which is always a negative (stabilizing) quantity. Equation (44) gives an approximate expression for the jet damping factor K_J . Also, it is appropriate to write in complex form

$$\delta M = \delta M_H \exp(i \phi) = \delta K_H \omega, \quad (126)$$

where ϕ is the phase angle between the perturbing moment and the spacecraft perturbation angular velocity vector as defined in equation (119). Notice that both the gasdynamic driving and the jet damping are proportional to the moment scaling parameter δ defined earlier as

$$\delta = M_O / I_1 \omega_z^2 = \rho_O R_O^4 v_O / I_1 \omega_z.$$

Thus equation (122) becomes

$$d\omega / dt - \beta_J \omega = \delta K_H \omega, \quad (127)$$

which gives for the rate of change of the lateral angular velocity:

$$\begin{aligned} d\omega / dt &= [\beta_J + \delta K_H] \omega \\ &= [(\alpha_J + \delta K_1) + i (\lambda_s + \delta K_2)] \omega. \end{aligned} \quad (128)$$

Equation (128) is easily solved if it is assumed that the spacecraft and motor parameters change slowly with time. Thus the approximate solution is

$$\omega = \omega_0 \exp [(\alpha_j + \delta K_1) + i(\lambda_s + \delta K_2)] t \quad (129)$$

where ω_0 is the instantaneous amplitude of the lateral angular rate. This indicates that the instantaneous growth rate of the lateral angular velocity perturbation is

$$\alpha = (\alpha_j + \delta K_1) = (\delta K_j + \delta K_1), \quad (130)$$

which is equivalent to equation (121). That is, the growth rate is positive, indicating instability, whenever K_1 is greater than $-K_j$.

There is also a frequency modification generated by the gasdynamic torque. The instantaneous vehicle wobbling frequency becomes

$$\lambda = (\lambda_s + \delta K_2) \quad (131)$$

and λ_s is the free precession frequency as before. Since K_1 and K_2 are intimately related as can be seen in equation (118), it is to be expected that large growth rate changes seen in coning data should correlate with perturbations in the disturbance frequency. This in fact can be seen in the data. For example the frequency and growth rate plots for WESTAR V (see Figures (5) and (15)) show this clearly.

Before undertaking detailed spacecraft simulation computations, it is useful to determine the orders of magnitudes of the various terms. Figure 45 is a plot of the two dimensionless parameters δK_1 and δK_j as functions of time evaluated for the WESTAR spacecraft configuration. The computational algorithm is described in the next section. The same functions are plotted in dimensional form in Figure 46 so that the units are (ft-lb)/(rad/sec). Multiplying by the value of the perturbation angular velocity present in the system at a corresponding time gives the magnitude of the internally generated torques acting on the system. At the end of the burn, the observed angular velocity disturbance was about 24 degrees/sec (0.42 radians/sec). Thus at 85 seconds after ignition the jet damping torque is approximately - 40 ft-lb compared to the gasdynamic moment of 84 ft-lb. Notice that the jet damping dominates early in the motor burn. Then about midway through the burn the system becomes unstable. The growth rate (dimensional) at 85 seconds is $\alpha = \omega_z(\delta K_1 + \delta K_j) = 0.30 \text{ sec}^{-1}$. This agrees closely with the observed behavior described in detail in Section 2. (Note that conversion from dimensionless to dimensional form of growth rates and frequencies is accomplished by multiplying by the spin rate Ω).

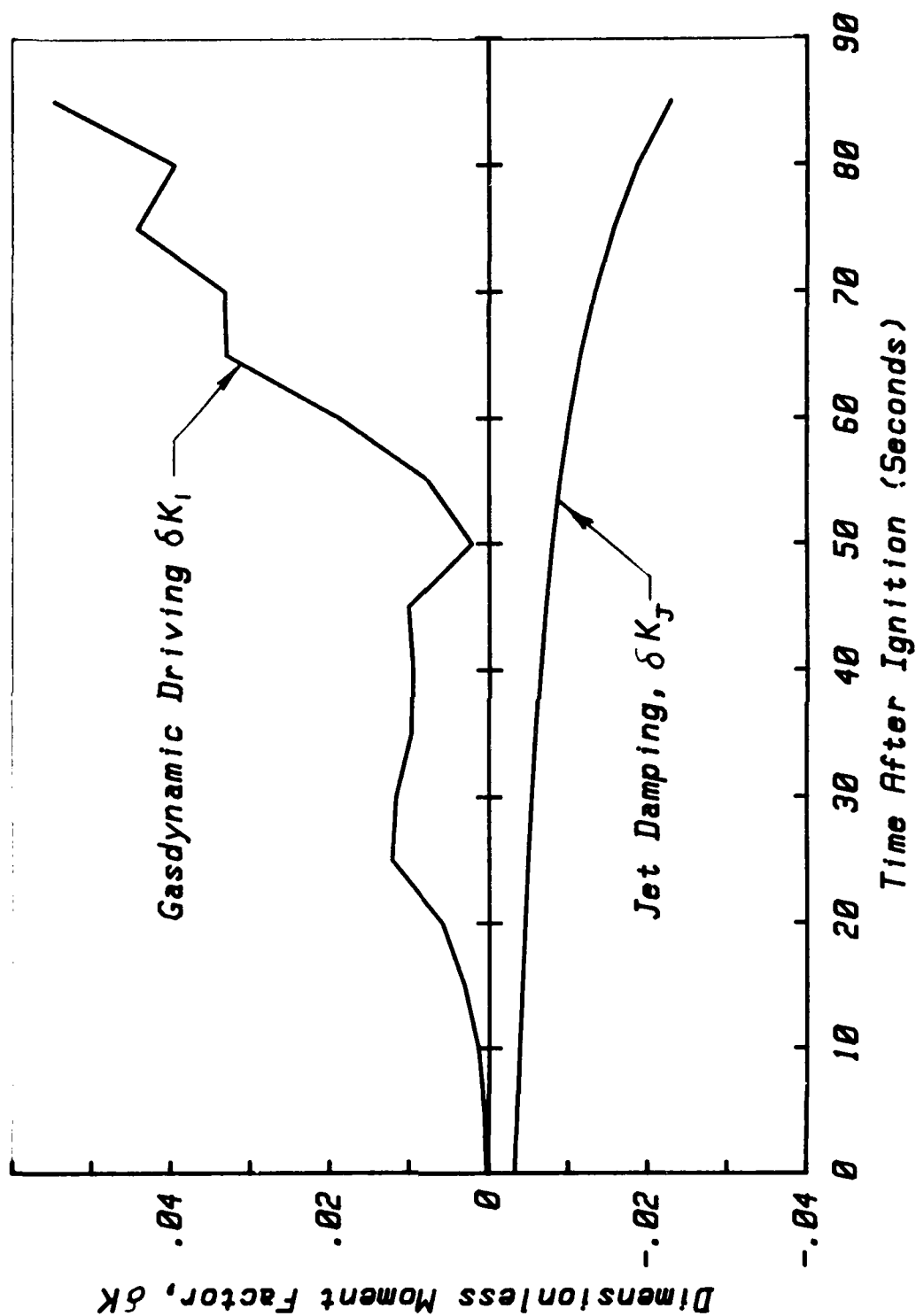


Figure 45. Dimensionless Disturbing Moments (WESTAR V)

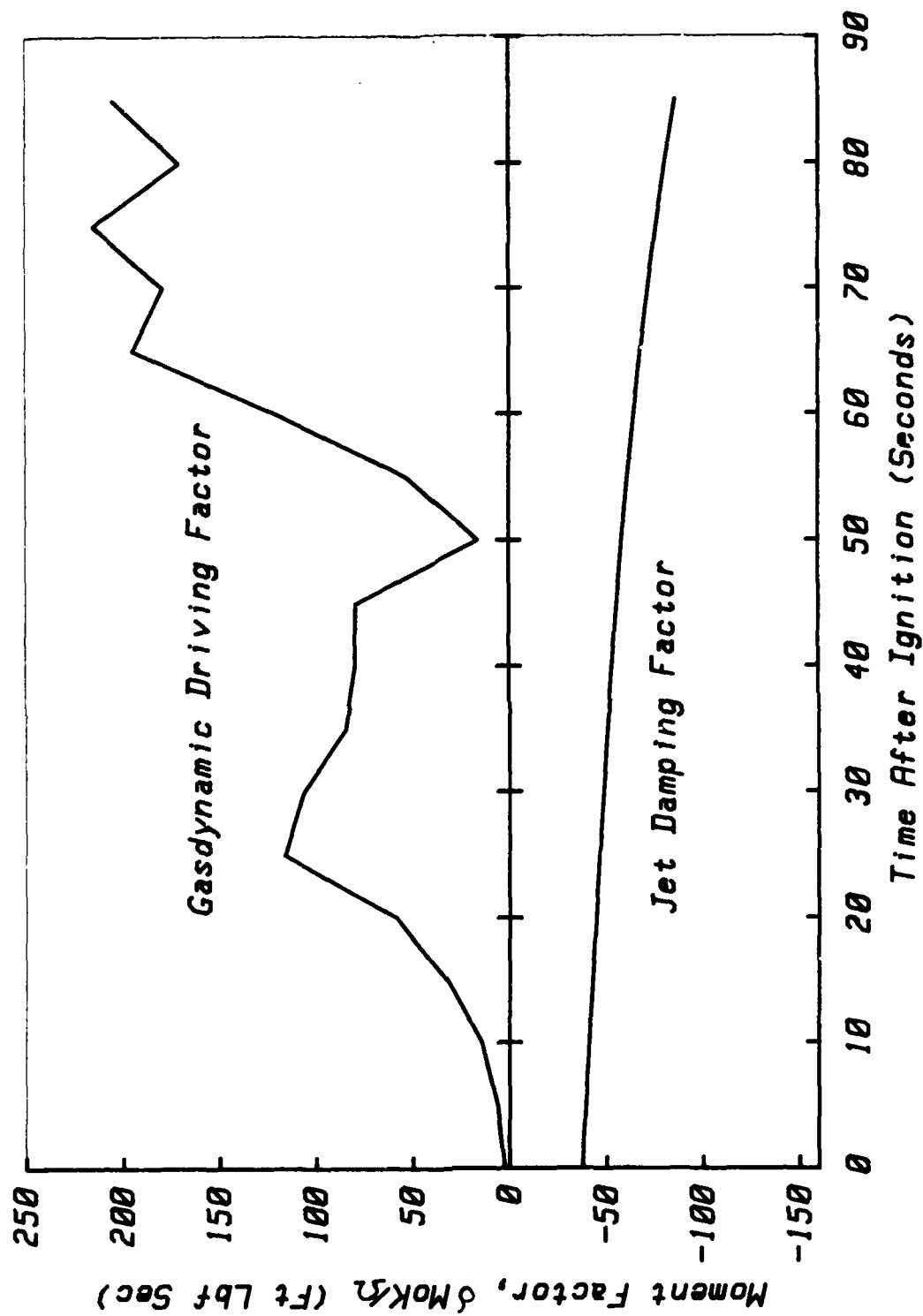


Figure 46. Disturbing Moment Factors (WESTAR V)

Other investigators have preferred to express the growth in terms of the "time-constant" in assumed exponential growth. It will be noted that the time constant is simply the inverse of the growth rate. Thus, the average time constant over the last 7 seconds of motor burn reported for Westar V of 5.27 seconds corresponds to a growth rate of 0.189. It would appear that the validity of the proposed gasdynamic instability mechanism is convincingly established.

Figure 47 shows the calculated instantaneous growth rate (dimensional) for the WESTAR V spacecraft. The results shown are in reasonable agreement with the measured growth rate data presented in Figure 15. Figure 48 shows how the phase angle varies through the motor run. The disturbing moment lags the perturbation angular velocity vector (see Figure 44) by an increasingly greater angle as the burn progresses. However, the magnitude of the disturbing torque is also rapidly growing during the last few seconds and the largest projection of M_H on ω occurs during this time period.

Figure 49 shows the predicted effect of the gasdynamic disturbance on the spacecraft nutation frequency. The results are in good qualitative agreement with the experimental frequency data shown in Figure 5.

The next section of the report carries the testing of the model further by applying it in the form of a detailed simulation of the spacecraft motion during the entire motor burn for a variety of vehicle motor combinations for which experimental data exist. Only in this way can a truly comprehensive test of validity be accomplished.

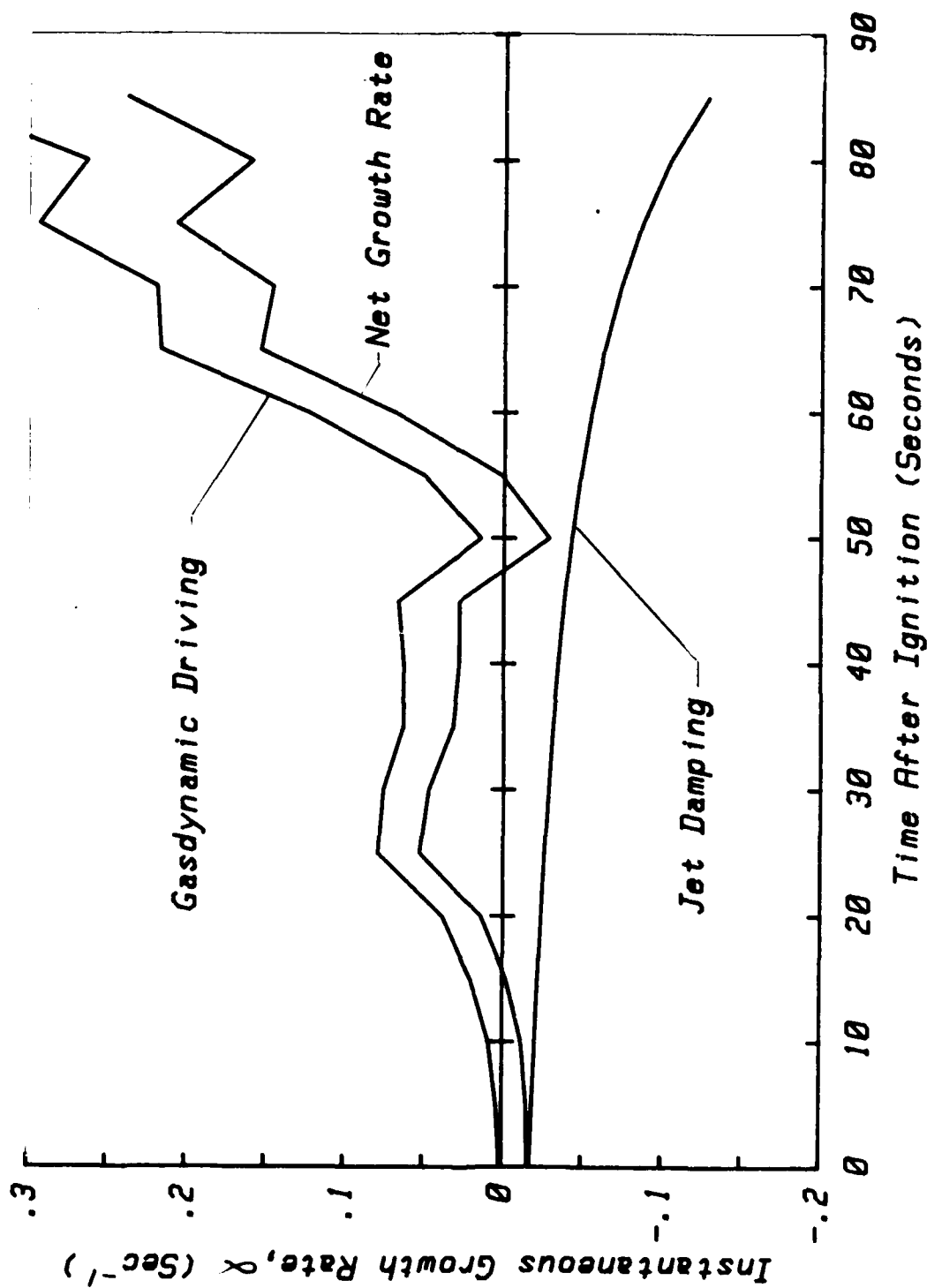


Figure 47. Instantaneous Growth Rate vs Time (WESTAR V)

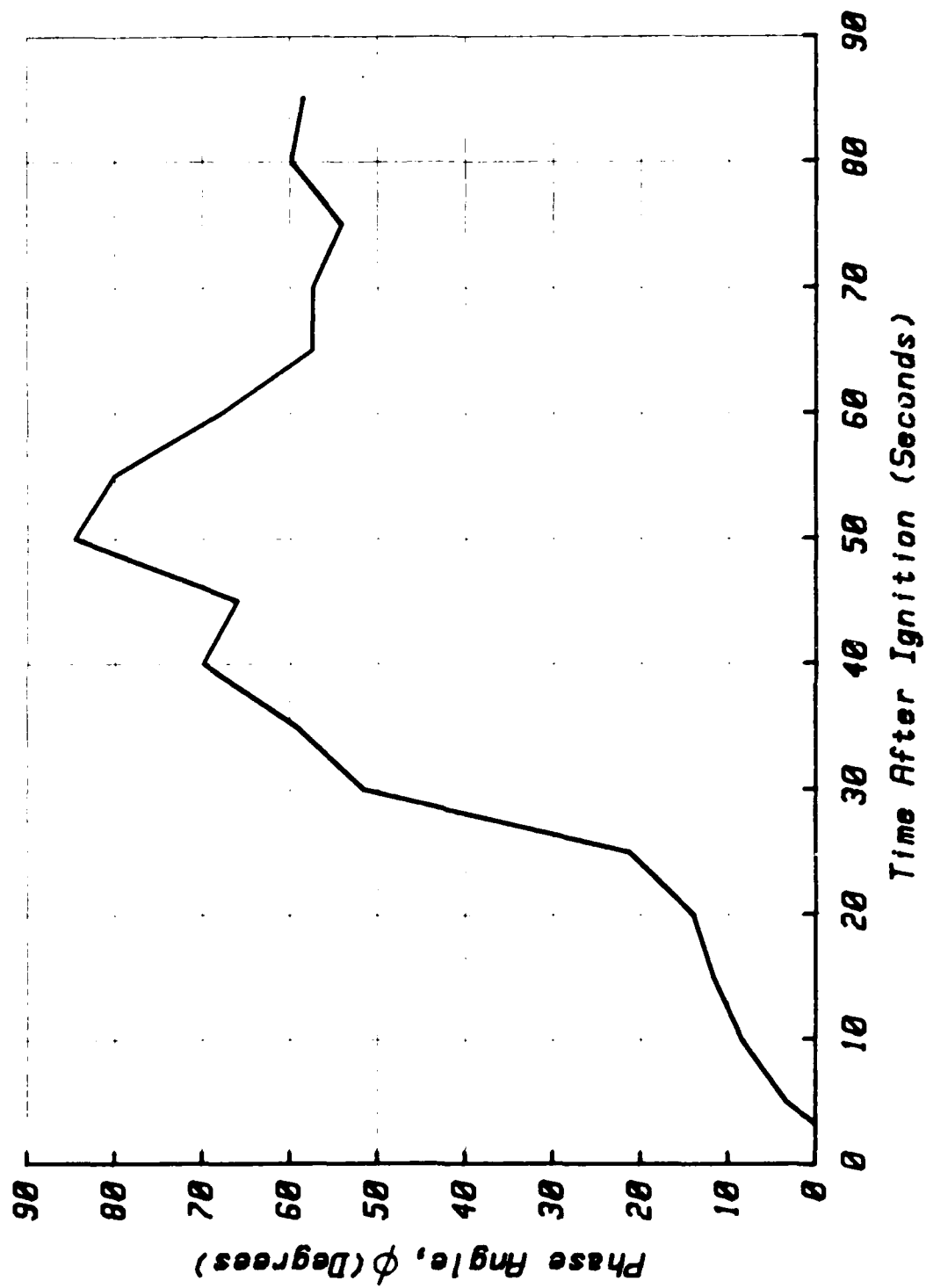


Figure 48. Phase Lag of Disturbing Moment (WESTAR V)

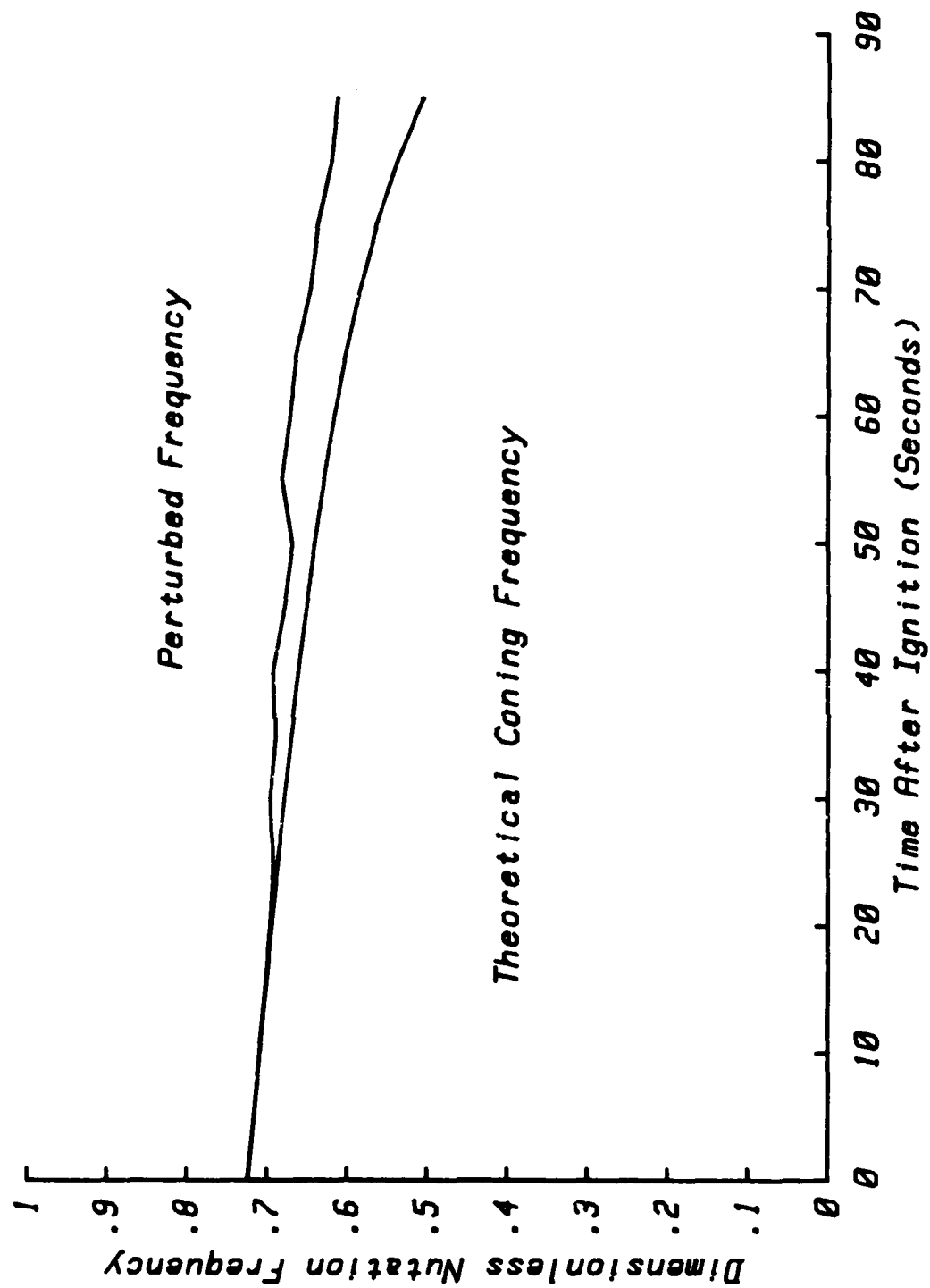


Figure 49. Effect of Gasdynamic Disturbance on Coning Frequency

8.0 COMPARISON OF ANALYTICAL RESULTS TO FLIGHT DATA

All elements of the spacecraft system description required for a detailed nutation stability assessment have now been assembled in a form that makes possible their application to actual vehicle configurations. The spacecraft dynamical model was set forth in Section 3. Sections 5-7 describe the calculation of the reaction moment acting on the spacecraft as a result of excitation of unsteady gas motions within the combustion chamber. In addition to the jet damping reaction moment, several other gasdynamic interactions were identified and analyzed. These are combined to form a complete spacecraft dynamic simulation. Since the geometry and spacecraft mass properties change during motor operation, the Euler equations are solved numerically. Figure 50 is a block diagram of the computer algorithm that integrates all the elements of the analysis and enables their application in the simulation of an actual spacecraft system.

In this section, the computational model is exercised strenuously to determine its ability to describe what actually takes place in flight. Attention is first directed to the PAM-D series of spacecraft, which used the STAR-48 motor. The WESTAR V system is used as a model for this set of vehicles, since a fairly detailed description of the spacecraft geometry and physical parameters was made available by McDonnell Douglas¹. The SGS-II (Stage 2) mission provides an excellent case to test the modeling of the other STAR-48 propelled vehicles, since its mass properties and geometry are quite different from the WESTAR V spacecraft properties. As described in Section 2, this vehicle was equipped with a nutation control device that was not activated during the motor run since the nutation rate did not exceed the $\pm 2^\circ$ deadband (see Figure 17). If the gasdynamics coning model cannot predict this major difference in behavior, resulting apparently only when spacecraft properties are changed without changes in motor parameters, then this would be cause to reject it as a viable representation of the nutation instability problem.

The analysis is also applied to two of the STAR 37E vehicles (IMP-H and TELESAT-C). None of the STAR 37E flights exhibited significant nutation instability. Again, if the model were to generate results not agreement with these observations, then it would be of questionable applicability.

As a final test of validity, the analytical results are applied to the geometry and motor parameters describing a PAM-DII spacecraft, the RCA-Ku-Band that exhibited coning in a recent shuttle satellite launch operation. Since there are extensive differences between this vehicle and the earlier PAM-D spacecraft, it is important to determine the capability of the analysis to properly reflect these differences in the coning behavior. Unfortunately, a detailed description of the RCA-Ku-Band coning data was not available for comparison to the predictions. It will be of interest later to determine how closely the analysis comes to being a truly

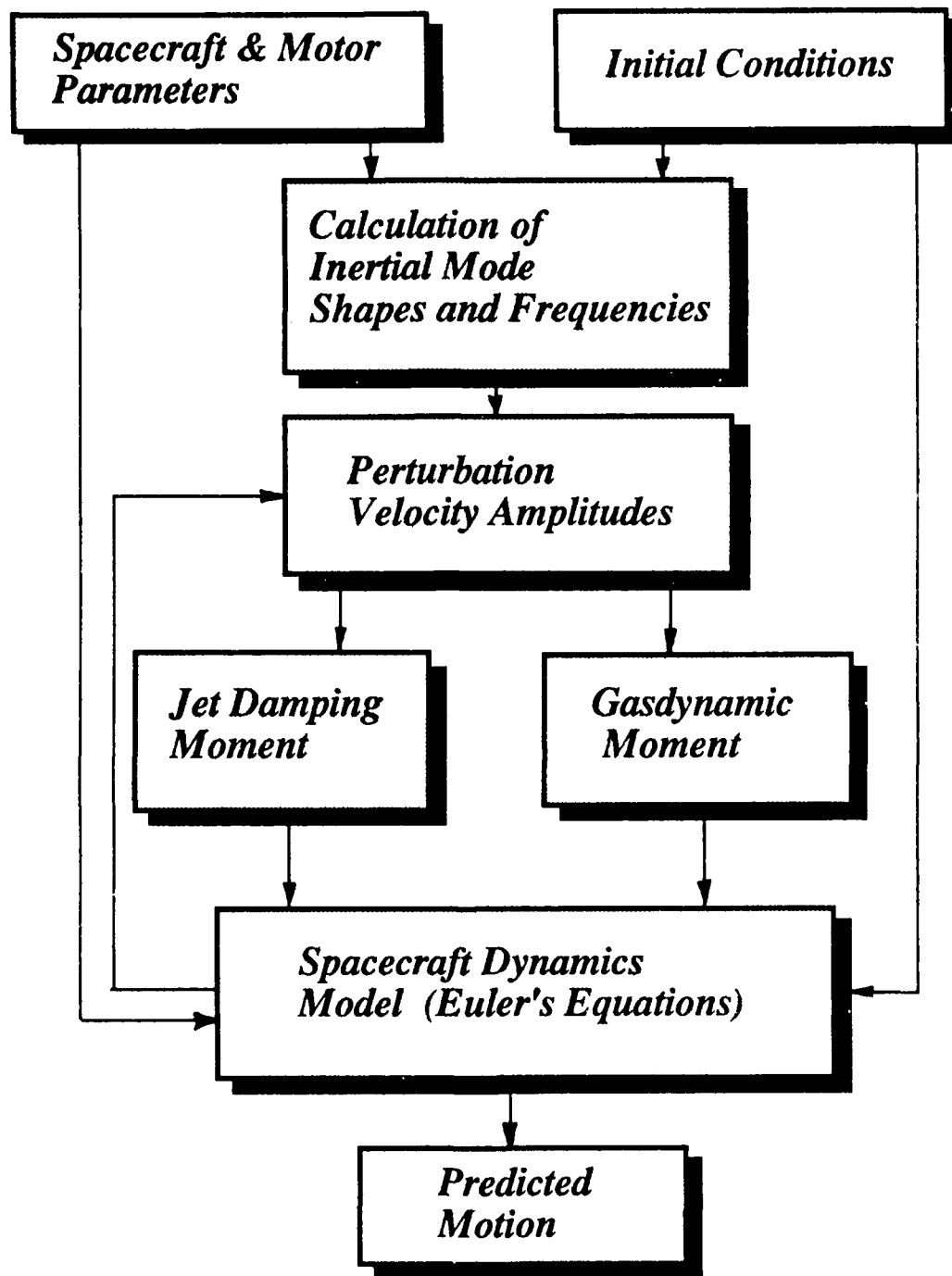


Figure 50. Block Diagram of Nutation Instability Algorithm

predictive tool. It is expected that some differences in coning growth rate and final cone angle should result because of the several assumptions and simplifications that were made in the calculations as described in Section 7. Also, since the final cone angle is sensitive to the initial amplitude of the coning rate at motor ignition and the exact length of motor burn, then differences between predicted and actual behavior are to be expected.

8.1 SIMULATION OF WESTAR V NUTATION OSCILLATIONS

To test the validity of the theory in a complete way, it is necessary to determine the spacecraft/gas combined motion over the entire period of motor operation. This means that the effects of slow changes in spacecraft and motor parameters must be accounted for; the Euler equations now have time-varying coefficients and numerical integration must be employed. Variations with time of spacecraft geometric parameters such as mass, moments of inertia, and center of mass location were represented by polynomial fits of the dynamical data supplied by McDonnell Douglas. The motor parameters were handled in similar fashion. The chamber radius and fineness ratio, mass flow rate, and nozzle throat area are all represented by polynomial fits of actual motor test data. Figures 51-53 show plots of some of these functions vs time. Figures 54 and 55 are graphs of the moment scaling parameter δ and the Rossby number ϵ vs time for the WESTAR V data. The Rossby number decreases with time, which implies that inertial wave energy is more likely to accumulate in the chamber near the end of the motor run with a resulting increase in interaction with the spacecraft dynamics. This is clearly indicated in Figure 54; the interaction moment scaling parameter increases rapidly during the latter part of the motor run. This is due both to the increase in motor size and to the decrease in spacecraft lateral moment of inertia. The explanation for the appearance of coning instability late in motor operation is obvious when the properly nondimensionalized dynamics problem is formulated. For emphasis, the behavior of the moment scaling parameter δ which determines the effectiveness of the fluid dynamics interactions (including the jet damping) in altering the spacecraft coning motion, clearly describes the time-history of the disturbing moment. Study of the manner in which δ changes during the motor run provides an approximate picture of the expected influence of the gasdynamic driving.

Figure 45 shows the dimensionless jet damping moment. It is clear that the magnitude of the jet damping also increases with time, mainly as a result of the increasing distance between the center of mass and the nozzle. The gasdynamic moments are dependent not only on the mass center location, but are also very dependent on motor combustion chamber radius, and nozzle area. The time-dependent gas interactions dominate near the end of the motor run. This effect is also indicated in Figure 47. Plots of the instantaneous jet damping growth rate and the net growth rate including the driving effects are superposed. The jet damping

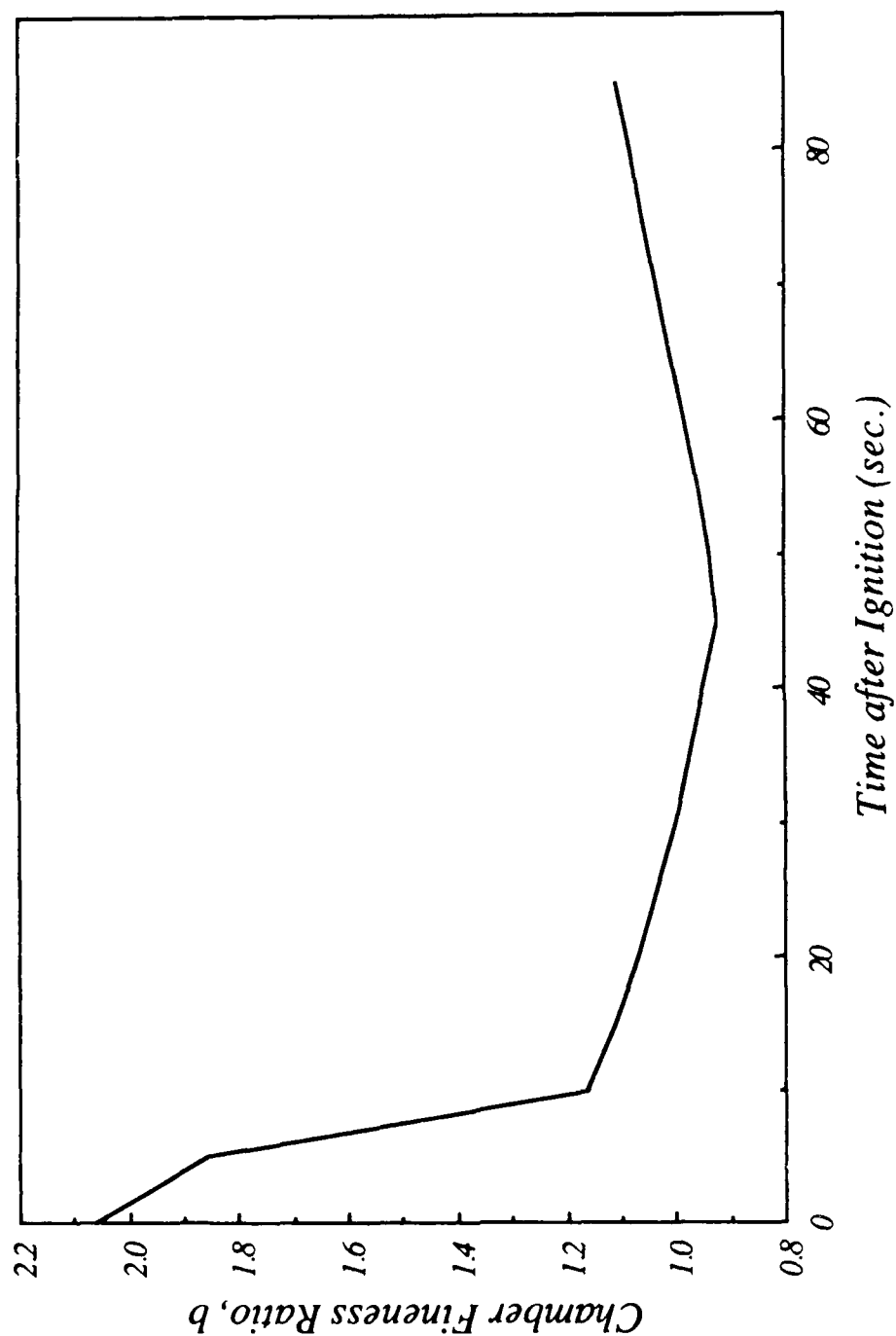


Figure 51. Chamber Fineness Ratio vs Time (STAR 48)

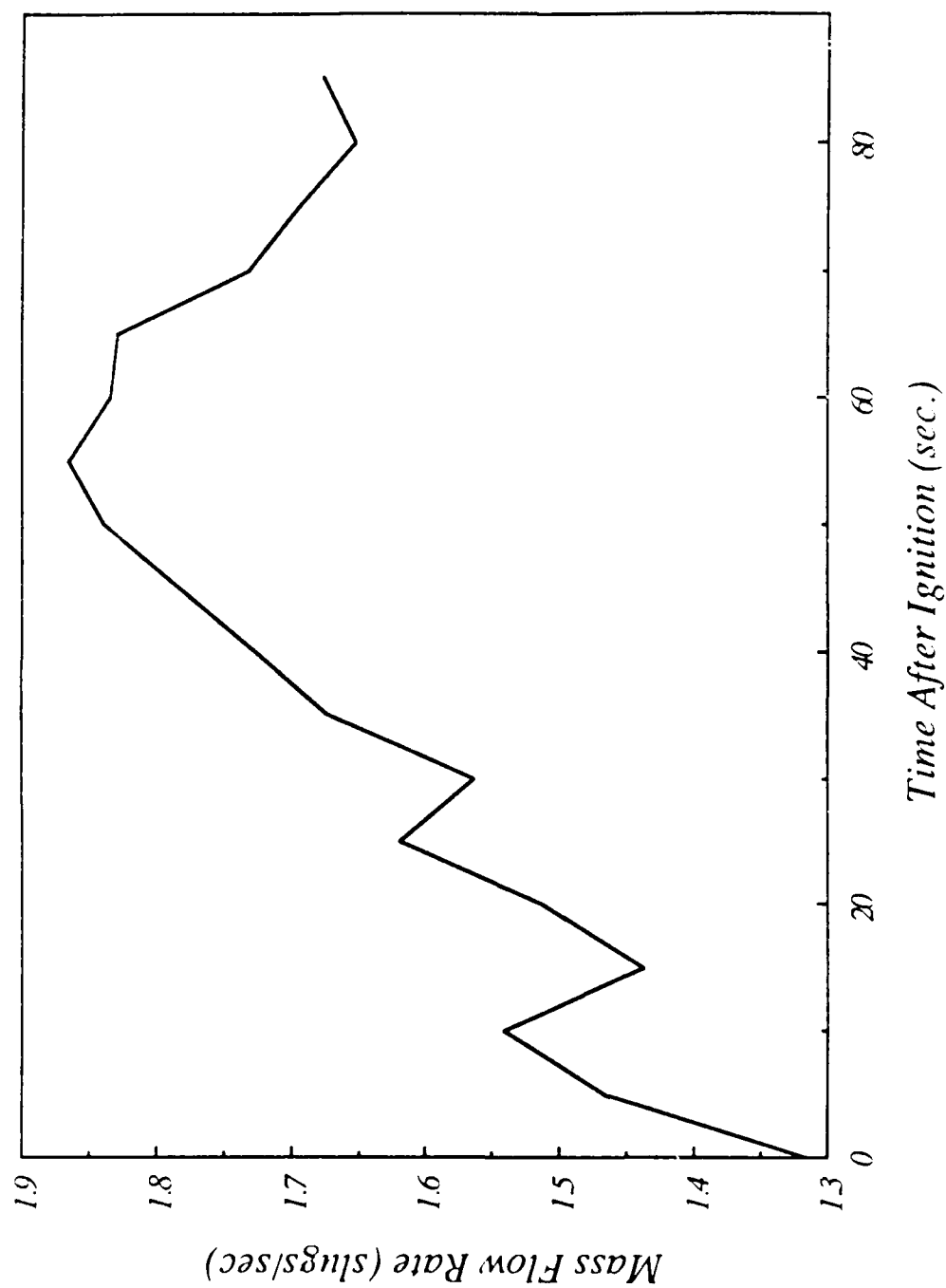


Figure 52. Mass Flow Rate vs Time (STAR 48)

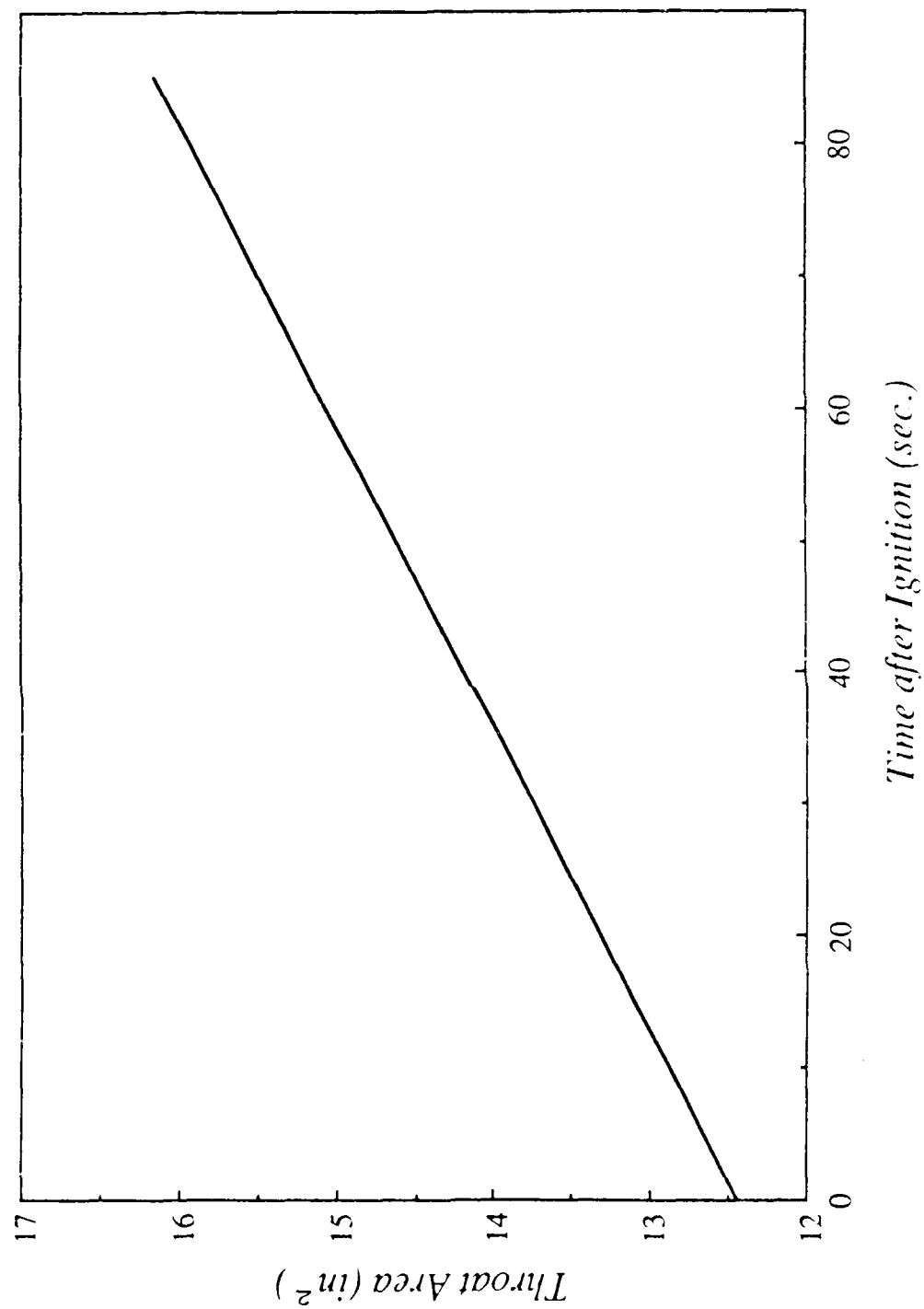


Figure 53. Nozzle Throat Area vs Time (STAR 48)

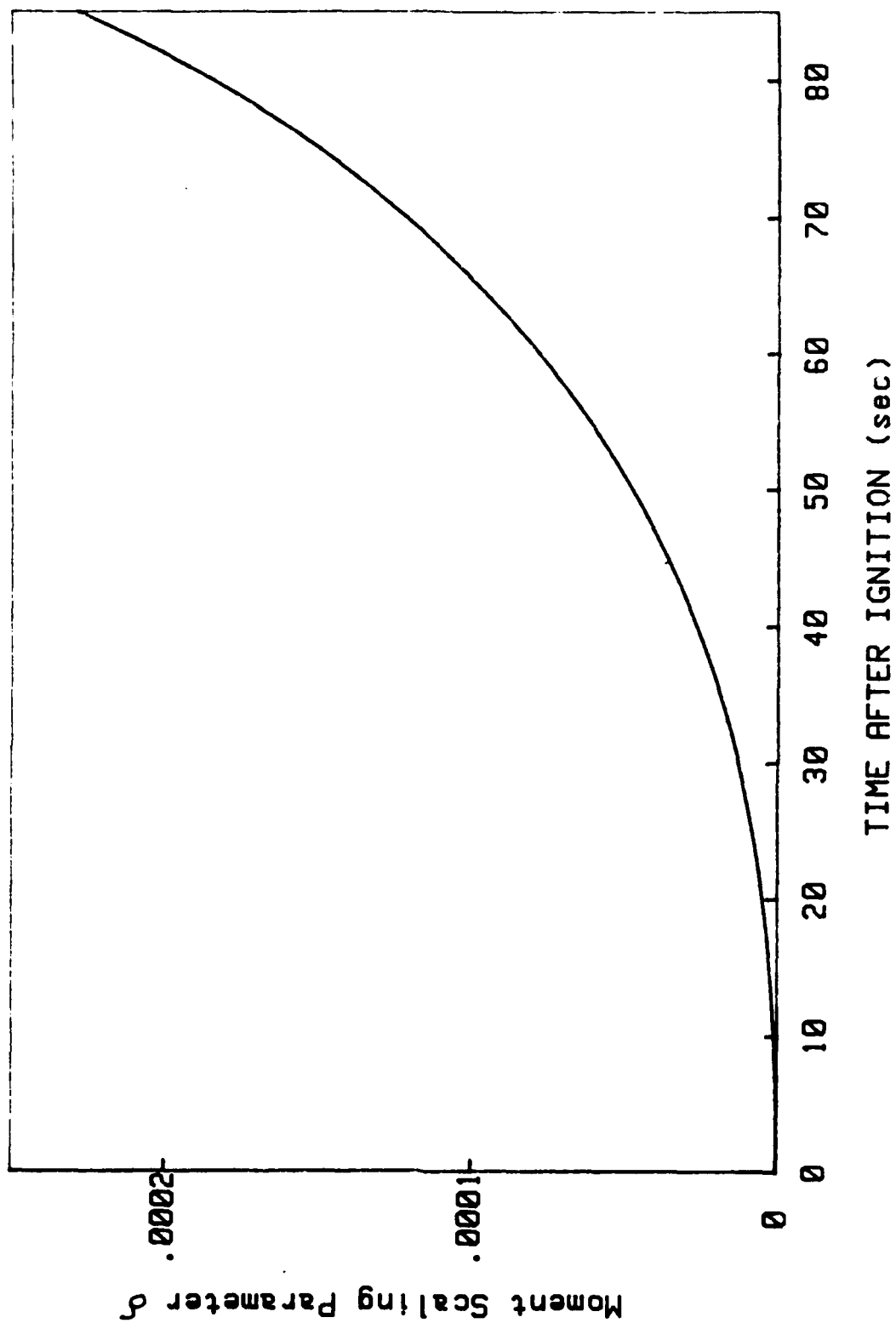


Figure. 54. Moment Scaling Parameter vs Time (WESTAR V)

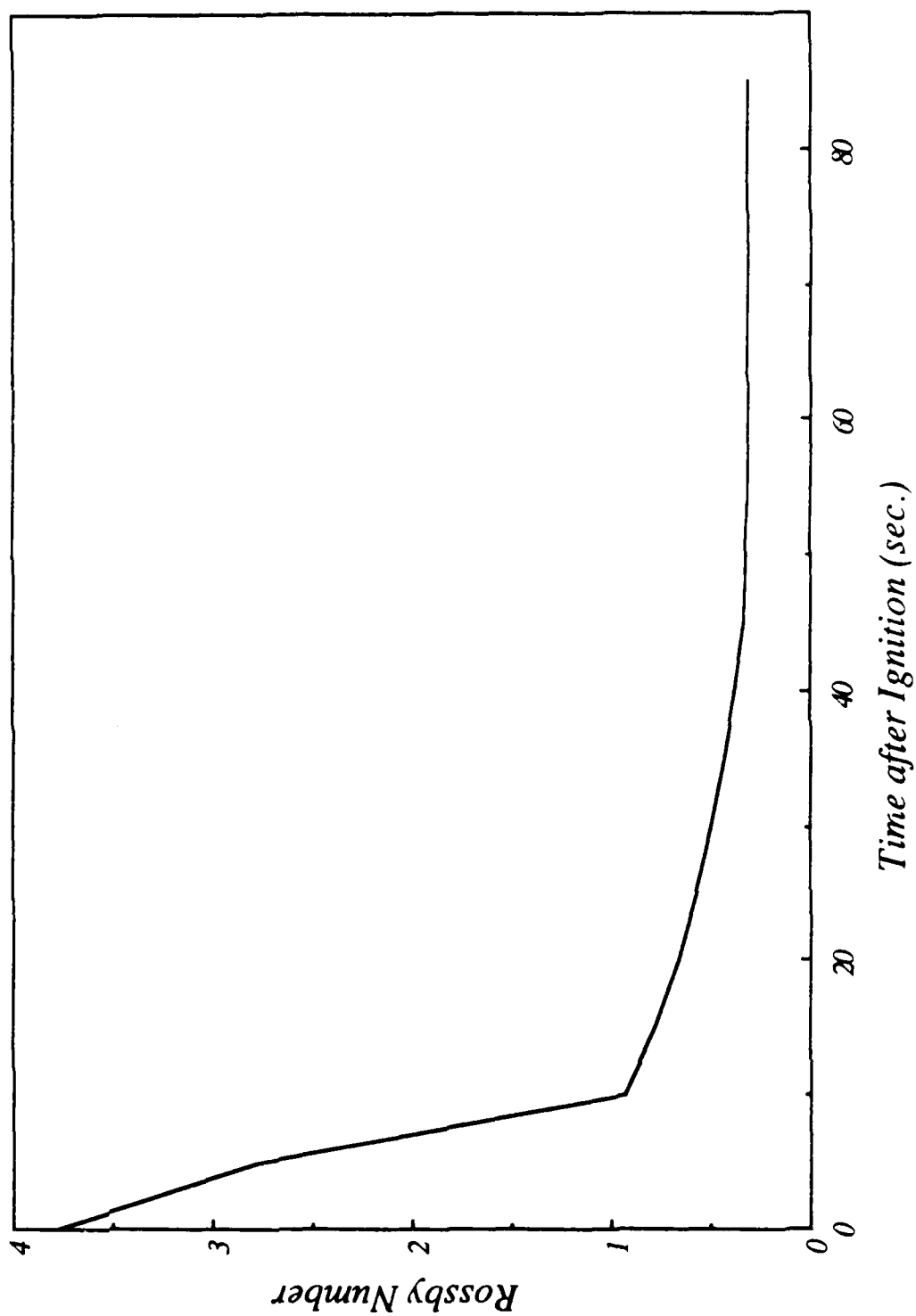


Figure 55. Rossby Number vs Time (STAR 48)

dominates the motion initially, and the system angular velocity amplitude decays for the first few seconds of motor operation. It is interesting to note that if only the classical jet damping was present, the rate amplitude decay would be expected to increase rapidly during the motor run as shown in the lower part of Figure 10. There is no evidence in the flight data (upper part of Figure 10) to indicate that this happens. In fact the damping does not increase during the early part of the motor run in the anticipated manner. The net damping rate shown in the Figure 47 is much more representative of what actually occurs. The computations indicate that the perturbing moment fluctuates in amplitude exhibiting both damping and forcing of nutation at different periods of the motor run. On the average, the driving increases toward the end of the run because of the increasing motor diameter and the forward travel of the center of mass relative to the propulsion system.

The growth rate plot in Figure 47 was based on evaluation of a truncated series for the velocity fluctuations with $m=n=25$ (625 inertial modes). It was found that at least this many modes must be evaluated for converged results. Much of the numerical data shown in this section was based on a larger number of modes. Figure 56 shows how the growth rate result depends on the number of inertial modes used to represent the gas response. The series converges if approximately 30 terms in the axial mode integer and 30 terms in the radial mode integer are accumulated. That is, about 900 modes must be evaluated in determining the response of the combustion gases to the spacecraft motion. System growth rate calculations spaced every 5 seconds were adequate to give acceptable plotting resolution; a cubic spline routine provides the intermediate points needed in the numerical integration of the equations of motion.

The growth rate calculations were carried out in parallel with the numerical integration of the Euler dynamical equations. A fourth order predictor-corrector algorithm was employed. Figure 57 shows the predicted lateral angular rates for WESTAR V for the entire motor run. Figure 58 is the last part of the nutation growth on a larger scale to emphasize the detail. It would appear that a very acceptable simulation of the spacecraft wobbling motion has been produced. It would be appropriate at this point to review the assumptions that were made in producing the plots of Figures 57 and 58. It is emphasized that only the actual motor and spacecraft geometrical functions were used. Actual nozzle radius, nozzle length, CG location, spacecraft mass and moment of inertia, measured spin rate from the flight, and mass flow rate from motor static test data were used. Since a detailed representation of the gas flow through the nozzle was not available, the phase angle changes through were ignored, but an approximation for the lateral angular momentum losses in the nozzle was included by reducing the disturbing torque by 20% of the predicted value. The most important assumption made in the modeling was the simplification of the motor combustion chamber shape, which was represented by a best fit cylinder.

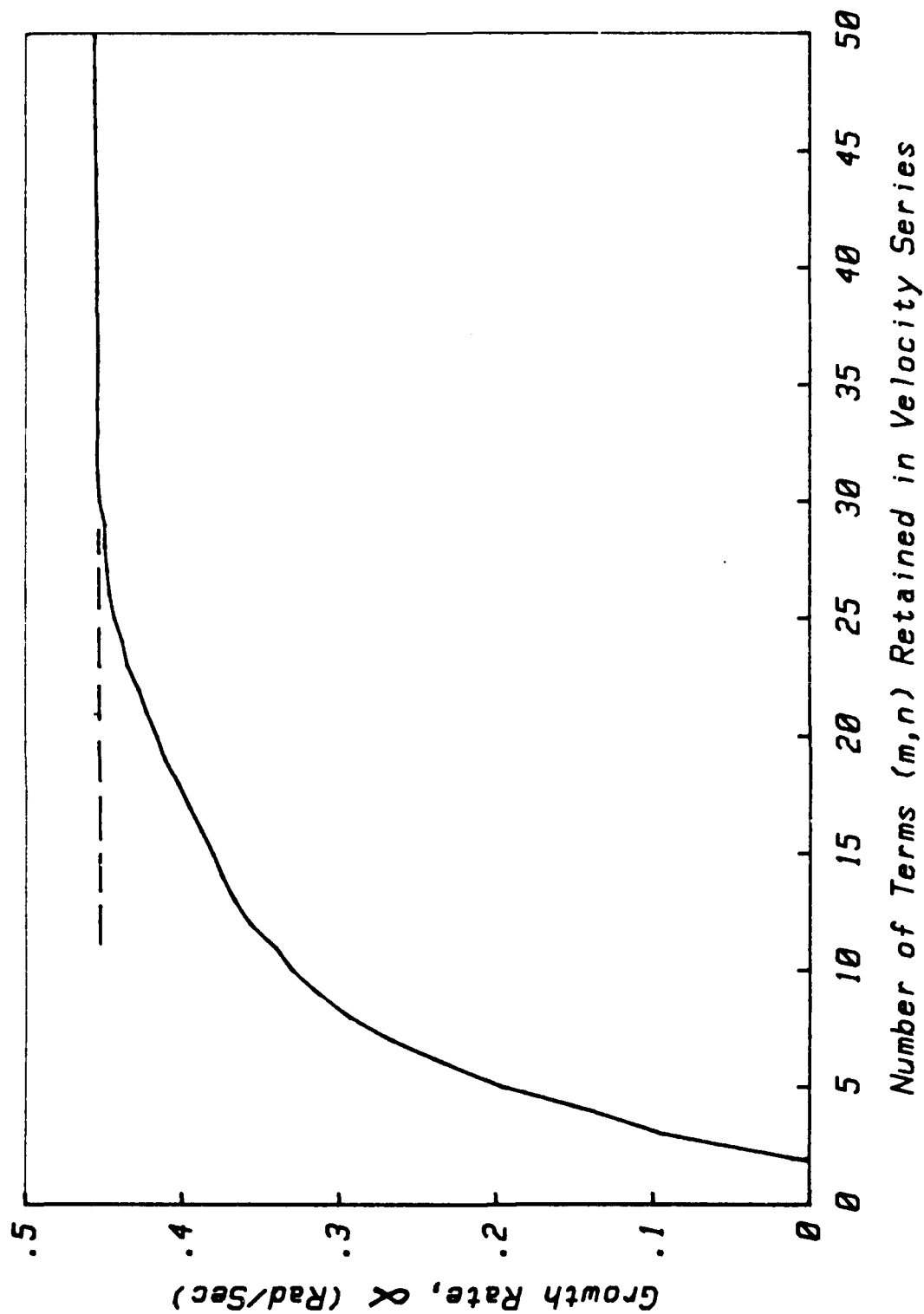


Figure 56. Effect of Number of Modes on Convergence (WESTAR V at 80 Sec.)

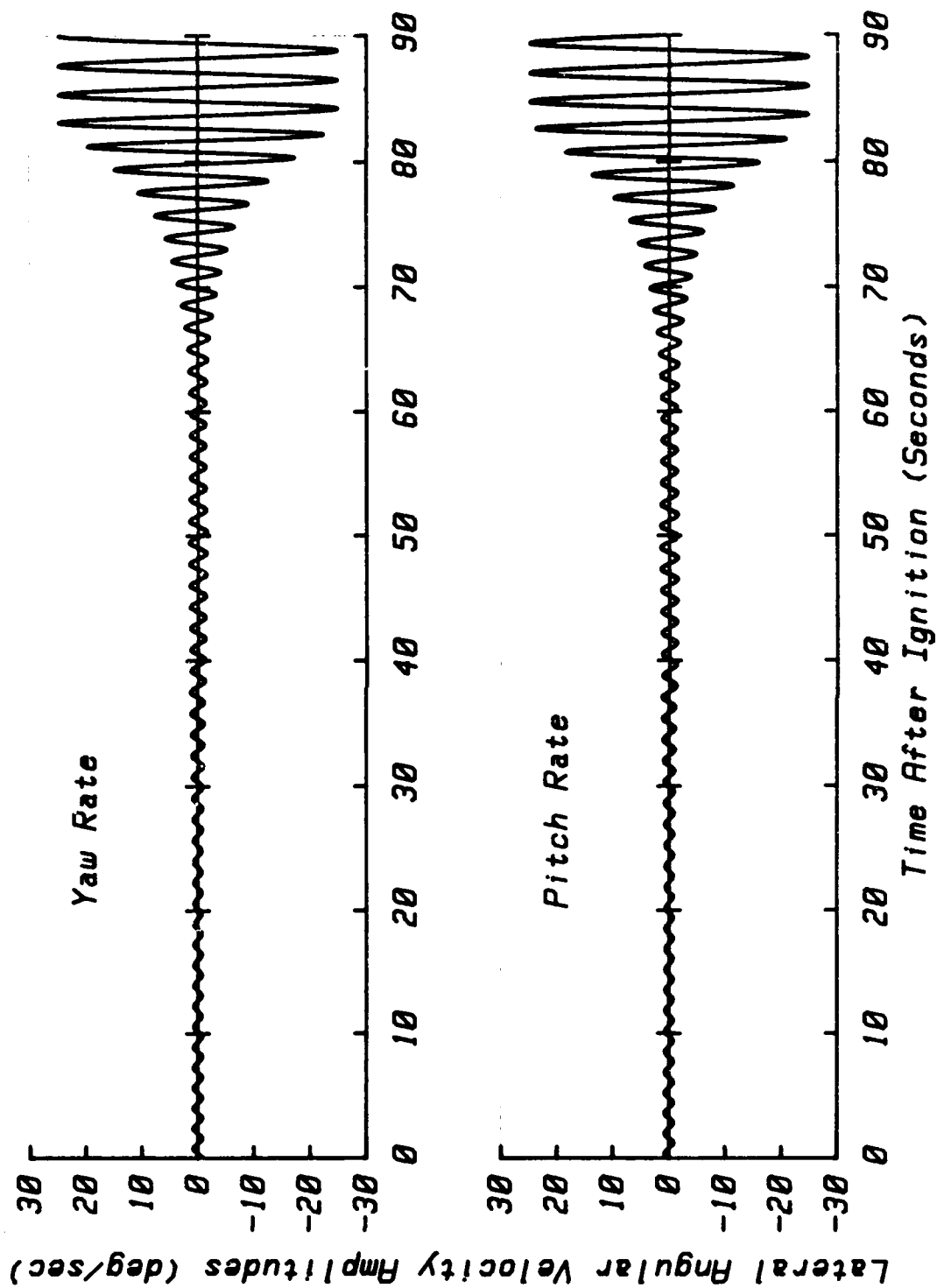


Figure 57. Simulated Coning Perturbation, WESTAR V

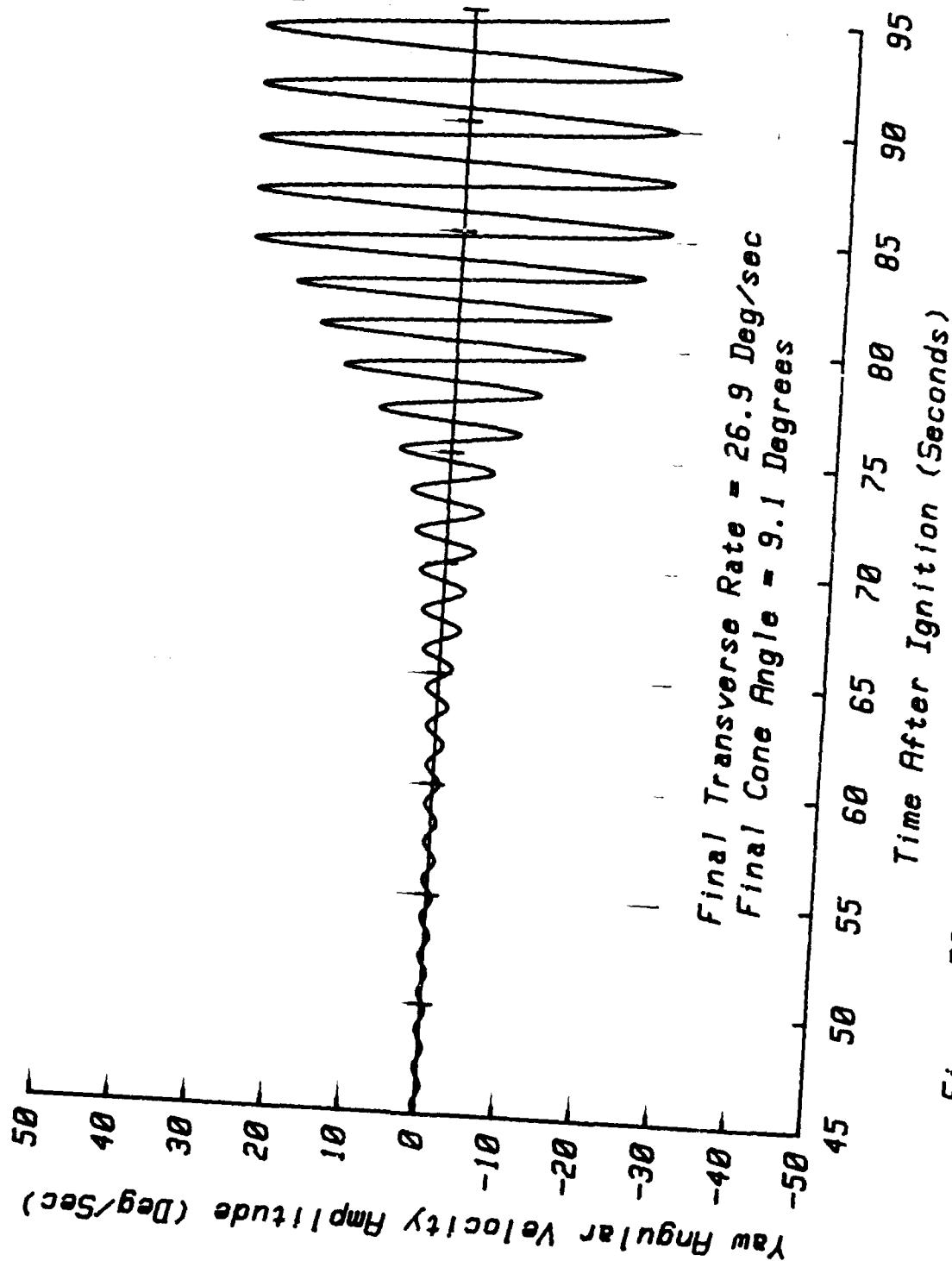


Figure 58 - Simulated Yaw Rate Perturbation, WESTAR V

Figure 14 shows the actual WESTAR V yaw rate gyro signal. In comparing this with the simulated lateral angular rate, shown in Figures 57 and 58, it can be seen that the major features of the actual motion are well reproduced by the analytical model despite the various assumptions. The short burst of growth seen in the data between 1320 and 1330 seconds on the WESTAR V timeline is not reproduced accurately in the simulation. However, as the growth rate plots (Figure 47) indicates, there is evidence in the simulated results that a similar increase in growth rate should occur in this time period. One should not expect the approximate results to produce a detailed time history because of the simplifications in the development of the motor burning surface distribution brought about by the use of the cylindrical representation. The assumed mean flow pattern clearly does not represent all of the subtle changes that occur during the regression of the burning surface in the actual motor. The rapid transition to an end-burning configuration takes place during this time period. It is also likely that other mechanisms such as slag deposition, nozzle motions, and flexing of the spacecraft structure are involved in the generation of the fine structure of the actual rate data. What is most important is that the most significant features of the coning instability are represented without consideration of anything but the motor gas flow interactions. The initial decay, the transition to coning growth at approximately 50 seconds after ignition, and the subsequent rapid coning growth during the final 10-15 seconds of motor operation are all very convincingly reproduced in the simulation. For emphasis, no parameter adjustments (other than the reduction of the gasdynamic impulse to account for nozzle losses) were employed in the simulations. All parameters are taken to be those scaled directly from motor and spacecraft prints and from dynamics data supplied by McDonnell Douglas.

Another effect of the gasdynamic interactions is the modification of the wobbling frequency as discussed in the last section. This comes about because the disturbing moment vector lags the angular velocity vector as illustrated in Figure 44. The phase lag angle for the WESTAR V flight is plotted vs time in Figure 48. Since the phase angle is fairly large during coning growth, then there is a sizable torque component normal to the rate vector. Inspection of the equations of motion shows that this directly modifies the nutation frequency. Figure 49 shows the WESTAR V nutation frequency history with the calculated perturbations superimposed. These predictions should be compared to the actual flight data shown in Figure 5. Although one would not expect close agreement because of the simplifying assumptions used in the analysis, there is indication that the predicted trends are in reasonable agreement with the observations. In particular, the calculations show that the nutation frequency should be larger, on the average, over the last part of the motor burn indicating that the disturbing moment lags the angular velocity disturbance. This behavior is clearly depicted in the telemetry data.

8.2 SIMULATION OF SGSII (STAGE 2) NUTATION

Since the second stage of the SGSII vehicle also utilized the STAR 48 motor and spin stabilization with a higher rate of rotation, it makes a very valuable test case. The spacecraft mass and moments of inertia are much larger than the typical PAM-D vehicles and therefore would be expected to display considerably different response to the coning perturbations. The second stage, and the SGSII third stage that also used a STAR 48 motor, were both equipped with nutation control packages⁷ to damp any coning tendencies. This system worked well in keeping the third stage lateral rates ± 2 degrees per second deadband. The attitude control system was not activated during the stage 2 motor operation, so it is of interest to test the present model to see if it properly predicts what was observed. Figure 59 shows the calculated net growth rate vs time for SGSII (Stage 2). The general response to the changes in system geometry with time are similar to the PAM-D results except that the amplitude of positive growth in the last fifteen seconds is considerably lower than the PAM-D. Figure 60 shows the vehicle motion with the gasdynamic driving effects represented. The initial lateral rate was estimated from actual flight data. As usual, there is a decay in amplitude for the first half of the motor run followed by coning growth in the last twenty seconds. However, the amplitude does not grow beyond about four degrees in the simulation. This is very similar to what was observed in flight as described in Section 2. Again, the pronounced burst of growth before the final coning growth is not accurately represented. However, the simulation shows a fine structure not unlike that portrayed in the flight data shown in Figure 17. A major difference is the behavior of the actual vehicle at motor taildown showing a rapid decay. A second SGS-II flight did not exhibit this feature.

8.3 SIMULATION OF STAR-37E VEHICLES

Prior to the PAM-D experience, there was a series of spin stabilized orbit raising vehicles powered by the smaller STAR-37E motor. One reason the PAM-D coning problem was not anticipated was that no hint of such a problem was observed in these earlier, and very similar, vehicles. Again, it is useful to test the proposed gasdynamic interaction theory in a predictive fashion with motor and spacecraft data representative of these missions. Two cases were chosen on the basis that the spacecraft dynamic characteristics were significantly different. These are the IMP-H and the TELESAT-C missions. Figures 61 and 62 show the growth rate vs time and resulting lateral angular rate vs time for the IMP-H. It is very interesting that there is a small positive growth at the very last of the burn resulting in a barely discernible increase in yaw and pitch rate amplitude. It would appear that had the motor run been longer (the STAR 37E burn time is about half the length of the STAR 48 burn), a more noticeable coning growth might have been observed.

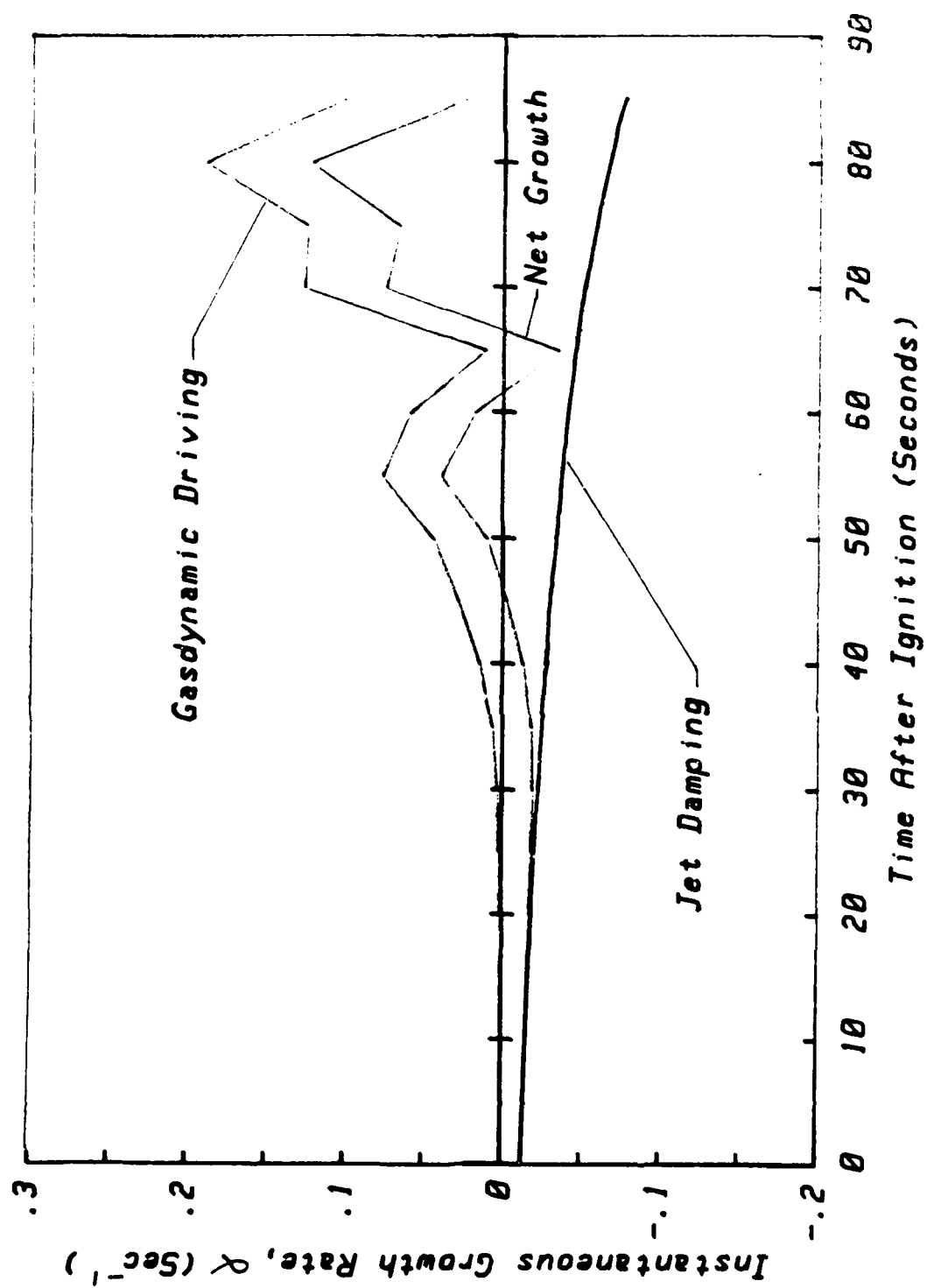


Figure 59. Nutation Growth Rate vs Time (SGSII, Stage 2)

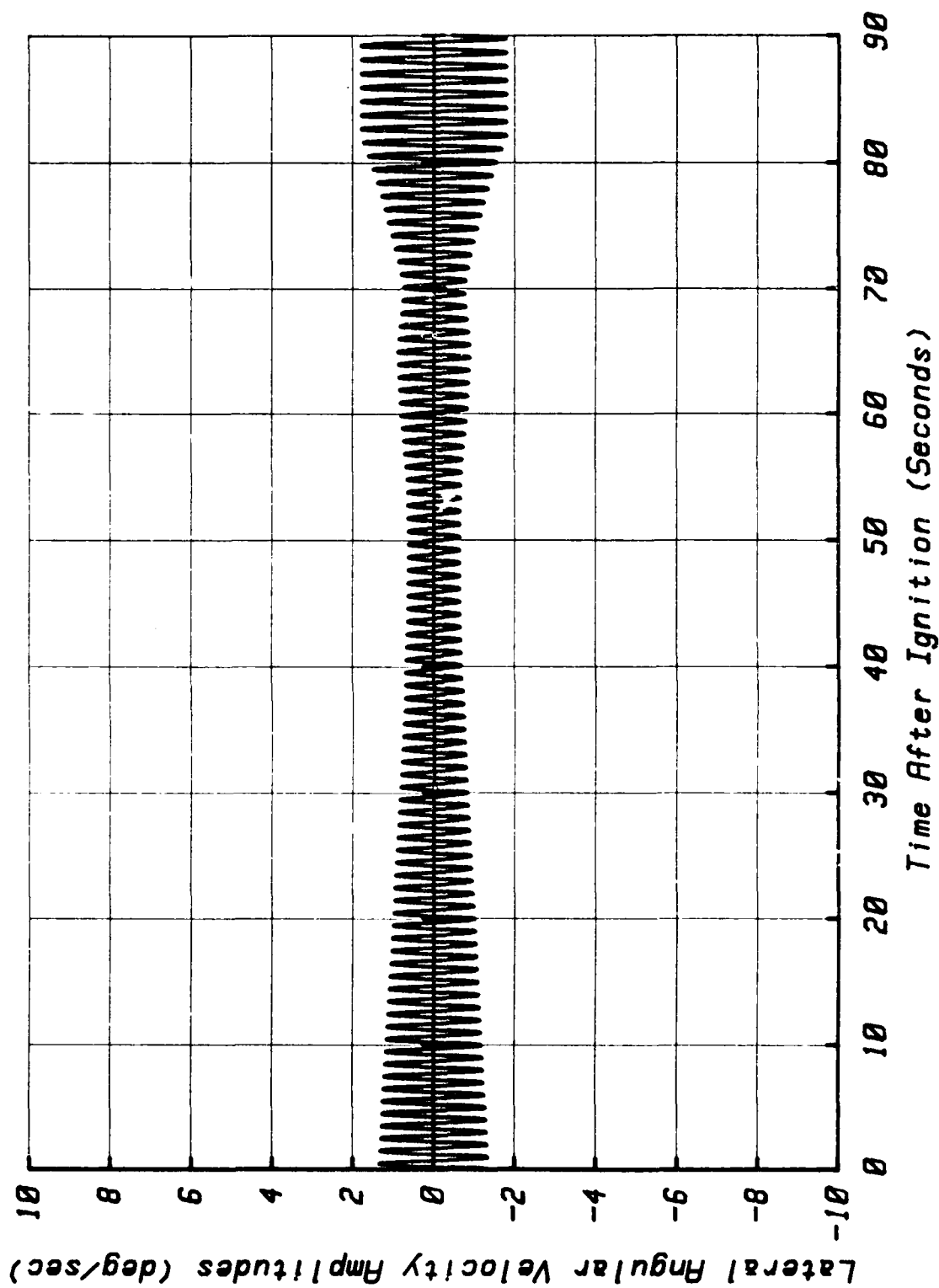


Figure 6C. Simulated Yaw Rate History (SGS-II)

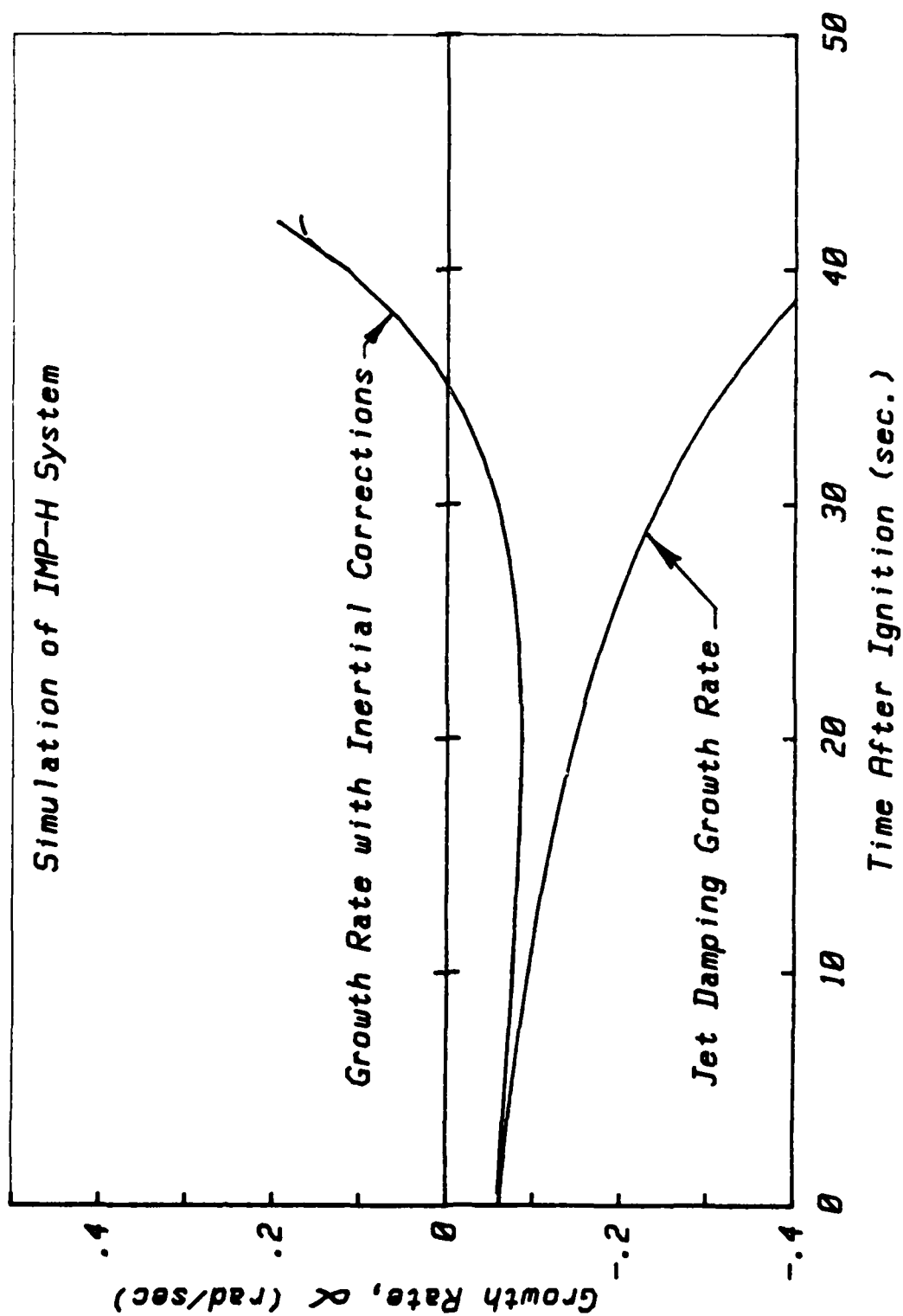


Figure 61. Growth Rate Plots for IMP-H (STAR-37E Motor)

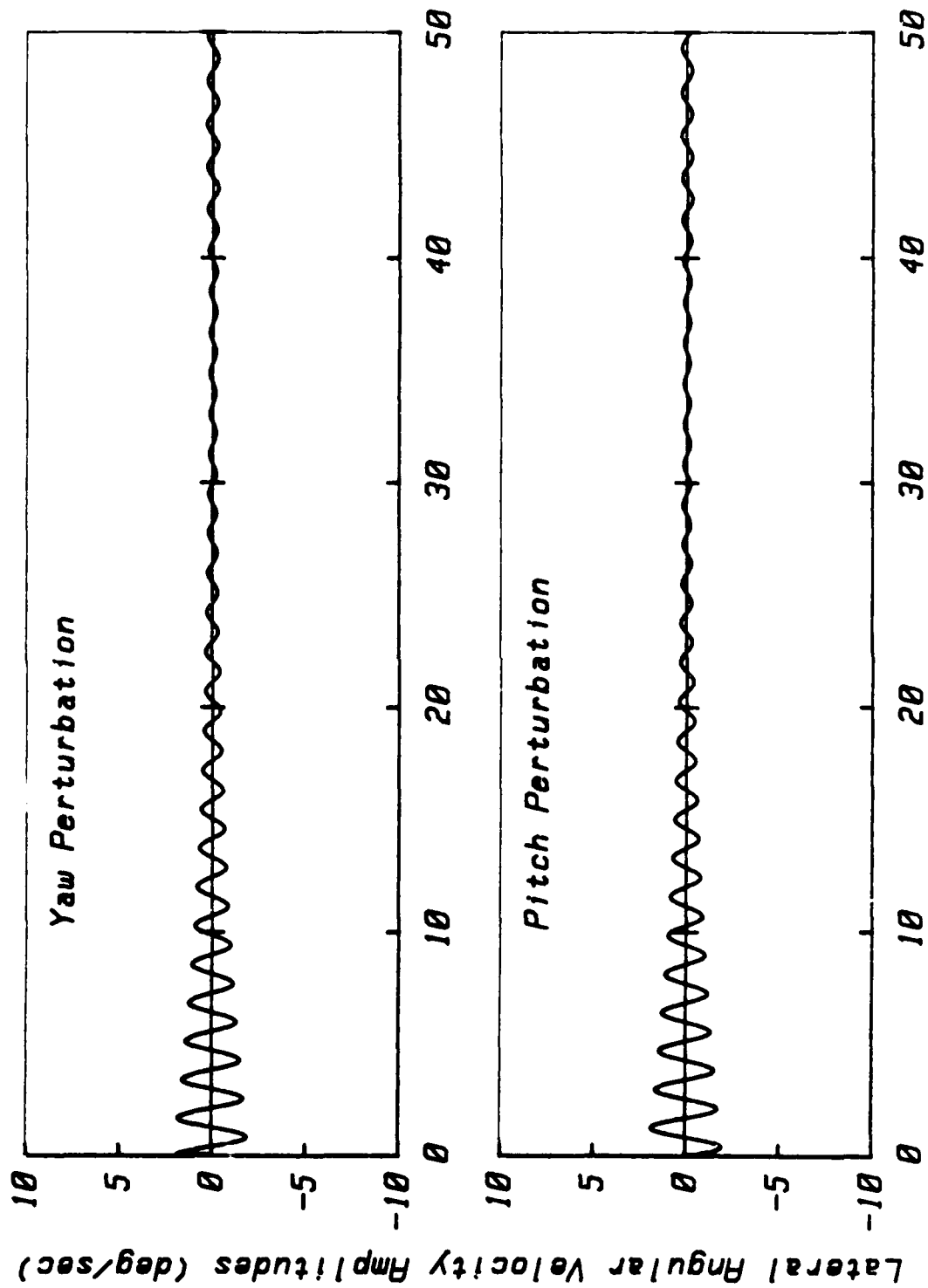


Figure 62. Simulated Spacecraft Motion (IMP-H)

Figures 63 and 64 show similar results for the TELESAT-C. The different dynamical configuration is apparent in the lower oscillation frequency. Again, there is a slight tendency for coning growth in the last few seconds of motor burn, but only a very small final cone angle results. These predictions appear to be consistent with the actual flight data. Unfortunately no rate gyroscope data was collected preventing a detailed comparison. It would appear that a small coning growth did occur based on accelerometer data as indicated in Table 1.

8.4 SIMULATION OF PAM-DII NUTATION BEHAVIOR

It is of considerable importance to be able to predict the potential coning problems in new spacecraft configurations. This was attempted at an early stage in the present program before launch of the first PAM-DII spacecraft. The analysis used in that attempt included the effect of only a single inertial mode, since it had been anticipated that only the lowest order modes would be excited by vehicle wobbling. On this basis, it appeared that coning should not occur in the DII because of the low fineness ratio oblate combustion chamber shape, which for the first transverse inertial mode would not have produced instability. Because of the failure of the oversimplified version of the model, it was realized that only by properly superimposing many inertial modes could the gas response be adequately represented. Previous sections of the report have detailed the complete analysis.

It is now proper to test the results using mass property data for an actual PAM-DII flight vehicle, the RCA-Ku-Band spacecraft. The actual rate gyroscope data for the mission had not yet been made available for comparison to the predictions at the time of writing. It will be of great interest to determine the correspondence to the flight data at a later time. It is also to be hoped that the model can be exercised in a true predictive mode for future DII missions. Figure 65 shows the RCA (PAM-DII) predicted coning growth rate vs time. As in the PAM-D series, the system exhibits instability starting at about 50 seconds after ignition. The growth rate remains small until about 80 seconds when two peaks appear followed by a large peak growing to a maximum value of about 0.4 sec^{-1} (time constant = 2.5) just before burnout. Some of the fine scale changes in the growth rate may not show up in the plots since the plotting resolution was 5 seconds. This is especially true after the 80 second point when fairly large perturbations are present. Since the burn time is long, about 118 seconds, significant coning growth takes place even though the maximum growth rate is somewhat smaller than that experienced in the STAR 48 missions. Figure 66 illustrates the predicted spacecraft response. A final angular rate of about 40 degrees per second is predicted, which is apparently of the order of magnitude of the disturbance measured by the flight instrumentation.

It is of interest to note that had the motor operation been terminated at about 85 seconds, no important coning growth would have appeared. That is, if the motor

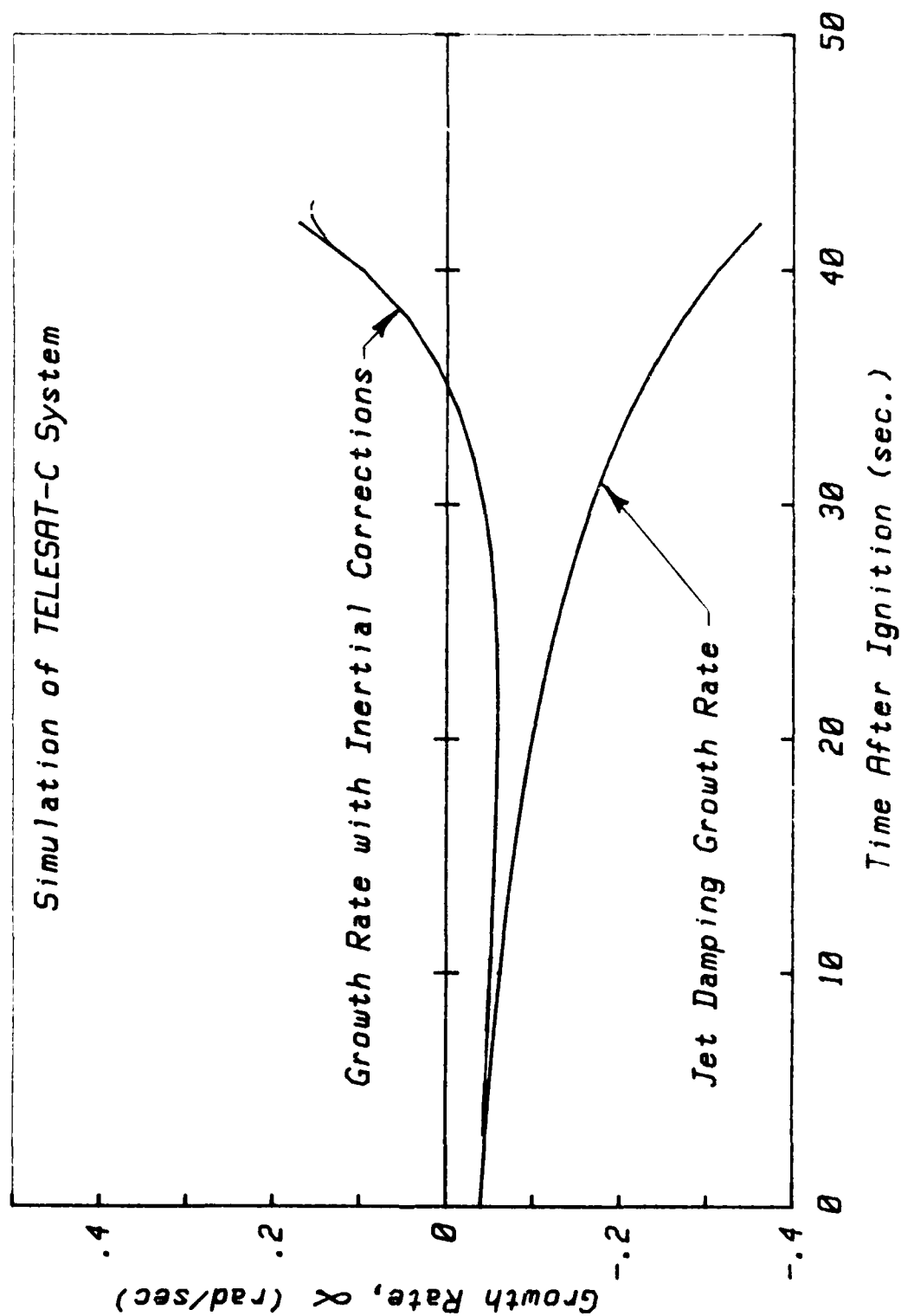


Figure 63. Growth Rate Plots for TELESAT (STAR-37E Motor)

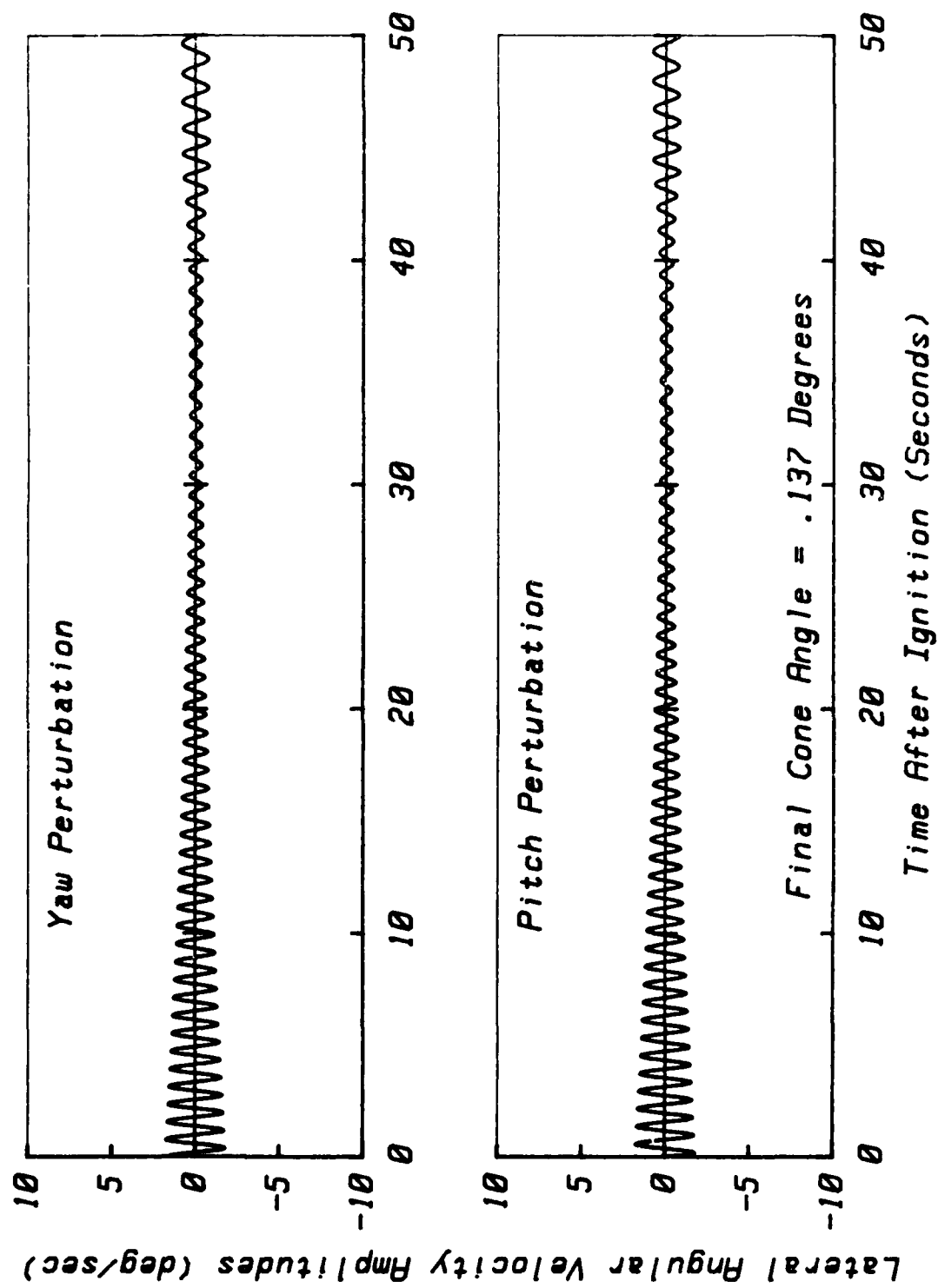


Figure 64. Simulated Spacecraft Motion (TELESAT-C)

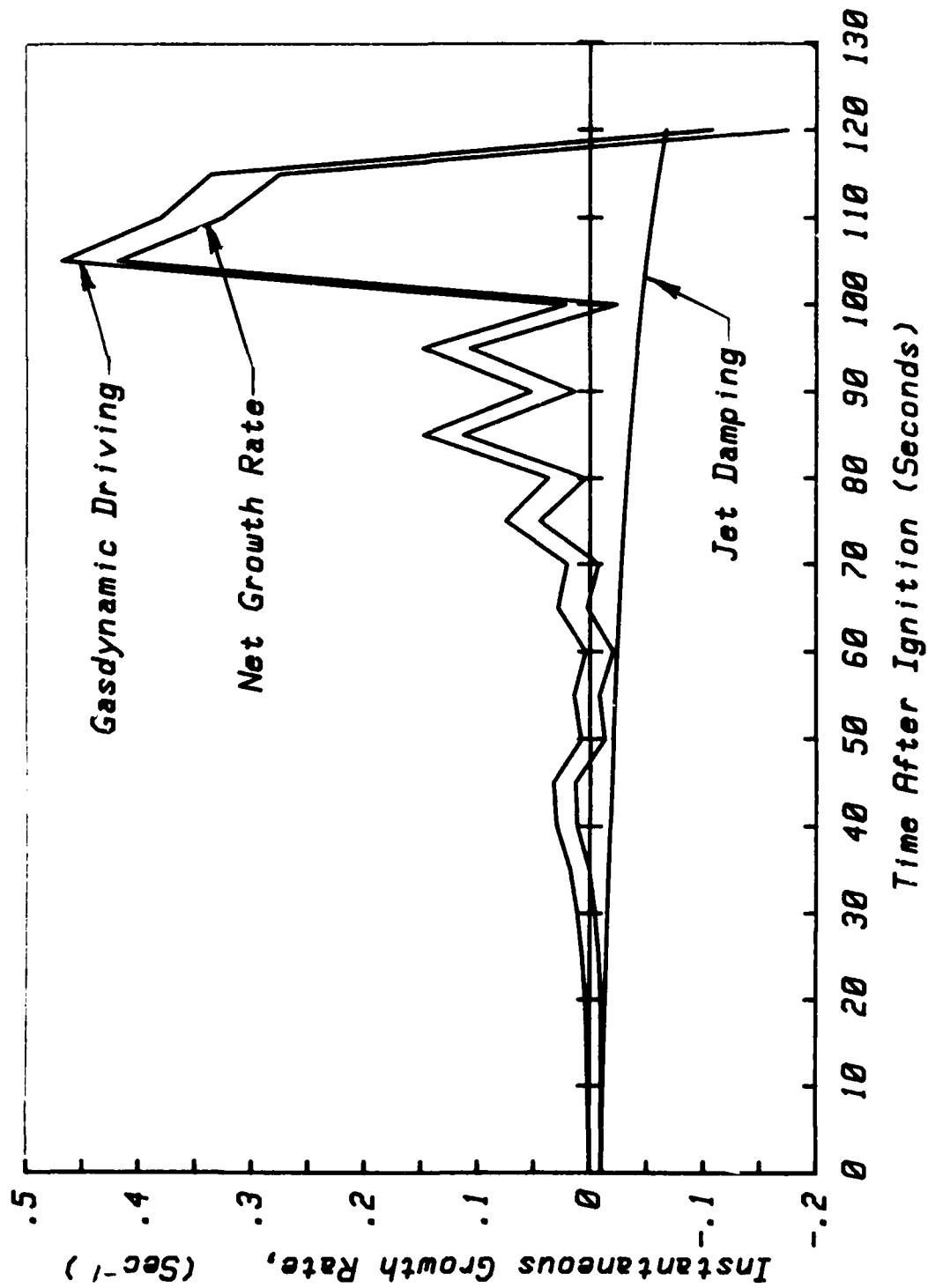


Figure 65. Instantaneous Growth Rate vs Time (RCA-KuBand, PAM-DII)

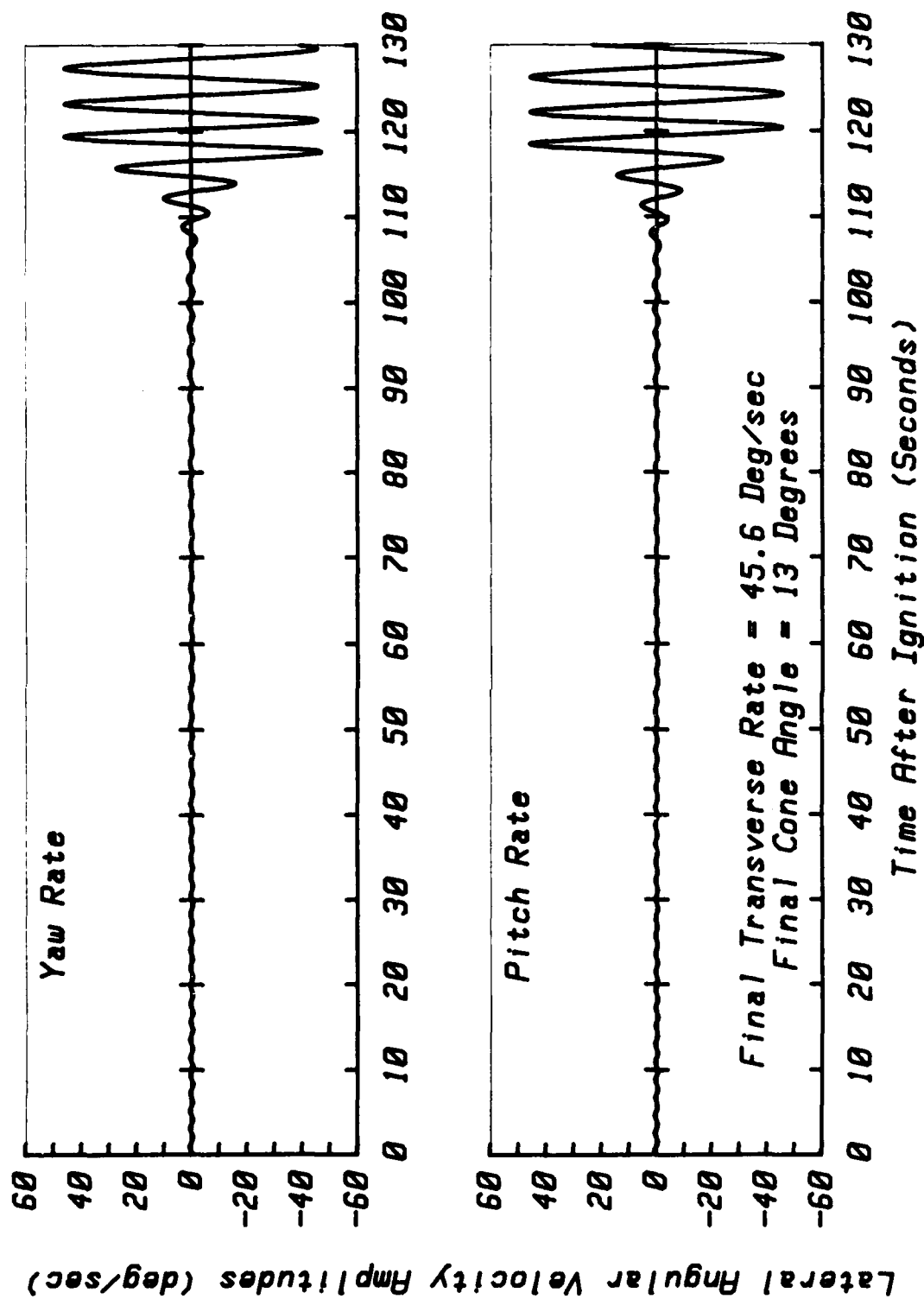


Figure 66. Simulated Coning Perturbation

stopped after a run time equal to that of the STAR 48 motor, nutation instability would not have been observed. This appears to be partially the result of the difference in chamber shapes. The IPSM motor has a significantly smaller fineness ratio than the STAR 48; in fact it is roughly oblate in shape whilst the STAR 48 combustion chamber is prolate for most of the motor run. Similarly, if a PAM-D motor were to have an increased web thickness, and attendant increase in burn time, then much larger coning growth would have occurred (all other parameters remaining equal). A preliminary sensitivity was carried out, as discussed in the next section, which showed that smaller combustion chamber fineness ratio results in relatively less nutation growth.

8.5 OTHER FEATURES OF THE ANALYTICAL RESULTS

To conclude this section, it is useful to emphasize that the analysis predicts several features of a subtle nature seen in the flight data. For example, as the high-resolution angular rate data show, the growth of the nutation is far from a smoothly varying function of time. There is usually evidence of several periods of intense growth before the final rapid growth at the end of the motor run. These are also apparent in the frequency data. It is of interest that the simulations made with the analytical model predict very similar behavior. Figure 65 is a good example of this effect. The largest peaks appear to be correlated with changes in the slope of the mass flow rate within the motor caused by geometry variations as the grain surface recedes. Such changes would be reflected in the amount of vortex stretching in the nozzle entrance region and could, therefore, affect the important time-dependent flow interactions taking place there. This feature of the phenomenon is worthy of further study.

Although the comparisons between the theoretical results and the flight measurements do not display exact agreement, it must be pointed out that the orders of magnitude of the net coning growth and the event times, such as appearance of periods of increased nutation driving, are in reasonable agreement with the data. It should be noted that the analysis correctly predicts what actually took place in four completely different spacecraft/motor systems. Thus, there is considerable hope that with further development and refinement, especially in terms of the handling of the mean flow field and chamber geometry effects, the model can be made into a useful design tool.

9. CORRECTIVE PROCEDURES

It is quite useful to summarize what has been learned in this study regarding the sensitivity of the coning instability to key physical parameters. Although only preliminary evaluations of this kind could be made before the research program ended, some of these findings are pertinent and should be documented. It is likely that continued refinement of the numerical model will lead to somewhat different interpretations at a later time. On the basis of the current understanding of the results, suggestions are made for avoidance of nutation instability at the design stage of the spacecraft or the solid propellant propulsion system. Also, suggestions for developing corrective procedures in existing systems are set forth.

9.1 SENSITIVITY OF CONING TO SPACECRAFT/ MOTOR PARAMETERS

It is of interest to assess the sensitivity of the coning instability to key physical parameters. This is done in a preliminary fashion in what follows. No attempt could be made to account for all interactions between parameters, so only the local sensitivity is represented. For example, the effect of nozzle throat radius is estimated by varying R_t while all other parameters are left unchanged. Thus account is not taken of the effect this would have on the motor chamber pressure, burning rate, and mass flow rate. Later models should include a complete motor internal ballistic simulation in order that all linkages between variables are properly represented. The results presented here give only an approximate indication of the sensitivity for very small changes in the parameters.

Flight measurements have indicated that the coning phenomenon is not particularly sensitive to spin rate, thus it is of interest to see if the gasdynamic instability model sheds any light on this finding. Since the rotational energy stored in the vehicle spin is the ultimate reservoir from which the coning wobble must draw its energy, it would seem that reducing the spin rate would be beneficial. Figure 67 shows the effect of motor spin rate on nutation growth rate assessed at the 75 second burn time in the WESTAR V, STAR 48 system. Lowering the spin rate from the standard range (about 50 RPM) is seen to have little effect until a very low rate, say about 10 RPM is reached. The sensitivity to rotation rate is very nonlinear as shown. This nonlinearity appears to explain the flight observations in a quite satisfactory way; no flight spin rate was below the knee of the curve as shown.

The importance of the nozzle entrance size has been indicated in the analysis in terms of its affect on vortex stretching, which significantly influences the amount of nutation growth. The numerical evaluations clearly verify this as shown in Figure 68. One possible reason for the appearance of the coning instability in the PAM-D systems is that the nearly spherical motor configuration leads to a rather small value for the ratio of the throat radius to the combustion chamber radius. A smaller

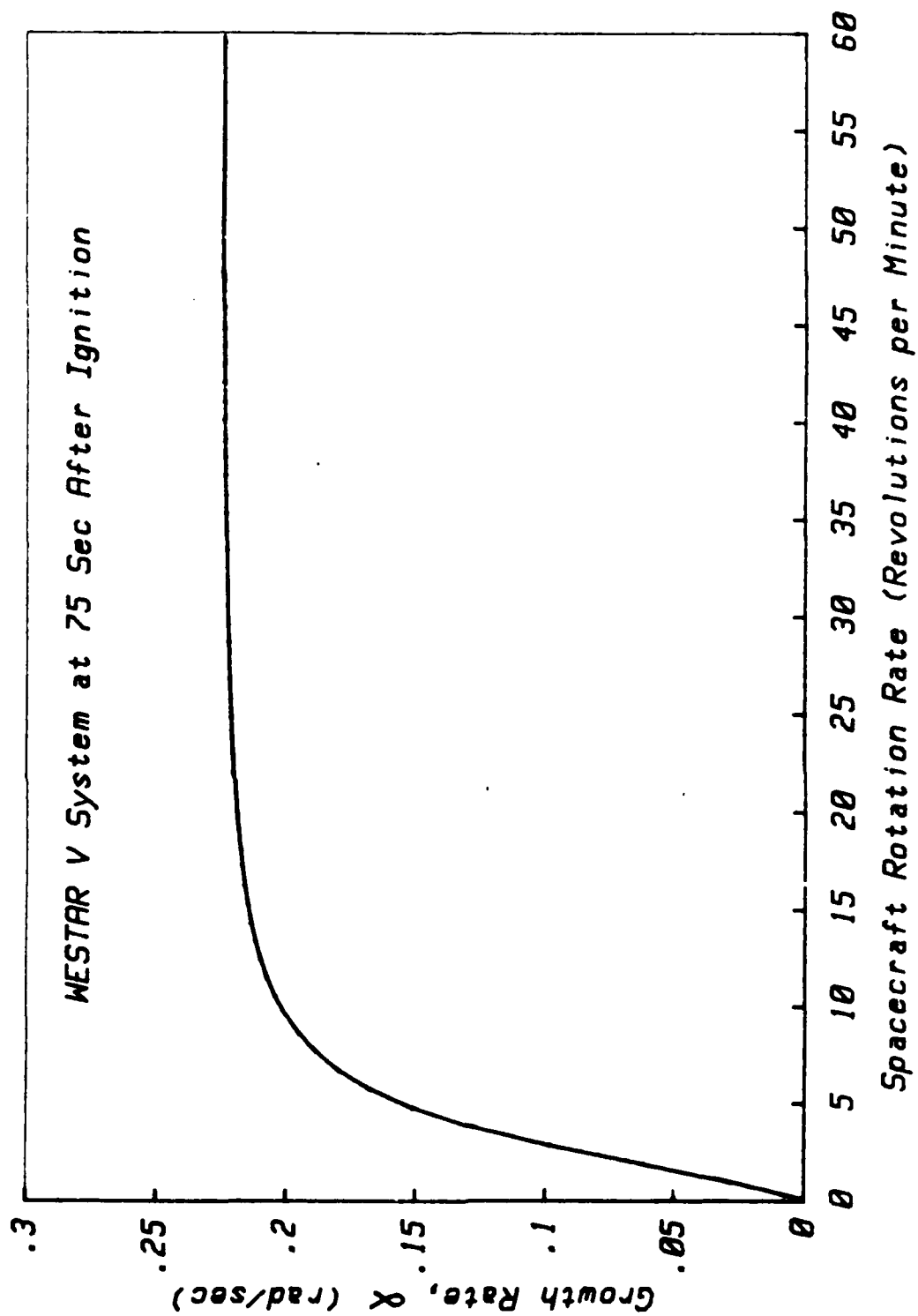


Figure 67. Effect of Spin Rate on Nutation Instability Growth

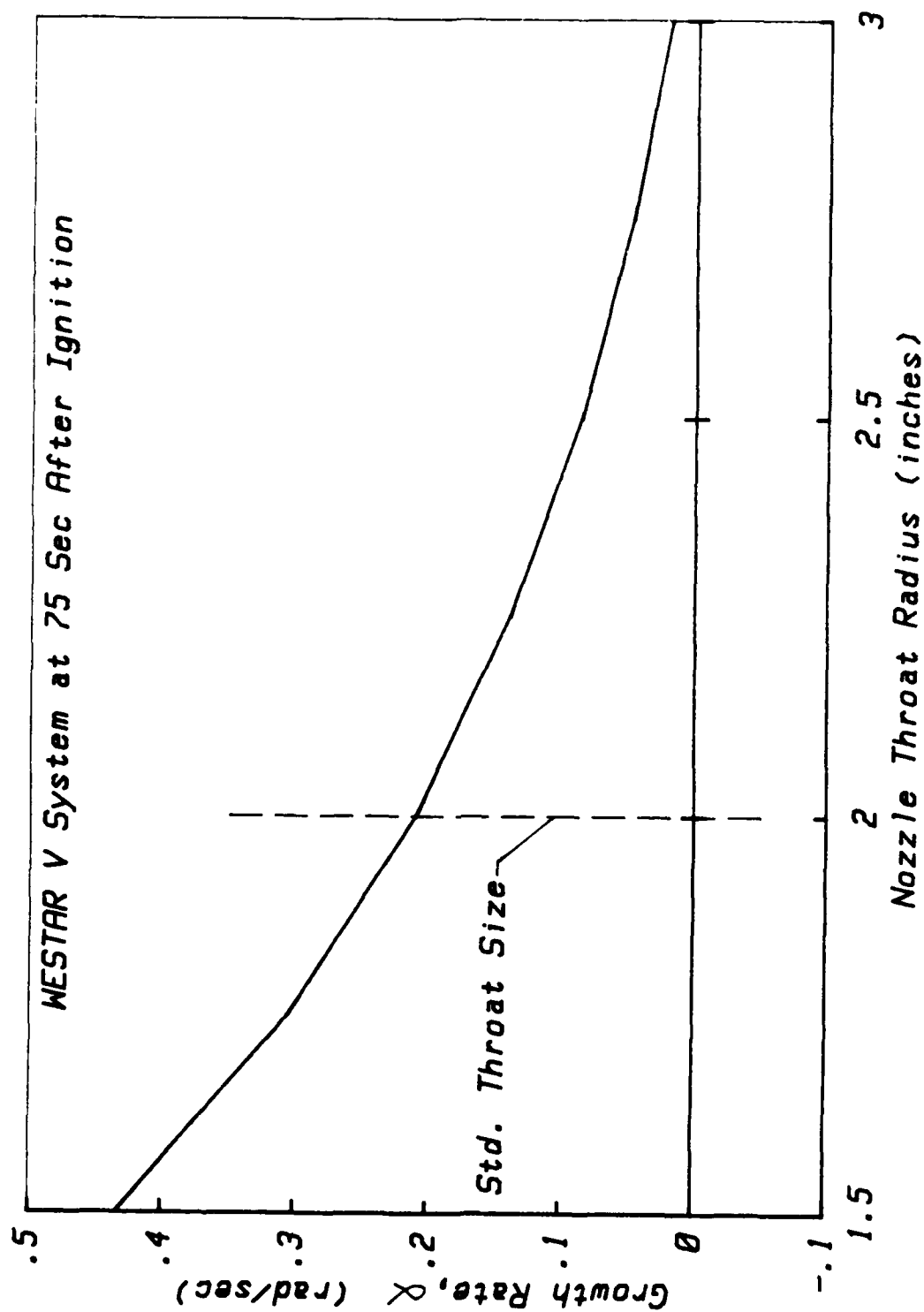


Figure 68. Sensitivity of Growth Rate to Throat Radius

nozzle entrance places the entrance region at an optimal radial position in terms of angular momentum transport. The relative lateral gas motions are largest near the motor centerline, and the flux of lateral angular momentum is enhanced when the nozzle entrance is small. The nozzle submergence sensitivity comes about in a similar manner. Figure 69 shows the effect of submergence on the growth rate. Examination of Figures 40 and 42 will show that moving the nozzle into the chamber places it at a region of larger values of the axial perturbation velocity amplitude. The significance of this in terms of the lateral angular momentum pumping was discussed in Section 6. Thus, over a certain range of submergence lengths, the nutation growth is greatly enhanced. On this basis, it appears that nozzle submergence is one of the key design factors affecting the coning instability problem.

It has been emphasized several times that the severity of the nutation instability is affected by the initial conditions at the beginning of the motor run. A small nutation wobble is imparted to the spacecraft upon separation from the spin platform. This motion persists throughout the pre-burn coast phase, and the residual nutation rate just after motor ignition is typically of the order of 1 degree per second. It may be that nonuniformities in the initiation of the propellant grain affect the initial magnitude of the wobble, but there is little evidence of this in the telemetry data. Figure 70 shows the effect of the residual nutation angular velocity amplitude on the final coning amplitude at the end of burn. The initial conditions strongly affect the final outcome of the instability growth. This result makes it clear that any reduction in the initial coning is quite beneficial, and that it is possible to control the coning problem effectively if means can be found to reduce the residual nutation at ignition. If a longer preliminary coasting phase can be justified, then it may be possible to employ simple passive nutation damping to reduce the final nutation angle.

Figure 71 illustrates the lack of sensitivity of the coning growth rate to the moment of inertia ratio I_0/I_1 . Configurations tending toward an oblate mass distribution ($I_0/I_1 > 1$) are only slightly better in terms of reduction of coning growth. However, account was not taken in these estimates of the reduction in the lever arm between the rocket motor and the vehicle center of mass that would accompany increases in I_0/I_1 .

Figure 72 shows the effect on final coning angular velocity of changing the lateral moment of inertia I_1 without altering the roll moment of inertia. This is an effective method for reducing the instability, because it directly affects the vehicle response to the disturbing torques. Changes in spacecraft mass distribution in the direction of a more prolate shape is beneficial due to increased inertial resistance to lateral disturbing moments. This benefit could be negated if the moment arm, L_{cg} between the motor and the mass center is increased in the process of increasing I_1 .

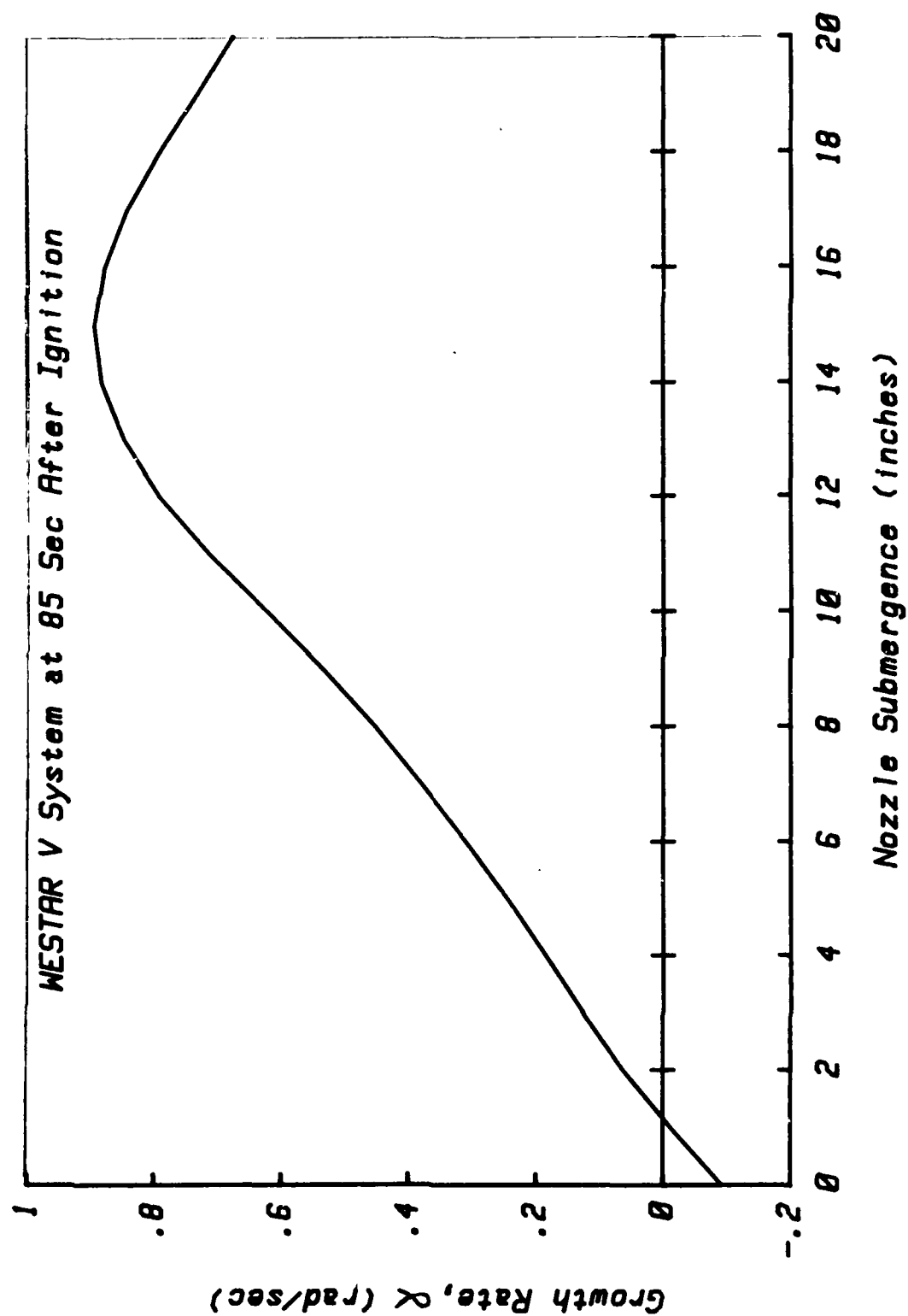


Figure 69. Sensitivity of Growth Rate to Nozzle Submergence

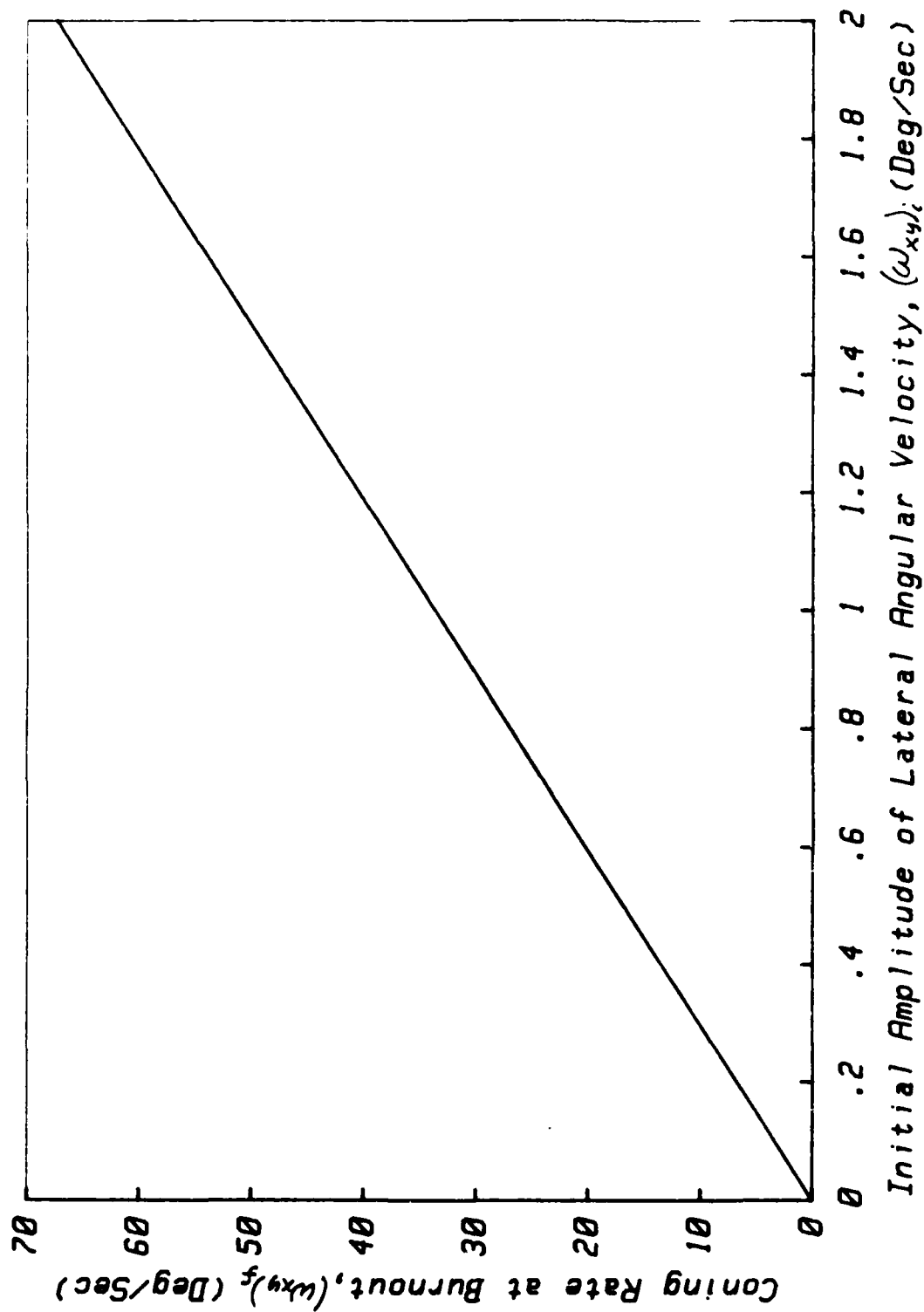


Figure 70. Effect of Residual Nutation at Ignition on Final Nutation Amplitude

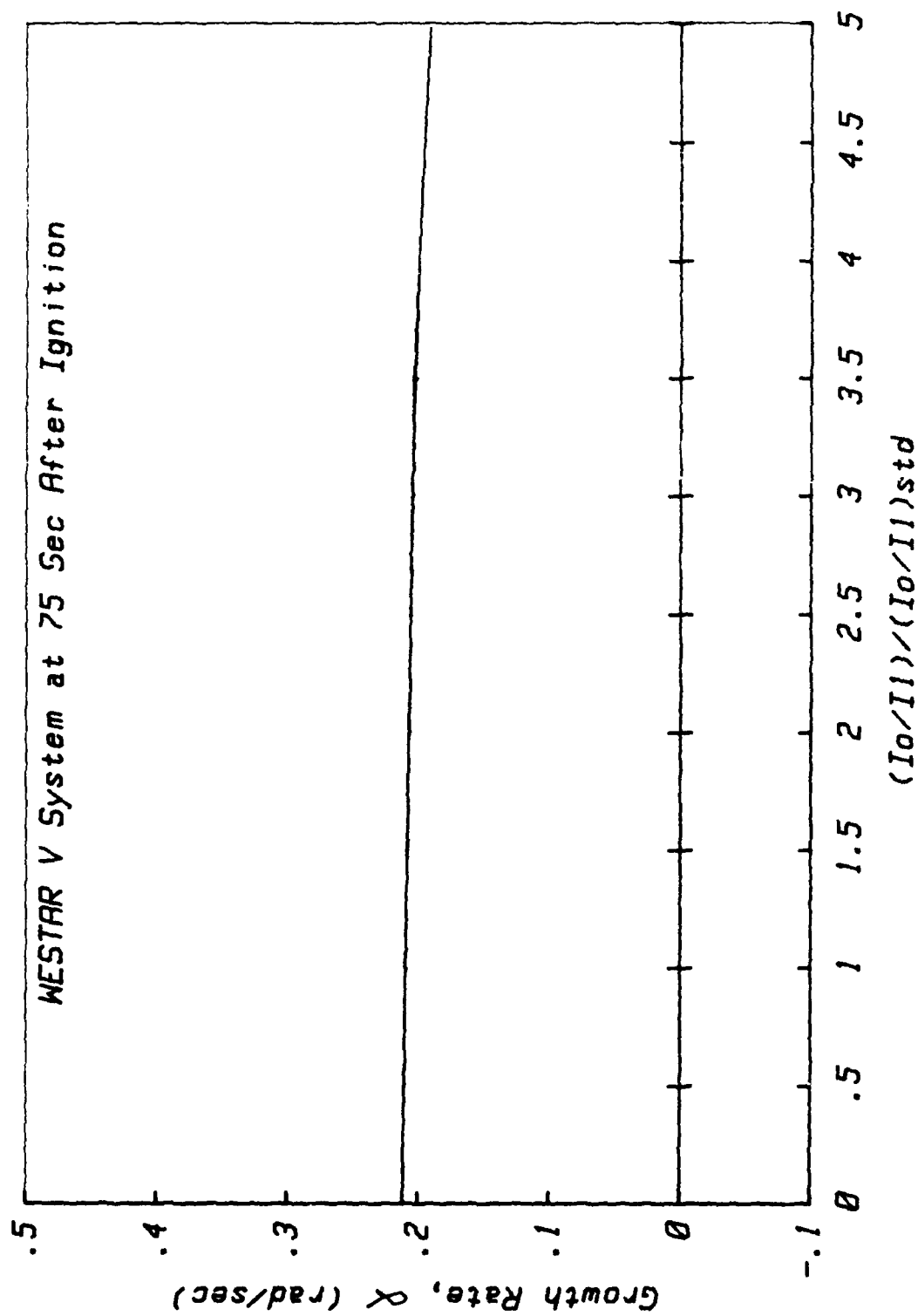


Figure 71. Sensitivity of Growth Rate to Moment of Inertia Ratio

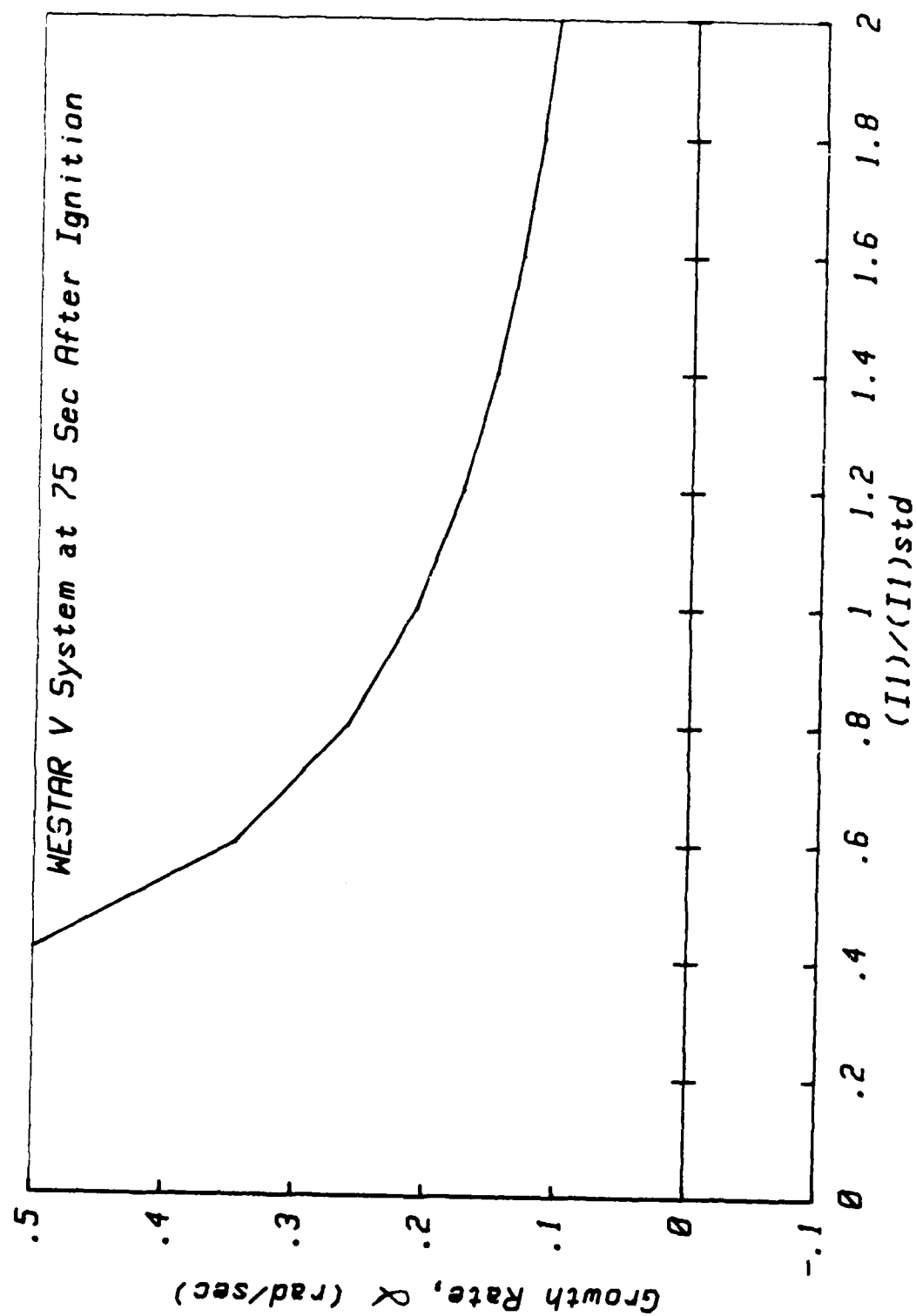


Figure 72. Effect of Lateral Moment of Inertia on Nutation Growth Rate

Figure 73 illustrates the sensitivity to the combustion chamber fineness ratio, b . It is apparent that more prolate chambers produce larger growth, everything else remaining equal. Earlier predictions of the gasdynamic interactions were based on evaluation of only a single inertial mode in the representation of the unsteady internal flow. It appeared from these estimates that oblate combustion chambers ($b < 1$) would not generate coning instability. That same *trend* is evident in the more complete analysis as Figure 73 indicates. More oblate combustion chambers show relatively less coning growth. For the spacecraft configuration and burn time evaluated, it appears that if the chamber L/D is less than about .7, serious coning growth would not occur. This might appear to be contrary to the recent PAM-DII experience. Coning occurred in those missions although the combustion chamber shape remained oblate throughout the entire motor run. Examination of the simulation presented in Section 8 indicates that the DII growth rate was relatively lower at, say $t = 75$ seconds corresponding to the numerical values shown in Figure 73. Thus the coning growth in the PAM-DII would appear to result from the long motor burning period which was approximately 30 seconds longer than the STAR-48 propelled missions.

Far more detailed sensitivity analyses than presented here should be undertaken in the assessment of any actual system design. It will be important in the design process to model all of the *interactions* between parameters in addition to the isolated effect caused by changes in single parameters as is done in these preliminary estimates.

9.2 MINIMIZATION OF CONING IN EXISTING VEHICLES

It is appropriate to indicate what design features or parameters might be modified to reduce the coning in existing spacecraft. Unfortunately, it would appear, on the basis of the analysis described herein, that there are very few procedures that would decrease the amount of coning that do not require rather major modifications of the spacecraft configuration. Assuming that changes to the propulsion system cannot be undertaken, then there are apparently only two spacecraft modifications (short of incorporation of active nutation attitude control packages) that can reduce the coning.

The first, and by far the most practical modification is the reduction of the tipoff angular velocities. If the initial spacecraft wobble can be reduced from 1 degree per second to, say, 0.2 degrees per second, then a major reduction in final cone angle would result as indicated in Figure 70. It is possible that a passive nutation damping device could be employed during the pre-ignition coast. If the spacecraft carries liquids or structures capable of relative motion, care should be exercised, obviously, that tipoff wobbling is not enhanced by liquid sloshing or structural vibration during the pre-burn coast.

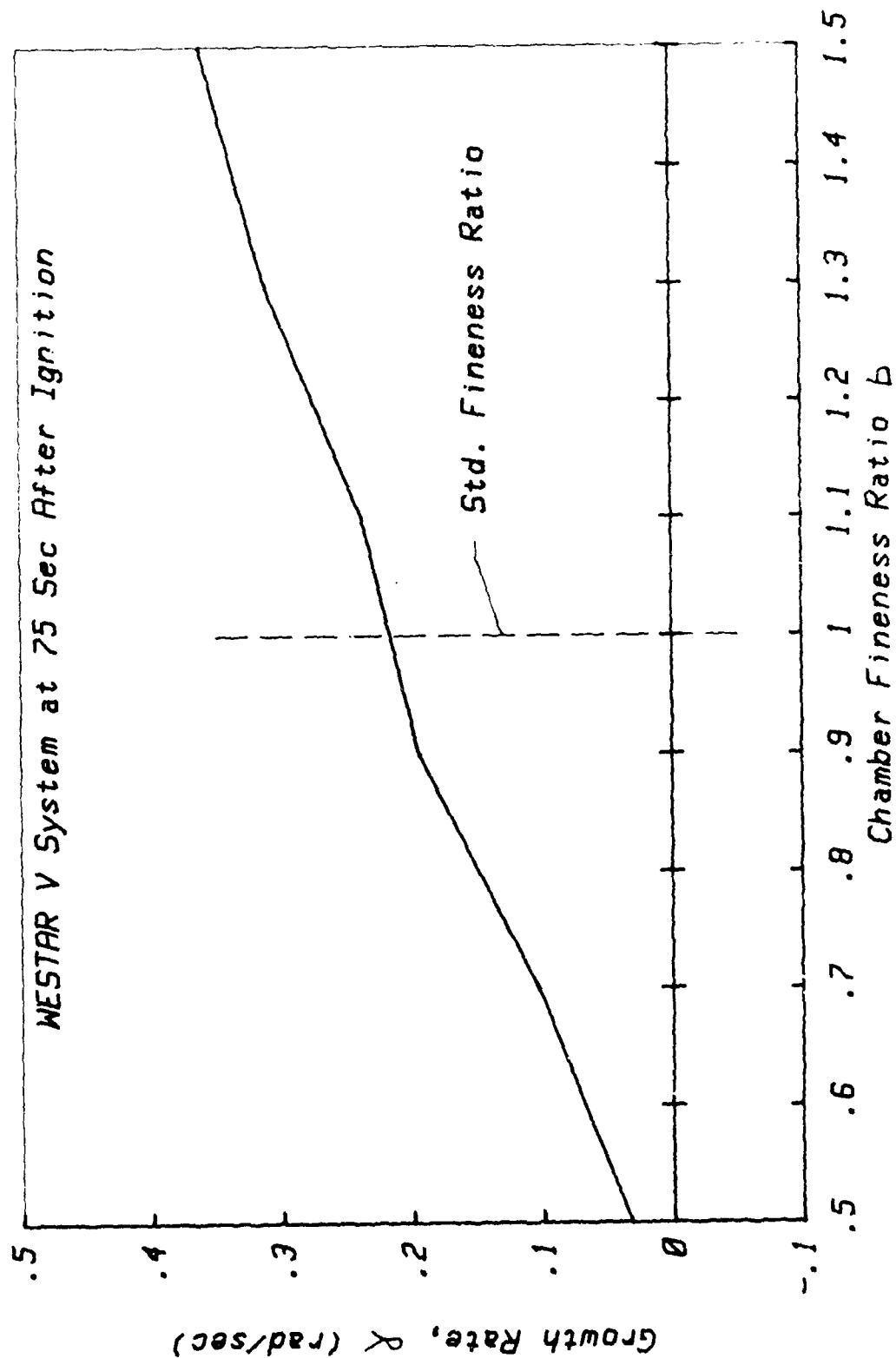


Figure 73. Sensitivity of Growth Rate to Combustion Chamber Fineness Ratio

The only other spacecraft configuration changes that would yield a reduction in coning is modification of the positioning of the propulsion system relative to the spacecraft mass center, or redistributing the payload itself relative to the structure. Figure 72 indicates that mass redistribution has an important effect on the nutation instability if the lateral moment of inertia can be increased. For a given payload mass, this would imply lengthening the vehicle. Since this also would cause an increase in the motor/mass center distance, the effect on coning cannot be determined without a detailed tradeoff computation. For a given vehicle there will be an optimum mass distribution that yields the smallest coning growth. It is expected that rather more prolate mass distributions would be best. Given the usual situation that the vehicle layout is strongly conditioned by external constraints, then mass redistribution is unlikely to be a practical undertaking.

The third procedure for reduction of coning amplitude is to decrease the vehicle spin rate. As shown in Figure 67, it is possible to control the growth rate to any degree required by selection of the appropriate spin angular velocity. However, very small spin rates (of the order of a tenth of those currently used) would be necessary to reduce final nutation angle to a desirable degree. This raises questions related to the procedure now being employed for spin rate selection. This selection process involves many tradeoffs and it is suggested that a critical review be undertaken to determine the impact of using smaller rates of axial spin. It is respectfully suggested that the effects of rocket motor unsteady internal ballistics be incorporated into such discussions.

9.3 AVOIDANCE OF NUTATION INSTABILITY IN SYSTEM DESIGN

The key to avoiding the coning phenomenon in the design of a new vehicle is a sufficiently complete physical understanding of all potentially destabilizing elements. For this discussion, it is assumed that the gasdynamics model correctly represents the essential features of nutation instability as it was experienced in the PAM-D missions. On this basis, it is possible to list various design features that can be selected in such a way to minimize or avoid the nutation phenomenon.

Since the gas flow is directly involved in generating the instability, it is appropriate to consider motor design characteristics that could be manipulated to minimize coning. Unfortunately, most of the motor characteristics that affect coning are strongly conditioned by external constraints. The nearly spherical shape is dictated by performance considerations and by the need to minimize propulsion system volume. For the same reasons, the nozzle length and throat radius tend to be small. The most serious feature of this design from the coning standpoint is that the motor radius is relatively large (compared to motor length and nozzle throat size). This has a direct influence on the tendency to coning growth. The situation can be improved by utilizing a more oblate combustion chamber shape. Large nozzle submergence also directly affects the instability. Highly submerged nozzles

are also dictated by the need to reduce motor length. It is possible that the use of smaller multiple nozzles with entrances placed as far as possible from the motor axis would be beneficial. Also, application of annular or plug nozzle designs would be useful in reducing the gasdynamic torques. Further study of these possibilities appears to be warranted.

It was shown in the analysis that combustion effects do not appear to directly influence the coning growth. Thus, there appear to be no propellant modifications that would be beneficial. However, a faster burning rate is advantageous, since the length of the motor burn would then be shortened and the nozzle throat size would be increased. Any design feature which tends to shorten the motor run will reduce the final vehicle cone angle. It is possible that new case materials will allow the application of the higher operating pressures associated with faster burning propellants without a serious weight penalty.

Finally, a brief review will be made of spacecraft geometrical features that affect coning. A layout which maximizes the lateral moment of inertia is desirable. Mass distributions that increase I_1 also tend to increase the lever arm between the mass center and the motor, which in turn increases the disturbing moment. Thus these would appear to be opposing factors. However, the net affect on the coning growth rate is represented by the *ratio* of the CG distance to the lateral moment of inertia, L_{cg}/I_1 . Since the moment of inertia depends on the square of a characteristic vehicle length, and L_{cg} is linearly proportional to that length, then increased lateral moment of inertia would appear to be a desirable layout option. It is highly recommended that vehicle layouts be studied that bury the propulsion system as deeply within the structure and as close to the mass center as possible. In the PAM-D spacecraft, the motor is suspended behind the mass center with the payload well forward. A better layout would be to surround the propulsion system to the greatest possible degree by the payload. If L_{cg} can be kept nearly zero, then coning growth would be minimized.

As expected, most spacecraft design features that affect nutation growth are strongly conditioned by external constraints. What is required is a design optimization procedure that incorporates a complete system simulation algorithm. It would then be possible to determine the best set of configuration parameters that simultaneously satisfies the set of external constraints and minimizes nutation instability tendencies. The interactions between variables are so complex that no simple design rules are apparent at this juncture. It is strongly suggested that necessary design software development be undertaken. Inclusion of the gasdynamic driving effects is clearly required.

10.0 EXPERIMENTAL STUDIES

A very ambitious experimental program was undertaken in support of the analytical and computational tasks described in this report. These studies are described very briefly in this section. Although the experimental results did not play a decisive role in the resolution of the PAM-D nutation instability problem, much useful information was generated, and methods that can be further developed in future work were devised. Progress was also made in building a comprehensive cold flow facility for future study of rotating flows.

An important experimental task was to verify the existence of inertial pressure oscillation in the presence of a mean flow. Critics of the work presented in this report, have often based their objections on the incorrect concept that inertial waves can be sustained only in closed systems. It is certainly true that a vast amount of the experimental research on rotating flows has concentrated on contained fluids. The recent work on nutation instability of liquid filled projectiles is an excellent example²⁰⁻²⁸. However, careful perusal of the literature shows that there are many examples of inertial wave effects in situations involving a superposed mean flow. Many such effects can be observed in nature. A favorite example of the present writer is the complex time-dependent motions observed in the atmosphere of Jupiter. Many of the phenomena invoked in the analytical discussions in earlier sections can be seen in the Jovian atmosphere on a grand scale. For instance, vortex stretching and inertial wave effects dominate the atmospheric dynamics of that rapidly spinning planet.

It is obviously true that wave energy induced in a spinning gas flow by wobbling of the chamber will be convected out of the system through the nozzle. However, in situations of this type, one must account for the possibility of accumulation of energy in the wave system. In other words, an energy gain/loss balance must be considered. In fact, as should be clear from the analysis, convection and vortex stretching are important factors in the production of nutation disturbing moments. Thus an important task was to demonstrate that inertial waves could be sustained in the presence of mean flow convection.

10.1 DESCRIPTION OF EXPERIMENTAL TASKS

The principal goals of the experimental program were to:

- Develop flow visualization techniques to promote physical understanding of the flow effects in spinning chambers with mean through flow.
- Develop methods for measuring unsymmetrical pressure waves in spinning, nutating chambers.

- Develop techniques for precision unsteady velocity field measurements in rotating systems using laser-doppler anemometry.

Additional targets of opportunity appeared during the course of the program, and initial steps were taken to implement some of these. For example, it became clear that there is a great need to demonstrate procedures for measuring unsteady flow fields in laboratory scale spinning rocket motor firings. An experiment of this sort was designed, and part of the necessary equipment was organized during the program.

The most valuable experiments proved to be those in which the complex time-dependent flow in the spinning chamber could be made visible. These were of great utility in guiding the analytical efforts. The next sections briefly describe what was learned from each of the experiments.

10.2 FLOW VISUALIZATION EXPERIMENTS

The earlier work of Fultz⁴¹ provided the guidance for the flow visualization of inertial waves. His study involved the excitation of symmetrical inertial modes in a spinning cylindrical chamber by means of a reciprocating piston arranged to oscillate along the longitudinal axis. Dye particles within the liquid rendered the fluid response visible, and photographs were made using a camera carried with the turntable.

We devised a modification of Fultz' experimental setup to simulate the unsymmetrical inertial waves that would be driven by nutational wobbling of a rocket chamber. It is useful to think of the walls of the chamber as oscillating pistons in the generation of an inertial wave response. Using a piston mounted parallel to, but off the axis of spin made it possible to excite the same wave patterns expected in a spinning rocket chamber. A vidicon camera mounted with the test chamber on the turntable allowed the resultant wave motions to be monitored visually. Ink was introduced into the chamber by use of an automatically activated syringe to make the flow field visible. The ability to control the driving rate independently of the chamber spin rate made it easy to investigate various inertial modes. As expected, the lowest order inertial modes were most easily activated, and it was verified that both mode shapes and frequencies matched the classical theoretical results. A video tape of numerous runs was produced.

10.3 MEASUREMENT OF UNSYMMETRICAL INERTIAL PRESSURE FIELD

The pressure field in a spinning, nutating rocket is expected to be dominated by inertial wave motions. To verify the theoretical treatment of this part of the

problem, a series of measurements were undertaken using the test facility developed for flow visualization as described above. A sensitive hydrophone was employed to measure the pressure fluctuations. Water was used as the working fluid. This is acceptable in these simulations, since compressibility is not a factor in the phenomena of interest. In the rocket motor situation, compressibility effects are not activated at the low frequencies associated with the coning motion (of the order of 1 Hz or less). Figure 74 shows a typical set of pressure measurements demonstrating a resonant peak close to the frequency of the first unsymmetrical inertial mode. This particular mode proved quite easy to excite, and was the one responsible for the flow patterns recorded in the flow visualization experiments.

The apparatus was modified to simulate the flow through a rocket chamber. Liquid was introduced through a porous surface at the top of the cylinder and pumped in a continuous loop through a nozzle at the lower closure. The piston arrangement again proved valuable as a means for exciting unsymmetrical inertial waves. When flow was introduced into the rotating chamber, the expected vortex core was observed to form along the axis. Much effort was expended to prevent air entrapment within the vortex core, but such cavitation limited the flow rate that could be used. The vortex stretching effects in the nozzle area were clearly evident. Hydrophone measurements were utilized to verify that a finite amplitude inertial wave could be sustained in the chamber with fluid flowing through it continuously at a low rate. Again, the measurements confirmed the theoretical treatment of the inertial mode pressure waves in a qualitative manner.

10.4 DEVELOPMENT OF FIBER OPTIC LASER-DOPPLER FACILITY

A major expenditure of resources and individual effort was made in the development of a facility to enable detailed measurement of unsteady velocities in a spinning, nutating chamber. A specially constructed laser-doppler anemometer formed the central element in this system. Fiber optics techniques were employed to facilitate measurements within the rotating frame of reference. An enormous amount of time and effort was necessary to align the complex rotating head and fiber optics components. Although a rather large percentage of the resources provided were devoted to this facility, it was not possible to make it operational before the end of the program, and no useful measurements were made. It is suggested that future use of this facility be made in producing detailed measurements of the time-dependent flow fields in simulated spinning rockets.

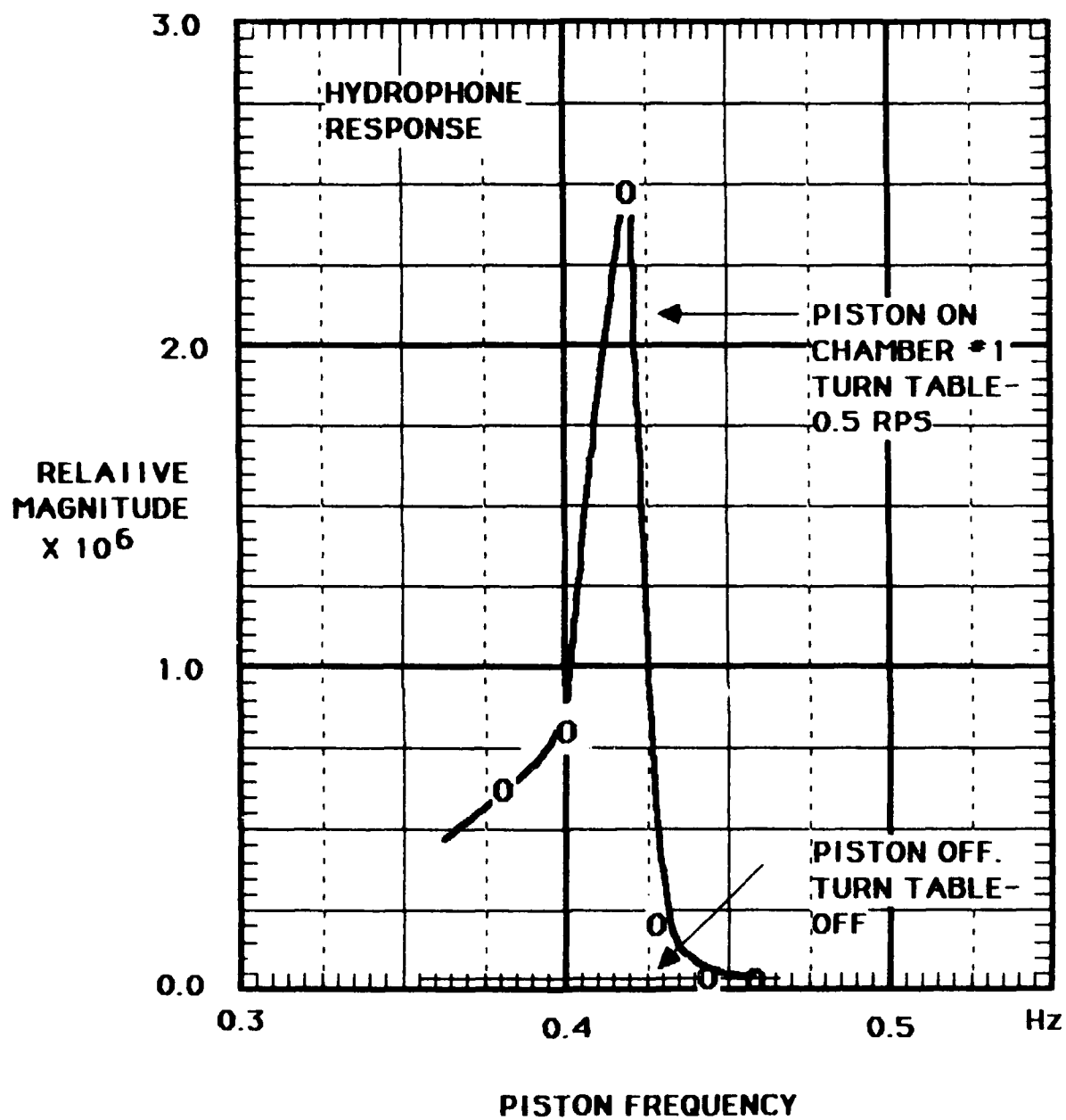


Figure 74. Experimental Demonstration of Inertial Mode Resonance

11. CONCLUSIONS

The results of the program are summarized in what follows. The main findings of the research are emphasized, and the resulting nutation instability mechanism is assessed. Finally, suggestions are made for continued investigation of the spinning solid propellant rocket nutation instability phenomenon aimed at further clarification of its features and for its experimental verification.

11.1 ASSESSMENT OF GASDYNAMIC NUTATION INSTABILITY MODEL

The gasdynamic instability model developed in this program has been applied to several spin stabilized spacecraft. The computational algorithm which implements the theory predicts a slow transition from a decaying nutation (due to jet damping) into a growing wobble as unsteady gas dynamic effects become dominant. The jet damping and the gasdynamic driving interactions have the same source: *the transfer of angular momentum to and from the flow of combustion products by the relative motion of the combustion chamber and nozzle boundaries*. The instability is the result of interaction terms that have been ignored in previous analyses of gas flow interactions. The influence of the *time-dependent* response of the combustion chamber flow to the motion of the spinning spacecraft has not been accounted for before. The main source of instability is the flow of lateral angular momentum out of the propulsion system with the mean flow of combustion products. Complex three-dimensional oscillation of the rotating gases is induced by the wobbling; the relative time-dependent gas motion is similar to the classical inertial wave phenomenon except that it is superimposed on a mean flow field with an axial vortex component. The coupling is magnified by the vortex stretching of both the quasi-steady axial vortex and the fluctuating lateral vorticity induced by the wobbling as the composite flow passes into the nozzle. Late in the motor burn, the increasing size of the chamber and the forward movement of the mass center cause these interactions to become more important relative to the jet damping, which is less dependent on the radial size of the combustion chamber. Both these gas flow interactions depend in a similar way on the *position* of the rocket motor relative to the vehicle center of mass

The physical processes described in this report are present in any spinning rocket motor, and it is emphasized that they represent a *natural phenomenon* that is not peculiar to any particular motor or spacecraft design. Gasdynamic driving may or may not cause coning instability depending upon a number of environmental conditions and relative magnitudes of a set of key parameters. In rotating motors with short burning time, the flow interactions may be present, but since they always become important near the end of burn as they chamber size increases, they may not act for a sufficient period of time to generate an appreciable coning growth. The final cone angle and lateral angular rate are sensitive to the initial nutation

amplitude at motor ignition, the spin rate, and also on the length of motor burn. These sensitivities are responsible for much of the variability that is apparent in the observations. The coning behavior is not significantly affected by the ratio of the axial to lateral moments of inertia. That is, the wobbling frequency does not affect coning growth in a major way. However, the growth rate is strongly dependent on the lateral moment of inertia and on the *dimensional* free-precession frequency, since the latter quantity is proportional to the spin rate. The reason instability occurs late in the motor run is partially the result of the decrease in lateral moment of inertia as the propellant is consumed. Another reason is the increasing volume of the combustion chamber. This is significant in that it allows gas particles emerging from the burning propellant to remain within the system for a longer period of interaction with inertial forces such as the Coriolis effect.

Some of the fine detail seen in part of the coning data such as the short growth/decay periods at about the middle of the motor run in some of the observations is only approximately reproduced by the analytical model. However, the simulated nutation shows very similar qualitative characteristics. It is of course unreasonable to expect the model to be a truly accurate representation of actual vehicle behavior because of the simplified combustion chamber shape and mean flow models used to represent the actual complex geometrical situation. Also, only approximate account was taken of the influence of the nozzle flow on dissipation or further amplification of the unsteady flow after it enters the nozzle entrance.

Since the unsteady flow interactions are complex, an attempt will be made here to describe the flow pattern generated in the motor chamber in a less mathematically intensive form than used in the body of the report. If one were able see within a spinning, wobbling rocket motor and could observe the motions of individual gas particles as they emerge from the burning zone, the major feature would be the intense vortex core stretching from the head end and out the nozzle. The rate of rotation increases rapidly as particles pass through the nozzle due to vortex stretching. Close scrutiny of the vortex would show that its motion is not steady. That is, it would not lie exactly along the motor axis of symmetry. Instead, it would precess around the axis in a direction opposite to the vehicle spin. Each gas particle leaving through the nozzle would be seen to have a distinct oscillatory motion with axial, radial and circumferential fluctuations about its mean position on the mean flow streamline. These motions become more pronounced later in the motor burn since the average stay time of a particle within the motor grows longer as the size of the combustion chamber increases due to regression of the burning propellant surfaces. The oscillatory behavior intensifies near the motor axis due to angular momentum conservation; this is another example of the vortex stretching effect. Vorticity is introduced to the gas particles at the burning zone because of the nutation and the spin. This vorticity remains with the same particles in accordance with the Helmholtz vortex laws. Thus as particles move with the mean flow toward the nozzle entrance, the oscillatory motions are intensified by vortex stretching

(conservation of angular momentum). Since the most intense oscillations act near the centerline, then the flow of angular momentum out of the system is enhanced by the small radius of the nozzle entrance relative to the chamber size. The intense flux of angular momentum in the nozzle region implies the presence of local unsymmetrical pressure patterns that produce the actual disturbing forces.

In observing particles just entering the nozzle, it would be seen that the flow oscillations are asymmetrical. That is, a particle with an upward or radially inward motion at one point is balanced by one with a downward or radially outward motion on the opposite side. Again, the vortex core does not leave through the nozzle along the centerline, but rather it precesses about the symmetry axis in the retrograde direction. It should be plain that the pressure distribution within the nozzle under the conditions described qualitatively in this paragraph would not be uniform. There is an unbalanced side force associated with the flow that travels about the channel in a direction opposite to the rotation. This side force produces a disturbing moment that can either drive or damp coning oscillations of the vehicle depending on the direction of the force relative to the instantaneous position of the chamber. The phase is controlled mainly by the time of travel of gas particles from the burning surface to the nozzle entrance.

It is difficult to calculate effects of the sort just described by determining the time-dependent pressure distributions within the system. It is always simpler to examine such situations from the standpoint of control volumes and related momentum balances. The present problem is completely analogous to that arising in the generation of axial momentum thrust by a rocket. It is an article of faith that the propulsion engineer does not need to integrate the pressure forces over the internal surface of the rocket motor in estimating the thrust. He simply determines the flux of linear momentum emerging from the exhaust nozzle and applies a control volume momentum balance. The entire analysis described in this report was carried out from this point of view. It is the flux of a *lateral component of angular momentum* emerging from the system through the nozzle that balances the nutation growth. The plume left behind the vehicle is filled with angular momentum that was imparted to the gas by the rocking motions and by the spin.

11.2 RECOMMENDATIONS FOR CONTINUED RESEARCH

No phenomenon as complex as the nutation instability effect can be understood in depth on the basis of a short research program with limited laboratory scale experimentation of the type described. Although much progress has been made in reaching an improved understanding of the physics underlying the PAM-D problem, many new questions have been raised. In the last few paragraphs, the attempt will be made to describe further efforts needed in the search for a more complete theoretical understanding of the problem, and perhaps more importantly, the experimental demonstration of its features.

Experimental study of simulated spinning rocket fluid dynamics is a very difficult undertaking, since it is necessary to perform precision measurements in a rotating coordinate frame. Thus, it would appear that cold flow testing shows the most promise in yielding detailed information on the time-dependent fluid motions in spinning chambers. The situation is much more difficult in generating needed data from actual rocket motor firings. *It is not possible to simulate conditions in static firings that are representative of the free-flight conditions if a fixed axis of rotation is used.* Also, it is not usually possible to instrument operational solid rockets in the manner required for high-resolution determination of the internal flow field. However, useful information could be obtained from motors like the STAR 48 in free flight by measuring the pressure field in the vicinity of the nozzle entrance. Since access to this region of the motor interior is available through the nozzle support structure, this should be a feasible undertaking. High-resolution pressure measurements (Kistler gauges for example) should be made at at least two azimuthal locations separated by, say, 135 degrees to facilitate phase angle determination. The best location for the pressure ports would be within the nozzle entrance forward of the throat, but measurements on the outside surface of the submerged nozzle as far forward as possible would yield useful data.

Tests that simulate the coning phenomenon should also be devised using laboratory scale motors. A feasibility study was carried out during this program indicating that all of the main features of the instability can be represented in an economical manner using small motors operating in a spinning, nutating test fixture. High rates of spin must be used to yield sufficient data resolution, so it will probably not be possible to match the full scale Rossby number in such experiments.

Unfortunately, the only experiments that will be truly convincing in the resolution of the PAM-D problem will be those carried out in actual spaceflight. It is recommended that a preliminary design of such a test program be undertaken. It may not be necessary to utilize full-scale vehicles, although final verification should be made with properly instrumented PAM-D or PAM-DII spacecraft. Since it is also possible that there will be additional satellite launches using the STAR-37E class propulsion system, it is suggested that more complete instrumentation be employed in at least one of these. High-resolution rate gyroscope measurements would be very helpful. Even though this propulsion system does not exhibit pronounced coning, such instrumented flights would provide direct verification of the presence of time-dependent spacecraft/gas interactions and would thus represent a major step toward a full understanding of the problem.

11.3 CONCLUDING REMARKS

It is appropriate to conclude this discussion by reiterating the reasons, as based on the findings of this research program, for the appearance of an unexplained nutation instability phenomenon in the PAM-D spacecraft system when such

events had not been detected in earlier spaceflight programs based on similar technology.

A main system feature contributing to the instability is the relatively large, nearly spherical STAR 48 rocket motor with its thick propellant web. This combination results in a long burning period, which is typically twice that of previous systems. This allows small perturbing torques the time necessary to generate significant nutation growth.

The large burning surface to throat distance near the end of the motor run leads to increasing gas particle stay time within the system as the propellant surfaces recede. This in turn allows inertial acceleration effects to influence the relative motion of the combustion gases significantly. The resulting unsteady flow is responsible for a flux of lateral angular momentum out of the system (and an associated unsymmetrical pressure distribution) representing an unbalanced torque on the spacecraft.

Another design feature shown to affect the nutation instability is the highly submerged nozzle with its small throat. Key elements of the gas flow are affected by this geometry in such a way that the disturbances are enhanced. The stretching of the central vortex core through the narrow nozzle entrance and its interaction with locally intensified fluctuating flow components directly influences the internal traveling pressure distributions and the resulting side force.

The prolate spacecraft shape with the motor suspended quite far aft of the center of mass also strengthens the perturbing effects generated within the chamber. The combination of the decreasing moments of inertia, the increasing lever arm, and the increasing gas particle travel distance from the burning surface to the nozzle are responsible for the the apparition of the instability late in the motor burn.

In conclusion, it has been shown that an unsteady internal gas flow in the form of traveling inertial pressure waves is induced by the rocking motion of the spacecraft. An intense axial vortex is caused by the spin of the rocket motor chamber. The combined flow pattern is responsible for coning instability in spacecraft of the PAM-D or PAM-DII type. Combustion effects are shown to have negligible influence. Most of the unbalanced side force comes from a traveling unsymmetrical pressure pattern in the nozzle entrance region. This pressure field is associated with the helical motion of the vortex core as it passes into the nozzle. Measurement of the pressure fluctuations in the nozzle entrance region will verify the proposed model. Such measurements must either be made in actual spaceflight or in spinning test stands with capability to simulate the rocking motion component. Motor tests in fixed-axis rotation will not yield useful data. Detailed simulation of the interaction with vehicle dynamics indicates that all major features of the nutation instability phenomenon are represented in considerable detail without the need to arbitrarily adjust the physical parameters describing either the spacecraft or the rocket motor.

REFERENCES

1. Cantwell, M. N., (Personal Communication), McDonnell Douglas Astronautics Company, Huntington Beach, California, 1984.
2. Thomson, W. T., Introduction to Space Dynamics, John Wiley and Sons New York, 230-235, 1961.
3. Thomson, W. T., and Reiter, G. S., "Jet Damping of a Solid Rocket: Theory and Flight Results," AIAA J.3, 413-417, 1965.
4. Rott, N. and Pottsepp, L., "Simplified Calculation of the Jet Damping Effects," AIAA J. 2, 764-766, April 1964.
5. Pottsepp, L., "Pam Coning Problem," McDonnell Douglas Astronautics Co., TM-82-101, 1982.
6. Pottsepp, L., and Lebovitz, N. R., "A General Formulation of the Equations of Motion of a Missile," Douglas Report SM-49217, 1965.
7. Webster, E. A., "Active Nutation Control for Spinning Solid Motor Upper Stages," AIAA 21st Joint Propulsion Conference, Monterey, CA July 1985.
8. Meyer, R. X., "Convective Instability in Solid Propellant Rocket Motors," AAS Paper 83-368, Astrodynamics 1983, Vol. 54, Advances in the Astronautical Sciences.
9. Abramson, H. N., "The Dynamic Behavior of Liquids in Moving Containers," NASA SP-106, 1966.
10. Sumner, I. N., "Experimentally Determined Pendulum Analogy of Liquid Sloshing in Spherical and Oblate-Spheroidal Tanks," NASA TND-2737, 1965.
11. Ono, S., "Engineering Test Satellite V Spindynamics Simulations with Sloshing Effects and Geostationing Analyses," IAF-85-76, Oct 1985.
12. Agrawal, B. N., "Stability of Spinning Spacecraft with Partially Liquid-Filled Tanks," J. Guidance and Control, 1982.

13. Hocking, L. M., "On the Unsteady Motion of a Rotating Fluid in a Cavity," *Mathematika* 12, 97-106, 1965.
14. Berlot, R. R., "Production of Rotation in a Confined Liquid Through Translational Motion of the Boundaries," *J. Applied Mechanics*, 513-516, December 1959.
15. Stewartson, K., "On the Stability of a Spinning Top Containing Liquid," *J. Fluid Mech.* 5, 577-592, 1959.
16. Stewartson, K., and Roberts, P. H. "On the Motion of a Liquid in a Spheroidal Cavity of a Precessing Rigid Body," *J. Fluid Mech.* 17, 1-10, 1963.
17. Roberts, P. H., and Stewartson, K., "On the Motion of a Liquid in a Spheroidal Cavity of a Precessing Rigid Body. II," *Proc. Camb. Phil. Soc.* 61, 279-288, 1965.
18. Ono, Shuji, "Spindynamics with Sloshing Effects for Solid Motor Burning Phase," NASDA TR 1985.
19. Kaplun, M. H., Modern Spacecraft Dynamics and Control, John Wiley & Sons, Inc., 1976.
20. D'Amico, W. P., and Miller, M. C., "Flight Instability Produced by Rapidly Spinning Highly Viscous Fluid," *J. Spacecraft and Rockets* 16, 62-64, 1979.
21. Murphy, C. H., "Angular Motion of a Spinning Projectile with a Viscous Liquid Payload," *J. Guidance, Control, and Dynamics* 6, 280-286, 1983.
22. D'Amico, W. P., and Rogers, T. H., "Yaw Instabilities Produced by Rapidly Rotating, Highly Viscous Liquids," AIAA Paper No. 81-0224, AIAA 19th Aerospace Sciences Meeting, St. Louis, MO., Jan. 1981.
23. Murphy, C. H., "Liquid Payload Roll Moment Induced by a Spinning and Coning Projectile," AIAA Paper No. 83-2142, AIAA Atmospheric Flight Mechanics Conference, Gatlinburg, TN, Aug. 1983.
24. D'Amico, W. P., Beims, W. G., and Rogers, T. H., "Pressure Measurements of a Rotating Liquid for Impulsive Coning Motion," AIAA Paper No. 82-0246, AIAA 20th Aerospace Sciences Meeting, Orlando, FL, Jan. 1982.

25. Mermagen, W. H., "Measurements of the Dynamical Behavior of Projectiles over Long Flight Paths," J. Spacecraft and Rockets 8, 380-385, 1971.
26. Gans, R. F., "Dynamics of a Near-Resonant Fluid-Filled Gyroscope," AIAA J. 22, 1465-1471, 1984.
27. Karpov, B. G., Frasier, J. T., and D'Amico, W. P., "Experimental Studies with a Liquid-Filled Gyroscope," J. Spacecraft and Rockets 9, 220-222, 1972.
28. Vaughn, H. R., Oberkampf, W. L., and Wolfe, W. P., "Fluid Motion Inside a Spinning Nutating Cylinder," J. Fluid Mech. 150, 121-138, 1985.
29. Shi, Y. Y., and Lee, R. S., "On the Resonance Interaction of Pam Coning Motion and Inertial Waves in the Contained Liquid Slag. I. Theoretical Analysis," A3-203-AATA-83-039, McDonnell Douglas Astronautics Co., July 1983.
30. Bolster, W., "Delta/PAM Coning", Internal Memorandum (with attachment by J. F. McGarvey), NASA Goddard Spaceflight Center, Greenbelt, MD., July 1982.
31. Meyer, R. X., "STAR 48 Motor Coning, Current Status," Aerospace Corporation Presentation, Los Angeles, CA., Jan 1985.
32. Walters, A. G., "Non-symmetric Flow in Laval Type Nozzles," Roy. Soc. Phil. Trans., A, Vol. 273, 185-235, 1972.
32. Rosser, J. B., Newton, R. R., and Gross, G. L., Mathematical Theory of Rocket Flight, McGraw-Hill Book Co., 1947.
33. Davis, L. Jr., Follin, J. W. Jr., and Blitzer, L., Exterior Ballistics of Rockets, D. Van Nostrand Co., 1958.
34. Kolk, W. R., Modern Flight Dynamics, Prentice-Hall, Inc., 1961.
35. Clayton, C. D., "Numerical Model of the Time Independent Mean Flow in a Rotating Rocket Motor," PhD Thesis, Department of Mechanical Engineering, University of Utah, 1985.
36. Thomson, W. (Lord Kelvin), "On an Experimental Illustration of Minimum Energy," Nature 15, 297, 1877.

37. Greenhill, A. G., "On the General Motions of a Liquid Ellipsoid,"
Proc. Camb. Phil. Soc. 4,4, 1880.
38. Stewartson, K., "On the Stability of a Spinning Top Containing Liquid,"
J. Fluid Mech. 5, 557-592, 1959.
39. Kudlick, M. D., "On Transient Motions in a Contained Rotating Fluid,"
PhD Thesis, Dept. of Mathematics, Massachusetts Institute of Technology
1966.
40. Greenspan, H. P., The Theory of Rotating Fluids, Cambridge
University Press, 1968.
41. Fultz, D., "A Note on Overstability and the Elastoid-Inertia
Oscillations of Kelvin, Solberg, and Bjerknes," J. Meteorology 16,
199-208, 1959.
42. Poincare', H., "Sur la Precession des Corps Deformables,"
Bull. Astronomique 27, 321-356, 1910.
43. Cartan, E., "Sur les Petites Oscillations d'une Masse Fluid,"
Bull. Sci. Math. 46, 317-369, 1922.
44. Lighthill, M. J., "On Waves Generated in Dispersive Systems by
Travelling Forcing Effects, with Applications to the Dynamics of
Rotating Fluids," J. Fluid Mech. 27, 725-752, 1967.
45. Rayleigh, "On the Dynamics of Revolving Fluids," Proc. Roy.
Soc. London, A93, 148 154, 1917.
46. Baines, P. G., "Forced Oscillations of an Enclosed Rotating Fluid,"
J. Fluid Mech. 30, 533-546, 1967.
47. Stewartson, K., "On the Stability of a Spinning Top Containing
Liquid," J. Fluid Mech. 5, 577-592, 1959.
48. Stewartson, K., and Roberts, P. H. "On the Motion of a Liquid in a
Spheroidal Cavity of a Precessing Rigid Body," J. Fluid Mech. 17,
1-10, 1963.
49. Roberts, P. H., and Stewartson, K., "On the Motion of a Liquid in a
Spheroidal Cavity of a Precessing Rigid Body. II," Proc. Camb.
Phil. Soc. 61, 279-288, 1965.

50. Greenspan, H. P., "On the Transient Motion of a Contained Rotating Fluid," J. Fluid Mech. 20, 673-696, 1964.
51. Greenspan, H. P., "On the General Theory of Contained Rotating Fluid Motions," J. Fluid Mech. 22, 449-462, 1965.
52. Scott, W. E., "The Large Amplitude Motion of a Liquid-Filled Gyroscope and the Non-interaction of Inertial and Rossby Waves," J. Fluid Mech. 72, 649-660, 1975.
53. Wedemeyer, E. H., "The Unsteady Flow within a Spinning Cylinder," J. Fluid Mech. 20, 383-399, 1964.
54. Hocking, L. M., "On the Unsteady Motion of a Rotating Fluid in a Cavity," Mathematika 12, 97-106, 1965.
55. Berlot, R. R., "Production of Rotation in a Confined Liquid Through Translational Motion of the Boundaries," J. Applied Mechanics, 513-516, December 1959.
56. Aldridge, K. D., "Axisymmetric Inertial Oscillations of a Fluid in a Rotating Spherical Shell," Mathematika 19, 163-168, 1972.
57. Bennetts, D. A. and W. D. N. Jackson, "Source-Sink Flows in a Rotating Annulus: A Combined Laboratory and Numerical Study," J. Fluid Mechanics 66, Pt. 4, 689-705, 1974.
58. Price, E. W., "Experimental Solid Rocket Combustion Instability," Tenth Symposium (International) on Combustion, Combustion Institute, Pittsburgh, Pa, 1067-1082, August 1964.
59. Culick, F. E. C., "Stability of Longitudinal Oscillation with Pressure and Velocity Coupling in a Solid Propellant Rocket," Comb. Sci and Technology, 2, 179-201, 1971.
60. Flandro, G. A., "Energy Balance Analysis of Nonlinear Combustion Instability," J. Propulsion and Power 1, 210-221, May-June 1985.
62. Brown, R. S., et al, "Vortex Shedding Studies," AFRPL TR-80-13, Contract No. FO4611-77-C-0060, United Technologies, Chemical Systems Division, April 1980.
63. Sigman, R. K., "Boundary Condition for Rocket Motor Stability," AIAA J. 23, 1079-1085, July 1985.

NOMENCLATURE

b	Fineness Ratio of combustion chamber, L/D
D	Chamber diameter
E	Ekman number = $\nu/\Omega R^2$
e_n	Unit vector in direction of coordinate n (k is also used to represent z -axis)
k_{mn}	Inertial mode integers
L	Combustion chamber length
M	Moment vector
n	Unit normal vector (positive outward from origin)
p	Reduced pressure
P	Thermodynamic pressure
Q	Spatial part of inertial wave velocity vector
r, θ, z	Polar coordinates
r	Position vector relative to center of mass
R_0	Chamber radius
R_b	Propellant pressure coupled response function
S	Area
u	Velocity vector
U	Mean flow velocity vector
V	Volume
x, y, z	Pitch, yaw and roll body fixed cartesian axes

Greek Symbols:

α	Exponential growth rate
β	Complex frequency $\alpha + i\lambda$
γ	Ratio of specific heats

δ	Moment scaling parameter in Euler's equations of motion
ϵ	Rossby number = $v_b/R\Omega$
ϕ	Phase angle between moment and vehicle angular velocity vector
ζ	Spatial part of inertial pressure disturbance
λ_n	Inertial mode frequency (n denotes triplet [kmn] for a particular mode)
λ_s	Spacecraft free-precession frequency
ρ	Gas density
ω	Angular velocity vector
ω_{xy}	Perturbation angular velocity in lateral plane
Ω	Spin angular velocity (same as ω_z)
ψ	Amplitude of vehicle perturbation angular velocity
Γ	Strength of axial vortex flow

Other notation:

Primes denote oscillatory quantities

Vectors are indicated by boldface type

Subscript o indicates constant mean reference value

Subscript i refers to imaginary part (also denoted by superscript (i))

Subscript r refers to real part (also denoted by superscript (r))

* indicates complex conjugate

APPENDIX

EXPANSIONS OF FUNCTIONS C_m , D_m , E_m^2 , F_m^2 and G_m

The complicated functions resulting from integration of various expressions in the Section 6 analysis are displayed in detailed form in what follows. The expansions were made assuming a cylindrical chamber geometry. Prime indicates derivative of Bessel function with respect to its argument.

Function C_m : $C_m = C_m^{(r)} + iC_m^{(i)}$, where

$$C_m^{(r)} = 4\pi (\cos n\pi - 1) \left[8b^2 J_1(\xi) / (n\pi)^2 + [\xi J_0(\xi) - 2 J_1(\xi)] / (\xi^2 \lambda_m) \right] / E_m^2$$

$$C_m^{(i)} = 4\pi (\cos n\pi - 1) \left[(\xi - 2J_1(\xi)) / (\xi^2 \lambda_m) \right] / E_m^2$$

Function D_m :

$$D_m = 4\pi (\cos n\pi - 1) \left[[2 / (\xi^2 \lambda_m) + 4b^2 / (n\pi)^2 (2 - \lambda_m)] J_1(\xi) - J_0(\xi) / (\xi \lambda_m) \right] / E_m^2$$

Function E_m^2 : (Normalization function for inertial velocity eigenfunctions)

$$E_m^2 = 2\pi b \left[(4 + \lambda_m^2) [(\xi^2/2)(J_0'^2(\xi) + J_0'^2(\xi)) - J_1'^2(\xi)] + 4\lambda_m J_1'^2(\xi) \right] / (4 - \lambda_m^2)^2 + \\ + (n\pi/2\lambda_m b)^2 \pi b [J_1'^2(\xi) + (1 - 1/\xi) J_1'^2(\xi)]$$

Function F_m^2 :

$$F_m^2 = \pi \left[(1 + 2b) J_1'^2(\xi) + J_0(\xi)(J_0'(\xi) - 2J_1'(\xi)/\xi) \right]$$

Function G_m : $G_m = G_m^{(r)} + i G_m^{(i)}$, where

$$G_m^{(r)} = 8\pi b \xi \left[(J_1'^2(\xi) [2 - (4 + \lambda_m^2)/2\lambda_m] - \xi^2 [J_0'^2(\xi) + J_0'^2(\xi)]) \right] / (4 - \lambda_m^2)^2 E_m^2$$

$$G_m^{(i)} = 4\pi^3 n^2 \left[[1 - J_0'^2(\xi) - J_1'^2(\xi) - J_1'(\xi)/\xi^2] / \lambda_m + \right. \\ \left. + (J_1'^2(\xi)/2 - J_0(\xi) J_2'(\xi)/2) \right] / (4 - \lambda_m^2) E_m^2 \\ - n\pi^2 \sin(n\pi z/b) \left[[1 - J_0'^2(\xi) - J_1'^2(\xi)] \lambda_m/2 + \right. \\ \left. + J_1'^2(\xi) \right] / 2b R_t^2 \lambda_m (4 - \lambda_m^2) E_m^2$$

END

4-~~scribble~~-87

DTIC